UNIVERSITÀ DEGLI STUDI DI TRIESTE
e
UNIVERSITÀ CA' FOSCARI DI VENEZIA

XXXII CICLO DEL DOTTORATO DI RICERCA IN

CHIMICA

Design of Bismuth-based luminescent materials for multi-modal imaging and optical thermometry

Settore scientifico-disciplinare: **CHIM/02**

DOTTORANDA
ELISA CASAGRANDE

COORDINATORE
PROF. BARBARA MILANI

SUPERVISORE DI TESI
PROF. PIETRO RIELLO

CO-SUPERVISORE DI TESI
Dr. MICHELE BACK

ANNO ACCADEMICO 2018/2019

Index

List of Abbreviations

2D	two-dimensional
3D	three-dimensional
ATP	Adenosine triphosphate
BET	Brunauer-Emmett-Teller theory
BSE	backscattered electrons
BSO	Bismuth silicon oxide (or bismuth silicate)
CCD	charge-couple device
CD	carbon dot
CFU	colony forming unit
CIE	*Commission internationale de l'éclairage* diagram
CLU	cooperative luminescence upconversion
CR	cross-relaxation
CSU	cooperative sensitization upconversion
CT	computed X-ray tomography
DC	downconversion
DS	downshifting
DSC	differential scanning calorimetry
EBT	energy back-transfer
EDS	energy-dispersive X-ray spectroscopy
EG	Ethylene glycol
ESA	excited state absorption
ET	energy transfer
ETU	energy transfer upconversion
FE-SEM	field emission scanning electron microscopy
FIR	fluorescence intensity ratio
FRET	Förster resonance energy transfer
FT-IR	Fourier Transform Infrared Spectroscopy
FWHM	full width at half maximum
GSA	ground state absorption
IC_{50}	half maximal inhibitory concentration
IR	infrared
IUPAC	International Union of Pure and Applied Chemistry
LDH	layered double hydroxide
LED	light emitting diode
LPE	lone pair electron
MO	Methyl-Orange
MW	molecular weight
NA	nutrient agar
NB	nutrient broth

NCs	nanocrystals
NIR	near infrared
NPs	nanoparticles
PA	photon avalanche
PAT	photoacoustic tomography
PL	photoluminescence
PMT	photomultiplier
PVP	polyvinylpyrrolidone
QC	quantum cutting
QDs	quantum dots
RE	rare earths
RGB	red-green-blue
RLU	relative luminescence unit
SGH	second harmonic generation
SPECT	single-photon emission computed tomography
SVR	surface to volume ratio
TEM	transmission electron microscopy
TEOS	Tetraethyl orthosilicate
TGA	thermogravimetric analysis
TPA	two-photon absorption
UC	upconversion
UCNCs	upconverting nanocrystals
UCNPs	upconverting nanoparticles
UCPL	upconversion photoluminescence
UV	ultraviolet
VB	valence band
VIS	visible
XRPD	X-ray powder diffraction

List of Tables

Chapter 2

Chapter 3

Chapter 5

Chapter 7

Chapter 8

List of Figures

Chapter 1

Chapter 2

Chapter 3

Fig. 5 Image of mice tumors (a), with $LaF_3:Nd^{3+}$ NPs injected only in the left side (right-side tumor was used as control); Infrared fluorescence (b) and Infrared Thermal (c) images under 808 nm laser irradiation (4 W cm^{-2}).

Chapter 4

Fig. 1 Bi_2O_3-SiO_2 binary system phase diagram.

Fig.2 Stable and metastable polymorphs of Bi_2O_3 and their temperature dependence.

Chapter 5

Fig.1 Schematic illustration of the synthesis procedure for lanthanide-doped $Bi_2SiO_5@SiO_2$

Fig.2 SEM images of Bi_2O_3 NPs synthetized by varying the precipitant agent: (a) KOH, (b) NaOH, (c) NH_4OH and (d) $CO(NH)_2$. Mean size of each sample (estimated by stastically sampling N=500 NPs) is indicated underneath SEM images.

Fig.3 SEM images of two series of Bi_2O_3 NPs synthetized by varying the molecular weight of PVP capping agent, either with NaOH or Urea as precipitant agent: (a, f) MW=10 kg/mol, (b, g) MW=29 kg/mol, (c, h) MW=40 kg/mol, (d, i) MW=360 kg/mol and (e, j) MW=1300kg/mol. Mean size (estimated by statistically sampling N=500 NPs) is indicated underneath SEM images.

Fig.4 Uniform Bi_2O_3 NPs, synthetized with PVP with MW=40 kg/mol as capping agent and either with NaOH or Urea as precipitant agent: (a,e) SEM images, (b,f) size distributions (N=700), (c,g) single particle TEM and (d,h) HR-TEM images.

Fig.5 N_2 adsorption/desorption isothermal curves for Bi_2O_3 NPs, synthetized either with (a) NaOH or (b)urea as precipitant agent.

Fig.6 (a) FT-IR spectrum of Bi_2O_3 NPs before (black line) and after (blue line) the thermogravimetric analysis (780°C) showing the typical peaks for stretching and bending vibrations in EG and PVP, (b) TG (blue line) and DTG (red line) showing weight loss peaks relative to EG and PVP calcination at 240 and 350°C, respectively.

Fig.7 XRPD pattern of the synthetized Bi_2O_3 NPs.

Fig.8 FE-SEM images of Er-doped Bi_2O_3 NPs, synthetized with urea as precipitant agent, with different at.% content of Er: (a) 0.5%, (b) 1%, (c) 2%, (d) 4%, (e) 6% and (d) 8%.

Fig.9 Size distributions of the Er-doped Bi_2O_3 NPs as a function of the Er content

Fig.10 (a) FE-SEM, (b, c) HR-TEM images and (d, e) EDS analysis of Er-doped Bi_2O_3 NPs with 10%at. of Er.

Fig.11 FE-SEM images of Yb-Er co-doped Bi_2O_3 NPs, synthetized with urea as precipitant agent, with different at.% content of Yb and Er: (a) Yb6-Er1% and (b) Yb10-Er1%.

Fig.12 FE-SEM images of Er-doped and Yb-Er co-doped Bi_2O_3 NPs, synthetized with NaOH as precipitant agent, with different at.% content of Yb and Er: (a) Er 5%, (b) Er 10%, (c) Yb6-Er1% and (d) Yb10-Er1%.

Fig.13 (a, c) DSC curves and (b, d) the XRPD patterns for the resulting crystalline phase of the undoped and 2 at.% Er-doped Bi_2O_3 NPs.

Fig.14 Effect of a single addition of equivalent volume of TEOS at once on the silica shell growth. (a, b, c) SEM images for a TEOS (μL):Bi_2O_3 (mg) ratio of 2, 4 and 8 eventually showing the formation of non-shelling silica NPs (indicated by red arrows), (d, e, f) size distributions (N=700) eventually showing the presence of a second population of SiO2 NPs and (g, h, i) gaussian distributions of NPs, showing mean size of Bi_2O_3 and SiO_2 NPs, when present.

Fig.15 Effect of subsequent additions of equivalent aliquots of TEOS on the silica shell growth. (a,b) Conventional secondary electrons (SE) and backscattered electrons (BSE) SEM images for a TEOS (μL):Bi_2O_3 (mg) ratio of 4. The red arrows evidence the silica NPs formed during the SiO_2 shell growth on Bi_2O_3 NPs surface. (c,d) Representative SE and BSE SEM images of the silica shells grown on Bi_2O_3 NPs with two subsequent TEOS additions strategy of 2 μL of TEOS per mg of Bi_2O_3 NPs.

Fig.16 Fine control of the silica shell thickness on the Bi_2O_3 NPs surface. Representative SEM (a) and TEM (b) images of the core-shell Bi_2O_3@SiO_2 prepared by a single addition of 2μL of TEOS per mg of Bi_2O_3 NPs synthetized by using urea. (c) Distributions of the diameter of the NPs as a function of the TEOS (μL):Bi_2O_3 (mg) ratio (0, 1, 2, 4, 8 and 12) for the Bi_2O_3 NPs synthetized with NaOH. Representative SEM images of a single Bi_2O_3@SiO_2 nanoparticle as a function of silica shell growth (increasing thickness from left to right) for Bi_2O_3 prepared with (d) urea and (e) NaOH. (f) Experimental and theoretical shell thickness as a function of the mL of TEOS used for a fixed amount of NPs (40 mg). The error bars represent the deviation of the mean value of three experiments. Inset: schematic geometrical representation used for the theoretical model of eq. 1.

Fig.17 Schematic geometrical representation used for the theoretical model of Eq. 1, where r_{cs} and r_c represent the radius of the core NPs (Bi_2O_3) with and without the silica shell respectively and t_{shell} represents the thickness of the silica embedding layer.

Fig.18 Representative HR-TEM single particle images for different SiO_2 shell thickness for the Bi_2O_3 NPs prepared with NaOH (a-c) and urea (d-f). The numbers represent the TEOS (μL):Bi_2O_3 (mg) ratio (1, 2, and 8).

Fig.19 (a) DSC curves, (b) XRPD patterns and (c,d,e) SEM images of the Bi_2O_3:Er@SiO_2 NPs with different silica shell thickness (11±2 nm, 23±1 nm and 40±2 nm) after the DSC analysis.

Fig.20 In-situ temperature dependent synchrotron radiation XRPD patterns (λ=1.12576 Å) of the undoped Bi_2O_3@SiO_2 system with a shell of about 40 nm.

Fig.21 Study of thermal effect on the structural and morphological properties during

the Bi_2O_3:Er@SiO_2 NPs: Bi_2SiO_5:Er@SiO_2 transition: (a) Temperature dependent XRPD patterns and (b) Rietveld refinement of the nanosystem annealed at 700 °C. (c) HR-TEM images of a single particle as a function of thermal treatment at different temperatures from 400 to 700°C, SE and BSE SEM images of 2%at. Er^{3+}-doped Bi_2O_3:Er@SiO_2 treated at (d) 400 °C and (e) 700 °C.

Fig.22 HR-TEM image (left) and EDS spectra (right) recorded for the Bi_2SiO_5:Er@SiO_2 sample treated at 700 °C: (1) SiO_2 shell, (2) Bi_2SiO_5:Er layer and (3) the centre of the hollow particle.

Fig.23 UC PL spectra (a, b, c) and double logarithmic plot (d, e, f) with linear fit of the luminescence intensity versus pump power to determine the order of the upconversion excitation processes, of Yb-Er, Yb-Tm and Yb-Ho co-doped Bi_2SiO_5@SiO_2 NPs, respectively. Capital letters represent the transitions of Er^{3+} (A: $^2H_{11/2} \rightarrow {}^4I_{15/2}$; B: $^4S_{3/2} \rightarrow {}^4I_{15/2}$; C: $^4F_{9/2} \rightarrow {}^4I_{15/2}$), Tm^{3+} (D: $^1G_4 \rightarrow {}^3H_6$; E: $^1G_4 \rightarrow {}^3F_4$; F: $^3F_{2,3} \rightarrow {}^3H_6$; G: $^3H_4 \rightarrow {}^3H_6$) and Ho^{3+} (H: $^5S_2$,$^5F_4 \rightarrow {}^5I_8$; I: $^5F_5 \rightarrow {}^5I_8$; J: $^5S_2$,$^5F_4 \rightarrow {}^5I_7$).

Fig.24 UC PL spectra (a, b, c, d) of Bi_2SiO_5@SiO_2 NPs doped with multiple combinations of Ln^{3+} ions, i.e. Yb-Er-Tm, Yb-Ho-Tm and Yb-Er-Ho-Tm, respectively. Capital letters represent the transitions of Er^{3+} (A: $^2H_{11/2} \rightarrow {}^4I_{15/2}$; B: $^4S_{3/2} \rightarrow {}^4I_{15/2}$; C: $^4F_{9/2} \rightarrow {}^4I_{15/2}$), Tm^{3+} (D: $^1G_4 \rightarrow {}^3H_6$; E: $^1G_4 \rightarrow {}^3F_4$; F: $^3F_{2,3} \rightarrow {}^3H_6$; G: $^3H_4 \rightarrow {}^3H_6$) and Ho^{3+} (H: $^5S_2$,$^5F_4 \rightarrow {}^5I_8$; I: $^5F_5 \rightarrow {}^5I_8$).

Fig.25 CIE diagram for all the Ln^{3+}-doped Bi_2SiO_5@SiO_2 NPs produced, including the relative picture under 977 nm diode exposure. The white-light emitting sample corresponds to the triple doping Yb-Er-Tm with at.% of 6, 1 and 0.5, respectively.

Fig.26 Diffuse reflectance spectra (a, b, c) of Yb-Er, Yb-Tm and Yb-Ho co-doped Bi_2SiO_5@SiO_2 NPs, respectively, with the Kubelka–Munk function (inset) and bandgap estimation (d, f, e) as the intercept of the fitted straight line at F(R)=0 in the $(F(R)\cdot h\nu)^2$ versus hν plot. Capital letters represent the transitions of Er^{3+} (A: $^4I_{15/2} \rightarrow {}^2F_{7/2}$, B: $^4I_{15/2} \rightarrow {}^2H_{11/2}$, C: $^4I_{15/2} \rightarrow {}^4S_{3/2}$, D: $^4I_{15/2} \rightarrow F_{9/2}$, E: $^4I_{15/2} \rightarrow {}^4I_{9/2}$), Tm^{3+} (F: $^3F_4 \rightarrow {}^1D_2$, $^3H_6 \rightarrow {}^1G_4$, G: $^3F_4 \rightarrow {}^1G_4$, H: $^3H_6 \rightarrow {}^3F_{2,3}$, I: $^3H_6 \rightarrow {}^3H_4$), Ho^{3+} (J: $^5I_8 \rightarrow {}^5G_5$, K: $^5I_8 \rightarrow {}^5G_6$, L: $^5I_8 \rightarrow {}^5F_3$, M: $^5I_8 \rightarrow {}^5S_2$, $^5F_4$, N: $^5I_8 \rightarrow {}^5F_5$).

Fig. 27 (a) Size distribution gaussian bells for the four samples of the $(Bi_{1-x}Nd_x)_2O_3$ series with x=0.005, 0.01, 0.02 and 0.05; (b) EDS spectrum of Bi_2O_3 NPs with a 2%at. content of Nd^{3+}.

Fig.28 FE-SEM images (a, b, c) and corresponding size distributions (N=700) (d, e, f) of Bi_2O_3, Bi_2O_3@SiO_2 and Bi_2SiO_5@SiO_2 samples, with a 2%at. content of Nd^{3+}.

Fig.29 XRPD patterns of (a) the synthetized Bi_2SiO_5 nanoparticles, with different Nd^{3+} content and (b) $(Bi_{0.98}Nd_{0.02})_2SiO_5$ NPs compared to the corresponding ICSD#245035 crystal structure.

Fig.30 (a) PL spectra and (b) integrated intensities of $^4F_{3/2} \rightarrow {}^4I_{9/2}$ transition relative to the various samples of the $(Bi_{1-x}Nd_x)_2O_3$ series with x=0.005, 0.01, 0.02 and 0.05,

Chapter 6

Fig.5 (a) Calibration curve with absorbance values at 465 nm of different Methyl Orange concentrations in aqueous solution, (b) Photo-oxidation of an aqueous solution of MO as a function of time, under UV LED irradiation for TiO_2 P25 powder (red squares) and $Bi_2SiO_5@SiO_2$ NPs (black squares). The grey frame represents the equilibration time in the dark.

Fig.6 Solution decolouration as a function of MO degradation in time, in the presence of (a) TiO_2 P-25 powders and (b) $Bi_2SiO_5@SiO_2$ NPs.

Fig.7 SEM images of Bi_2O_3 and $Bi_2SiO_5@SiO_2$ NPs before and after the exposure to acid solutions, either HCl or HNO_3, with different pH values for 3 hours.

Fig.8 XRPD patterns of $Bi_2SiO_5@SiO_2$ NPs exposed for increasing time intervals, to HNO_3 1M.

Chapter 7

Fig.1 Temperature dependence of PL emission spectra in the 80−800 K range, normalized to the $^4S_{3/2}$ line.

Fig.2 Temperature dependence of integrated UC PL intensities of the Er^{3+} transitions from $^2H_{11/2}$ (green dots) and $^4S_{3/2}$ (yellow dots) $^4F_{9/2}$ (red dots) to ground state $^4I_{15/2}$ and the total sum of their intensities (black dots) (a) in the whole temperature range tested and (b) in the physiological range (290-320 K).The lines between symbols have been added for guiding the eye. (c) Arrhenius plot in the temperature range of linearity for the Boltzmann law (280-800 K) and estimation of the distance in energy (ΔE) between the two thermally coupled levels (d)Fit of the spectrum collected at 300 K, for the empirical estimation of ΔE as the distance between the barycenters ($x_{4S3/2}$= 18.3x10^3 cm^{-1}, $x_{2H11/2}$= 19.1x10^3 cm^{-1}) of the two multiplets. (e) Absolute sensitivity of the Yb^{3+}/Er^{3+}-based thermometric system, (f) Relative sensitivity of the Yb^{3+}/Er^{3+}-based thermometric system. (The blue frame indicates the physiological temperature range).

Fig.3 (a) Temperature uncertainty. (b) Repeatability, upon four subsequent temperature cycling between 300 and 800 K. The computed parameter R was >99%.

Fig.4 (a) Temperature dependence of PL emission spectra in the 80−800 K range, normalized to the $^3H_4$ line. (b) Temperature dependence of integrated UC PL intensities of the Tm^{3+} transitions from $^3F_{2,3}$ (orange dots) and $^3H_4$ (red dots) to ground state $^3H_6$. The dotted lines between symbols have been added for guiding the eye. (c) Arrhenius plot, where the linearity for the Boltzmann law is true in a selected range of temperatures (400-800 K), and estimation of the distance in energy (ΔE) between the two thermally coupled levels. (d) Fit of the spectrum collected at 300 K, for the empirical estimation of ΔE as the distance between the barycenters (x_{3H4}=12.5x10^3 cm^{-1}, $x_{3F2,3}$=14.3x10^3 cm^{-1}) of the two multiplets. (e) Absolute sensitivity of the $^3F_{2,3}/^3H_4$ Yb^{3+}/Tm^{3+}-based thermometric system, in the range of validity of the Boltzmann law. (f) Relative sensitivity of the $^3F_{2,3}/^3H_4$ Yb^{3+}/Tm^{3+}-based thermometric system, in the range of validity of the Boltzmann law.

Fig.5 Arrhenius plot, between 280 and 400 K, where the Boltzmann law is not effective.

Fig.6 (a) Temperature dependence of PL emission spectra in the 80−500 K range, normalized to the $^1G_4$ line. (b) Temperature dependence of integrated UCPL intensities of the Tm^{3+} transitions from $^3F_{2,3}$ level to ground state $^3H_6$ (red dots) and from $^1G_4$ to $^3F_4$ level (orange dots). The dotted lines have been added for guiding the eye. (c) Arrhenius plot, where the linearity for the Boltzmann law is true in a selected range of temperatures (260-400 K), and estimation of the distance in energy (ΔE) between the two thermally coupled levels. (d) Fit of the spectrum collected at 300 K, for the empirical estimation of ΔE as the distance between the barycenters ($x_{3F2,3}$=14.27x10^3 cm^{-1}, x_{1G4}=15.44 x10^3 cm^{-1}) of the two bands. (e) Absolute sensitivity of the $^3F_{2,3}/^1G_4$ Yb^{3+}/Tm^{3+}-based thermometric system, in the range of validity of the Boltzmann law, (f)Relative sensitivity of the $^3F_{2,3}/^1G_4$ Yb^{3+}/Tm^{3+}-based thermometric system. (The blue frame indicates the physiological temperature range).

Chapter 8

Fig.1(a) Temperature dependence of PL emission spectra in the 80−850 K range, normalized to the $^4F_{3/2}$ line; (b) Temperature dependence of integrated PL intensities of the Nd^{3+} transitions from $^4F_{5/2}$ (red dots), $^4F_{3/2}$ (brown dots) and the total sum of their intensities (grey dots); (c) Arrhenius plot in the temperature range of linearity for the Boltzmann law (280-850 K) and estimation of the distance in energy (ΔE) between the two thermally coupled levels; (d) Fit of the spectrum collected at 300 K, for the empirical estimation of ΔE as the distance between the barycenters ($x_{4F3/2}$=11.4x10^3 cm^{-1}, $x_{4F5/2}$=12.3x10^3 cm^{-1}) of the two multiplets; (e) Absolute sensitivity of the Bi_2SiO_5: Nd^{3+}@SiO_2 thermometric system; (f) Relative sensitivity of the Bi_2SiO_5: Nd^{3+}@SiO_2 thermometric system. (The blue frame indicates the physiological temperature range).

Fig.2 Repeatability upon temperature cycling between 250 and 850 K, R>99%.

Fig.3 (a) Temperature dependence of PL emission spectra in the 100−700 K range, normalized to the $^4F_{3/2}$ line; (b) Temperature dependence of integrated PL intensities of the Nd^{3+} transitions from $^4F_{5/2}$ (red dots), $^4F_{3/2}$ (brown dots) and the total sum of their intensities (grey dots); (c) Arrhenius plot in the temperature range of linearity for the Boltzmann law (260-700 K) and estimation of the distance in energy (ΔE) between the two thermally coupled levels; (d)Fit of the spectrum collected at 300 K, for the empirical estimation of ΔE as the distance between the barycenters ($x_{4F3/2}$=11.3x10^3 cm^{-1}, $x_{4F5/2}$=12.3x10^3 cm^{-1}) of the two multiplets, (e)Absolute sensitivity of the $Bi_4Si_3O_{12}$:Nd^{3+}@SiO_2 NPs thermometric system; (f) Relative sensitivity of the $Bi_4Si_3O_{12}$:Nd^{3+}@SiO_2 NPs thermometric system. (The blue frame indicates the physiological temperature range).

Fig.4 (a) Temperature dependence of PL emission spectra in the 80−700 K range, normalized to the $^4F_{3/2}$ line; (b) Temperature dependence of integrated PL intensities

of the Nd^{3+} transitions from $^4F_{5/2}$ (red dots), $^4F_{3/2}$ (brown dots) and the total sum of their intensities (grey dots); (c) Arrhenius plot in the temperature range of linearity for the Boltzmann law (260-700 K) and estimation of the distance in energy (ΔE) between the two thermally coupled levels; (d) Fit of the spectrum collected at 300 K, for the empirical estimation of ΔE as the distance between the barycenters ($x_{4F3/2}=11.1x10^3$ cm^{-1}, $x_{4F5/2}=12.2x10^3$ cm^{-1}) of the two multiplets; (e) Absolute sensitivity of the $Bi_{12}SiO_{20}:Nd^{3+}@SiO_2$ NPs thermometric system; (f)Relative sensitivity of the $Bi_{12}SiO_{20}:Nd^{3+}@SiO_2$ NPs thermometric system. (The blue frame indicates the physiological temperature range).

Acknowledgements

Many people have earned my gratitude during the past three years.

First, I would like to thank Prof. Riello. This work would not have been possible without him. His support and encouragement constantly accompanied me.

I am especially indebted to Dr. Michele Back, for his unwavering guidance despite distance and time difference. He introduced me to the field of Luminescence and patiently pushed me to pursue my goals. He taught me more than I could ever give him credit for.

I am grateful to Prof. Benedetti for giving me precious advice during this long journey and for remembering me how to adopt a positive attitude towards any problem.

I wish to thank Prof. Trave for his readiness to help me with measurements and for the inspiring chats about the results.

I am grateful to all of those with whom I have had the pleasure to work during this and other related projects.

I would like to thank all the technicians. Tiziano, Davide and Martina, you are the roots that hold together the ETA Building. A special mention goes to Tiziano, always ready to help. I will forever be thankful to Francesca, whose administration support was priceless.

I wish to acknowledge Emmanuele and Riccardo, they both contributed to enhance my professional skills. Besides, they have been great friends, along with Benedetta, Vincenzo and Gabriele.

Thank you, Federica. We shared our path only for a short period of time, but you have been inspiring, pushing me to be more self-confident.

To the “Fioi di via Torino”, I am glad I met you all and had the chance to spend time with you. In random order: Eleonora, Leonardo, Sara, Mirena, Emanuele, Anna, Nicolò, Gloria, Laura, Francesca, Alessandro and anyone else I may have forgotten.

I would also like to say a heartfelt thank you to the members of my family, for the constant support. Mom and Dad, you taught me the most precious lesson: success requires sacrifice.

And last, but not least, Tommaso. Thank you, just for being there whenever I needed you.

Abstract

Upconversion phosphor materials, usually consisting of crystals doped with lanthanide ions, are attracting increasing attention and several possible applications in various fields have been proposed so far: e.g. solar cells with improved efficiency, nanomaterials for bio-imaging, microtags in anti-counterfeiting inks and lasers and novel display technologies.

In recent years, lanthanide (Ln^{3+})-doped upconverting nanoparticles (UCNPs) have proved to be photostable and basically nontoxic, thus have been presented as efficient and versatile bioimaging probes. This type of nanoparticles can be excited with near-infrared (NIR) light, while emitting higher-energy photons in a wide range of the electromagnetic spectrum, from the ultraviolet (UV), to visible (VIS) and near infrared (NIR) regions, via a multiphoton process. In particular, operating within the biological window leads to several advantages, such as drastically reduced photodamage and autofluorescence background, and remarkable tissue penetration.

On the other hand, bismuth-based luminescent materials have proved to be excellent candidates for the design of bulk and nanosized phosphors, thanks to peculiar optical characteristics and appealing properties such as low cost of production and almost non-toxicity.

Driven by these factors our work is mainly focused on the development of novel nanostructures, i.e. lanthanide-doped bismuth silicate-silica core-shell nanoparticles, to be employed as biological probes. A new synthetic procedure is here developed to obtain NPs composed of a crystalline Bi_2SiO_5 core embedded in a glassy shell of dense SiO_2. Uniform, monodispersed, crystalline and non-toxic nanoparticles are obtained. The tunability of the UC emission is investigated by co-doping the system with different combinations and relative concentrations of lanthanide ions (Yb, Er, Ho, Tm). Lanthanide-doped $Bi_2SiO_5@SiO_2$ NPs are thoroughly characterized, allowing to assess their potential as bioimaging and temperature sensing nanoprobes. In fact, the strongly temperature-dependent behaviour of the upconversion photoluminescence (UCPL) in lanthanide ions, allows to develop ratiometric luminescent thermal sensors, emitting in the VIS or NIR regions, with promising properties in the biological field. The Nd^{3+} singly-doped $Bi_2SiO_5@SiO_2$ system is also investigated as thermal bio-probe and its optical properties are compared with that of two others bismuth silicate phases of the Bi_2O_3-SiO_2 phase diagram, namely $Bi_4Si_3O_{12}$ and $Bi_{12}SiO_{20}$. Moreover, the synthesized NPs are multifunctional, potentially being multi-modal probes for combined optical imaging and X-ray computed tomography (CT)/single-photon emission CT (SPECT)/photoacoustic tomography (PAT), thanks to the X-ray attenuating properties of the bismuth-based matrix.

CHAPTER 1

General Introduction

1.1 Nanoparticles

Nanoparticles are defined as an ultrafine particulate material, which composing units have at least one dimension between 1 and 100 nm[1-3].

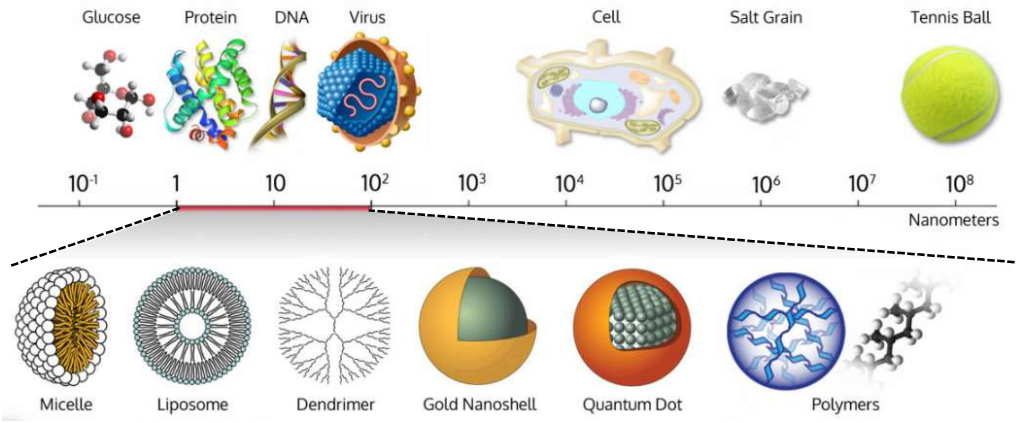

Fig. 1 Size comparison of biological samples and nanoscale materials (from www.wichlab.com)

They can be produced with various geometric shapes, such as spheres[4,5], stars[6], cages[7], planes[8,9], rods[10,11] and wires[12], through well-controlled synthetic processes. Moreover, NPs possess unique properties that are very different from their bulk counterparts, such as high surface-to-volume ratio, high surface energy, unique mechanical, thermal, optical, magnetic and electrical features[13,14], that make them candidates for a wide variety of applications, ranging from electronics, to communications, to energy harvesting and storage, to biology and medicine.

1.2 Luminescent Nanomaterials

During the last decades, luminescent nanomaterials have attracted great interest worldwide because of their unusual optical properties, together with efforts to obtain miniaturised devices. Their peculiar properties can be manipulated to obtain tailored performances, particularly suitable for the desired end-use application. Moreover, their size and properties paved the way for innovative fields of application, such as bioimaging[15-17], theragnostic medicine[16-18], contact-less thermal sensing[19-20], anti-counterfeiting[21] and many others. For this reason, luminescent NPs might have in the future a tremendous potential in revolutionizing everyday life, involving different fields of cutting-edge optical technology, and demanding ongoing research on more efficient materials[22].

Luminescent nanomaterials are generically assigned to four classes (Fig. 1): (a) semiconductor quantum dots (QDs) and carbon dots (CDs), (b) metal nanoclusters, (c) metal-doped nanomaterials and (d) organic–inorganic composites and hybrids. QDs, CDs and metal nanocluster luminescence emission is based on quantum-confinement effects, thus different emission colours are obtained simply by tuning their size. On the other hand, in the case of luminescent centres embed in nanoparticles, the luminescence emission is independent from the size of the particle, facilitating the synthesis but, at the same time, limiting the emission to a single colour.

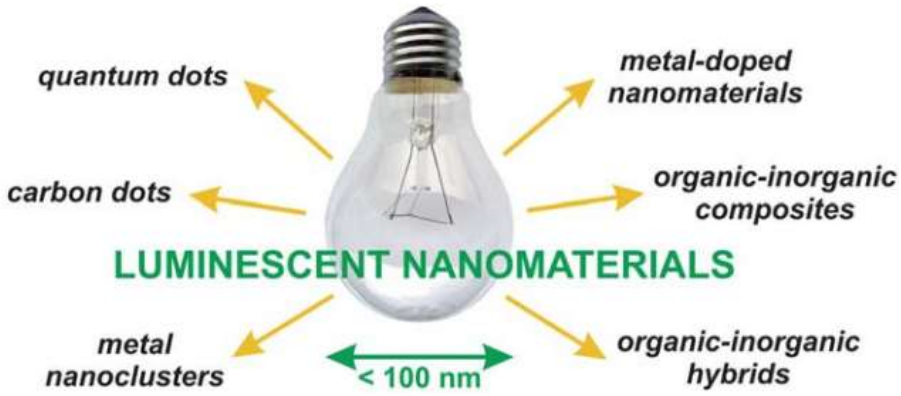

Fig. 2 Different types of luminescent materials.

Optically active inorganic nanoparticles doped with lanthanide ions are able to produce fluorescence under a suitable light irradiation. Their advantages include controllable size, excellent photostability (nonblinking, nonphotobleaching), tunable and narrow spectra and resistance to environmental conditions such as pH and temperature[23].

Rare-earth doped NPs emissions are spread throughout all the UV-VIS-NIR emission spectrum (Fig.2).

The UC output colour can be finely tailored by controlling different parameters, such as dopant composition[24] and concentration[25], excitation wavelength[26], power density[27], and host lattice[28] of the nanocrystals.

Thanks to the ladder-like energy structure of lanthanide ions, selective doping allows to control and modulate the population distribution of different emitting levels, via energy transfer (ET) phenomena[15].

Rare-earth doped NPs have a plethora of applications, from traditional energy conversion (i.e. solar cells and photocatalysis) and displays (i.e. RGB and 3D displays), to remarkable nanomedicine (i.e. bio-imaging, bio-detection, drug delivery, photodynamic and photothermal therapy and temperature sensing) up to innovative applications such as security, barcoding, optical storage, RGB printing and so on (Fig.4) [15].

The nano-size is of tremendous importance speaking of biomedical applications. Other important properties that NPs must possess in this case are biocompatibility, non-toxicity and solubility, these largely depend on their surface chemistry and can be adjusted by means of various functionalizations[29].

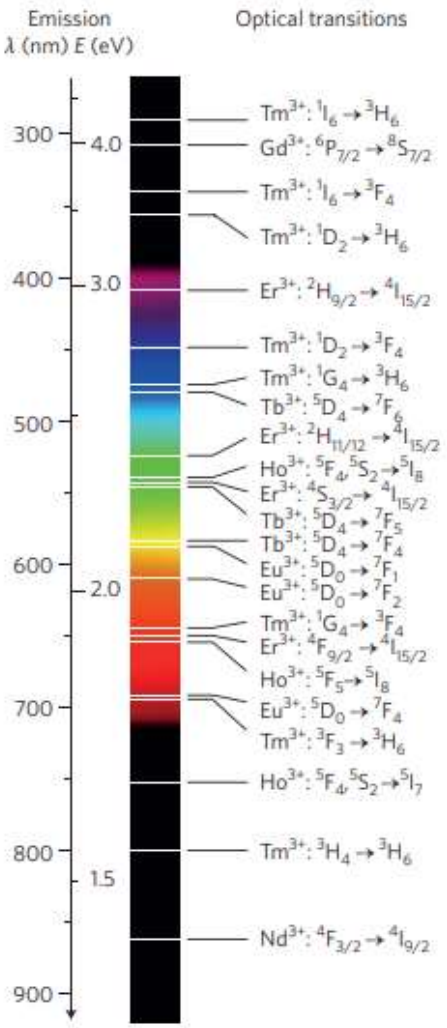

Fig.3 Typical Ln^{3+}-based upconversion emission bands covering a broad range of wavelengths from ultraviolet (~290 nm) to NIR (~880 nm) and their corresponding main optical transitions.

By carefully choosing the dopants, it is possible to match absorption and emission of the optically active NPs with the biological optical transparency window (650-1800 nm), obtaining deep tissue penetration. This window is separated in three distinctive regions, NIR-1 (650-950 nm), NIR-2 (1000-1350 nm) and NIR-3 (1500-1800 nm), because of two intense absorption peaks of water at around 980 nm and 1450 nm[30].

With lanthanide-doped NPs, two types of luminescent processes are possible: down shifting (DS), i.e. the conversion of higher energy photons into lower energy ones following Stokes law, and upconversion (UC), i.e. the sequential absorption of two or more low-energy photons (usually NIR light) that are converted in higher energy

photons (UV/VIS/NIR light) by means of anti-Stokes processes, via long-lived intermediate states of lanthanide ions[31]. The presence of real intermediate electronic states accounts for efficient UC processes, even when using low cost continuous-wave laser diodes or incoherent light sources with excitation power density as low as $\sim 10^{-1}$ W/cm^2 [16].

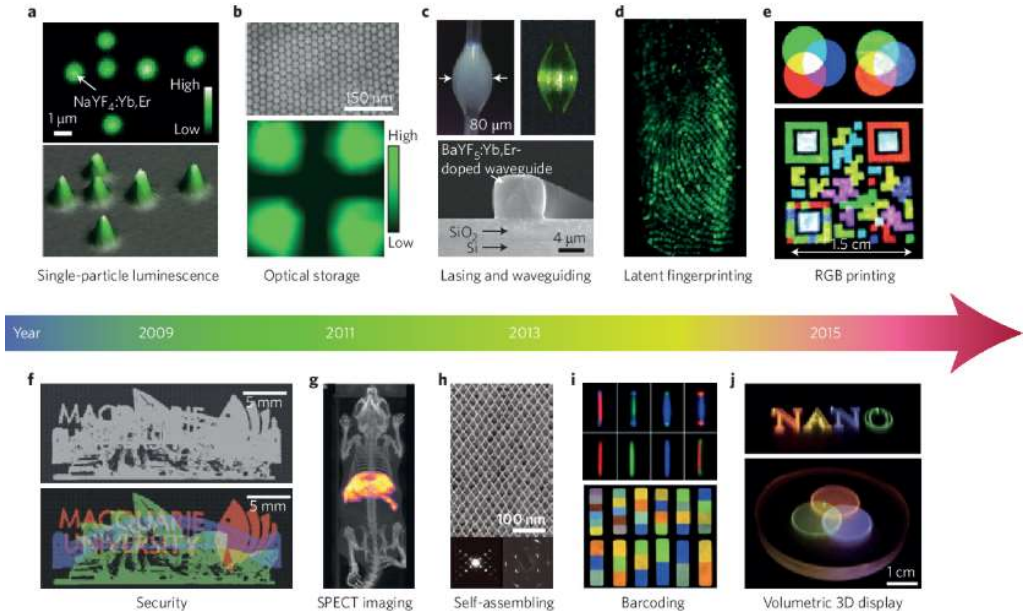

Fig.4 Multifunctional upconverting nanoparticles for emerging applications: (a) Confocal imaging of $NaYF_4$:Yb,Er nanoparticles at the single-particle level, (b) Rewritable optical storage enabled by light responsive nanoparticles, (c) Lasing and waveguide amplifier using the nanoparticles as gain media, (d) Latent fingerprinting through the use of $NaYF_4$:Yb,Er nanoparticles, (e) Red–green–blue (RGB) printing involving nanoparticle inks, (f) document security printing, through lifetime encoded $NaYF_4$:Yb,Tm nanoparticles, (g) In vivo whole-body 3D imaging (SPECT) with $NaLuF_4$:Yb,Tm nanoparticles, (h) Self-assembly of fluoride-based nanoplates, (i) Multicolour barcoding through single particles, (j) Full-colour volumetric 3D display using pulse-duration-sensitive nanoparticles. (See Zhou et al. (2015)[15] for references).

Downshifting nanoparticles (DS NPs) are commonly doped with Ln^{3+} ions that possess significant visible emission transitions following UV excitation, e.g. Sm^{3+}, Eu^{3+}, Tb^{3+} and Dy^{3+}. However, Nd^{3+} is the most adequate for biological applications, having excitation and emission wavelengths within the biological optical transparency window[29].

Upconverting nanoparticles (UC NPs) proved to be particularly suitable for bio-imaging purposes. Most of the literature on UCNPs focuses on Yb as sensitizer, since it can be conveniently excited with 980 nm common lasers, and other lanthanide ions (typically Er, Tm and Ho) as activators, with interesting UC emissions. The most studied UCNPs have fluoride- (i.e. $NaYF_4$[32,33], $NaGdF_4$[34], $NaLuF_4$[9], $LiYF_4$[35], $BaYF_5$[36], SrF_2[37,38], CaF_2[39,40], LaF_3[41-44], LuF_3[45], YF_3[46,47]), oxide- (i.e. Y_2O_3[48-50], Lu_2O_3[51], La_2O_3[52],

Gd_2O_3[53]) and oxysulfide-based (i.e. Y_2O_2S[54], Gd_2O_2S[55], La_2O_2S[56]) hosts, chosen because of low phonon energy of the lattice.

Upconverting lanthanide-doped nanocrystals (UCNCs) were even employed to assess the temperature in biological environments, as a function of the luminescence output[19,20,57-61], enabling ratiometric temperature sensing with high spatial resolution and with zero background arising from NIR photoexcitation[58]. Dual-emitting phosphors (Fig. 5), with resolvable emission intensities from two different emitting levels, proved to be more efficient and precise. Recently, several Ln^{3+}-based luminescent nanothermometers have been reported: ZnO:Er^{3+} [62], $BaTiO_3$:Er^{3+} [63], Gd_2O_3:Er^{3+}/Yb^{3+} [53] and Nd^{3+} [64], SrF_2:Er^{3+}/Yb^{3+} [65], PbF_2:Er^{3+}/Yb^{3+} [66,67], LaF_3:Nd^{3+} [68], $NaYF_4$:Er^{3+}/Yb^{3+} [69] and Tm^{3+}/Yb^{3+} [70], CaF_2:Er^{3+}/Yb^{3+} and Tm^{3+}/Yb^{3+} [40].

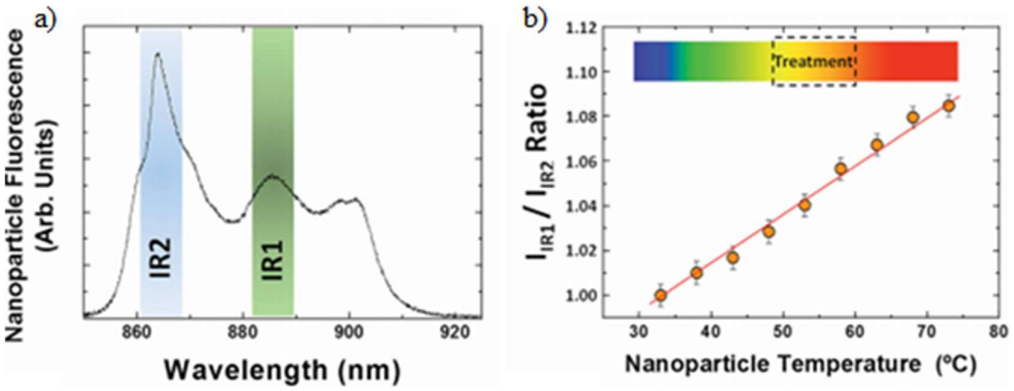

Fig. 5 (a) Near infrared (850–930 nm) room temperature emission spectra of Nd-doped LaF_3 NPs, evidencing the two spectral ranges used for fluorescence thermal sensing (IR1 and IR2) b) Temperature dependence of the IR1/IR2 intensity ratio. Dots are experimental data, while the solid line is the best linear fit[41].

1.3 Summary of the thesis

Considering what described above about lanthanide-doped NPs and considering the advantages of employing bismuth-based host materials, such as low toxicity, low cost and the possibility to obtain multifunctional probes for different imaging techniques, this work focused on the study of new bismuth-based luminescent materials doped with lanthanide ions. Synthesis, physico-chemical characterization and optical studies are reported. Moreover, the applicability of luminescent nanoparticles in various fields, such as multi-modal imaging and ratiometric contact-less optical thermometry, is further discussed.

The present work is structured in different thematic sections, providing, when necessary, an overview on the state-of-the-art and some basic theoretical knowledge. The thesis is organized as follows.

Basic theoretical concepts on luminescence phenomena are provided in Chapter 2, deepening photoluminescence processes from localized luminescent centres and

dealing with themes such as energy transfer (ET), downconversion (DC), upconversion (UC), lanthanide ions and their typical sensitizer-activator pairs.
Basic knowledge of contact-less optical thermometry is given in Chapter 3, describing the method here adopted to assess the thermometric performance of the proposed system, based on the fluorescence intensity ratio (FIR) between two closely spaced emitting levels or two Stark components of an excited state, that are thermally coupled.
Chapter 4 gives a brief overview on bismuth-based materials, outlining their potentialities as host for luminescent centres, with an insight on the three different crystalline structures of bismuth silicate herein investigated and on bismuth oxide polymorphs.
In the first section of Chapter 5 we propose Bi_2SiO_5 nanoparticles, as a new class of UCNPs, deepening various aspects such as the synthetic route and the effect of temperature and concentration of dopants on the crystalline structure of the material. Subsequently, an extensive investigation of physico-chemical parameters and a detailed photophysical investigation of the optical properties have been carried out, with the aim to assess the suitability of this materials as a new generation of UC nanophosphors. Furthermore, the synthesis of various Nd^{3+}-doped Bismuth-based (nano)systems is described, i.e. Bi_2SiO_5@SiO_2 and $Bi_4Si_3O_{12}$@SiO_2 NPs, and bulk $Bi_{12}SiO_{20}$.
Chapter 6 introduces upconverting Bi_2SiO_5 nanoparticles, doped with Yb^{3+} as sensitizer and Er^{3+} or Tm^{3+} as activators, as new probes for ratiometric optical thermometry, judging their thermometric performance based on key parameters such as the relative and absolute sensitivity, the temperature uncertainty and the repeatability of measurements.
In Chapter 7 some features of Bi_2SiO_5@SiO_2 NPs are investigated, such as biocompatibility, anti-microbial and photocatalytic properties and resistance to strong acidic medium.
Chapter 8 deals with Nd^{3+}-doped bismuth silicate nano- and bulk materials, as ratiometric NIR-emitting optical temperature sensors. PL spectra as a function of temperature are reported, and the suitability of each material for thermal sensing is assessed based on a figure of merit, i.e. the relative sensitivity.
Finally, Chapter 9 summarizes the main achievements of this work, outlining future perspectives on the subject dealt.

References

[1] Biswas, P., Wu, C.Y., Nanoparticles and the environment, *J Air Waste Manag Assoc.,* **2005**, 55(6), 708-46.

[2] Prasad, P.N., Nanophotonics, *Wiley Interscience*, **2004**, ISBN 978-0-4716-4988-5.

[3] Khan, I., Saeed, K., Khan, I., Nanoparticles: Properties, applications and toxicities, *Arabian Journal of Chemistry*, **2019**, 12(7), 908-931.

[4] Perrault, S. D., Chan, W. C., Synthesis and Surface Modification of Highly Monodispersed Spherical Gold Nanoparticles of 50−200 nm, *J. Am. Chem. Soc*., **2009**, 131 (47), 17042−17043.

[5] Gao, X. H., Cui, Y. Y., Levenson, R. M., Chung, L. W. K., Nie, S. M., In vivo cancer targeting and imaging with semiconductor quantum dots, *Nat. Biotechnol.*, **2004**, 22 (8), 969−976.

[6] Hao, F., Nehl, C. L., Hafner, J. H., Nordlander, P., Plasmon resonances of a gold nanostar, *Nano Lett*., **2007**, 7 (3), 729−732.

[7] Chen, J., Saeki, F., Wiley, B. J., Cang, H., Cobb, M. J., Li, Z. Y., Au, L., Zhang, H., Kimmey, M. B., Li, X. D., Xia, Y. N., Gold nanocages: Bioconjugation and their potential use as optical imaging contrast agents, *Nano Lett*., **2005**, 5 (3), 473−477.

[8] Coleman, J. N., Lotya, M., O'Neill, A., Bergin, S. D., King, P. J., Khan, U., Young, K., Gaucher, A., De, S., Smith, R. J., Two Dimensional Nanosheets Produced by Liquid Exfoliation of Layered Materials, *Science*, **2011**, 331(6017), 568−571.

[9] Shi, F., Wang, J. S., Zhai, X. S., Zhao, D., Qin, W. P., Facile synthesis of beta-$NaLuF_4$:Yb/Tm hexagonal nanoplates with intense ultraviolet upconversion luminescence, *Cryst. Eng. Comm*., **2011**, 13 (11), 3782−3787.

[10] Nikoobakht, B., El-Sayed, M. A., Preparation and growth mechanism of gold nanorods (NRs) using seed-mediated growth method, *Chem. Mater*., **2003**, 15(10), 1957−1962.

[11] Kan, S., Mokari, T., Rothenberg, E., Banin, U., Synthesis and size dependent properties of zinc-blende semiconductor quantum rods, *Nat. Mater*., **2003**, 2(3), 155−158.

[12] Cui, Y., Wei, Q. Q., Park, H. K., Lieber, C. M., Nanowire nanosensors for highly sensitive and selective detection of biological and chemical species, *Science*, **2001**, 293(5533), 1289−1292.

[13] Ozin, G. A., Nanochemistry - Synthesis in Diminishing Dimensions, *Adv. Mater*., **1992**, 4(10), 612−649.

[14] Burda, C., Chen, X. B., Narayanan, R., El-Sayed, M. A., Chemistry and properties of nanocrystals of different shapes, *Chem. Rev.*, **2005**, 105(4), 1025−1102.

[15] Zhou, B., Shi, B., Jin, D., Liu, X., Controlling upconversion nanocrystals for emerging applications, *Nat. Nanotechnol.,* **2015**, 10, 924-936.

[16] Chen, G., Roy, I., Yang, C., Prasad, P.N., Nanochemistry and nanomedicine for nanoparticle-based diagnostics and therapy, *Chem. Rev.,* **2016**, 116, 2826-2885.

[17] Jaque, D., Richard, C., Viana, B., Soga, K., Liu X., García Solé, J., Inorganic nanoparticles for optical bioimaging, *Adv. Opt. Photonics,* **2016**, 8, 1-103.

[18] Lucky, S.S., Soo, K.C., Zhang, Y., Nanoparticles in photodynamic therapy, *Chem. Rev.,* **2015**, 115, 1990-2042.

[19] Brites, C.D.S., Millán A., Carlos, L.D., Lanthanide in luminescent thermometry. in J.-C. Bünzli and V.K. Pecharsky Eds., Handbook on the Physiscs and Chemistry of Rare Earth, *Elsevier*, **2016**, Chapter 281, vol. 49, pp. 339-427.

[20] Brites, C.D.S., Lima, P.P., Silva, N.J.O., Millán, A., Amaral, V.S., Palacio F., Carlos L. D., Thermometry at the nanoscale, *Nanoscale,* **2012**, 4, 4799-4829.

[21] Kumar, P., Singh S., Gupta, B.K., Future prospects of luminescent nanomaterial-based security inks: from synthesis to anti-counterfeiting applications, *Nanoscale,* **2016**, 8, 14297-14340.

[22] Tiwari, S., Yakhmi, J. V., Recent Advances in Luminescent Nanomaterials for Solid State Lighting Applications, *Defect and Diffusion Forum*, **2015**, 361, 15-68.

[23] Sreenivasan, V., Zvyagin, A., Goldys, E., Luminescent nanoparticles and their applications in the life sciences, *Journal of physics Condensed matter*, **2013**, 25(19), 194101.

[24] Wang, F., Liu, X., Upconversion multicolor fine-tuning: visible to near-infrared emission from lanthanide-doped $NaYF_4$ nanoparticles, *J. Am. Chem. Soc*., **2008**, 130, 5642–5643.

[25] Zhao, J., Zhang, R., Liu, Y., Liu, D., Goldys, E., Yang, X., Xi, P., Sunna, A., Lu, J., Shi, Y., Leif, R., Huo, Y., Shen, J., Piper, J., Robinson, J., Jin, D., Tunable lifetime multiplexing using luminescent nanocrystals, *Nature Photon*., **2013**, 8, 32–36.

[26] Xie, X., Gao, N., Deng, R., Sun, Q., Xu, Q.H., Liu, X., Mechanistic investigation of photon upconversion in Nd^{3+}-sensitized core−shell nanoparticles, *J. Am. Chem. Soc*., **2013**, 135, 12608–12611.

[27] Zhao, J., Jin, D., Schartner, E.P., Lu, Y., Liu, Y., Zvyagin, A.V., Zhang, L., Dawes, J.M., Xi, P., Piper, J.A., Goldys, E.M., Monro, T.M., Single-nanocrystal sensitivity achieved by enhanced upconversion luminescence, *Nature Nanotech*., **2013** 8, 729–734.

[28] Zhao, J., Lu, Z., Yin, Y., McRae, C., Piper, J.A., Dawes, J.M., Jin, D., Goldys, E.M., Upconversion luminescence with tunable lifetime in $NaYF_4$:Yb,Er nanocrystals: role of nanocrystal size, *Nanoscale*, **2013**, 5, 944–952.

[29] Prodi, L., Rampazzo, E., Rastrelli, F., Speghini, A., Zaccheroni, N., Imaging agents based on lanthanide doped nanoparticles, *Chem. Soc. Rev*., **2015**, 44(14), 4922-4952.

[30] Anderson, R. R., Parrish, J. A., The Optics of Human Skin, *Journal of Investigative Dermatology*, **1981**, 77(1), 13-19.

[31] Chen, G., Agren, H., Ohulchanskyy, T. Y., Prasad, P. N., Light upconverting core−shell nanostructures: nanophotonic control for emerging applications, *Chem. Soc. Rev*., **2015**, 44 (6), 1680−1713.

[32] Gao, L., Ge, X., Chai, Z.L., Xu, G.H., Wang, X., Wang, C., Shape-controlled synthesis of octahedral αNaYF$_4$ and its rare earth doped submicrometer particles in acetic acid, *Nano Res*., **2009**, 2,565–74.

[33] Wang, M., Liu, J.L., Zhang, Y.X., Hou, W., Wu, X.L., Xu, S.K., Two-phase solvothermal synthesis of rareearth doped NaYF$_4$ upconversion fluorescent nanocrystals, *Mater. Lett*., **2009**, 63, 325–7.

[34] Naccache, R., Vetrone, F., Mahalingam, V., Cuccia, L.A., Capobianco, J.A., Controlled synthesis and water dispersibility of hexagonal phase NaGdF$_4$:Ho^{3+}/Yb^{3+} nanoparticles, *Chem. Mater*., **2009**, 21, 717–23.

[35] Pei, X.J., Hou, Y.B., Zhao, S.L., Xu, Z., Teng, F., Frequency upconversion of Tm^{3+} and Yb^{3+} codoped YLiF$_4$ synthesized by hydrothermal method, *Mater. Chem. Phys.*, **2005**, 90, 270–4.

[36] Vetrone, F., Mahalingam, V., Capobianco, J.A., Near-infrared-to-blue upconversion in colloidal BaYF$_5$:Tm^{3+},Yb^{3+} nanocrystals, *Chem. Mater.*, **2009**, 21, 1847–51.

[37] Przybylska, D., Ekner-Grzyb, A., Grześkowiak, B. F., Grzyb, T., Upconverting SrF$_2$ nanoparticles doped with Yb^{3+}/Ho^{3+}, Yb^{3+}/Er^{3+} and Yb^{3+}/Tm^{3+} ions – optimisation of synthesis method, structural, spectroscopic and cytotoxicity studies, *Scientific Reports*, **2019**, 9(1).

[38] Quintanilla, M., Cantarelli, I. X., Pedroni, M., Speghini, A., Vetrone, F., Intense ultraviolet upconversion in water dispersible SrF$_2$:Tm^{3+},Yb^{3+} nanoparticles: the effect of the environment on light emissions, *J. Mater. Chem. C*, **2015**, 3(13), 3108-3113.

[39] Wang, G., Peng, Q., Li, Y., Upconversion Luminescence of Monodisperse CaF$_2$:Yb^{3+}/Er^{3+} Nanocrystals, *J. Am. Chem. Soc*., **2009**, 131(40).

[40] Dong, N.-N., Pedroni, M., Piccinelli, F., Conti, G., Sbarbati, A., Ramírez-Hernández, J. E., Maestro, L. M., Iglesias-de la Cruz, M. C., Sanz-Rodriguez, F., Juarranz, A., Chen, F., Vetrone, F., Capobianco, J. A., Solé, J. G., Bettinelli, M., Jaque, D., Speghini, A., NIR-to-NIR Two-Photon Excited CaF$_2$:Tm^{3+},Yb^{3+} Nanoparticles: Multifunctional Nanoprobes for Highly Penetrating Fluorescence Bio-Imaging, *ACS Nano*, **2011**, 5(11), 8665-8671.

[41] Carrasco, E., del Rosal, B., Sanz-Rodríguez, F., De la Fuente, A.J., Haro Gonzalez, P., Rocha, U., Kumar, K.U., Jacinto, C., García Solé J., Jaque, D., Intratumoral thermal reading during photo-thermal therapy by multifunctional fluorescent nanoparticles, *Adv. Funct. Mater.,* **2015**, 25, 615-626.

[42] Yi, G.S., Chow, G.M., Colloidal LaF$_3$:Yb,Er, LaF$_3$:Yb,Ho and LaF$_3$:Yb,Tm nanocrystals with multicolor upconversion fluorescence, *J. Mater Chem*., **2005**, 15, 4460–4.

[43] Liu, C.H., Chen, D.P., Controlled synthesis of hexagon shaped lanthanide-doped LaF$_3$ nanoplates with multicolor upconversion fluorescence, *J. Mater. Chem*., **2007**, 17, 3875–80.

[44] Hu, H., Chen, Z.G., Cao, T.Y., Zhang, Q., Yu, M.X., Li, F.Y., Hydrothermal synthesis of hexagonal lanthanide-doped LaF$_3$ nanoplates with bright upconversion luminescence, *Nanotechnology*, **2008**, 37, 375702.

[45] Xiao, S.G., Yang, X.L., Ding, J.W., Yan, X.H., Up-conversion in Yb^{3+}-Tm^{3+} co-doped lutetium fluoride particles prepared by a combustion-fluorization method, *J. Phys. Chem. C*, **2007**, 111, 8161–5.

[46] Yan, R.X., Li, Y.D., Down/up conversion in Ln^{3+}-doped YF_3 nanocrystals, *Adv. Funct. Mater*., **2005**, 15,763–70.

[47] Wang, G.F., Qin, W.P., Zhang, J.S., Wang, Y., Cao, C.Y., Wang, L.L., Synthesis, growth mechanism, and tunable upconversion luminescence of Yb^{3+}/Tm^{3+}-codoped YF_3 nanobundles, *J. Phys. Chem. C*, **2008**, 112, 12161–7.

[48] Vetrone, F., Boyer, J.C., Capobianco, J.A, Speghini, A., Bettinelli, M., Significance of Yb^{3+} concentration on the upconversion mechanismsin codoped Y_2O_3:Er^{3+},Yb^{3+} nanocrystals, *J. Appl. Phys.*, **2004**, 96, 661–7.

[49] Matsuura, D., Red, green, and blue upconversion luminescence of trivalent-rare-earth ion-doped Y_2O_3 nanocrystals, *Appl. Phys. Lett*., **2002**, 81, 4526–8.

[50] Yang, L.M., Song, H.W., Yu, L.X., Liu, Z.X., Lu, S.H., Unusual power-dependent and time-dependent upconversion luminescence in nanocrystals Y_2O_3:Ho^{3+}/Yb^{3+}, *J. Lumin*., **2006**, 116, 101–6.

[51] Yang, J., Zhang, C.M., Peng, C., Li, C.X., Wang, L.L., Chai, R.T., Controllable red, green, blue (RGB) and bright white upconversion luminescence of Lu_2O_3:Yb^{3+}/Er^{3+}/Tm^{3+} nanocrystals through single laser excitation at 980 nm, *Chem. Eur. J*., **2009**, 15, 4649–55.

[52] Liu, H.Q., Wang, L.L., Chen, S.G., Effect of Yb^{3+} concentration on the upconversion of Er^{3+} ion doped La_2O_3 nanocrystals under 980 nm excitation, *Mater Lett.*, **2007**, 61, 3629–31.

[53] Singh, S., Kumar, K., Rai, S.B., Multifunctional Er^{3+}-Yb^{3+} codoped Gd_2O_3 nanocrystalline phosphor synthesized through optimized combustion route, *J. Appl. Phys. B*., **2009**, 94, 165–73.

[54] Pires, A.M., Serra, O.A., Davolos, M.R., Yttrium oxysulfide nanosized spherical particles doped with Yb and Er or Yb and Tm: efficient materials for up-converting phosphor technology field, *J. Alloy Compd*., **2004**, 374, 181–4.

[55] Hirai, T., Orikoshi, T., Preparation of Gd_2O_3:Yb,Er and Gd_2O_2S:Yb,Er infrared-to-visible conversion phosphor ultrafine particles using an emulsion liquid membrane system, *J. Colloid. Interf. Sci*., **2004**, 269, 103–8.

[56] Luo, X.X., Cao, W.H., Ethanol-assistant solution combustion method to prepare La_2O_2S:Yb,Pr nanometer phosphor, *J. Alloys Compd*., **2008**, 460, 529–34.

[57] Jaque, D., Vetrone, F., Luminescence nanothermometry, *Nanoscale*, **2012**, 4, 4301-4326.

[58] Fischer, L.H., Harms, G.H., Wolfbeis, O.S., Upconverting nanoparticles for nanoscale thermometry, *Angew. Chem. Int. Ed*., **2011**, 50, 4546-4551.

[59] Wang, X.-D., Wolfbeis, O.S., Meier, R.J., Luminescent probes and sensors for temperature, *Chem. Soc. Rev*., **2013**, 42, 7834-7869.

[60] Vetrone, F., Naccache, R., Zamarrón, A., de la Fuente, A.J., Sanz-Rodríguez, F., Martinez Maestro, L., Martin Rodriguez, E., Jaque, D., García Solé, J., Capobianco J.A., Temperature sensing using fluorescent nanothermometers, *ACS Nano*, **2010**, 4, 3254-3258.

[61] Hao, S., Chen, G., Yang., C., Sensing using rare-earth-doped upconversion nanoparticles, *Theranostics*, **2013**, 3, 331-345.

[62] Wang, X., Kong, X. G., Yu, Y., Sun Y. J., Zhang, H., Effect of annealing on upconversion luminescence of ZnO:Er^{3+} nanocrystals and high thermal sensitivity, *J. Phys. Chem. C*, **2007**, 111, 15119–15124.

[63] Alencar, M. A. R. C., Maciel, G. S., de Araujo, C. B., Patra, A. Er^{3+}-doped $BaTiO_3$ nanocrystals for thermometry: Influence of nanoenvironment on the sensitivity of a fluorescence-based temperature sensor, *Appl. Phys. Lett*., **2004**, 84, 4753–4755.

[64] Balabhadra, S., Debasu, M. L., Brites, C. D. S., Nunes, L. A. O., Malta, O. L., Rocha, J., Bettinelli, M., Carlos, L. D., Boosting the sensitivity of Nd^{3+}-based luminescent nanothermometers, *Nanoscale,* **2015**, 7, 17261−17267.

[65] Balabhadra, S., Debasu, M. L., Brites, C. D. S., Ferreira, R., Carlos, L. D., Upconverting Nanoparticles Working as Primary Thermometers in Different Media, *The Journal of Physical Chemistry C*., **2017**, 121(25), 13962-13968.

[66] Aigouy, L., Tessier, G., Mortier, M., Charlot, B., Scanning thermal imaging of microelectronic circuits with a fluorescent nanoprobe, *Appl. Phys. Lett.,* **2005**, 87, 184105.

[67] Aigouy, L., Saïdi, E., Lalouat, L., Labeguerie-Egea, J., Mortier, M., Löw, P., Bergaud, C., AC thermal imaging of a microwire with a fluorescent nanocrystal: influence of the near field on the thermal contrast, *J. Appl. Phys.,* **2009**, 106, 074301.

[68] Rocha, U., Jacinto da Silva, C., Ferreira Silva, W., Guedes, I., Benayas, A., Martinez Maestro, L., Acosta Elias, M., Bovero, V., van Veggel, F. C. J. M., García Solé, J. A., Jaque, D. Subtissue thermal sensing based in neodymium-doped LaF_3 nanoparticles, *ACS Nano* **2013**, 7, 1188−1199.

[69] Vetrone, F., Naccache, R., Zamarrón, A., Juarranz de la Fuente, A., Sanz-Rodríguez, F., Martinez Maestro, L., Martin Rodriguez, E., Jaque, D., García Solé, J., Capobianco, J. A., Temperature sensing using fluorescent nanothermometers, *ACS Nano* **2010**, 4, 3254−3258.

[70] Zhou, S. S., Jiang, G. C., Li, X. Y., Jiang, S., Wei, X. T., Chen, Y. H., Yin, M., Duan, C.K., Strategy for thermometry via Tm^{3+}-doped $NaYF_4$core-shell nanoparticles, *Opt. Lett.*, **2014**, 39, 6687.

CHAPTER 2

Luminescence: basis and processes

2.1 Photoluminescence

The term *Luminescence*, adopted for the very first time by German physicist Wiedemann in 1888, refers to the emission of light from an excited electronic state of any substance. Different types of luminescence can be distinguished, depending on the source and the nature of light excitation, i.e. bioluminescence, crystalloluminescence, chemiluminscence, electroluminescence, cathodoluminescence, mechanoluminescence, photoluminescence, radioluminescence, sonoluminescence and thermoluminescence.

2.1.1 Light absorption

In the case of photoluminescence, the process starts with the absorption of photons. Since the electronic absorption of light is extremely quick, the nuclei are assumed to be "static" in this short time-frame. The assumption of negligible nuclear displacement is known as the Franck-Condon principle and is represented by vertical transitions in energy level diagrams (transition A in Fig.1). Transitions that are not "vertical", such as the one terminating in the lowest vibrational level of the excited state (transition B) or the one terminating in a triplet excited state (transition C), are not possible because of the large displacement between the two levels involved.

The displacement of the excited state respect to the ground state position is due to differences in the bonding properties between the molecular orbitals representing the two states. The extent of the nuclear displacement may vary widely. For example, in the case of zero excited state distortion (Fig. 2a), the vibronic transition 0-0 has the greatest probability to occur, thus has the strongest intensity in both absorption and emission spectra. On the other hand, in the case of significant excited state displacement (Fig. 2b) the same vibronic transitions becomes less probable, thus the weaker intensity in the spectra.

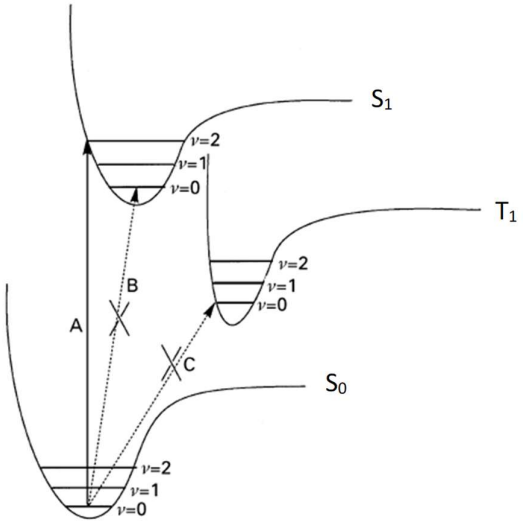

Fig.1 Illustration of the Franck-Condon principle[1].

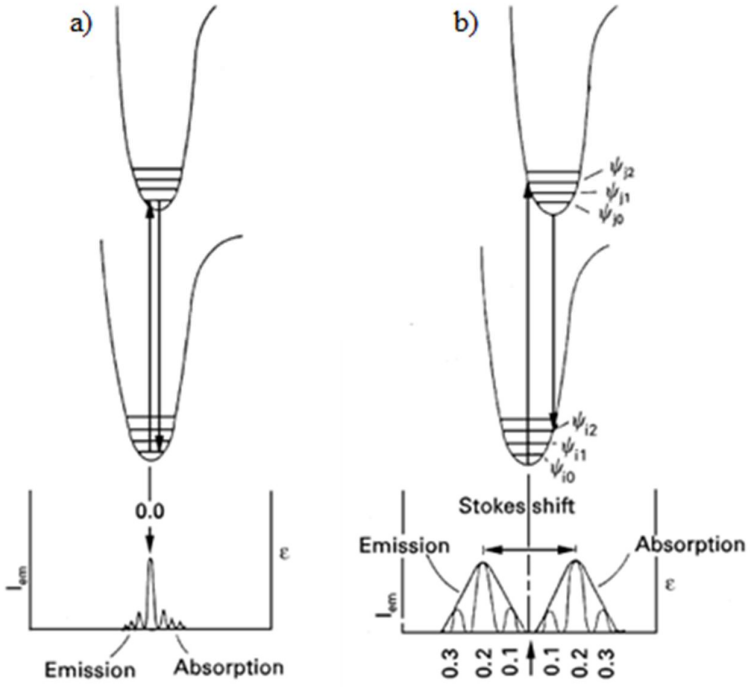

Fig.2 Two cases of excited state distortions: (a) zero and (b) non-zero displacement, with corresponding absorption and emission spectra depicted below[1].

The energy difference between absorption and emission spectra, defined as the Stokes shift (Fig. 3), as well as the band width (FWHM) are both a quantitative measure of the excited state distortion. In the case of zero excited state distortion, the emission bands appear very sharp, with small FWHM values, whereas in the opposite case the bands are much broader[2].

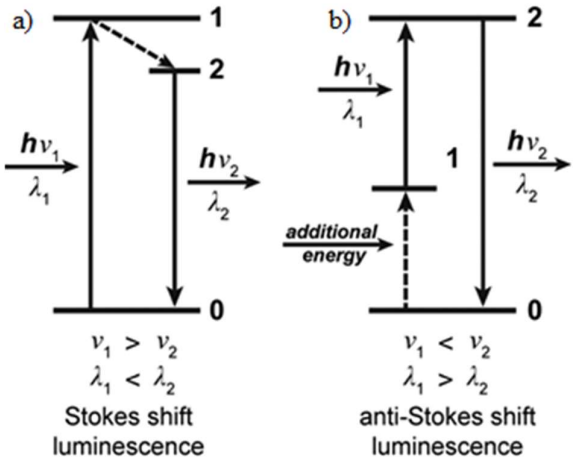

Fig.3 (a) Stokes and (b) anti-Stokes shifts[3].

2.1.2 Light emission

The mechanism of light emission can be easily illustrated with the aid of the Jablonski energy level diagram (Fig. 4). The multiplicity of an electronic state can be either a singlet S_n (paired electrons, with opposite spin), or a triplet T_n (unpaired electrons, with same spin). Both absorption and emission transitions are more likely to take place if spin-allowed. The emission from an excited state, with same spin multiplicity as the ground state, occurs rapidly through the emission of a photon; on the contrary, transitions from the triplet excited state to the ground-state are forbidden because of the selection rules for electronic transitions, thus the emission rates are slow. This results in shorter fluorescence lifetimes (in the order of nanoseconds) respect to phosphorescence lifetimes (in the order of milliseconds to seconds).

Following the absorption of light, various radiative or non-radiative processes occur. Concerning non-radiative relaxation events, the possible phenomena are:

- Vibrational relaxation from a higher vibrational level to the lowest level of the excited state, within 10^{-14}-10^{-12} s, thus is generally complete prior to luminescence emission (arrow 1 in the Jablonski diagram).
- Internal conversion from a higher singlet excited state (such as S_2) to the lowest one (S_1), within 10^{-12} s (arrow 2).
- Intersystem crossing between excited states with different spin multiplicity as for example the relaxation from S_1 to T_1 (arrow 3), usually less probable than internal conversion because of the different spin multiplicity, and thus slower, occurring within 10^{-8} s.
- Non-radiative de-excitation, consisting in the decay from a singlet excited state to the ground state through the release of thermal energy in the form of infinitesimal amounts of heat (arrow 4), as an alternative to the emission of photons (therefore causing luminescence quenching). In the solid phase, phonons (i.e. crystal vibrations) provide the mechanism for this non-radiative phenomenon.

► Cross relaxation, also called self-quenching, occurring via energy exchange between two identical ions, one in the excited state and one in the ground state. This results in both ions changing to excited states that are energetically halfway the initial excited state and the ground state, and then their eventual non-radiative decay.

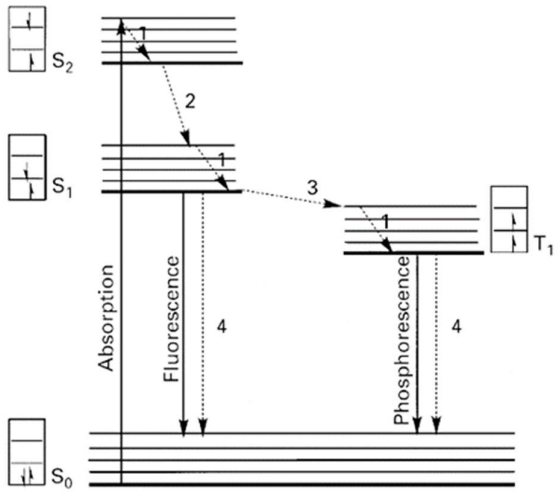

Fig.4 Jablonski level diagram. Singlet ground, first and second electronic states are denoted by S_0, S_1 and S_2, respectively. Triplet excited state is indicated by T_1. Radiative processes are depicted as solid lines, non-radiative ones as dashed lines[1].

Radiative events comprise either fluorescence ($S_1 \rightarrow S_0$) or phosphorescence ($T_1 \rightarrow S_0$), depending on the nature of the excited state, and thus on its average lifetime. The energy of the emission is typically lower than that of absorption, thus fluorescence usually occurs at longer wavelengths (downconversion). Nevertheless, also the opposite mechanism is possible (upconversion).
The table below[4] summarizes basic radiative and non-radiative processes represented in the Jablonski diagram, with relative time scales:

Transition	Time scale (s)	Process type
Absorption	10^{-15}	R
Internal Conversion	10^{-14}-10^{-11}	NR
Vibrational Relaxation	10^{-14}-10^{-11}	NR
Fluorescence	10^{-9}-10^{-7}	R
Intersystem Crossing	10^{-8}-10^{-3}	NR
Phosphorescence	10^{-4}-10^{-1}	R

Table 1: time scales for various basic radiative (R) and non-radiative (NR) processes[4].

Quantum yield and fluorescence lifetime are probably the most important characteristics of fluorescent species[5]. The quantum yield is expressed as the ratio between emitted and absorbed photons, with a maximum value of 1, representing the efficiency of the conversion of absorbed light into emitted light[6]. According to Eq. 1 the quantum yield can be described by two constants: k_r, the radiative rate constant, and k_{nr}, the non-radiative rate constant comprising all possible non-radiative pathways (i.e. internal conversion, intersystem crossing and other quenching mechanisms)[7]:

$$\Phi_f = \frac{photons\ emitted}{photons\ absorbed} = \frac{k_r}{k_r + \Sigma\ k_{nr}} \quad (1)$$

The radiative lifetime of a fluorophore in absence of non-radiative processes is termed as intrinsic lifetime and is given by:

$$\tau_r = \frac{1}{k_r} \quad (2)$$

The average time a molecule spends in the singlet excited sate, before fluorescence emission, is denoted as fluorescence lifetime and is expressed by the following equation:

$$\tau_f = \frac{1}{k_r + \Sigma\ k_{nr}} \quad (3)$$

The fluorescence quantum yield can thus be expressed in terms of luminescence lifetime as the probability of emitting, as follows:

$$\Phi_f = \frac{k_r}{k_r + \Sigma\ k_{nr}} = \frac{\tau_f}{\tau_r} \quad (4)$$

However, many non-radiative processes can compete efficiently with the emission of photons and thus reducing the fluorescence quantum yield.

2.1.3 Quenching of emission

In luminescence spectroscopy, quenching processes lead to the reduction in the emission intensity. Two types of mechanisms are possible: dynamic, if dependent on the speed of quencher diffusion towards the fluorophore, or static, if independent on the diffusive processes.

- Dynamic, or collisional, quenching occurs when the fluorophore is deactivated upon collision of an excited luminophore (L*) with a quencher (Q) molecule. The fluorophore transfers its energy to the quencher and returns to the ground state without emitting photons.
- Static quenching occurs upon the formation of complexes between fluorophores at the ground state (L) and quenchers (Q), thus not relying on diffusion or molecular collisions. The resulting ground-state complexes (L-Q) are not luminescent, thus the fluorescence quantum yield decreases because of the reduced concentration of free luminophore upon its complexation.

Quenching can also occur by a variety of other non-radiative mechanisms, such as the concentration quenching, if light is reabsorbed by the fluorophore itself or other absorbing species especially when the dopant concentration is high; multi-phonon relaxation, when surrounding ions vibrate at high frequencies, causing the dissipation of energy by non-radiative processes; thermal quenching, when the system relaxes non-radiatively through vibrational levels because of high temperature; or cross relaxation mechanisms related to migrations of the luminescent ions up to defects or impurities that cause non-radiative relaxation[8].

2.2 Lanthanides

Luminescence in solids can be distinguished in intrinsic or extrinsic luminescence, based on the spatial location where the emission phenomena rise from. Electronic transitions generated from the host material (such as electron-hole recombinations) give rise to intrinsic luminescence, on the other hand electronic transitions arising from impurities introduced into the host generate extrinsic luminescence. Impurities are intentionally created by doping the host material and are termed sensitizers (or donors) if they absorb the excitation radiation and activators (or acceptors) if they receive energy from the sensitizers, and consequently reemit light[9]. Different types of localized luminescent centres are possible, each with specific electronic transitions. Among them are F centres, T^{l+} type ions, transition metal ions, lanthanide ions (divalent or trivalent) and actinide ions. The effect of the host material on the emission properties of active centres depends on the nature of the localized centres and on their distinctive type of electronic transition. For example, f-f lanthanide transitions, unlike f-d transitions, are weakly affected by the surrounding matrix, thanks to the configuration of the orbitals involved. This property enriches trivalent lanthanide ions (Ln^{3+}) with unique and fascinating luminescent properties[10].

The lanthanide series of chemical elements comprises 15 elements, with atomic numbers 57 to 71, from Lanthanum through Lutetium. The ground state electronic configuration of Ln^{3+} ions is $[Xe]4f^n$ (n=0-14), and its distance in energy from the $[Xe]4f^{n-1}\,5d^1$ configuration is fairly enough ($\Delta E \sim 32000\ cm^{-1}$)[11].

The fluorescence from lanthanide ions results from 4f-4f intraconfigurational transitions, but also from $4f^n$ ground state to $4f^{n-1}5d^1$ excited state in some lanthanide ions. Laporte's parity selection rule, which states that electronic transitions between energy levels with the same parity cannot occur[12], implies that this type of transitions is forbidden. However, Ln^{3+} ions perturbations, such as electron vibration coupling and uneven crystal filed, can lead to the relaxation of the parity selection rule, and some f –f transitions become partially allowed as magnetic dipole transitions[13].

4f orbitals are shielded by higher filled 5s and 5p sub-shells, therefore they are not involved in the chemical bonding between lanthanide ions and the embedding matrix. This characteristic property of 4f orbitals and the limited influence of the matrix, result in intrinsic spectroscopic properties, such as low emission rates because of small

extinction coefficients[5], sharp-line spectra resembling those of free ions[13], and long lifetimes of excited states[10].

The shielding effect and the consequent small interference from the chemical surroundings allow to build the diagram of $4f^n$ energy levels depicted in Fig.5, irrespectively of the embedding matrix.

It is evident that larger energy gaps lead to less non-radiative processes. Because of the absence of intermediate states, the emission from Gd^{3+} is located at a shorter wavelength in the ultraviolet region, limiting its application as a luminescent center. On the contrary, energy gaps of Sm^{3+}, Eu^{3+}, Tb^{3+}, Dy^{3+} and Ho^{3+} give stronger emissions in the visible region, while smaller energy gaps of Nd^{3+}, Er^{3+} and Tm^{3+} give rise to infrared emissions[10]. Thus, the emission spectra of lanthanides cover the entire UV-VIS spectrum.

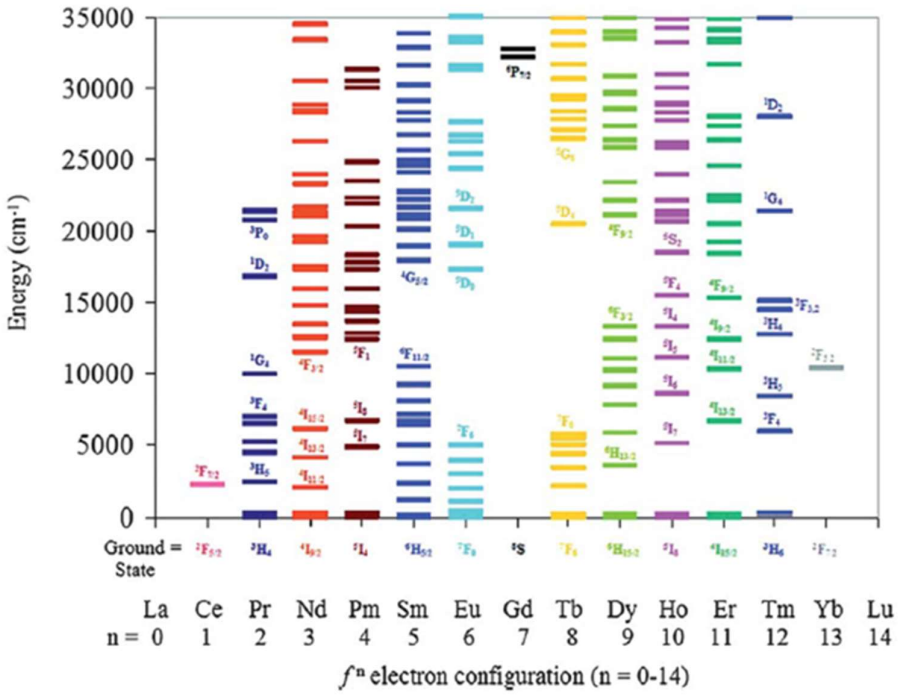

Fig.5 Energy diagram for Ln^{3+} ions in a $LaCl_3$ lattice[14].

The outer 5d orbitals are more extended than 4f orbitals and thus are not shielded. Consequently, f-d allowed transitions are more sensitive to the host matrix, resulting in broad spectral bands and strong absorption cross-sections.

The energy levels of $4f^n$ configurations are identified by the spectroscopic notation $^{2S+1}L_J$, where L and S are the quantum numbers related to the total orbital angular momentum and the total spin angular momentum, respectively, while J is associate with the total angular momentum defined as $\vec{J} = \vec{L} + \vec{S}$, with values comprised between $|L - S| = J = |L + S|$.

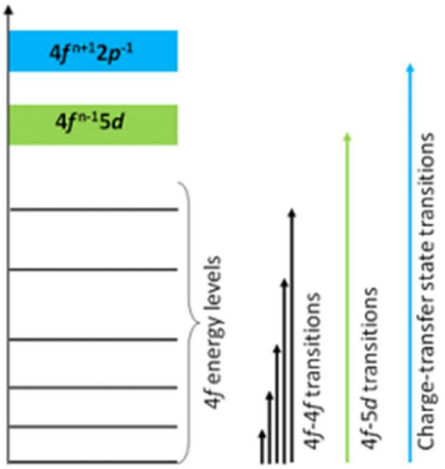

Fig.6 Schematic representation of the electronic absorption transitions of a lanthanide ion, displaying 4f-4f, 4f-5d and charge-transfer state transitions[10].

As represented in Fig. 7, the substitution of lanthanide ions in a crystalline matrix, removes the degeneracy of the free-ion levels because of coulombic, spin-orbit and crystal field interactions. Coulombic, or electrostatic, interactions are due to the repulsion between 4f electrons of lanthanide ions and result in the splitting of the free ions levels into the ^{2S+1}L levels. Typical separation due to coulombic interactions is about $\geq 10^4$ cm^{-1}. Spin-orbit interactions cause the splitting of each ^{2S+1}L level into (2J+1) states termed as $^{2S+1}L_J$, with a separation of about 10^3 cm^{-1}. Finally, the interaction with the crystal field breaks the spherical symmetry of the Hamiltonian wavefunction, resulting in the Stark splitting of the $^{2S+1}L_J$ levels into (2J+1) terms, if the number of 4f electrons are even, or (J+1/2) terms if the number of 4f electrons is odd. Stark splitting is typically 10^2 cm^{-1}. In lanthanide ions, unlike in transition metal ions, the crystal field splitting is smaller than the spin-orbit separation because of the shielded character of 4f electrons[15].

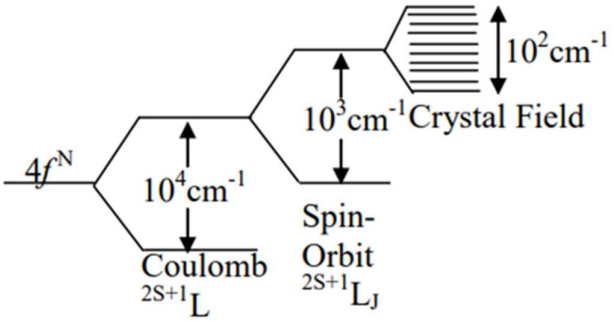

Fig.7 Schematic splitting of energy levels of 4f electronic configuration of lanthanide ions.

Typical examples of luminescence spectra of Ln^{3+}, that are commonly used as dopants for imaging purposes, are given in Fig.8. Depending on the surrounding environment

of the ions, the shape (i.e. intensity, width and crystal-field splitting) of the peaks may differ, however the energy of the transitions remains almost unchanged.

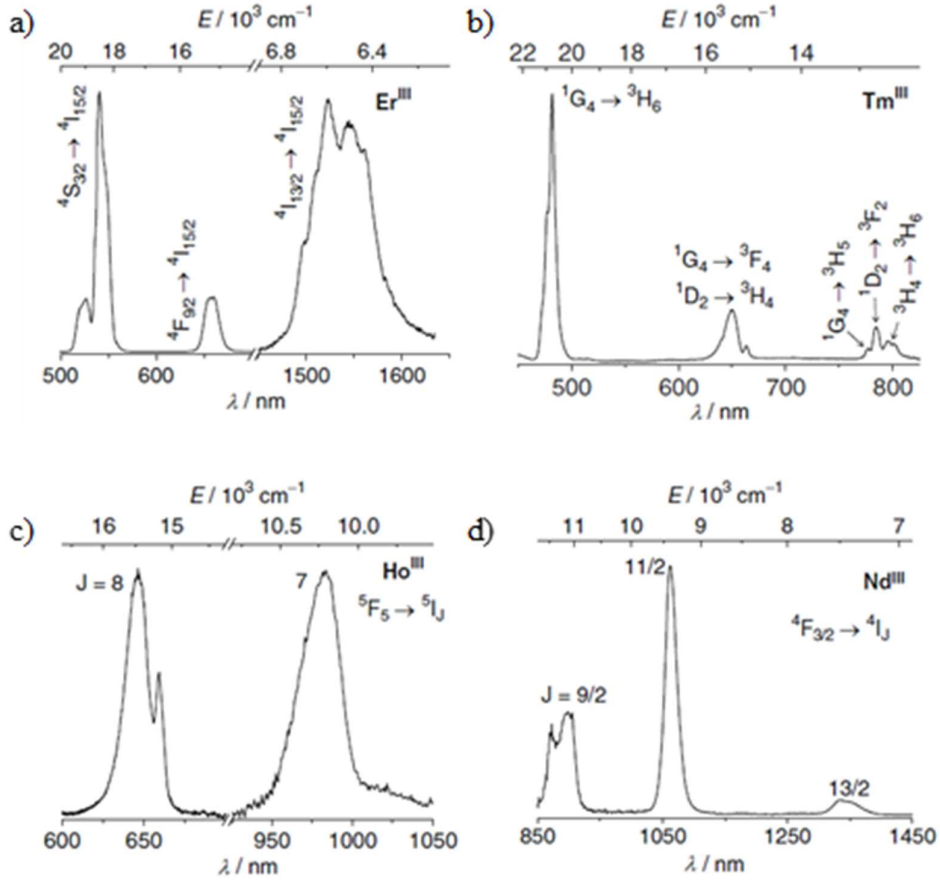

Fig.8 Typical examples of Ln^{3+} spectra from (a) microcrystalline $NaYF_4$:Yb/Er (λ_{ex}=980 nm) and from microcrystalline [Ln(hfa)$_3$(4-cyanopyridine-N-oxide)$_2$] for Ln = (b) Tm, (c) Ho and (d) Nd respectively (under ligand excitation λ_{ex}=320-340 nm)[11].

2.3 Energy Transfer (ET)

The energy transfer mechanism (ET) is an electronic excitation process in which the energy acquired by an excited ion (the donor, or sensitizer, D) is transferred during its fluorescence lifetime to neighbouring ions (the acceptor, or activator, A). As a result, the donor returns to the ground state, while the acceptor is promoted to an excited state. If the acceptor is itself luminescent, it can emit resulting in sensitized emission (excited by the donor). Two types of mechanisms can take place:

- Radiative ET: the excited donor emits a photon, that is subsequently absorbed by the groundstate acceptor: D* → D + hυ → hυ + A → A*
  This process is important if the acceptor absorbs at the emission wavelength of the donor. No interaction between the two species is required.

► Non-radiative ET: the excited donor transfers energy to the ground-state acceptor via a non-radiative process: D* + A → D + A*. Two major processes are responsible for non-radiative ET: Förster resonance and Dexter exchange mechanisms.

Förster resonance energy transfer (FRET) (Fig.9) involves the electrostatic interaction between the two species D and A. It does not require contact (donor-acceptor distances may be as long as 50-100 Å), however for an efficient energy transfer, the energies of the two transitions D*→D and A→A* must be very similar. When small energy differences exist, the presence of phonons may facilitate the process (phonon-assisted ET), even if too high phonon energies promote non-radiative de-excitation instead of ET.

In order to define the strength of ET for a donor-acceptor couple, Förster introduced the parameter R_0, namely the critical radius, that represents the separation between the two species D-A at which the probability of ET and that of radiative emission from the donor are equal.

The energy probability in the case of dipole-dipole (dd) transitions can be written as:

$$W_{dd}^{DA}(R) = \frac{1}{\tau_D}\left(\frac{R_0}{R}\right)^6 \qquad (5)$$

where τ_D is the radiative lifetime of the donor and R is the separation between D and A.

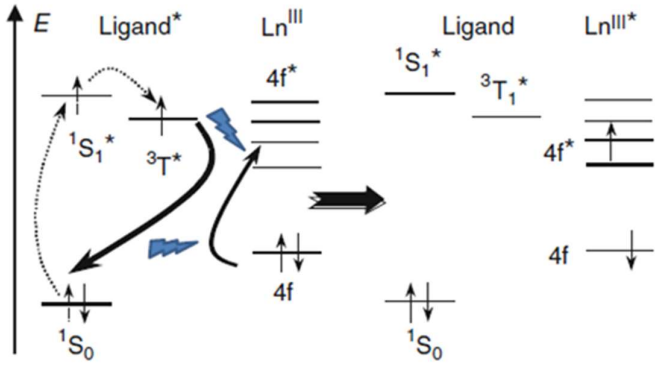

Fig.9 Förster resonance mechanism[11].

Dexter then extended Förster's dipole-dipole mechanism to other types of interactions, such as dipole-quadrupole, quadrupole-quadrupole and electric dipole-magnetic dipole, each with a specific distance dependence. The Dexter Exchange Mechanism requires a direct contact between donor ad acceptor ions/molecules and is more likely to occur if the donor-acceptor distance is below 5Å. The donor, after being excited, transfers an electron to the acceptor, that relocates an electron back to the donor (Fig. 10). Since this process occurs at short distances it is usually connected to quenching phenomena.

Since Dexter's interaction occurs at a shorter distance, other electric multipolar interactions, such as dipole-quadrupole (dq) and quadrupole-quadrupole (qq), become relevant. The probability of ET was thus generalized as[16]:

$$W_{dd}^{DA}(R) = \frac{1}{\tau_D}\left(\frac{R_0}{R}\right)^s \tag{6}$$

where s is equal to 6, 8 or 10 for (dd), (dq) and (qq) interactions, respectively.

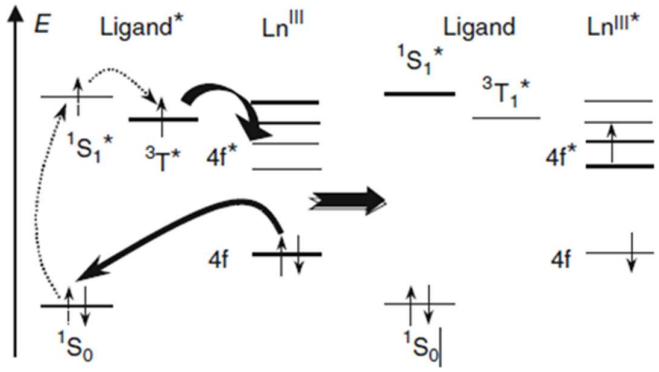

Fig.10 Dexter Exchange Mechanism[11].

Both non-radiative ET mechanisms require the spectral overlap between the donor emission and the acceptor absorbance spectra (Fig. 11) as showed in the following equation for the energy transfer rate:

$$k_{ET} = f\,(r_{D-A}) \int I_D \varepsilon_A d\bar{\nu} \tag{7}$$

where I_D represents the donor emission, ε_A the acceptor absorption, the integral represents the spectral overlap and the factor $f(r_{D\text{-}A})$ is a function of the distance between the centres of the two species.

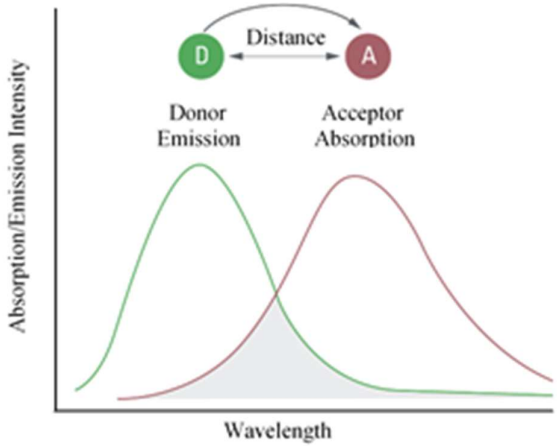

Fig.11 Emission and absorption of the donor and acceptor in ET.

Some energy transfer mechanisms may be detrimental to fluorescence quantum yield, such as the non-radiative processes described above, however many other radiative mechanisms can occur between ions, leading to phenomena such as downconversion (DC) and upconversion (UC) luminescence (Fig.12), depending on the relationship between absorption and emission wavelengths of the transitions involved in the process. Both are nonlinear optical processes, however DC consists in the quantum cutting (QC) of one photon of higher energy into a couple, or more, photons of lower energy (Stokes emission), while UC consists in the sequential absorption of two, or more, photons that leads to the emission of light at shorter wavelength (anti-Stokes emission).

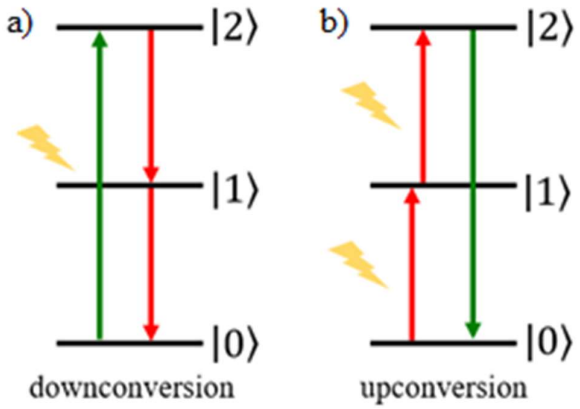

Fig.12 Schematic diagram of the (a) downconversion and (b) upconversion processes.

2.4 Downconversion

Various downconversion mechanisms may occur. Visible quantum cutting of a single ion with sequential emission of two visible photons (Fig. 12a) is possible, however it can become inefficient because of competing processes (IR and UV emissions). Other different pathways, involving the energy transfer between two types of ions (I and II), can occur, such as cross-relaxation (Fig. 13a) and cooperative energy transfer (Fig. 13b). During cross-relaxations, part of the excitation energy is transferred to an acceptor ion. If the donor, that is in an intermediate state, and the acceptor both emit, a 1-to-2 photon conversion process occurs. In the case of cooperative ET, the excitation energy is simultaneously transferred to two nearby acceptors, resulting in two emitted photons for every one that is absorbed. Thus, both mechanisms give a quantum efficiency of 200%.

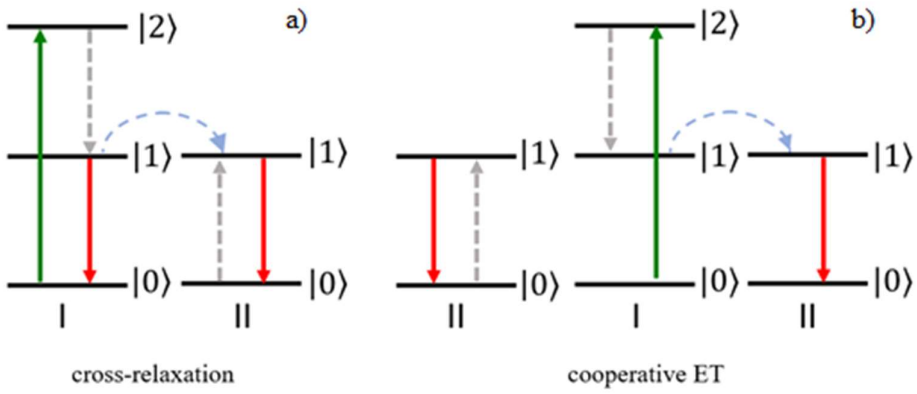

Fig.13 Schematic diagram of the (a) cross-relaxation and (b) cooperative energy transfer processes.

2.5 Upconversion

Upconversion (UC) is a nonlinear multiphoton optical process that consists in the sequential absorption of two or more photons that are then re-emitted as anti-Stokes radiations, with shorter wavelength and higher energy[10,17-19], thus allowing the conversion of NIR light to higher energy light such as UV, visible and also less energetic than the source NIR[20].The indispensable condition is the presence of a metastable absorbing state between the ground and the emitting states[19]. Other less efficient anti-Stokes mechanisms, that require the presence of virtual levels, are two-photon absorption (TPA) and second harmonic generation (SHG), that will not be discussed further, with an efficiency η of 10^{-13}-10^{-12} cm^2W^{-1} and 10^{-11} cm^2W^{-1}, respectively[18].

Upconversion comes with various advantages respect to direct excitation, among them the main are the possibility to adopt commercially available cheap diodes and the suitability of NIR light as excitation light, able to generate emission transitions spanning from UV to NIR regions[20].

Five main upconversion mechanisms may occur (Fig. 14), either alone or simultaneously[21]: excited state absorption (ESA), energy transfer upconversion (ETU), sensitized energy transfer upconversion (sensitized ETU), cooperative luminescence upconversion (CLU) and cooperative sensitization upconversion (CSU) (see the following simplified energy level diagram). Besides, Photon Avalanche (PA) is responsible for the population of the UC emitting levels above a pumping threshold.

2.5.1 Excited State Absorption (ESA)

Excited state absorption (Fig. 14a) involves a single dopant ion and consists in the sequential absorption of two photons, firstly populating an intermediate level, |1⟩, and then, if |1⟩ lifetime is long enough, the higher-energy excited state |2⟩, from which UC

emission happens, relaxing the ion back to the ground state. The same pump wavelength may be used if the energy gap separating the levels is equal, otherwise multi-pumping sources will be required[18]. Moreover, this process requires a source with high pumping power, and for this reason is considered to be the least efficient among upconversion mechanisms ($\eta = 10^{-5}$ cm^2W^{-1})[10]. Lanthanide ions with an ESA suitable ladder-like energy level structure are for example Er^{3+}, Tm^{3+}, Ho^{3+} and Nd^{3+}.

2.5.2 Energy Transfer Upconversion (ETU)

Energy transfer mechanism exists in two forms (Fig. 14 b and c) depending on the neighboring dopant ions involved in the process. The dopants can be identical ions, in this case both are excited to the intermediate state via GSA and then one of the two ions is promoted to a higher energy level via ET, such as in the case of Er^{3+} ions. As an alternative, two types of ions can be involved, one is denoted as the donor, or sensitizer, (e.g. Yb^{3+}) the other as the acceptor, or activator, (e.g. Er^{3+}, Ho^{3+}, Tm^{3+}). The donor harvests the incident photons, transferring then the energy to the acceptor that will emit, and finally relaxes to a lower-energy or ground state. If the intermediate levels of the two types of ions are not resonant, the energy transfer process must be phonon-assisted. The donor dopant concentration typically ranges from 10 to 50 times that of the acceptor concentration. The efficiency of the ETU mechanism is influenced by both the choice of the dopant ions, since the cross-section of the acceptor at the emission wavelength of the donor plays a critical role, and their relative concentration[17,19]. Generally, it is the most efficient among upconversion mechanisms ($\eta = 10^{-3}$-10^{-1} cm^2W^{-1}).

2.5.3 Cooperative Luminescence Upconversion (CLU)

Cooperative luminescence occurs between a pair of ions and a third, single ion (Fig. 14 d). The two ions are excited to an intermediate state, they then transfer their energy to a neighboring third ion that emits a single photon of higher energy (i.e. the sum of the energies involved) from a virtual level. This process is observable only with high and spatially focused pump intensity[22] and is very inefficient ($\eta = 10^{-8}$ cm^2W^{-1}).

2.5.4 Cooperative Sensitization Upconversion (CSU)

The cooperative sensitization mechanism is similar to the previously described CLU process, however it involves a real emitting state (Fig. 14 e) instead of a virtual one,

with consequent higher efficiency ($\eta = 10^{-6}$ cm^2W^{-1}) respect to CLU. This mechanism has been previously reported for Yb^{3+}-Tm^{3+} co-doped systems.

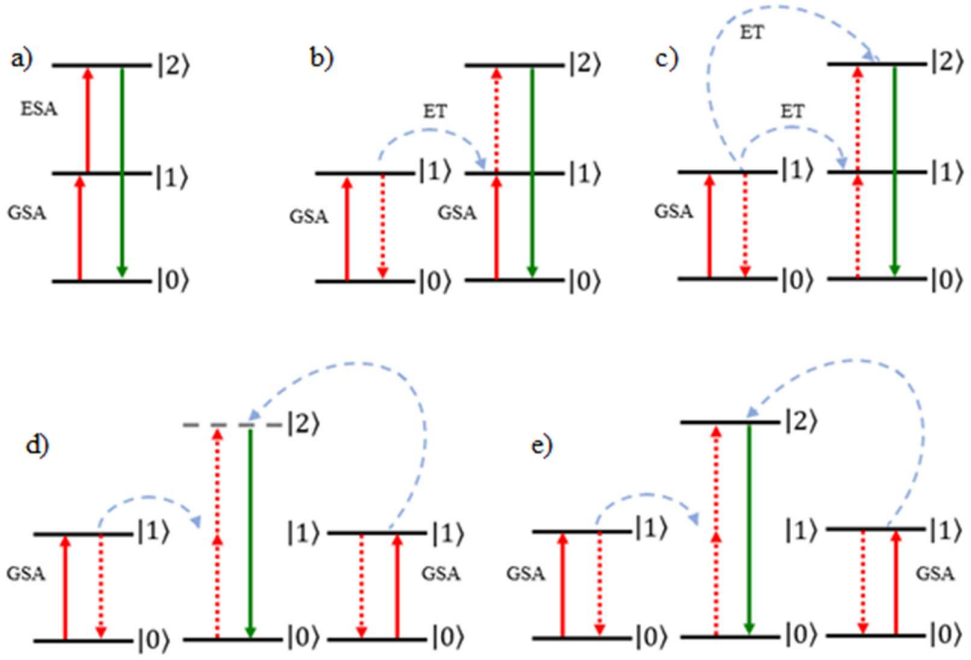

Fig.14 Main UC mechanisms: (a) excited-state absorption ESA, (b) energy transfer upconversion ETU, (c) sensitized energy transfer upconversion ETU, (d) cooperative luminescence upconversion CLU and (e) cooperative sensitization upconversion CSU.

2.5.5 Photon Avalanche (PA)

Photon avalanche effect occurs only above a certain pumping threshold, when the cross-relaxation (CR) probability is higher than the relaxation rate from the up-converted excited state to the levels located below the metastable intermediate state[23]. It is a looping process based on several energy transfer processes (CR and ESA). Fig.15 offers a simplified diagram of two neighboring ions: the intermediate excited state |1⟩ of one ion is populated via ground state absorption and then the higher-energy level |2⟩ is then populated via excited state absorption. Finally, cross-relaxation energy transfer occurs, resulting in both ions excited at the metastable |1⟩ state. The loop continues with the energy transfer from one to the other ions in the intermediate state, resulting in the relaxation of the first to the ground state |0⟩ and the promotion of the second ion to the excited state |2⟩[10]. The process is then repeated[18], the higher energy level is thus populated exponentially, with an avalanche mechanism, leading to high UC yields. This process is dependent on the pumping power and shows slow response times[19, 24].

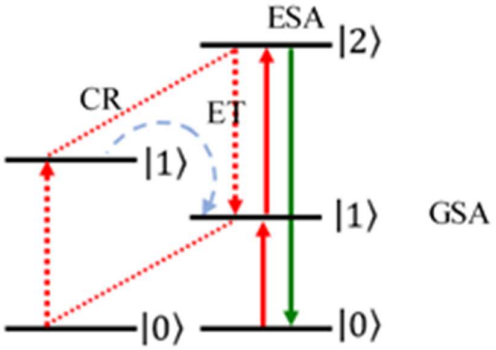

Fig.15 Photon avalanche looping mechanism.

2.6 Typical systems activated by donor-acceptor ion pairs

Two major parameters affect the UC efficiency: the distance among the neighbouring dopant ions and their absorption cross-section σ_A[18].

Single doped nanoparticles have relatively low UC efficiencies and the resultant attempts to increase the dopant content are limited by the concentration quenching effect. The strategy based on co-doping with a sensitizer, having a reasonable absorption cross-section in the NIR range, has the beneficial effect of enhancing the UC efficiency. Thanks to its absorption cross section of 9.11 x 10^{-21} cm^{-2}, Yb^{3+} is particularly suitable as sensitizer[26]. The energy level diagram of Yb^{3+} is very simple and consists only of the $^2F_{7/2}$ ground state and the $^2F_{5/2}$ excited level, separated of about 10000 cm^{-1}. The energy gap between the two levels of Ytterbium is resonant with f–f transition of many lanthanide ions, facilitating ETU processes[25].

Typical up-conversion systems are (Yb, Er), (Yb, Tm) and (Yb, Ho), thanks to the ladder-like energy level structure and the long-lived excited states of these activators [25, 27]. Usually, the dopants are added in relatively low concentrations to the host lattice (≤20%at. Yb^{3+}, ≤2%at. Er^{3+}, 0.2%≤Tm^{3+}≤0.5%at., ≤2%at. Ho^{3+},). Higher concentrations of Yb^{3+} ions might promote energy back-transfer (EBT) from the activators to the sensitizers, depopulating the emitting levels and thus affecting UC quantum yield[29].

2.6.1 Yb Er pair

Yb^{3+}-Er^{3+} pair of dopants shows particularly high UC efficiency. This is due to the similarity between the energy levels structures of the two ions, namely between the energy gap of $^4I_{11/2}$ and $^4I_{15/2}$ levels of Er^{3+} and that of $^4F_{7/2}$ and $^4I_{11/2}$ of Yb^{3+} ions (Fig.16). In Yb^{3+}-Er^{3+} co-doped hosts, the emission colors most commonly observed are green (emission band at 520-550 nm) and red (650-660 nm), involving two photon processes, plus a weak violet emission at 415 nm, involving a three photon process observed at high pumping powers[26].

After 980 nm light irradiation, the efficient energy transfer ET takes place between the sensitizer and the activator. This two-photon process is responsible for the $^4I_{15/2}\rightarrow{}^4I_{11/2}$ and $^4I_{11/2}\rightarrow{}^4F_{7/2}$ transitions to populate Er^{3+} excited states. A non-radiative relaxation occurs then from $^4F_{7/2}$ level to $^2H_{11/2}$ and $^4S_{3/2}$ emitting levels, which correspond to the two green emissions at around 520 and 540 nm. Another pathway leads to the population of $^4F_{9/2}$ emitting level, resulting in the radiative transition to the ground state corresponding to the red emission at around 650 nm, and through partial non-radiative relaxation to the population of $^4I_{9/2}$ level, resulting in the NIR emission at around 800 nm. A three-photon ET process leads to the population of $^4G_{11/2}$ level, that gives the weak violet emission at around 415 nm.

Different strategies to tune the emission intensities are possible. For example, the red/green intensity ratio can be increased by rising the concentration of Yb^{3+} in the host lattice. This leads to the reduction of Yb-Er inter-atomic distance, promoting the energy backtransfer (EBT) from Er^{3+} to Yb^{3+} and resulting in the reduction of green emissions intensity as well as the enhancement of red emission[30-32].

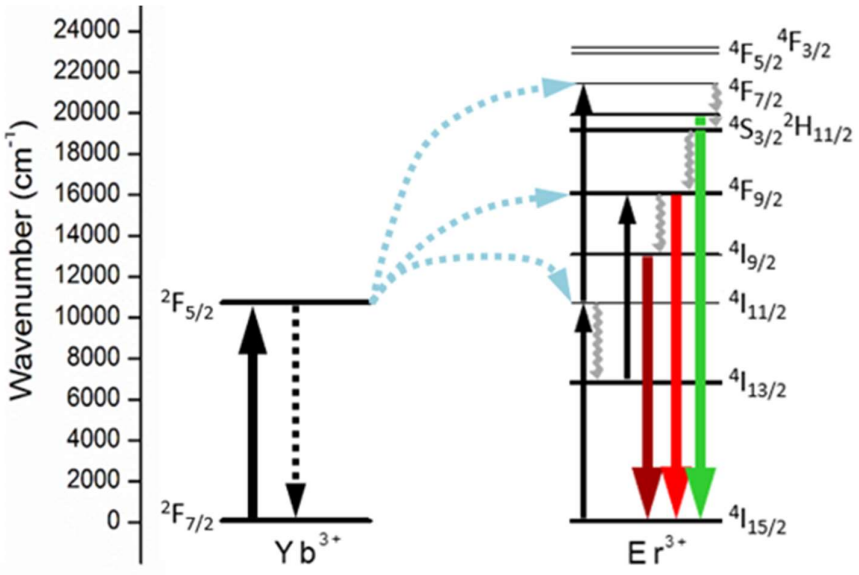

Fig.16 Schematic energy level diagram for Yb^{3+}-Er^{3+} ion pair, representing common two-photons radiative transitions ($^2H_{11/2}\rightarrow{}^4I_{15/2}$, $^4S_{3/2}\rightarrow{}^4I_{15/2}$, $^4F_{9/2}\rightarrow{}^4I_{15/2}$, $^4I_{9/2}\rightarrow{}^4I_{15/2}$).

2.6.2 Yb Tm pair

The excitation pathway in Yb^{3+}-Tm^{3+} pair is more complex, as it is a multi-photon process, involving up to five photons. After the excitation with a 980 nm light, energy is transferred from Yb^{3+} $^2F_{5/2}$ excited level to Tm^{3+} ions in a series of subsequent steps (1 to 5 photons absorbed) bringing Tm^{3+} to ascending excited levels: $^3H_6 \rightarrow ^3H_5$, $^3F_4 \rightarrow ^3F_2$, $^3H_4 \rightarrow ^1G_4$, $^1G_4 \rightarrow ^1D_2$, $^1D_2 \rightarrow ^3P_2$[33].

From Fig. 17 the different multi-photon transitions can be assigned to various emission processes:

- emissions at 695 and 800 nm are two-photon processes corresponding to the $^3F_2 \rightarrow ^3H_6$ and $^3H_4 \rightarrow ^3H_6$ transitions, respectively;
- emissions at 475 and 650 nm are three-photon processes due to the $^1G_4 \rightarrow ^3H_6$ and $^1G_4 \rightarrow ^3F_4$ transitions;
- emissions at 360 and 450 nm are four-photon processes respectively attributed to the $^1D_2 \rightarrow ^3H_6$ and $^1D_2 \rightarrow ^3F_4$ transitions
- emissions at 290 and 345 nm (not shown in the picture) are five photon processes corresponding to the $^1I_6 \rightarrow ^3F_4$ and $^1D_2 \rightarrow ^3H_6$ transitions, respectively[26].

The emission at 800 nm is the most intense, making Tm^{3+} doped hosts excellent candidates as NIR to NIR imaging probes[34]. UV emissions are also important for a variety of applications, however practical applications are restricted because of the weak emission intensities[35].

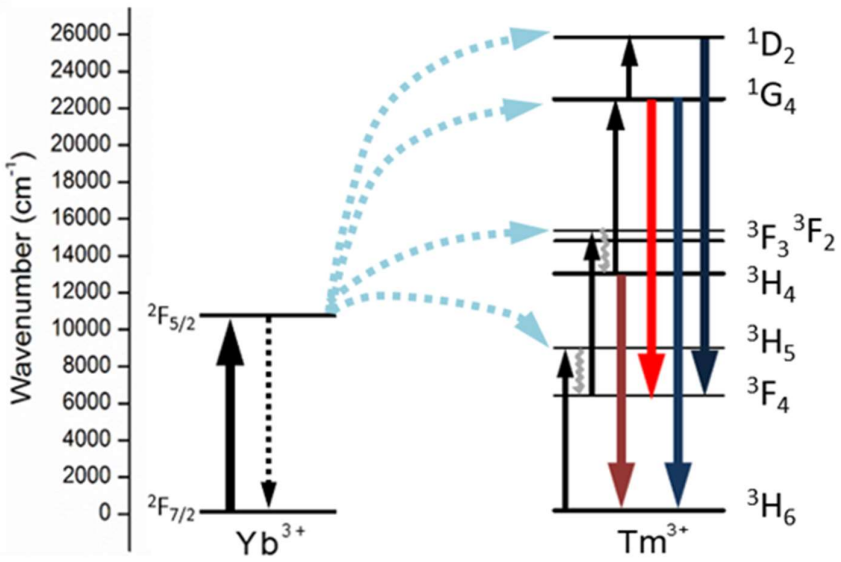

Fig.17 Schematic energy level diagram for Yb^{3+}-Tm^{3+} ion pair, representing common two- ($^3H_4 \rightarrow ^3H_6$), three- ($^1G_4 \rightarrow ^3H_6$ and $^1G_4 \rightarrow ^3F_4$) and four-photons ($^1D_2 \rightarrow ^3F_4$) UC processes.

2.6.3 Yb Ho pair

After 980 nm light irradiation, an energy transfer ET process takes place between the sensitizer and the activator (Fig.18). This two-photon process is responsible for the $^5I_8 \rightarrow {}^5I_6$ and $^5I_6 \rightarrow {}^4F_4(^5S_2)$ transitions to populate Ho^{3+} excited states. The radiative transitions $^4F_4(^5S_2) \rightarrow {}^5I_8$ and $^4F_4(^5S_2) \rightarrow {}^5I_7$ are responsible for the green and NIR emissions at about 540 and 760 nm, respectively.

Another two-photon pathway (by means of $^5I_8 \rightarrow {}^5I_6$ and $^5I_7 \rightarrow {}^5F_5$ transitions) leads to the population of $^5F_5$ emitting level, resulting in the radiative transition to the ground state corresponding to the red emission at around 650 nm[36-37].

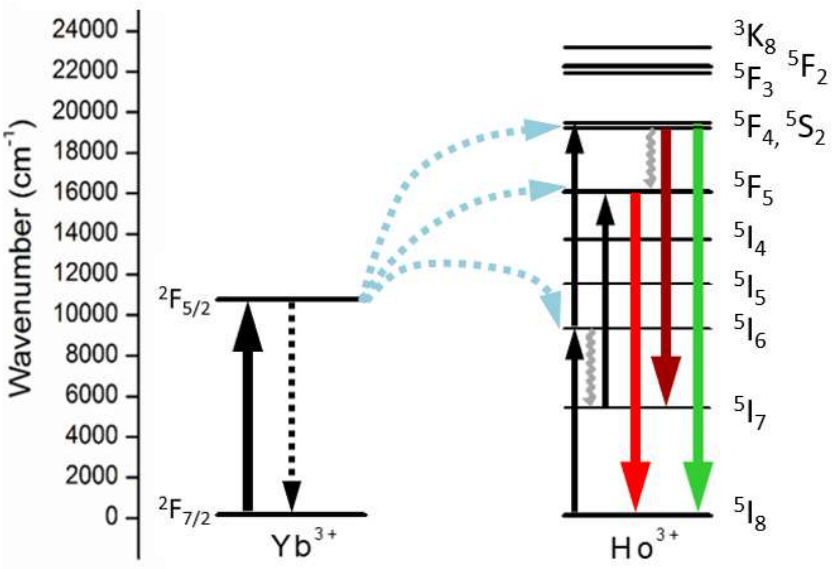

Fig.18 Schematic energy level diagram for Yb^{3+}-Ho^{3+} ion pair, representing common two-photons radiative transitions ($^4F_4(^5S_2) \rightarrow {}^5I_8$ and $^4F_4(^5S_2) \rightarrow {}^5I_7$ and $^5F_5 \rightarrow {}^5I_8$).

2.7 Nd^{3+} luminescence

After 590 nm light irradiation a one-photon process is responsible for the $^4I_{9/2} \rightarrow {}^4F_{5/2}$ transition to populate Nd^{3+} excited state (Fig.19). The radiative transition from $^4F_{5/2} \rightarrow {}^4I_{9/2}$ corresponds to the NIR emission at 810 nm. A non-radiative relaxation can also occur from $^4F_{5/2}$ to $^4F_{3/2}$ level. The radiative transition from $^4F_{3/2}$ to $^4I_{9/2}$, $^4I_{11/2}$ and $^4I_{13/2}$ are responsible for the NIR emissions at about 950, 1050 and 1350 nm, respectively. In the case of Nd^{3+} also an upconversion process is possible, associated to ESA from $^4F_{3/2}$ to $^2D_{5/2}$ level with the absorption of a second photon. A non-radiative relaxation leads to the $^4G_{7/2} \rightarrow {}^4I_{11/2}$, $^4G_{7/2} \rightarrow {}^4I_{13/2}$ and $^4G_{5/2} \rightarrow {}^4I_{11/2}$ transitions, corresponding to VIS emissions at about 585, 660 and 680 nm, respectively.

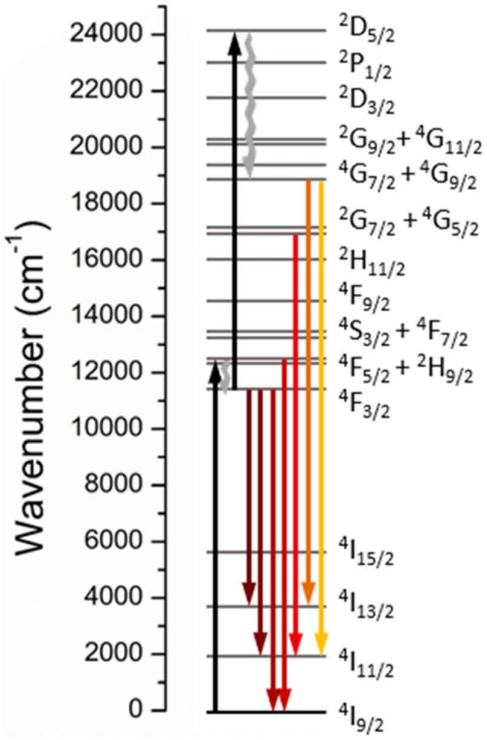

Fig.19 Schematic energy level diagram for Nd^{3+}-doped systems*, representing radiative transitions (*$^4F_{3/2} \rightarrow {}^4I_{13/2}$, $^4F_{3/2} \rightarrow {}^4I_{11/2}$, $^4F_{3/2} \rightarrow {}^4I_{9/2}$, $^4F_{5/2} \rightarrow {}^4I_{9/2}$, $^4G_{5/2} \rightarrow {}^4I_{11/2}$, $^4G_{7/2} \rightarrow {}^4I_{13/2}$ *and* $^4G_{7/2} \rightarrow {}^4I_{11/2}$*).*

References

[1] Wehry, E. L., Concepts in Inorganic Photochemistry, *Journal of Chemical Education*, **197**7, 54, 3.

[2] Omary, M. A., Patterson, H. H., Luminescence Theory, Encyclopaedia of Spectroscopy and Spectrometry, *Academic Press*, **1999**, ISBN 978-0-123-74413-5.

[3] Zhu, X., Su, Q., Feng, W., Li, F., Anti-Stokes shift luminescent materials for bio-applications, *Chem. Soc. Rev*., **2017**, 46(4), 1025-1039.

[4] Murthy, K.V.R., Virk, H. S., Luminescence Phenomena: An Introduction, *Defect and Diffusion Forum*, **2014**, 347, 1-34.

[5] Lakowicz, J. R., Principles of Fluorescence Spectroscopy, *Springer US*, **2006**, ISBN 978-0-387-46312-4.

[6] Würth, C., Grabolle, M., Pauli, J., Spieles, M., Resch-Genger, U., Relative and absolute determination of fluorescence quantum yields of transparent samples, *Nature Protocols*, **2013**, 8, 1535-1550.

[7] Sauer, M., Hofkens, J. and Enderlein, J., Basic Principles of Fluorescence Spectroscopy in Handbook of Fluorescence Spectroscopy and Imaging, *Wiley-VCH*, **2011**, ISBN 978-3-527-31669-4.

[8] Di Bartolo, B., Forte, O., Advances in Spectroscopy for Lasers and Sensing, *Springer Netherlands*, **2006**, 403-433, ISBN 978-1-4020-4787-9.

[9] Dramićanin, M., Luminescence Thermometry, chapter 3, Woodhead Publishing Series in *Electronic and Optical Materials*, **2018**, ISBN 978-0-081-02029-6.

[10] Dong, H., Sun, L. D., Yan, C. H., Basic understanding of the lanthanide related upconversion emissions, *Nanoscale*, **2013**, 5, 5703.

[11] Bünzli, J.-C., Eliseeva, S., Basics of Lanthanide Photophysics, *Lanthanide Luminescence*, **2010**, 7, 1-45.

[12] Harris, D. C., Bertolucci, M. D., Symmetry and spectroscopy: an introduction to vibrational and electronic spectroscopy, Oxford University Press, **1978**.

[13] Werts M. H., Making sense of lanthanide luminescence., *Sci Prog*., **2005**, 88(2), 101-131.

[14] Moore, E. G., Samuel, A. P. S., Raymond, K. N., From Antenna to Assay: Lessons Learned in Lanthanide Luminescence, *Acc. of Chem. Res*., **2009**, 42(4), 542-552.

[15] Reisberg, L.A., Weber, M. J., in Progress in Optics Vol. XIV, *E. Wolf ed.*, **1976**, 89-159.

[16] Dexter, D. L., A theory of sensitized luminescence in solids, *J. Chem. Phys*., **1953**, 21, 836-850.

[17] Auzel, F., Materials and devices using double-pumped phosphors energy transfer, *Proc. IEEE*, **1973**, 61, 758–786.

[18] Auzel, F., Upconversion and anti-stokes processes with f and d ions in solids, *Chem. Rev*., **2004**, 104(1), 139–174.

[19] Scheps, R., Upconversion laser processes., *Prog. Quant. Electron*., **1996**, 20, 271–358.

[20] Rodriguez-Burbano, D. C., Naccache, R., Capobianco, J. A., Near-IR Triggered Photon Upconversion: Imaging, Detection, and Therapy in Handbook on the Physics and Chemistry of Rare Earths, Chapter 273, *Elsevier*, **2015**, 47, 273-347.

[21] Gamelin, D.R., Gudel, H.U., Transition Metal and Rare Earth Compounds, Chapter 1, *Springer-Verlag*, **2001**.

[22] Sivakumar, S., Veggel, Red, green and blue light through cooperative upconversion in sol–gel thin films made with $Yb_{0.80}La_{0.15}Tb_{0.05}F_3$ and $Yb_{0.80}La_{0.15}Eu_{0.05}F_3$ nanoparticles, *J. Disp. Technol*., **2007**, 3(2), 176–183.

[23] Joubert, M. F., Guy, S., Jacquier, B., Model of the photon-avalanche effect, *Phys. Rev. B*, 1993, **48**, 100-131.

[24] Joubert, M.F., Photon avalanche upconversion in rare earth laser materials, *Opt. Mater*., **1999**, 11(2–3), 181–203.

[25] Wang, F., Liu, X., Recent advances in the chemistry of lanthanide-doped upconversion nanocrystals, *Chem. Soc. Rev*., **2009**, 38, 976-89.

[26] Dong, H., Sun, L.-D., Yan, C.-H., Energy transfer in lanthanide upconversion studies for extended optical applications, *Chem. Soc. Rev*., **2015**, 44(6), 1608-1634.

[27] Chamarro, M. A., Cases, R., Energy up-conversion in (Yb, Ho) and (Yb, Tm) doped fluorohafnate glasses, *Journal of Luminescence*, **1988**, 42(5), 267-274.

[28] Haase, M., Schäfer, H., Upconverting nanoparticles, *Angew. Chem*., **2011**, 50, 5808–5829.

[29] Liang, L., Wu, H., Hu, H., Wu, M., Su, Q., Enhanced blue and green upconversion in hydrothermally synthesized hexagonal $NaY_{1-x}Yb_xF_4:Ln^{3+}$(Ln^{3+}= Er^{3+} or Tm^{3+}), *J. alloys compd.*, **2004**, 368, 94-100.

[30] Chen, G., Qiu, H., Fan, R., Hao, S., Tan, S., Yang, C., Han, G., Lanthanide-doped ultrasmall yttrium fluoride nanoparticles with enhanced multicolor upconversion photoluminescence, *J. Mater. Chem*., **2012**, 22, 20190-6.

[31] Niu, N., Yang, P., He, F., Zhang, X., Gai, S., Li, C., Lin, J., Tunable multicolor and bright white emission of one-dimensional $NaLuF_4:Yb^{3+},Ln^{3+}$ (Ln = Er, Tm, Ho, Er/Tm, Tm/Ho) microstructures, *J. Mater. Chem*., **2012**, 22, 10889-99.

[32] Wang, F., Liu, X., Upconversion multicolor finetuning: visible to near-infrared emission from lanthanide-doped $NaYF_4$ nanoparticles, *J. Am. Chem. Soc*., **2008**, 130, 5642-3.

[33] Qiu, H., Yang, C., Shao, W., Damasco, J., Wang, X., Ågren, H., Prasad, P., Chen G., Enhanced upconversion luminescence in Yb^{3+}/Tm^{3+}- codoped fluoride active core/active shell/inert shell nanoparticles through directed energy migration, *Nanomaterials*, **2014**, 4, 55-68.

[34] Ehlert, O., Thomann, R., Darbandi, M., Nann, T., A four-color colloidal multiplexing nanoparticle system, *ACS Nano*, **2008**, 2, 120-4.

[35] Li, D., Wang, Y., Zhang, X., Yang, K., Liu, L., Song, Y., Optical temperature sensor through infrared excited blue upconversion emission in Tm^{3+}/Yb^{3+} codoped Y_2O_3, *Optics Communications*, **2012**, 285, 1925–1928.

[36] Watts, R. K., Richter, H. J., Diffusion and Transfer of Optical Excitation in YF_3: Yb, Ho, *Phys. Rev. B*, **1972**, 6(4), 1584-1589.

[37] Liu, S., Ye, X., Liu, S., Chen, M., Niu, H., Hou, D., You, W., Intense upconversion luminescence and energy-transfer mechanism of Ho^{3+}/Yb^{3+} co-doped $SrLu_2O_4$ phosphor, *J. of the Am. Cer. Soc.*, **2017**, 100(8).

CHAPTER 3

Temperature sensing

Temperature sensing is crucial in many fields, ranging from industrial manufacturing and automotive, heating and cooling devices, food storage, scientific research, defense and aerospace, to even biomedicine[1]. Thermometers are commonly distinguished between primary or secondary, where primary ones are self-calibrating and based on equations that directly relate measured values to absolute temperature; on the other hand, secondary thermometers do need to be calibrated and provide only temperature changes, acting as sensors[2].

In the last decade, the research on non-invasive thermometry techniques, featured with a high spatial resolution (defined as the minimum distance required to sense a temperature change greater than the sensitivity of the thermometer[2]) at the micrometric and nanometric scale, faced an escalating trend. Fields that were requiring submicron spatial resolution, becoming the driving force to technological innovation, were, among the others, microfluidics[3-10], photonics, microelectronics[11-21], micro-optics and nanomedicine, especially for what concerns intracellular temperature fluctuations[22-38].

3.1 Thermometry at the nanoscale

The methods to determine the temperature of a system may be classified as contact or non-contact. The more common contact temperature sensors have a major drawback, being unable to work at submicron scale, thus being inappropriate to measure small systems, at scales below 10 μm, or in fast moving objects[2].

The first attempt consisted in a miniaturization approach, trying to reduce the geometrical size of conventional contact-thermometers[39-40]. Examples encompass among the others: liquid-filled nanotubes, based on thermal expansion of liquids[41-42], co-doped sub-micrometric crystals, based on fluorescence thermal quenching[12], nanoscale thermocouples, based on point contact junctions[43-45] and cantilever probes for scanning thermal microscopy[46]; some of them managing to improve the spatial and temperature resolutions down to about 50 nm and 1 mK, but still not suitable for real time temperature mapping. Moreover, surface techniques allow to obtain only 2D

thermal images and as a further disadvantage, contact measurements imply conductive heat transfer, therefore causing a disturbing connection between the sensor and the sample, especially when working with small objects[47]. These limitations lead to the development of non-contact nanothermometers: luminescent temperature sensors are the most promising among non-invasive spectroscopic methods.

The determination of the temperature of the system generally relies on the changes of the passive optical properties of the probe and a great variety of techniques are available, based either on Raman spectroscopy (variation in the vibration modes), IR thermography (change in the emissivity at a specific spectral range), optical interferometry (change in the optical path length of a transparent system), thermoreflectance (variation in polarization and intensity of reflected light), or luminescence (change in the properties of emitted photons)[48-49].

It is important to state that a universal thermal sensor cannot exist. Rarely a system fulfills all the conditions for an ideal thermometer, that are stability, accuracy and reproducibility[2, 42]. Moreover, heterogeneous applications call for different properties. For example, biological applications require water-soluble, non-toxic and stable under light irradiation probes with great thermal sensitivity, whereas in opto-fluidics physical and chemical stable sensors are preferred due to high laser intensities within micro-channels[48].

Table 1 provides a summary of popular methods for high-resolution thermal techniques, including advantages and disadvantages[2, 50-51].

Method	**Principle**	**Resolution**			**Advantages**	**Disadvantages**
		δx (μm)	δT (K)	δt (μs)		
Infrared thermography	Plank blackbody emission	10	10^{1}	10	- Temperature profile of the surface - Commercial technique	- Detector saturation at high T - Ryleigh limited δx
Thermoreflectance	Tempera-ture dependence of the reflection	10^{-1}	10^{-2}	10^{-1}	- High δT and δt - Quantitative/ - qualitative	- Requires calibration of RI - δx limited by diffraction limit
Raman	Inelastic scattering of light	1	10^{-1}	10^{6}	- Works in liquids and solids, even with small volumes	- Time-consuming technique - Low signal and crosstalk with fluorescent species
Optical interferometry	Thermal expansion or RI change	1	10^{-5}	10^{-3}	- All optical temperature determination - Integrated in remote systems	- Crosstalk with other stimulus - Low δx in the transverse direction

Fluorescence thermography	Tempera-ture dependence of spectral parameters	10^{-1}	10^{-2}	10	- High temperature sensitivity - Various techniques available - Independent of illumination source	- Intensity and lifetime limited by photobleaching - Expensive excitation sources and detectors for lifetimes
Near-field scanning optical microscopy	Near-field to improve optical resolution	10^{-2}	10^{-1}	10	- Spatial resolution below the Rayleigh limit	- Dependent on surface characteristics - Measures only surface temperature - Vacuum and/or cryogenic temperatures required
Liquid crystal thermography	Crystal phase transitions	10	10^{-1}	10^{2}	- Various materials depending on temperature range	- Semi-quantitative if not carefully calibrated - Not compatible with liquid systems
Scanning thermal microscopy	AFM with thermo-couple	10^{-1}	10^{-1}	10^{2}	- AFM tips measure simultaneously temperature and surface roughness - Sub-micrometric δx	- Time-consuming - Suitable only for solid samples - Tip-sample heat transfer
Transmission electron microscopy	Thermal expansion	10^{2}	10	10	- High δx - Compatible with various carbon NTs	- Requires vacuum - Uncomfortable for practical applications - Requires image analysis
Micro-thermocouple	Seebeck effect	10^{2}	10^{-1}	10	- High δx - Precise T calibration	- Thermometer separated from the active region of the device, limiting the access

Table 1 Summary of common high-resolution thermal techniques, including typical spatial (δx), temperature (δT) and time (δt) resolutions, and advantages and disadvantages of each method. Non-contact thermometric methods are underlined.

3.2 Contact-less optical thermometry

For what concerns luminescence nanothermometry, often referred to as fluorescence thermography or thermographic phosphor thermometry[2], various methods can be distinguished[52] as time-integrated, if the luminescence is photoexcited continuously, or time-resolved, in the case of a pulsed excitation source[53-54]. Different methods are based on the thermal reading of various parameters (see Fig.1):

- intensity, if thermal sensing is based on the luminescence intensity, which can become less or more intense due to thermal induced quenching and/or increasing probabilities in the non-radiative decay;
- band-shape, which change usually happens when the electronic levels involved in the emission are so close in energy that they are thermally coupled;
- spectral position, because the position of the emission lines is expected to be temperature dependent and varies with the energy separation between the emitter levels;
- polarization, in anisotropic media, where the intensity and shape of peaks are dependent on the non-isotropic polarization of the emitted radiation;
- bandwidth, because increasing temperatures correspond to a major density of phonons, that cause line broadening, thus establishing a linear relationship between temperature and bandwidth;
- lifetime, since the total decay probability from electronic levels is defined as the inverse of the luminescence lifetime. Many temperature-related factors affect the decay probability of the emitted intensity, such as phonon-assisted ET and multi-phonon decays[48].

It is evident that, speaking of luminescence nanothermometry, many options are available for thermal reading of emission spectra. Clearly, remarkable variations in luminescence parameters within small temperature changes will transduce in major temperature sensitivities, while spatial resolution is primarily influenced by the spatial dimension of the luminescent probe.
The advantage in lifetime-based methods is the independence of this parameter from light scattering or reflection, intensity fluctuations of the source and inhomogeneous distribution of the phosphor. However, its determination may be time-consuming, requiring a fitting procedure of decay curves, especially in case of complicated distributions of emitting centers with strong interactions. It may also demand for sophisticated and expensive equipment.

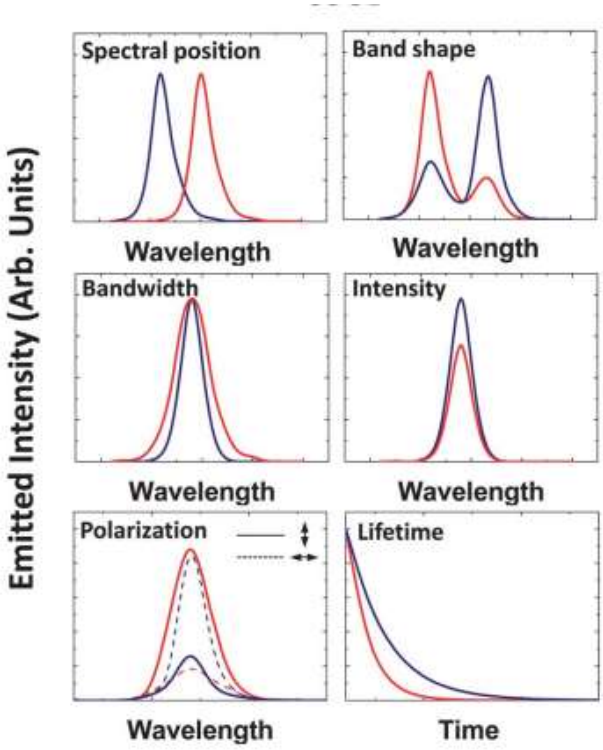

Fig. 1 Schematic representation of possible temperature-related effects on the luminescence. Red lines correspond to higher temperatures, blue lines to lower ones[48].

3.2.1 Fluorescence Intensity Ratio (FIR): method and thermometric performance

The fluorescence intensity ratio (FIR) technique (often referred to as two-color response), namely the intensity ratio between two closely spaced emitting levels (or two Stark components of an excited state) I_1 and I_2 of the same phosphor, that are thermally coupled[55] (200 $cm^{-1} \leq \Delta E \leq 2000\ cm^{-1}$ [56]) has the advantage of containing all the information needed to infer the absolute temperature, following the given equation[2] (eq. 1):

$$\Delta = \frac{I_1}{I_2} = \frac{g_1 A_1 h\upsilon_1}{g_2 A_2 h\upsilon_2}\ exp\left(-\frac{\Delta E_{12}}{k_B T}\right) = B\ x\ exp\left(-\frac{\Delta E_{12}}{k_B T}\right) \quad (1)$$

where I_1 and I_2 are the integrated intensities of the two emission peaks, g is the degeneracy of the state, A is the spontaneous emission rate, h is the Planck constant, υ is the frequency, k is the Boltzmann constant, ΔE is the energy gap between the levels and T is temperature.

In this case the temperature scale is based exclusively upon the validity of the Boltzmann distribution of electrons in given excited states at a temperature T, which

electronic populations translate proportionally to the intensities of each transition[57].
The well-known disadvantages of the methods based on the intensity of a single transition, such as dependence on variations of the sensor concentration, small material inhomogeneities, and optoelectronic drifts of the excitation source and detectors, are easily overwhelmed by ratiometric, self-referencing FIR measurements, that use two transitions, one of them as an internal standard to calibrate the response of the luminescent probe[2]. These systems are usually characterized by high-detection relative thermal sensitivity (>1% K^{-1}) and spatial resolution (<10 mm) in short acquisition times (<1 ms), even in biological fluids, strong electromagnetic fields, and fast-moving objects[48, 58] Ratiometric techniques require a simple UV excitation lamp and two photodetector diodes, each set to detect the dopant emission.
The performance, namely how efficiently the emission intensity is converted into temperature, of luminescent thermometers based on FIR, can be judged from the figures of merit that usually allow to compare different thermometers irrespective of their nature. The most frequently reported are: relative thermal sensitivity, temperature uncertainty and repeatability[57] (i.e. test-retest reliability). These parameters are computed starting from the thermometric parameter $\Delta=I_1/I_2$ (eq.1), that allows the conversion of integrated intensity into temperature.
The relative sensitivity S_r represents the relative change of Δ per degree of temperature change. It is always positive $S_r > 0$ and its maximum value is denoted as S_m[57]. The relative sensitivity is defined as follows (eq. 2):

$$S_r = \frac{1}{\Delta}\left|\frac{\partial \Delta}{\partial T}\right| \tag{2}$$

Respect to absolute sensitivity (eq. 3), that depends on experimental setup and sample characteristics such as absorption and lifetime, S_r has the advantage of being an independent parameter, despite the nature (i.e. optical, electrical, mechanical) of the thermometer[57]. This permits the quantitative comparison between different probes.

$$S_a = \left|\frac{\partial \Delta}{\partial T}\right| \tag{3}$$

The temperature uncertainty δT represents the smallest change of temperature that can be detected, depends only on the changes in Δ, and is defined by the following Taylor's series expansion of the temperature variation (eq. 4):

$$\delta T = \frac{\partial T}{\partial \Delta}\,\delta\Delta + \frac{1}{2!}\frac{\partial^2 T}{\partial \Delta^2}\,(\delta\Delta)^2 + \cdots + \frac{1}{n!}\frac{\partial^n T}{\partial \Delta^n}\,(\delta\Delta)^n \tag{4}$$

where $\delta\Delta$ represents the uncertainty in the determination of Δ. Since the expansion is dominated by the first term, equation (4) can be simplified as follows (eq. 5):

$$\delta T = \frac{1}{S_r}\frac{\delta \Delta}{\Delta} \tag{5}$$

It is then clear how the temperature uncertainty is dependent only on the thermometric performance, expressed as relative sensitivity S_r, and experimental setup, that affects $\delta\Delta/\Delta$[57]. Typical detection systems have $\delta\Delta/\Delta$ of about 0.1%, that for sensitivities in

the range 1-10%K^{-1}, means a temperature uncertainty in the range of 0.01 – 0.1 K. Advanced detectors such as charge-coupled devices (CCDs) and photomultiplier tubes (PMTs) may reach $\delta\Delta/\Delta$ values of 0.03%, and consequently a temperature resolution <0.003 K, several orders of magnitude lower than that of conventional contact thermometric systems[57].

δT values can be experimentally computed from temperature readout, in fact the relative uncertainty on Δ can be inferred from the integrated area of the transitions (δI/I). In this case $\delta\Delta/\Delta$, that is directly linked to the error propagation deriving from the determination of the emission integrated areas[59], is computed as follows (eq. 6):

$$\frac{\delta\Delta}{\Delta} = \sqrt{\left(\frac{\delta I_1}{I_1}\right)^2 + \left(\frac{\delta I_2}{I_2}\right)^2} \tag{6}$$

For each transition:

$$\frac{\delta I}{I} = \frac{\delta_{BL}}{\langle I \rangle} \tag{7}$$

where δ_{BL} is the uncertainty determined by the readout fluctuations of the baseline and $\langle I \rangle$ is the average intensity given by[59]:

$$\langle I \rangle = \frac{\int_{E_0}^{E_1} I(E)\, dE}{E_1 - E_0} \tag{8}$$

evaluated, for each transition, over the whole spectral region ($E_0 \leq E \leq E_1$).

By substituting the estimated value of S_r and $\frac{\delta\Delta}{\Delta}$ in eq. 5, the quantification of the temperature uncertainty δT is achieved.

Repeatability (or test–retest reliability) and reproducibility are imperative parameters for the assessment of the precision of a thermometric system. They refer to the variation that occur when repeating the measurement under identical conditions (due to errors in the measurement process itself[60]) or in reproducing the same results under modified experimental conditions[61], (e.g. different detector, measurement method or session etc.), respectively[59].

As stated by the British Standards Institution, a reasonable repeatability factor can be obtained if the deviation of the average measured temperature is lower than 2x the standard deviation of the data (quantified as δT) (Fig.2).

This ensures that 95% of the measurements are less than two standard deviations away from the mean value of temperature. Typically, the repeatability is estimated by cycling few times the temperature in a given interval, and then computed using the expression (eq. 9):

$$R = 1 - \frac{max(|\Delta_C - \Delta_i|)}{\Delta_C} \tag{9}$$

where Δ_c is the mean thermometric parameter and Δ_i is the value of the thermometric parameter for each measurement cycle.

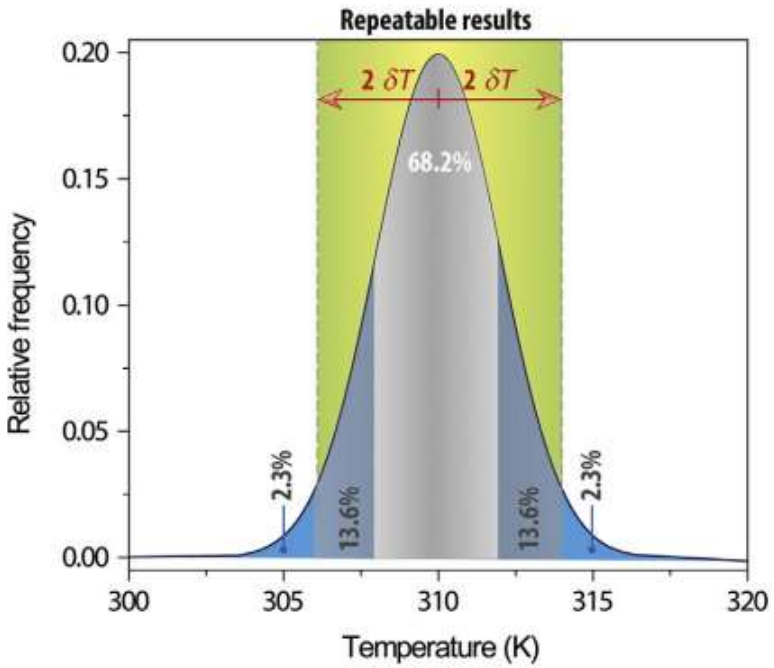

Fig.2 Bell curve for normal distribution. Two standard deviations from the mean include 95.45% of the results. In this case, if the difference with the mean temperature is lower than 2 δT, the value itself is considered as a repetition of the mean value[57].

3.2.2 Nano-sized phosphors for optical thermometry

Conventional phosphor consist of semiconductor materials, tipically with grain sizes of microns[62]. The grain size influences spatial resolution δx, by scattering both the excitation and emitted light. For example, a 10 μm grain will scatter one billion times more light than a 10 nm nanoparticle, since, according to Rayleigh's approximation, the intensity of scattered light from isotropic particles is equal to the particle diameter to the sixt power[63]. Consequently, scattering of light in nanoparticles is markedly less pronounced if compared to traditional micrometer-sized phosphors. For this reason, lanthanide-doped NPs and NCs are very attactive probes for ratiometric temperature sensing, allowing high-resolution thermal mapping, either in the liquid or solid phase[62,64]. Luminescent nanoparticles can have high quantum efficiencies, implying more sensitive temperature sensors. In addition, nanoparticles are less susceptible to photobleaching, respect to other lanthanide hosts, and being small can be easily injected into cells and can be conjugated to biomolecules (such as antibodies)[63] for targeted delivery. Another attractive characteristic of upconverting Ln^{3+}-doped nanoparticles is that they can be typically excited using low power and commercially available inexpensive NIR lasers, with wavelengths in the first biological window, where penetration of light is high (700-1000 nm). Moreover, NIR light does not

produce background autofluorescence, meaning a better signal-to-noise ratio of the detected signal[39]. Summarizing, upconverting nanoparticles (UCNPs) enable ratiometric temperature sensing with high spatial resolution and with zero background arising from NIR photoexcitation[65]. However, despite promising properties, some challenges remain, such as: improvement of quantum yields, better control of particle size (in particular in the case of oxides), optimization of ratio and relative concentrations of dopants, optimization of the host material, improvement of temperature resolution and sensitivity[2,65]. Even though continuous growth, promising progresses and large amount of work have been carried out in the last 10 years, the research on this topic is considered in an early stage. In the near future, innovation and improvements in the design of ratiometric thermometric systems will lead to progresses in the nanothermometry field, that are difficult to foresee, but will undoubtedly turn nano-thermometers prototypes in commercial reality.

Composition, size, and the crystallinity of the host, and on type and concentration of activators and sensitizers influence the thermometric performance of UCNPs. Moreover, matrices should have low lattice phonon energies in order to minimize nonradiative loss[57,66-69]. Generally, UCNPs consist of Ln^{3+} ions embedded in crystalline matrices such as fluorides, oxides, phosphates or sulphides[66,70]. Many lanthanides show luminescence from multiple excited states, for this reason are promising candidates for temperature sensing[71].

Dual-emitting phosphors have resolvable emission intensities from two different emitting levels, thus the temperature readout is based on relative intensities instead of absolute ones[71], reducing the effect of disturbing factors, such as probe concentration, detector efficiency, fluctuations in the emission intensity, or other local inhomogeneities that can affect absolute PL intensities. Fig.3 depicts three different strategies for dual emission PL, depending on the electronic structures of the luminophores involved. In the first case (a) the luminescent centers act as independent, each with its PL temperature dependence. In the second case (b) the two emitters are electronically coupled, so that energy transfer (ET) occurs from the Donor (sensitizer) to the Acceptor (activator) species. If the ET mechanism is simultaneous with Donor luminescence, emission from both the centers is observed. In the third scenario (c) the electronic population of two emitting levels are in thermal equilibrium, thus temperature influences population distributions and therefore emission intensities from the two luminescent excited states. In this case the populations of the two luminescent states can rapidly interconvert because the energy gap between them is small enough to be easily bridged by the available free thermal energy[71]. This is the ideal case for the application of the FIR method.

In the case of UCNPs, Yb^{3+} is usually added as sensitizer, because of its larger absorption cross section. It absorbs 980 nm IR light, transferring the energy to the activator through a double- or triple-photon mechanism. Common activators are characterized by a ladder-like energy level structure. The ratio of activators incorporated in the host matrix is typically lower than 2%at., in order to minimize cross-relaxation energy losses[57]. Table 3 summarizes thermally coupled energy levels of different trivalent lanthanide ions usually investigated with the FIR method[52].

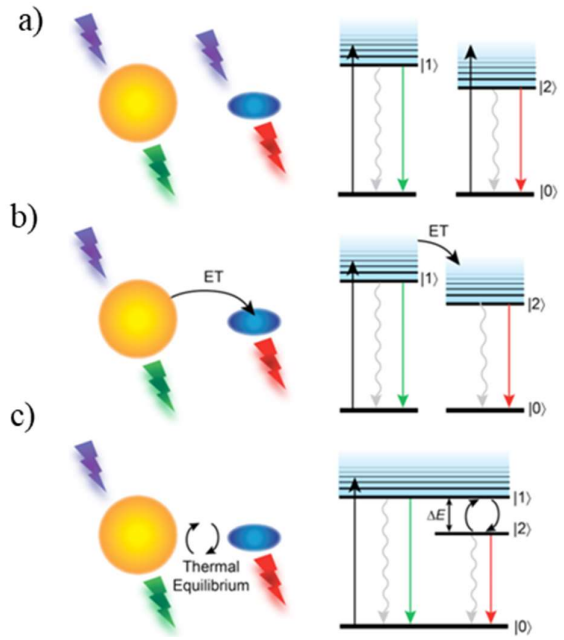

Fig. 3 Schematic representation of three different electronic structures leading to dual emission. (a) Two independent luminescent probes, (b) Two luminescent centers interacting through ET mechanism. (c) Two thermally coupled luminescent excited states[71].

Ln^{3+} ion	Coupled Excited levels		Emission color	ΔE (cm^{-1})	Relative Sensitivity S_r at 300 K ($\%K^{-1}$)
	High	Low			
Er^{3+}	$^2H_{11/2}$	$^4S_{3/2}$	green/red	800	1.25
Tm^{3+}	$^3F_{2,3}$	$^3H_4$	red/NIR	1700	2.72
Tm^{3+}	$^1G_4$	$^3F_{2,3}$	blue/red	6000	9.6
Tm^{3+}	$^3H_{4(a)}$	$^3H_{4(b)}$	NIR	150	0.2
Tm^{3+}	$^1G_{4(a)}$	$^1G_{4(b)}$	blue	100	0.16
Nd^{3+}	$^4F_{5/2}$	$^4F_{3/2}$	NIR	1000	1.60
Nd^{3+}	$^4F_{7/2}$	$^4F_{5/2}$	red/NIR	800	1.25
Nd^{3+}	$^4F_{3/2(a)}$	$^4F_{3/2(b)}$	NIR	100	0.16
Yb^{3+}	$^2F_{5/2(a)}$	$^2F_{5/2(b)}$	NIR	680	1.09
Ho^{3+}	$^5F_4$	$^5S_2$	green	120	0.19
Pr^{3+}	$^3P_1$	$^3P_0$	green or red	580	0.93
Eu^{3+}	$^5D_1$	$^5D_0$	green/red	1750	2.80
Dy^{3+}	$^4I_{15/2}$	$^4F_{9/2}$	blue	1000	1.60
Sm^{3+}	$^4F_{3/2}$	$^4G_{5/2}$	green/red	1000	1.60

Table 2 List of Ln^{3+} ions, with respective thermally coupled levels, emission color, energy difference (ΔE) and theoretical Relative Sensitivity (S_r) at 300 K, typically used for temperature read-out via FIR technique (published by Dramićanin[52]*).*

The most studied ion pair is Yb^{3+}/Er^{3+}[11-12,65,72-78]. Yb^{3+} ions are usually excited by a 975 nm NIR laser, at which wavelength the absorption cross-section is very large. Once excited they transfer energy to adjacent Er^{3+} ions, thanks to the large overlapping between Yb^{3+} emission and Er^{3+} absorption[79]. Er^{3+} ions will glow in the green ($^2H_{11/2}\rightarrow{}^4I_{15/2}$ and $^4S_{3/2}\rightarrow{}^4I_{15/2}$, at 520 and 550 nm respectively) and red ($^4F_{9/2}\rightarrow{}^4I_{15/2}$, 660 nm) spectral ranges. The intensity of the bands in the green region, that are separated by a very close energy gap of ~800 cm^{-1}, is a function of the electronic population of the emitting levels, that is strongly temperature-dependent[48,80-86]. The close vicinity in energy between these two levels, allows the $^2H_{11/2}$ level to be thermally populated by the $^4S_{3/2}$ level, with increasing temperature[87-89].

Tm^{3+} upconversion emissions also proved to be appropriate for optical thermometry, showing high sensitivity and good accuracy[56,90]. The ratiometric temperature parameter can be based on the energy difference between either (i) $^3F_{2,3}$ (~700 nm) and $^3H_4$ (~800 nm) thermally coupled energy levels[90], (ii) $^1G_4$ (~480 nm) and $^3F_{2,3}$ (~700 nm) thermally coupled energy levels[91], (iii) two Stark components of the $^1G_4$ (~480 nm) multiplet[92] or (iv) two Stark components of the $^3H_4$ (~800 nm) multiplet[93]. In the first case (i) $^3H_4$ states are populated by nonradiative relaxation from $^3F_{2,3}$ states; however, with increasing temperature, the thermal population of $^3F_{2,3}$ levels occurs[90], promoting radiative transitions from these levels and leading to the change of intensity ratio between the 700 and 800 nm emissions[91]. Traditionally little attention has been paid to Tm^{3+} ions, mainly because the weak 700 nm light signal is difficult to detect[56]. The sensitivity of the thermometer based on $^3F_{2,3}$ and $^3H_4$ thermally coupled energy levels is much higher if compared to other cases, because of the much larger energy gap between the two levels (evaluated to be about 1850 cm^{-1})[56], resulting in higher resolution. However, as a major drawback of large energy separation, the thermalizing rate from the $^3H_4$ to $^3F_{2,3}$ states will be reduced at lower temperatures, resulting in relatively large measurements errors[56]. Hence, this type of optical thermometer is especially suitable for high temperature range, respect to physiological temperatures[90]. In the second case (ii) the participation of phonons, that is temperature dependent, may affect the population of $^1G_4$ levels, enhancing the emission intensity. On the contrary, decreasing the temperature, the population may decrease because of phonon-assisted cross-relaxation. Moreover, decreasing temperatures promote the population of $^3F_{2,3}$ levels, at the expenses of $^3H_4$ levels, also reducing the population of $^1G_4$ levels, that are in turn populated at the expenses of $^3H_4$ levels via energy transfer ET. Hence, in this case, phonon-assisted processes dominate thermal population of $^1G_4$ excited levels, resulting in a different temperature dependence of its upconversion emission above a certain temperature (300-400K)[56].

Nd^{3+} single-doped systems are particularly adequate for biological applications because of the possibility to absorb and emit in the first biological window, where the transparency of the living tissues is high[55,94-104] (Fig.4), offering much penetration depth potential for deep-tissue imaging[95,105-106].

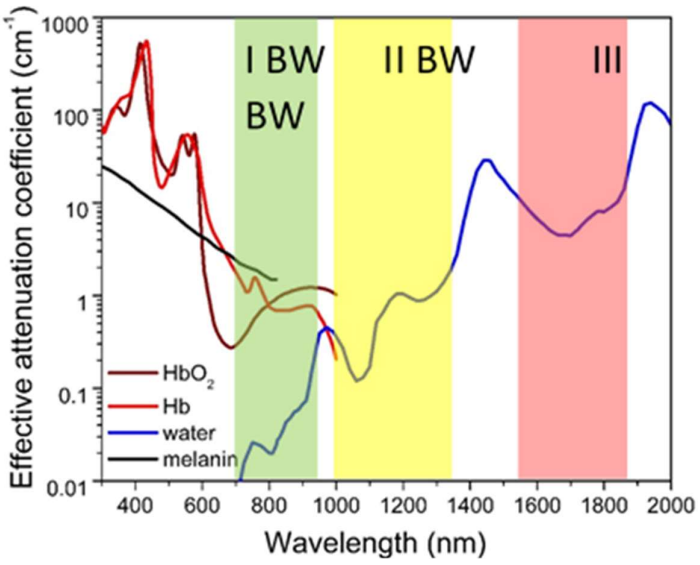

Fig.4 Schematic illustration of optical windows in biological tissues, representing the attenuation coefficient of typical elements encountered in vivo, including oxygenated and deoxygenated blood, water, and melanin.

The ratiometric temperature parameter can be based on the energy difference between either (i) the barycenters of the $^4F_{5/2}$ and the $^4F_{3/2}$ multiplets, or (ii) the barycenters of the $^4F_{7/2}$ and the $^4F_{5/2,3/2}$ multiplets, or (iii) two Stark components of the $^4F_{3/2}$ multiplet. In the two first cases, the relative sensitivity is significantly higher respect to the last one[94], enhancing the applicability of Nd^{3+} ions in optical thermal sensing and deep-tissue imaging (Fig.5). Until now, the vast majority of Nd^{3+}-doped thermal sensors reported in literature are based on the small energy difference between two Stark sublevels of the $^4F_{3/2}$ multiplet[96-97,107], and only few works[55,94,108] report on the FIR between the $^4F_{5/2} \rightarrow {}^4I_{9/2}$ and $^4F_{3/2} \rightarrow {}^4I_{9/2}$ transitions.

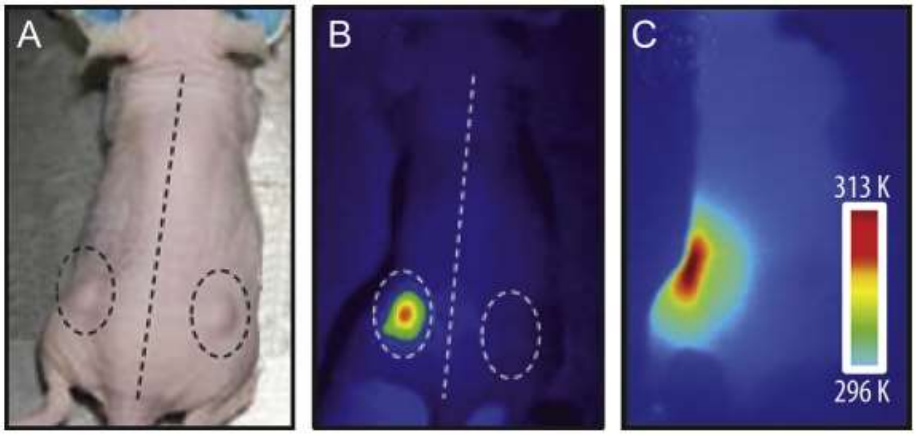

Fig. 5 Image of mice tumors (a), with $LaF_3:Nd^{3+}$ NPs injected only in the left side (right-side tumor was used as control); Infrared fluorescence (b) and Infrared thermal (c) images under 808 nm laser irradiation (4 W cm^{-2})[95].

Suitable luminescent probes may be derived from ruthenium complexes, organic dyes, polymers, layered double hydroxides (LDHs), spin crossover NPs, semiconductor quantum dots (QDs), and Ln^{3+}-based materials[57]. Among these luminescent probes, Ln^{3+}-based materials have been extensively explored, as they are versatile, stable, and narrow band emitters, generally with high emission quantum yields[109-112]. Rare earth nanothermometers present clear advantages such as superior physical and chemical stability, low toxicity, narrow luminescence lines, and absence of aging effects, among others[92].

By choosing various trivalent ions as optically active centers, it is possible to cover the entire electromagnetic spectrum, from UV to IR, obtaining tunable luminescent properties depending on the designed application[80,109,113-115]. Lanthanide-based systems include upconverting Yb-Er[72,116-117], Pr-Tb[118], and Tb-Eu[31,58,119-120] co-doped systems and Eu[121], Dy[122-123], Nd[94-97,107] single doped materials. Even transition metal Cr^{3+}-doped[59,124,125] or Cr-Ln co-doped systems have been investigated[126]. As evidenced, many Ln^{3+}-based molecular thermometers, covering a wide range from the cryogenic (T<100 K) to the physiological (298–323 K) even to very high (1000 K) temperatures, have been reported in the last years.

Table 2 provides a list of Ln^{3+}-based luminescent thermometers, displaying the maximum relative sensitivity value (S_r, % K^{-1}), the temperature range of operation (ΔT, K), the temperature at which S_r is maximum (T_r, K), and the thermometric parameter associated.

Phosphor	**S_r [%K^{-1}]**	**ΔT (T_r) [K]**	**Thermometric property**
YAG:Ce NPs[127]	0.2	315-350 (350)	Emission lifetime
Eu/Tb hybrid NPs[58]	4.7	10-350 (134)	FIR $^5D_0 \rightarrow {}^7F_2/{}^5D_4 \rightarrow {}^7F_5$
Y_2O_3:Eu^{3+}[128]	2.6	473-973 (973)	Rise time
Eu hybrid NPs[129]	3.1	283-323 (283)	$^5D_0 \rightarrow {}^7F_2$ intensity and $^5D_0$ lifetime
YVO:Dy^{3+}[130]	1.8	298-673 (298)	$^4F_{9/2}$ lifetime
ZnO:Er^{3+} NPs[73]	0.6	273-473 (273)	Emission intensity
$BaTiO_3$:Er^{3+} NPs[81]	0.5	333-466 (333)	FIR $^2H_{11/2} \rightarrow {}^4I_{15/2}/{}^4S_{3/2} \rightarrow {}^4I_{15/2}$
$Y_3Al_5O_{12}$:Er^{3+}[131]	0.5	295-973 (467)	FIR $^2H_{11/2} \rightarrow {}^4I_{15/2}/{}^4S_{3/2} \rightarrow {}^4I_{15/2}$
PbF_2:Er^{3+}/Yb^{3+} NPs[11,12]	1.0	315-415 (345)	FIR $^2H_{11/2} \rightarrow {}^4I_{15/2}/{}^4S_{3/2} \rightarrow {}^4I_{15/2}$
$NaYF_4$:Er^{3+}/Yb^{3+} UCNPs[72]	1.0	298-318 (318)	FIR $^2H_{11/2} \rightarrow {}^4I_{15/2}/{}^4S_{3/2} \rightarrow {}^4I_{15/2}$
Gd_2O_3:Er^{3+}/Yb^{3+} UCNPs[74]	0.2	295-1000 (600)	FIR $^2H_{11/2} \rightarrow {}^4I_{15/2}/{}^4S_{3/2} \rightarrow {}^4I_{15/2}$

Er^{3+}/Yb^{3+} co-doped fluoride amorphous glass particle[75]	1.1	335-375 (342)	FIR $^2H_{11/2}\rightarrow{}^4I_{15/2}/{}^4S_{3/2}\rightarrow{}^4I_{15/2}$
$CaF_2:Er^{3+}/Yb^{3+}$ and	2.3	293-318 (318)	FIR $^2H_{11/2}\rightarrow{}^4I_{15/2}/{}^4S_{3/2}\rightarrow{}^4I_{15/2}$
Tm^{3+}/Yb^{3+} UCNPs[93]	0.2	293-318 (315)	FIR between Stark levels of Tm: $^3H_4$ excited state
$SrWO_4:Er^{3+}/Yb^{3+}$[132]	1.5	299-518 (403)	$^4S_{3/2}$ lifetime
$SrF_2:Er^{3+}/Yb^{3+}$ NPs[133]	1.2	303-378 (303)	FIR $^2H_{11/2}\rightarrow{}^4I_{15/2}/{}^4S_{3/2}\rightarrow{}^4I_{15/2}$
$LiNbO_3:Tm^{3+}/Yb^{3+}$ crystal[90]	0.02	323-773 (773)	FIR $^3F_{2,3}\rightarrow{}^3H_6/{}^3H_4\rightarrow{}^3H_6$
$NaYF_4$: Tm^{3+}/Yb^{3+} NCs[91]	1.53	300-500 (417)	FIR $^3F_{2,3}\rightarrow{}^3H_6/{}^1G_4\rightarrow{}^3H_6$
$NaNbO_3:Tm^{3+}/Yb^{3+}$ NCs[92]	0.08	293-353 (293)	FIR between Stark levels of Tm^{3+}: $^1G_4$ excited state
$Gd_2O_3:Nd^{3+}$ NPs[94]	1.8	288-323 (288)	FIR $^4F_{5/2}\rightarrow{}^4I_{9/2}/{}^4F_{3/2}\rightarrow{}^4I_{9/2}$
$LaF_3:Nd^{3+}$ NPs[96]	0.1	283-333 (283)	FIR between Stark levels of Nd^{3+}: 4F3/2 excited state
$NaYF_4:Nd^{3+}$ NPs[97]	0.1	273-423 (273)	FIR between Stark levels of Nd^{3+}: $^4F_{3/2}$ excited state
YAG:Nd^{3+} NPs[107]	0.2	283-343 (283)	FIR between Stark levels of Nd^{3+}: $^4F_{3/2}$ excited state
$La_2O_2S:Nd^{3+}$[108]	2.0	270-600 (270)	FIR $^4F_{5/2}\rightarrow{}^4I_{9/2}/{}^4F_{3/2}\rightarrow{}^4I_{9/2}$
$NaYF_4:Nd^{3+}$ microcrystals[134]	0.6	323-673 (500)	FIR $^4F_{5/2}\rightarrow{}^4I_{9/2}/{}^4F_{3/2}\rightarrow{}^4I_{9/2}$

Table 3 List of Ln^{3+}-based luminescent thermometers including maximum relative sensitivity values (S_r, % K^{-1}), the temperature range tested (ΔT), the temperature at which the relative sensitivity is maximum (T_r), and the thermometric property.

Generally luminescent Ln^{3+}-based thermometers present slightly lower S_r values, respect to polymers- or dye-based ones. However they usually cover a wider temperature range, over the whole physiological temperature interval. For example, polymer-based thermometers tipically work in an interval of 10 K, being ascribable to on-off temperature sensors, rather than to wide-range thermometers. A relative sensitivity value of 0.5% K^{-1} (i.e. a relative variation in the thermometric parameter of 0.5% per degree) is a reasonable quality treshold, however this criteria may be more difficult to comply when speaking of ratiometric, self-referencing thermometric systems[2]. Despite the large amount of research carried out so far, it is still unavailable a single thermometer that complies with the following requirements, that should be satisfied simultaneously for intracellular temperature sensing:

- high temperature δT (<0.5 K) and spatial δx (<3μm) resolution;
- ratiometric and concentration-independent output;
- indipendency of: changes in surrounding pH and ionic strenght, presence of biomacromolecules.

References

[1] Brites, C. D. S., Balabhadra, S., Carlos, L. D. Lanthanide-Based Thermometers: At the Cutting-Edge of Luminescence Thermometry. *Advanced Optical Materials* **2018**, 7(5), 1801239.

[2] Brites, C.D.S., Lima, P.P., Silva, N.J.O., Millán, A., Amaral, V.S., Palacio, F., Carlos, L.D., Thermometry at the nanoscale, *Nanoscale* **2012**, 4, 4799–4829.

[3] Aigouy, L., Lalouat, L., Mortier, M., Löw, P., Bergaud, C. A scanning thermal probe microscope that operates in liquids. *Rev. Sci. Instrum.* **2011**, 82, 036106.

[4] Barilero, T., Le Saux, T., Gosse, C., Jullien, L. Fluorescent thermometers for dual emission-wavelength measurements: molecular engineering and application to thermal imaging in a microsystem. *Anal. Chem.* **2009**,81, 7988–8000.

[5] del Rosal, B., Sun, C., Yan, Y., Mackenzie, M.D., Lu, C., Bettiol, A.A., Kar, A.K., Jaque, D. Flow effects in the laser-induced thermal loading of optical traps and optofluidic devices. *Opt. Express* **2014**, 22, 23938–23954.

[6] Feng, J., Tian, K.J., Hu, D.H., Wang, S.Q., Li, S.Y., Zeng, Y., Li, Y., Yang, G.Q. A triarylboron-based fluorescent thermometer: sensitive over a wide temperature range. *Angew. Chem. Int. Ed*. **2011**, 50, 8072–8076.

[7] Feng, J., Xiong, L., Wang, S., Li, S., Li, Y., Yang, G. Fluorescent temperature sensing using triarylboron compounds and microcapsules for detection of a wide temperature range on the micro- and macroscale. *Adv. Funct. Mater.* **2013**, 23, 340–345.

[3] Graham, E.M., Iwai, K., Uchiyama, S., de Silva, A.P., Magennis, S.W., Jones, A.C. Quantitative mapping of aqueous microfluidic temperature with sub-degree resolution using fluorescence lifetime imaging microscopy. *Lab Chip* **2010**, 10, 1267–1273.

[9] Mao, H.B., Yang, T.L., Cremer, P.S. A microfluidic device with a linear temperature gradient for parallel and combinatorial measurements. *J. Am. Chem. Soc.* **2002**, 124, 4432–4435.

[10] Samy, R., Glawdel, T., Ren, C. L. Method for microfluidic whole-chip temperature measurement using thin-film poly (dimethylsiloxane)/rhodamine *B. Anal. Chem.* **2008**, 80, 369–375.

[11] Aigouy, L., Tessier, G., Mortier, M., Charlot, B. Scanning thermal imaging of microelectronic circuits with a fluorescent nanoprobe. *Appl. Phys. Lett.* **2005**, 87, 184105.

[12] Aigouy, L., Saïdi, E., Lalouat, L., Labeguerie-Egea, J., Mortier, M., Löw, P., Bergaud, C. AC thermal imaging of a microwire with a fluorescent nanocrystal: influence of the near field on the thermal contrast. *J. Appl. Phys.* **2009**, 106, 074301.

[13] Jung, W., Kim, Y.W., Yim, D., Yoo, J.Y. Microscale surface thermometry using SU8/rhodamine-B thin layer. *Sens. Actuators A: Phys.* **2011**, 171, 228–232.

[14] Kolodner, P., Tyson, J.A. Remote thermal imaging with 0.7mm spatial resolution using temperature-dependent fluorescent thin films. *Appl. Phys. Lett.* **1983**, 42, 117–119.

[15] Liu, W.J., Yang, B.Z. Thermography techniques for integrated circuits and semiconductor devices. *Sens. Rev.* **2007**, 27, 298–309.

[16] Liu, H.X., Sun, W.Q., Xiang, A., Shi, T.W., Chen, Q., Xu, S.Y. Towards on-chip timeresolved thermal mapping with micro-/nanosensor arrays. *Nanoscale Res. Lett.* **2012**, 7, 1–6.

[17] Mecklenburg, M., Hubbard, W.A., White, E.R., Dhall, R., Cronin, S.B., Aloni, S., Regan, B.C. Nanoscale temperature mapping in operating microelectronic devices. *Science* **2015**, 347, 629–632.

[18] Saïdi, E., Babinet, N., Lalouat, L., Lesueur, J., Aigouy, L., Volz, S., Labeguerie-Egea, J., Mortier, M. Tuning temperature and size of hot spots and hot-spot arrays. *Small* **2011**, 7, 259–264.

[19] Shi, L., Dames, C., Lukes, J.R., Reddy, P., Duda, J., Cahill, D.G., Lee, J., Marconnet, A., Goodson, K.E., Bahk, J.-H., Shakouri, A., Prasher, R.S., Felts, J., King, W.P., Han, B., Bischof, J.C. Evaluating broader impacts of nanoscale thermal transport research. *Nanosci. Microsc. Thermophys. Eng.* **2015**, 19, 127–165.

[20] Tessier, G., Bardoux, M., Filloy, C., Boué, C., Fournier, D. High resolution thermal imaging inside integrated circuits. *Sens. Rev.* **2007**, 27, 291–297.

[21] Wickberg, A., Mueller, J.B., Mange, Y.J., Fischer, J., Nann, T., Wegener, M. Three-dimensional micro-printing of temperature sensors based on up-conversion luminescence. *Appl. Phys. Lett.* **2015,** 106, 133103.

[22] Arai, S., Lee, S.C., Zhai, D., Suzuki, M., Chang, Y.T. A molecular fluorescent probe for targeted visualization of temperature at the endoplasmic reticulum. *Sci. Rep.* **2014**, 4, 6701.

[23] Arai, S., Suzuki, M., Park, S. J., Yoo, J. S., Wang, L., Kang, N.Y., Ha, H. H., Chang, Y.T. Mitochondria-targeted fluorescent thermometer monitors intracellular temperature gradient. *Chem. Commun.* **2015**, 51, 8044–8047.

[24] Chapman, C. F., Liu, Y., Sonek, G. J., Tromberg, B. J. The use of exogenous fluorescentprobes for temperature-measurements in single living cells. *Photochem. Photobiol.* **1995**, 62, 416–425.

[25] Donner, J. S., Thompson, S. A., Kreuzer, M. P., Baffou, G., Quidant, R. Mapping intracellular temperature using green fluorescent protein. *Nano Lett.* **2012**, 12, 2107–2111.

[26] Gota, C., Okabe, K., Funatsu, T., Harada, Y., Uchiyama, S. Hydrophilic fluorescent nanogel thermometer for intracellular thermometry. *J. Am. Chem. Soc.* **2009**, 131, 2766–2767.

[27] Hayashi, T., Fukuda, N., Uchiyama, S., Inada, N. A cell-permeable fluorescent polymeric thermometer for intracellular temperature mapping in mammalian cell lines. *PLoS One* **2015**, 10(2), e0117677.

[28] Homma, M., Takei, Y., Murata, A., Inoue, T., Takeoka, S. A ratiometric fluorescent molecular probe for visualization of mitochondrial temperature in living cells. *Chem. Commun.* **2015**, 51, 6194–6197.

[29] Hu, X.L., Li, Y., Liu, T., Zhang, G.Y., Liu, S.Y. Intracellular cascade FRET for temperature imaging of living cells with polymeric ratiometric fluorescent thermometers. *ACS Appl. Mater. Interfaces* **2015**, 7, 15551–15560.

[30] Huang, H., Delikanli, S., Zeng, H., Ferkey, D.M., Pralle, A. Remote control of ion channels and neurons through magnetic-field heating of nanoparticles. *Nat. Nanotechnol.* **2010**, 5, 602–606.

[31] Liu, G. Advances in the theoretical understanding of photon upconversion in rare-earth activated nanophosphors. *Chem. Soc. Rev.* **2015**, 44, 1635–1652.

[32] Okabe, K., Inada, N., Gota, C., Harada, Y., Funatsu, T., Uchiyama, S. Intracellular temperature mapping with a fluorescent polymeric thermometer and fluorescence lifetime imaging microscopy. *Nat. Commun.* **2012**, 3, 705.

[33] Qiao, J., Chen, C.F., Qi, L., Liu, M.R., Dong, P., Jiang, Q., Yang, X.Z., Mu, X.Y., Mao, L.Q. Intracellular temperature sensing by a ratiometric fluorescent polymer thermometer. *J. Mater. Chem. B* **2014**, 2, 7544–7550.

[34] Suzuki, M., Tseeb, V., Oyama, K., Ishiwata, S. Microscopic detection of thermogenesis in a single HeLa cell. *Biophys. J.* **2007**, 92(6), L46–L48.

[35] Uchiyama, S., Tsuji, T., Ikado, K., Yoshida, A., Kawamoto, K., Hayashi, T., Inada, N. A cationic fluorescent polymeric thermometer for the ratiometric sensing of intracellular temperature. *Analyst* **2015**, 140, 4498–4506.

[36] Vetrone, F., Naccache, R., de la Fuente, Á. J., Sanz-Rodriguez, F., Blazquez-Castro, A., Rodriguez, E.M., Jaque, D., Sol_e, J.G., Capobianco, J.A. Intracellular imaging of HeLa cells by non-functionalized $NaYF_4:Er^{3+}$, Yb^{3+} upconverting nanoparticles. *Nanoscale* **2010**, 2, 495–498.

[37] Wang, C.L., Xu, R.Z., Tian, W.J., Jiang, X.L., Cui, Z.Y., Wang, M., Sun, H.M., Fang, K., Gu, N. Determining intracellular temperature at single-cell level by a novel thermocouple method. *Cell Res.* **2011**, 21, 1517–1519.

[38] Zohar, O., Ikeda, M., Shinagawa, H., Inoue, H., Nakamura, H., Elbaum, D., Alkon, D.L., Yoshioka, T. Thermal imaging of receptor-activated heat production in single cells. *Biophys. J.* **1998**, 74, 82–89.

[39] Brites, C., Lima, P., Silva, N., Millán, A., Amaral, V., Palacio, F., Carlos, L. Lanthanide-based luminescent molecular thermometers, *New Journal of Chemistry*, **2011**, 35, 1177.

[40] Lan, Y., Wang, H., Chen, X., Wang, D., Chen, G., Ren, Z. Nanothermometer Using Single Crystal Silver Nanospheres, *Adv. Mater*., **2009**, 21: 4839-4844.

[41] Gao Y., Bando Y. Carbon nanothermometer containing gallium, *Nature*, **2002**, 415, 599.

[42] Wang, C. Y., Chen L. J., Nanothermometers for Transmission Electron Microscopy – Fabrication and Characterization, *European Journal of Inorganic Chemistry,* **2010,** 27, 4298-4303.

[43] Sadat, S., Tan, A., Chua, Y. J., Reddy, P. Nanoscale Thermometry Using Point Contact Thermocouples, *Nano Lett*., **2010**, 10, 2613–2617.

[44] Shapira, E., Marchak, D., Tsukernik, A., Selzer, Y. Segmented metal nanowires as nanoscale thermocouples, *Nanotechnology*, **2008**, 19, 125501.

[45] Chu, D. C., Wong, W. K., Goodson K. E., Pease, R. F. W., Transient temperature measurements of resist heating using nanothermocouples, *J. Vac. Sci. Technol. B*, **2003**, 21, 2985–2989.

[46] Shi, L., Kwon, O., Miner, A. C., Majumdar, A., Design and batch fabrication of probes for sub-100 nm scanning thermal microscopy, *Journal of microelectromechanical Systems*, **2001**, 10(3), 370-37.

[47] Wang, X.D., Wolfbeis, O.S., Meier, R.J. Luminescent probes and sensors for temperature, *Chem. Soc. Rev.* **2013**, 42, 7834–7869.

[48] Jaque, D., Vetrone, F. Luminescence nanothermometry. *Nanoscale* **2012**, 4, 4301–4326.

[49] Yue, Y., Wang, X. Nanoscale thermal probing, *Nano Rev.* **2012**, 3, 11586.

[50] Asheghi, M., Yang, Y., Micro- and nano-scale diagnostic techniques for thermometry and thermal imaging of microelectronic and data storage devices, *Microscale Diagnostic Techniques*, ed. K. S. Breuer, Springer-Verlag, Berlin, **2005**.

[51] Christofferson, J., Maize, K., Ezzahri, Y., Shabani, J., Wang, X., Shakouri, A. Microscale and Nanoscale Thermal Characterization Techniques, *J. Electron. Packaging*, **2008**, 130, 041101–041106.

[52] Dramićanin, M., Luminescence Thermometry, Woodhead Publishing Series in *Electronic and Optical Materials*, **2018**, ISBN 9780081020296.

[53] Heyes, A. L. On the design of phosphors for high-temperature thermometry, *Journal of Luminescence*, **2009**, 129(12), 2004-2009.

[54] Stich, M. I. J., Fischer, L. H., Wolfbeis, O. S. Multiple fluorescent chemical sensing and imaging, *Chem. Soc. Rev*., **2010**, 39(8), 3102-3114.

[55] Nunes, L. A. O., Souza, A. S., Carlos, L. D., Malta, O. L. Neodymium doped fluoroindogallate glasses as highly-sensitive luminescent non-contact thermometers. *Optical Materials.* **2016**, 63, 42-45.

[56] Xu, W., Gao, X., Zheng, L., Zhang, Z., Cao, W. An optical temperature sensor based on the upconversion luminescence from Tm3+/Yb3+ codoped oxyfluoride glass ceramic, *Sensors and Actuators B: Chemical*, **2012**, 173, 250-253.

[57] Brites C. D. S., Millán A., Carlos L. D., in Handbook on the Physics and Chemistry of Rare Earths, ed. J. C. Bünzli and V. K. Pecharsky, Elsevier, Amsterdam **2016**, vol. 49, Lanthanides in Luminescent Thermometry ch. 281, pp. 339–427.

[58] Brites, C. D. S., Lima, P. P., Silva, N. J. O., Millán, A., Amaral, V. S., Palacio, F., Carlos, L. D. A luminescent molecular thermometer for long-term absolute temperature measurements at the nanoscale. *Adv. Mater.* **2010**, 22, 4499–4504

[59] Back, M., Trave, E., Ueda, J., Tanabe, S., Ratiometric optical thermometer based on dual Near-Infrared emission in Cr^{3+}-doped bismuth-based gallate host, *Chem. Of Mater.,* **2016**, 28, 8347-8356.

[60] Bartlett, J.W., Frost, C., Reliability, repeatability and reproducibility: analysis of measurement errors in continuous variables, *Ultrasound Obstet. Gynecol*, **2008**, 31, 466–475.

[61] Taylor, B.N., Kuyatt, C.E., Guidelines for Evaluating and Expressing the Uncertainty of NIST Measurement Results, (NIST Technical Note 1297), **1994**.

[62] Allison, S. W., Gillies, G. T. Remote thermometry with thermographic phosphors: Instrumentation and applications, *Review of Scientific Instruments*, **1997**, 68(7), 2615-2650.

[63] Wang, S., Westcott, S., Chen, W., Nanoparticle Luminescence Thermometry, *J. Phys. Chem.* B, **2002**, 106(43), 11203-11209.

[64] Löw, P., Kim, B., Takama, N., Bergaud, C. High-Spatial-Resolution Surface-Temperature Mapping Using Fluorescent Thermometry *Small*, **2008**, 4, 908-914.

[65] Fischer, L. H., Harms, G. S., Wolfbeis, O. S. Upconverting nanoparticles for nanoscale thermometry, *Angew. Chem. Int. Ed. Engl*., **2011**,50(20), 4546-51.

[66] Wang, F., Liu, X., Recent advances in the chemistry of lanthanide-doped upconversion nanocrystals, *Chem. Soc. Rev*., **2009**, 38(4), 976-989.

[67] Zhou, J., Liu, Q., Feng, W., Sun, Y., Li, F. Upconversion luminescent materials: advances and applications, *Chem Rev.*, **2015**, 115(1), 395-465.

[68] Liu, J., Guo, X., Hu, R., Xu, J., Wang, S., Li, S., Li, Y., Yang, G. Intracellular fluorescent temperature probe based on triarylboron substituted polyN-isopropylacrylamide and energy transfer, *Anal Chem*., **2015**, 87(7), 3694-8.

[69] Bettinelli, M., Carlos, L., Liu, X Lanthanide-doped upconversion nanoparticles, *Physics Today,* **2015**, 68(9), 38-44.

[70] Zhou, J., Liu, Z., Li, F., Upconversion nanophosphors for small-animal imaging, *Chem. Soc. Rev*., **2012**, 41(3), 1323-1349.

[71] McLaurin, E. J., Bradshaw, L. R., Gamelin, D. R. Dual-Emitting Nanoscale Temperature Sensors, *Chem. Mater*., **2013**, 25(8), 1283-1292.

[72] Vetrone, F., Naccache, R., Zamarrón, A., Juarranz de la Fuente, A., Sanz-Rodríguez, F., Martinez Maestro, L., Martin Rodriguez, E., Jaque, D., García Solé, J., Capobianco, J. A. Temperature sensing using fluorescent nanothermometers. *ACS Nano* **2010**, 4, 3254−3258.

[73] Wang, X., Kong, X. G., Yu, Y., Sun Y. J., Zhang, H. Effect of annealing on upconversion luminescence of ZnO:Er^{3+} nanocrystals and high thermal sensitivity, *J. Phys. Chem. C*, **2007**, 111, 15119–15124.

[74] S. K. Singh, K. Kumar and S. B. Rai, Er^{3+}/Yb^{3+} codoped Gd_2O_3 nano-phosphor for optical thermometry, *Sens. Actuators, A*, **2009**, 149, 16–20.

[75] Saıdi, E., Samson, B., Aigouy, L., Volz, S., Low, P., Bergaud, C., Mortier, M. Scanning thermal imaging by near-field fluorescence spectroscopy, *Nanotechnology*, **2009**, 20, 115703.

[76] Peng, H., Huang, S.-H., Wolfbeis, O. Ratiometric fluorescent nanoparticles for sensing temperature, *Journal of Nanoparticle Research*, **2010**, 12, 2729-2733.

[77] Singh, S.K., Kumar, K., Rai, S.B., Er3+/Yb3+ codoped Gd_2O_3 nano-phosphor for optical thermometry, *Sensors and Actuators A: Physical*, **2009**, 149(1), 16-20.

[78] Tikhomirov, V. K., Adamo, G., Nikolaenko, A. E., Rodriguez, V. D., Gredin, P., Mortier, M., Zheludev, N. I., Moshchalkov, V. V. Cathodo- and photoluminescence in Yb^{3+}-Er^{3+}co-doped PbF_2 nanoparticles, *Opt. Expres*s, **2010**, 18, 8836-8846.

[79] Manzani, D., Petruci, da Silveira, J. F., Nigoghossian, K., Cardoso, A. A., Ribeiro, S. J. L., A portable luminescent thermometer based on green up-conversion emission of Er^{3+}/Yb^{3+} co-doped tellurite glass, *Scientific Reports*, **2017**, 7, 41596.

[80] Feng, J., Zhang, H. J., Hybrid materials based on lanthanide organic complexes: a review. *Chem. Soc. Rev.* **2013**, 42, 387–410.

[81] Alencar, M. A. R. C., Maciel, G. S., de Araujo, C. B., Patra, A. Er^{3+}-doped $BaTiO_3$ nanocrystals for thermometry: Influence of nanoenvironment on the sensitivity of a fluorescence based temperature sensor, *Appl. Phys. Lett*., **2004**, 84, 4753–4755.

[82] Petit, J., Viana, B., Goldner, P.Internal temperature measurement of an ytterbium doped material under laser operation, *Opt. Express*, **2011**, 19, 1138-1146.

[83] Quintanilla, M., Cantelar, E., Cussó, F., Villegas, M., Caballero, A. C. Temperature Sensing with Up-Converting Submicron-Sized $LiNbO_3$:Er^{3+}/Yb^{3+} Particles, *Applied Physics Express*, **2011**, 4(2).

[84] Haro-González, P., Martín, I.R., Martín, L.L., León-Luis, S. F, Pérez-Rodríguez, C., Lavín, V. Characterization of Er^{3+} and Nd^{3+} doped Strontium Barium Niobate glass ceramic as temperature sensors, *Optical Materials*, **2011**, 33(5), 742-745.

[85] Cai, Z.P., Xu, H.Y., Point temperature sensor based on green upconversion emission in an Er:ZBLALiP microsphere, *Sensors and Actuators A: Physic*al, **2003**, 108(1–3), 187-192.

[86] Cao, B.S., He, Y.Y., Feng, Z.Q., Li, Y.S., Dong, B. Optical temperature sensing behavior of enhanced green upconversion emissions from Er–Mo:$Yb_2Ti_2O_7$ nanophosphor, *Sensors and Actuators B: Chemical*, **2011**, 159(1), 8-11.

[87] León-Luis, S. F., Rodríguez-Mendoza, U. R., Lalla, E., Lavín, V. Temperature sensor based on the Er^{3+} green upconverted emission in a fluorotellurite glass, *Sensors and Actuators B: Chemical*, **2011**, 158(1), 208-213.

[88] Dong, B., Yang, T., Lei, M. K., Optical high temperature sensor based on green up-conversion emissions in Er^{3+} doped Al_2O_3, *Sensors and Actuators B: Chemical*, **2007**, 123(2), 667-670.

[89] Pandey, A., Som, S., Kumar, V., Kumar, V., Kumar, K., Rai, V. K., Swart, H.C. Enhanced upconversion and temperature sensing study of Er^{3+}–Yb^{3+} codoped tungsten–tellurite glass, *Sensors and Actuators B: Chemical*, **2014**, 202, 1305-1312.

[90] Xing, L.L., Xu, Y. L., Wang, R., Xu, W., Zhang, Z.G., Highly sensitive optical thermometry based on upconversion emissions in Tm^{3+}/Yb^{3+} codoped $LiNbO_3$ single crystal, *Opt. Lett*., **2014**, 39, 454.

[91] Zhou, S. S., Jiang, G. C., Li, X. Y., Jiang, S., Wei, X. T., Chen, Y. H., Yin, M., Duan, C.K., Strategy for thermometry via Tm^{3+}-doped $NaYF_4$core-shell nanoparticles, *Opt. Lett.*, **2014**, 39, 6687.

[92] Pereira, A.F., Upendra Kumar, K., Silva, W.F., Santos, W.Q., Jaque, D., Jacinto, C. Yb^{3+}/Tm^{3+} co-doped $NaNbO_3$ nanocrystals as three-photon-excited luminescent nanothermometers, *Sensors and Actuators B: Chemical*, **2015**, 213, 65-71.

[93] Dong, N. N., Pedroni, M, Piccinelli, F., Conti, G., Sbarbati, A., Ramirez-Hernandez, J. E., Maestro, L. M., Iglesias-de la Cruz, M. C., Sanz-Rodriguez, F., Juarranz, A., Chen, F., Vetrone, F., Capobianco, J. A., Sole, J. G., Bettinelli, M., Jaque D., Speghini, A. NIR-to-NIR two-photon excited $CaF_2:Tm^{3+},Yb^{3+}$ nanoparticles: multifunctional nanoprobes for highly penetrating fluorescence bio-imaging., *ACS Nano*, **2011**, 5, 8665–8671.

[94] Balabhadra, S., Debasu, M. L., Brites, C. D. S., Nunes, L. A. O., Malta, O. L., Rocha, J., Bettinelli, M., Carlos, L. D. Boosting the sensitivity of Nd^{3+}-based luminescent nanothermometers. *Nanoscale* **2015**, 7, 17261−17267.

[95] Carrasco, E., del Rosal, B., Sanz-Rodríguez, F., de la Fuente, A. J., Gonzalez, P. H., Rocha, U., Kumar, K. U., Jacinto, C., Solé, J. G., Jaque, D. Intratumoral thermal reading during photo thermal therapy by multifunctional fluorescent nanoparticles. *Adv. Funct. Mater.* **2015**, 25, 615−626.

[96] Rocha, U., Jacinto da Silva, C., Ferreira Silva, W., Guedes, I., Benayas, A., Martinez Maestro, L., Acosta Elias, M., Bovero, V., van Veggel, F. C. J. M., García Solé, J. A., Jaque, D. Subtissue thermal sensing based in neodymium-doped LaF_3 nanoparticles. *ACS Nano* **2013**, 7, 1188−1199.

[97] Wawrzynczyk, D., Bednarkiewicz, A., Nyk, M., Strek, W., Samoc, M. Neodymium(III) doped fluoride nanoparticles as noncontact optical temperature sensors. *Nanoscale* **2012**, 4, 6959−6961.

[98] Rocha, U., Kumar, K. U., Jacinto, C., Villa, I., Sanz-Rodríguez, F., Iglesias, de la Cruz, M. C., Juarranz, A., Carrasco, E., van Veggel, F. C., Bovero, E., Sol, J. G. Jaque, D., Neodymium-doped LaF_3 nanoparticles for fluorescence bioimaging in the second biological window, *Small 10* (**2014**), 1141.

[99] Tian, X., Wei, X., Chen, Y., Duan, C., Yin, M., Temperature sensor based on ladder-level assisted thermal coupling and thermal-enhanced luminescence in $NaYF_4:Nd^{3+}$, *Opt. Express* **2014**, 22, 30333.

[100] Jiang, G.C., Wei, X. T., Zhou, S. S., Chen, Y. H., Duan, C. K., Yin, M., Neodymium doped lanthanum oxysulfide as optical temperature sensors, J. *Lumin.* **2014**, 152, 156.

[101] Xu, W., Song, Q., Zheng, L., Zhang, Z., Cao, W., Optical temperature sensing based on the near-infrared emissions from Nd^{3+}/Yb^{3+} co-doped $CaWO_4$, *Opt. Lett.* **2014**, 39, 4635.

[102] Grattan, K. T. V., Palmer, A. W., Willson, C. A., A miniaturized microcomputer-based neodymium decay-time temperature sensor, *J. Phys. E Sci. Instrum.* **1987**, 20, 1201.

[103] Perez-Rodríguez, C., Martín, L. L., Léon-Luis, S. F., Martín, I. R., Kumar, K. K., Jayasankar, C. K., Relevance of radiative transfer processes on Nd^{3+} doped phosphate glasses for temperature sensing by means of the fluorescence intensity ratio technique, *Sensor Actuat. B Chem.,* **2014**, 195, 324.

[104] Lalla, E. A., Leon-Luis, S. F., Monteseguro, V., Perez-Rodríguez, C., Cáceres, J. M., Lavíin, V., Rodríguez-Mendoza, U. R., Optical temperature sensor based on the Nd^{3+} infrared thermalized emissions in a fluorotellurite glass, *J. Lumin.* **2015**, 166, 209.

[105] Li, X., Wang, R., Zhang, F., Zhou, L., Shen, D., Yao, C., Zhao, D. Nd^{3+} sensitized up/downconverting dual-mode nanomaterials for efficient in-vitro and in-vivo bioimaging excited at 800 nm, *Sci Rep.*, **2013**, 3, 3536.

[106] Savchuk, O., Carvajal, J. J., De la Cruz, L. G., Haro-González, P., Aguiló, M., Díaz, F., Luminescence thermometry and imaging in the second biological window at high penetration depth with Nd:$KGd(WO_4)_2$ nanoparticles, *J. Mater. Chem. C,* **2016**, 4(31), 7397-7405.

[107] Benayas, A., del Rosal, B., Pérez-Delgado, A., Santacruz-Gómez, K., Jaque, D., Hirata, G. A., Vetrone, F. Nd:YAG Near-Infrared luminescent nanothermometers. *Adv. Opt. Mater.* **2015**, 3, 687−694.

[108] Jiang, G., Wei, X., Zhou, S., Chen, Y., Duan, C.-K., Yin, M. Neodymium doped lanthanum oxysulfide as optical temperature sensors. *Journal of Luminescence*, **2014**, 152, 156-159.

[109] Bünzli, J. C. G., Lanthanide luminescence for biomedical analyses and imaging. *Chem. Rev.* **2010**, 110, 2729–2755.

[110] Bünzli, J. C. G., On the design of highly luminescent lanthanide complexes. *Coord. Chem. Rev.* **2015**, 293, 19–47.

[111] Bünzli, J. C. G., Eliseeva, S. V. Intriguing aspects of lanthanide luminescence. *Chem. Sci.* **2013**, 4, 1939–1949.

[112] Comby, S., Bünzli, J. C. G. in Handbook on the Physics and Chemistry of Rare Earths, New York **2007**, vol. 37, Lanthanide near-infrared luminescence in molecular probes and devices, Chapter 235, pp. 217–470.

[113] Binnemans, K. Lanthanide-based luminescent hybrid materials. *Chem. Rev.* **2009**, 109, 4283–4374.

[114] Carlos, L. D., Ferreira, R. A. S., de Zea B. V., Ribeiro, S. J. L., Lanthanide-containing light-emitting organic–inorganic hybrids: a bet on the future. *Adv. Mater.* **2009**, 21, 509–534.

[115] Chen, G.Y., Yang, C.H., Prasad, P.N., Nanophotonics and nanochemistry: controlling the excitation dynamics for frequency up- and down-conversion in lanthanide-doped nanoparticles. *Acc. Chem. Res.* **2013**, 46, 1474–1486.

[116] Hemmer, E., Quintanilla, M., Légaré, F., Vetrone, F. Temperature-Induced Energy Transfer in Dye-Conjugated Upconverting Nanoparticles: A New Candidate for Nanothermometry. *Chem. Mater.* **2015**, 27, 235−244.

[117] Gavrilović, T. V., Jovanović, D. J., Lojpur, V., Dramićanin, M. D. Multifunctional Eu^{3+}- and Er^{3+}/Yb^{3+}-doped $GdVO_4$ nanoparticles synthesized by reverse micelle method. *Sci. Rep.* **2014**, 4, 4209.

[118] Gao, Y., Huang, F., Lin, H., Zhou, J., Xu, J., Wang, Y. A. Novel optical thermometry strategy bsed on diverse thermal response from two intervalence charge transfer states. *Adv. Funct. Mater.* **2016**, 26, 3139−3145.

[119] Wang, Z., Ananias, D., Carné-Sánchez, A., Brites, C. D. S., Imaz, I., Maspoch, D., Rocha, J., Carlos, L. D. Lanthanide-organic framework nanothermometers prepared by spray-drying. *Adv. Funct. Mater.* **2015**, 25, 2824−2830.

[120] Ananias, D., Paz, F. A. A., Yufit, D. S., Carlos, L. D., Rocha, J. Photoluminescent thermometer based on a phase-transition lanthanide silicate with unusual structural disorder. *J. Am. Chem. Soc*. **2015**, 137, 3051−3058.

[121] Souza, A. S., Nunes, L. A. O.; Silva, I. G. N.; Oliveira, F. A. M.;da Luz, L. L.; Brito, H. F., Felinto, M. C. F. C., Ferreira, R. A. S., Júnior, S. A., Carlos, L. D., Malta, O. L. Highly-sensitive Eu^{3+} ratiometric thermometers based on excited state absorption with predictable calibration. *Nanoscale* **2016**, 8, 5327−5333.

[122] Boruc, Z., Kaczkan, M., Fetlinski, B., Turczynski, S., Malinowski, M. Blue emissions in Dy^{3+} doped $Y_4Al_2O_9$ crystals for temperature Sensing. *Opt. Lett.* **2012**, 37, 5214−5216.

[123] Cao, Z. M., Zhou, S. S., Jiang, G. C., Chen, Y. H., Duan, C. K., Yin, M. Temperature Dependent Luminescence of Dy^{3+} doped $BaYF_5$ Nanoparticles for Optical Thermometry. *Curr. Appl. Phys.* **2014**, 14, 1067−1071.

[124] Back, M., Ueda, J., Brik, M.G., Lesniewski, T., Grinberg, M., Tanabe, S., Revisiting Cr^{3+}-Doped $Bi_2Ga_4O_9$ Spectroscopy: Crystal Field Effect and Optical Thermometric Behavior of Near-Infrared-Emitting Singly-Activated Phosphors, *ACS Appl. Mater. Interfaces*, **2018**, 10(48), 41512-41524.

[125] Ueda, J., Back, M., Brik, M.G., Zhuang, Y., Grinberg, M., Tanabe, S., Ratiometric optical thermometry using deep red luminescence from $^4T_2$ and ^2E states of Cr^{3+} in $ZnGa_2O_4$ host, *Optical Materials*, **2018**, 85, 510-516.

[126] Marciniak, L., Bednarkiewicz, A., Kowalska, D., Strek, W. A New generation of highly sensitive luminescent thermometers operating in the optical window of biological tissues. *J. Mater. Chem. C* **2016**, 4, 5559−5563.

[127] Allison, S., Gillies, G., Rondinone, A., Cates, M. Nanoscale thermometry via the fluorescence of YAG:Ce phosphor particles from 7 to 77 C, *Nanotechnology*, **2003**, 14, 859–863.

[128] Khalid, A. H., Kontis, K. 2D surface thermal imaging using rise-time analysis from laser-induced luminescence phosphor thermometry, *Meas. Sci. Technol*., **2009**, 20, 025305.

[129] Peng, H. S., Stich, M. I. J., Yu, J. B., Sun, L. N., Fischer, L. H., Wolfbeis, O. S., Luminescent Europium(III) Nanoparticles for Sensing and Imaging of Temperature in the Physiological Range, *Adv. Mater*., **2010**, 22, 716–719.

[130] Kolesnikov, I. E., Kalinichev, A. A., Kurochkin, M. A., Golyeva, E. V., Terentyeva, A. S., Kolesnikov, E. Yu., Lähderanta, E. Structural, luminescence and thermometric properties of nanocrystalline YVO_4:Dy^{3+} temperature and concentration series, *Scientific Reports*, **2019**, 9(1).

[131] Dong, B., Cao, B. S., He, Y. Y., Liu, Z., Li, Z. P., Feng, Z., Temperature Sensing and in Vivo Imaging by Molybdenum Sensitized Visible Upconversion Luminescence of Rare-Earth Oxides, *Q. Adv. Mater.,* **2012**, 24, 1987−1993.

[132] Pandey, A., Rai, V. K., Kumar, V., Kumar, V., Swart, H. C. Upconversion based temperature sensing ability of Er^{3+}–Yb^{3+}codoped $SrWO_4$: An optical heating phosphor, *Sens. Actuators, B*, **2015**, 209, 352−358.

[133] Balabhadra, S., Debasu, M. L., Brites, C. D. S., Ferreira, R., Carlos, L. Upconverting Nanoparticles Working as Primary Thermometers in Different Media, *The Journal of Physical Chemistry C*., **2017**, 121(25), 13962-13968.

[134] Tian, X., Wei, X., Yonghu Chen, Duan, C., Yin, M. Temperature sensor based on ladder-level assisted thermal coupling and thermal-enhanced luminescence in $NaYF_4$: Nd^{3+}, *Opt. Express,* **2014**, 22, 30333-30345.

CHAPTER 4

Bismuth-based optical materials

Bismuth is one of the most investigated group of elements, the post-transition metals[1]. It is commonly found in nature in the form of oxide (Bi_2O_3), carbonate ($(BiO)_2CO_3$) or sulphide (Bi_2S_3)[2]. It has electronic configuration $(Xe)4f^{14}5d^{10}6s^26p^3$ and owes its easy involvement in chemical combinations to the electrons in the p orbital[3]. The electrons in the 6p, 6s, or 5d orbitals are rather sensitive to their coordination environment[4]. It shows a variety of oxidation states (0, +1, +2, +3, +5), a strong spin–orbit coupling effect and a propensity to form clusters, among which are molecular crystals[5-11], molten Lewis acids[12-15], and porous zeolitic solids[16].

Recently bismuth-based materials gained great attention because of excellent optical and electrical properties[17], low toxicity and reduced costs[18] and environmentally-friendly attributes[19]. They proved to be suitable for various fields of applications, as photocatalysts[20-23], UV filters[24-25], ferroelectrics[26-27], fuel cells[28], batteries[29-30] and multiferroics[31-33]. At the nanoscale, thanks to their physical properties, bismuth-based materials are also promising candidates in the nanomedicine field, as contrast agents for multimodal clinical imaging, allowing to integrate diverse techniques such as computed X-ray tomography (CT)[34-35], single-photon emission CT (SPECT)[36] and photoacoustic tomography (PAT)[37].

Speaking of photocatalysis, bismuth-based compounds generated great interest because of outstanding photocatalytic activity, non-toxicity, cost-effectiveness and superior stability. Bismuth-based materials take advantage of the strong visible light absorption and of the peculiar electronic structure of Bi^{3+} 6s orbitals, typical of p-block metals with a d^{10} configuration, including also Ag^+ 4d and Sn^{2+} 5s. 6s orbitals can hybridize O 2p levels forming a hybridized valence band (VB) and thus narrowing the band gap to efficiently collect visible light[38]. This hybridized VB favours the mobility of photogenerated holes, inducing the efficient separation of electron-hole pairs, thus improving the photocatalytic efficiency[39]. Among recently investigated bismuth-based materials with photocatalytic activity are: layered structure compounds of the Aurivillius family, such as $Bi_xO_yA_z$ (A= Cl, Br, I, F)[40-42], bismuth oxide (Bi_2O_3[43]), bismuth titanates (e.g. $Bi_4Ti_3O_{12}$, $Bi_2Ti_2O_7$, $Bi_{12}TiO_{20}$[44-46]), bismuth tungstate (Bi_2WO_6[47-48]), bismuth titanate niobate (Bi_3TiNbO_9[49]), bismuth vanadates ($BiVO_4$[50-

[54], Bi_7VO_{13}[55], $Bi_{11}VO_{19}$[56]), bismuth silicates (e.g. Bi_2SiO_5, $Bi_4Si_3O_{12}$ and $Bi_{12}SiO_{20}$[57-66]), bismuth phosphate ($BiPO_4$[67]), etc. These materials have been used in various photocatalytic processes[67] including antifogging, carbon dioxide reduction, organic pollutant degradation in water, air and waste water purification, self-cleaning, disinfection, water splitting for hydrogen generation, and so on.

Stereochemically active $6s^2$ lone pair electrons (LPE) are also responsible of non-centrosymmetric crystal structures that induce other peculiar features in the Bi-based materials, such as pyro-, ferro- and piezo-electricity and second harmonic generation (SGH)[68].

During the last decade, the interest in bismuth-activated photonic materials has grew significantly. Extensive studies have been carried out to develop materials suitable as fiber lasers[69], bioimaging probes[70] and phosphors[71-74]. The excitation and emission bands of the Bi-activated phosphors are typically located in the UV-VIS region, but usually any emission is observed at room temperature because of concentration quenching effects. The luminescence spectrum of Bi^{3+} shows a broad blue/green band ranging from 400 to 600 nm. The FWHM of this emission peak can be as large as 0.54 eV, comparable to other of s^2–sp transition such as those of Pb^{2+}, Sn^{2+} and Sb^{3+} and much broader than those of lanthanide ions. Many different classes of bismuth-activated hosts, such as phosphates[75-79], tungstates[80-85], alkaline-earth sulphides and fluorides[86-87], borates[88-89], vanadates[90-95], silicates[96], aluminates and gallates garnets[97-103] are reported in literature.

Even luminescence from bismuth-based compounds has been widely investigated. Among these luminescent materials are $Bi_4Ge_3O_{12}$[104], $Bi_2Al_4O_9$, $Bi_2Ga_4O_9$, $B_{12}TiO_{20}$ and Bi_2WO_6[105]. Also Sillen X1 series of $ABiO_2X$ (A=Cd, Ca, Sr, Ba, Pb; X=Cl, Br, I) compounds have been studied, showing a noteworthy colour tunability moving from blue ($BiSrO_2Cl$) to green-yellow ($BiBaO_2Br$)[106].

Besides luminescent features of Bi^{3+}, also its sensitizing properties to enhance the PL efficiency of other luminescent centres, thanks to its higher absorption cross-section, have been investigated. As reported in literature, the process is based on energy transfer mechanisms between Bi^{3+} and rare earth ions, that have the effect of enhancing their emission intensity. The most studied system consists in the Bi^{3+}-Eu^{3+} pair[107-110], but other ion pairs were also investigated (i.e. Bi^{3+}-Sm^{3+}[107,111-113], Bi^{3+}-Dy^{3+}[107,111-113], Bi^{3+}-Ho^{3+}[107,111-113], Bi^{3+}-Tb^{3+}[107], Bi^{3+}-Yb^{3+}[112]).

There has been comparatively limited research on the development of lanthanide doped Bi-based compounds, compared to d- and p-block metals. Nonetheless, Bi-based hosts show some promising features, such as intrinsic low phonon energy and high refractive index, that reduce non radiative relaxation increasing the emission probability[68], comparable ionic radius of Bi^{3+} with that of Ln^{3+} ions and common trivalent oxidation state. All together these properties make bismuth-based materials potential good hosts for lanthanide ions, for photonic and luminescent applications. Significant synthetic challenges remain, mainly due to differences in solubility and coordination geometry, often because of stereochemically active lone pair electrons of bismuth[19,114]. Recently, various works reported on the spectroscopic properties of lanthanide doped bismuth oxide Bi_2O_3 (Er^{3+}[115], Yb^{3+}, Er^{3+}, Ho^{3+}, Tm^{3+}[116], Yb^{3+},

Er^{3+}[117]); bismuth fluoride BiF_3 (Eu^{3+}, Tb^{3+}[68]); bismuth tungstate Bi_2WO_6 (Eu^{3+}, Pr^{3+}, Nd^{3+}, Tm^{3+}, Ho^{3+}[47]); bismuth vanadate $BiVO_4$ (Er^{3+}, Tm^{3+}, Yb^{3+}[118]); bismuth phosphate $BiPO_4$ (Ce^{3+}, Eu^{3+}[119] and Tb^{3+}, Eu^{3+}, Dy^{3+}, Sm^{3+}[120]); bismuth germanate $Bi_4Ge_3O_{12}$ (Nd^{3+}[121]); and bismuth silicates Bi_2SiO_5 (Dy^{3+}[122], Dy^{3+}-Eu^{3+}[122], Dy^{3+}-Tb^{3+}[122], Yb^{3+}–Er^{3+}, Yb^{3+}–Ho^{3+} and Yb^{3+}–Tm^{3+}[18]), Bi_4SiO_3 (Sm^{3+}[123], Er^{3+}[124-127], Dy^{3+}[128], Dy^{3+}-Eu^{3+}[129], Nd^{3+}[130]), and $Bi_{12}SiO_{20}$ (Pr^{3+}[131], Nd^{3+}[121]).
Among the investigated doped matrices, bismuth silicates, with excellent chemical and thermal stability, seem to be promising hosts for fluorescence applications.

4.1 Bismuth silicates as new host for upconversion (UC)

Bismuth silicate ceramics have attracted great interest because of their piezoelectric and photorefractive features, optical activity and photoconductivity, that make them suitable materials for disparate applications[126,132-135]. They have excellent mechanical, chemical, optical, photoluminescent, and thermoluminscence properties[123,136-138]. They are characterized by general formula $Bi_xSi_yO_z$, commonly abbreviated to BSO[17]. The Bi_2O_3-SiO_2 binary system (Fig.1) mainly consists of three compounds[139], depending on the molar ratio between the two oxides, each with a distinctive crystalline phase: the sillenite $Bi_{12}SiO_{20}$ (with molar ratio 6:1), the eulytite $Bi_4Si_3O_{12}$ (2:3) and the metastable Bi_2SiO_5 (1:1)[18,38,123,132,140]. However, because of the complex nature of the Bi_2O_3-SiO_2 system, complete phase relations and crystallizing behaviour of the system are still not explicit[17,140-142].

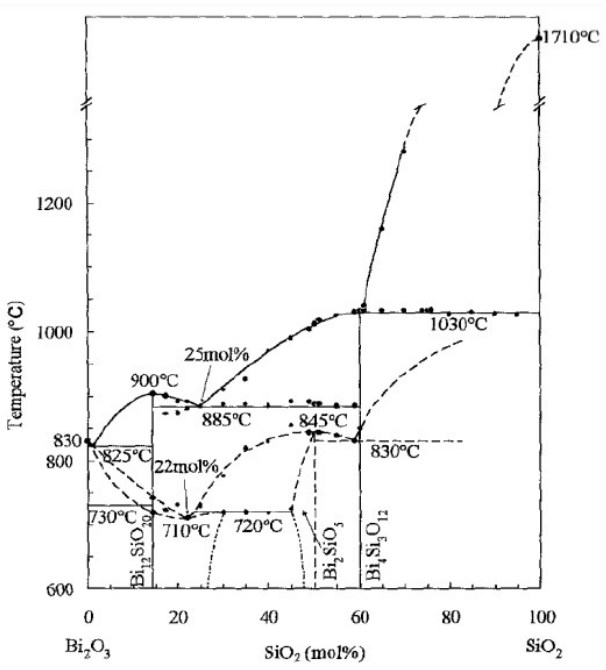

Fig.1 Bi_2O_3-SiO_2 binary system phase diagram.

The $Bi_{12}SiO_{20}$ phase belongs to the family of the so-called sillenite-type structures[143-147], isomorphic to γ-Bi_2O_3, and it is exploited in many optical devices due to its photorefractive, piezoelectric, electro-optic, dielectric and photocatalytic properties[148-155].

$Bi_4Si_3O_{12}$ structure is similar to that of $Bi_4Ti_3O_{12}$ perovskite[156], in which triple Ti-O octahedral is placed between $(Bi_2O_2)^{2+}$ layers[132,157]. It is a ferroelectric material[132] with many applications due to its low dielectric permittivity, high Curie temperature, and spontaneous polarization[158-162]. It is transparent in VIS-NIR regions, which makes it an attractive candidate for diode pumped microchip lasers[163]. $Bi_4Si_3O_{12}$ has also been widely investigated as a scintillator[164-166], due to its physical, optical and scintillation resemblance to $Bi_4Ge_3O_{12}$[17,164,167], and phosphor host[124-129,168].

Bi_2SiO_5 belongs to the Aurivillius family; its unique crystalline structure is composed of layers of pyroxene $(SiO_3)^{2-}$ and $(Bi_2O_2)^{2+}$, stacked alternatively[169]. This layered structure may be beneficial for the formation of 2D or 3D nanostructures, such as sheet-/flower-like morphologies[122]. It possesses relatively good dielectric and piezoelectric properties and nonlinear optical effects[38]. The less-explored metastable Bi_2SiO_5 phase has been previously reported for its photocatalytic activity[57-62, 170-171], heavy metal removal properties[172], and lead-free ferroelectricity[173-178]. Despite appealing properties, only few studies are available in literature about optical properties of Bi_2SiO_5[18,122]. Common synthetic methods of Bi_2SiO_5 are hydrothermal[38,57,178], sol-gel[179], molten salt[180-181] syntheses and more traditional solid-state-reaction methods. The hydrothermal method offers many advantages, compared to conventional ones. Among them are mild synthesis conditions, higher purity, a high degree of crystallinity and narrow distribution of particle size[122]. However, new synthetic strategies able to stabilize the single phase are requested, especially at the nanoscale.

Silicate-based nanophosphors are promising hosts for the doping with lanthanide ions, thanks to features such as wide band gap, compact crystalline structure, chemical and thermal stability, low synthesis cost etc[169]. Moreover, they can be easily synthesized with respect to nitrides or oxynitrides phosphors and are endowed with homogeneous distribution of the dopants and versatility of shapes and sizes[182-184].

4.2 Bi_2O_3 polymorphs

Since the starting NPs are composed of Bi_2O_3, and certain conditions may lead to the stabilization of specific crystalline structures, which can influence the performance of lanthanide ions, the polymorphic nature of this compound must be considered.

Bismuth oxide (Bi_2O_3) displays a complex polymorphism. Six different polymorphs of this oxide, i.e. the α-, β-, γ-, δ-, ε-, and ω-phases, have been reported in the literature. The monoclinic α-Bi_2O_3 phase is stable at room temperature. Upon heating, it transforms into the δ-form at about 730 °C [185]. The high temperature form δ- Bi_2O_3 is stable between 730 °C and approximately 825 °C, which is the melting temperature of the material. Cooling the δ-Bi_2O_3 form does not give directly the α-variety:

intermediate metastable tetragonal and body-centred cubic phases (β and γ, respectively) are observed at about 650°C and 640°C, respectively. The transformation of β during cooling, at about 300 °C, always leads to the α-form, whereas γ can persist to room temperature when the cooling rate is very low. More recently, an orthorhombic δ-Bi_2O_3 and a triclinic ε- Bi_2O_3 phases were stabilized in specific conditions[186]. Fig.2 summarizes the complex temperature dependence stabilization of the different polymorphs[186].

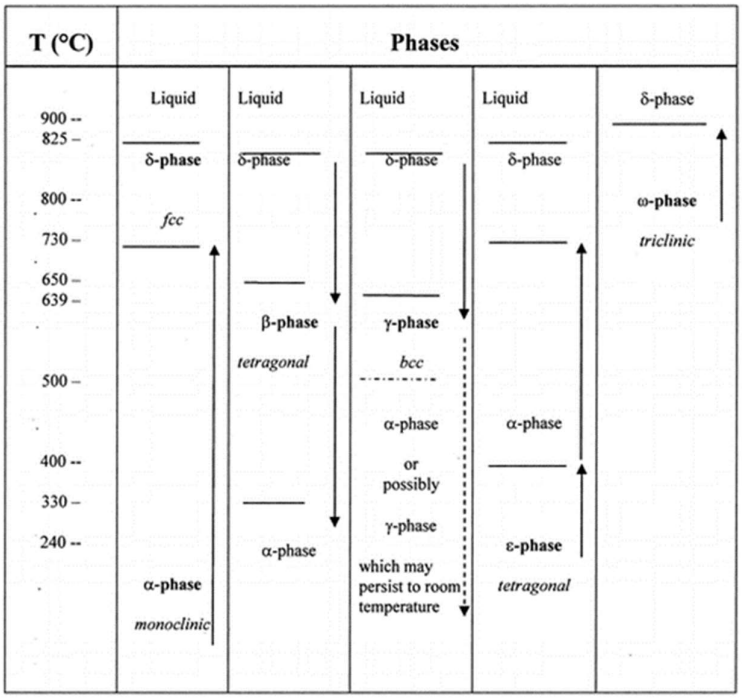

Fig.2 Stable and metastable polymorphs of Bi_2O_3 and their temperature dependence[186].

References

[1] Sun, H.T., Zhou, J., Qiu, J., Recent advances in bismuth activated photonic materials, *Progress in Materials Science*, **2014**, 64, 1–72.

[2] Sadler, P.J., Li, H., Sun, H., Coordination chemistry of metals in medicine: target sites for bismuth. *Coordin. Chem. Rev.*, **1999**, 185–186, 689–709.

[3] Hershaft, A., Corbett, J.D., The crystal structure of bismuth subchloride. Identification of the ion Bi_9^{5+}, *Inorg. Chem.*, **1963**, 2, 979–85.

[4] Gaft, M., Reisfeld, R., Panczer, G., Luminescence spectroscopy of minerals and materials. Berlin, *Springer*, **2005**, ISBN 978-3-540-26377-7.

[5] Ulvenlund, S., Ståhl, K., Kloo, L.B., Structural and quantum chemical study of Bi_5^{3+} and isoelectronic main-group metal clusters. The crystal structure of pentabismuth$^{(3+)}$ tetrachlorogallate(III) refined from X-ray powder diffraction data and synthetic attempts on its antimony analogue, *Inorg. Chem.*, **1996**, 35, 223–30.

[6] Lindsjö, M., Fischer, A., Kloo, L., Improvements of and insights into the isolation of bismuth polycations from benzene solution–single-crystal structure determinations of $Bi_8[GaCl_4]_2$ and $Bi_5[GaCl_4]_3$, *Eur. J. Inorg. Chem.*, **2005**, 670–5.

[7] Kuznetsov, A.N., Popovkin, B.A., Ståhl, K., Lindsjö, M., Kloo, L., Synthesis of main group polycations in molten and pseudo-molten $GaBr_3$ media, *Eur. J. Inorg. Chem.*, **2005**, 4907–13.

[8] Sun, H.T., Sakka, Y., Gao, H., Miwa, Y., Fujii, M., Shirahata, N., Ultrabroad near infrared photoluminescence from $Bi_5(AlCl_4)_3$ crystal, *J. Mater. Chem.*, **2011**, 21, 4060–3.

[9] Sun, H.T., Sakka, Y., Shirahata, N., Gao, H., Yonezawa, T., Experimental and theoretical studies of photoluminescence from Bi_8^{2+} and Bi_5^{3+} stabilized by $[AlCl_4]$ in molecular crystals, *J. Mater. Chem.*, **2012**, 22, 12837–41.

[10] Sun, H.T., Xu, B.B., Yonezawa, T., Sakka, Y., Shirahata, N., Fujii, M., Photoluminescence from $Bi_5(GaCl_4)_3$ molecular crystal, *Dalton Trans*, **2012**, 41, 11055–61.

[11] Krebs, B., Hucke, M., Brendel, C.J., Structure of the octabismuth$^{(2+)}$ cluster in crystalline $Bi_8(AlCl_4)_2$, *Angew. Chem. Int. Ed. Engl.*, **1982**, 21, 445–6.

[12] Davis, H.L., Bjerrum, N.J., Smith, J.P., Ligand field theory of $p^{2,4}$ configurations and its application to the spectrum of Bi^+ in molten salt media, *Inorg. Chem.*, **1967**, 6, 1172–8.

[13] Bjerrum, N.J., Smith, J.P., Lower oxidation states of bismuth. Bi_8^{2+} formed in $AlCl_3$–NaCl melts, *Inorg. Chem.*, **1967**, 6, 1968–72.

[14] Bjerrum, N.J., Davis, H.L., Smith, J.P., The optical spectrum of bismuth(I) in the molten aluminum bromide-sodium bromide eutectic, *Inorg. Chem.*, **1967**, 6, 1603–4.

[15] Bjerrum, N.J., Boston, C.R., Smith, J.P., Lower oxidation states of bismuth. Bi^+ and Bi_5^{3+} in molten salt solutions, *Inorg. Chem.*, **1967**, 6, 1162–72.

[16] Sun, H.T., Matsushita, Y., Sakka, Y., Shirahata, N., Tanaka, M., Katsuya, Y., Synchrotron X-ray, photoluminescence and quantum chemistry studies of bismuth embedded dehydrated zeolite Y, *J. Am. Chem. Soc*., **2012**, 134, 2918–21.

[17] Zhang, Z.G., Wang, X.F., Tian, Q. Q., Grain Orientation Distribution and Development of Grain Line in Highly Ordered $Bi_4Si_3O_{12}$ Micro-Crystals, *Science of Sintering*, **2010**, 42.

[18] Back, M., Trave, E., Zaccariello, G., Cristofori, D., Canton, P., Benedetti, A., Riello, P., Bi_2SiO_5@g-SiO_2 upconverting nanoparticles: a bismuth-driven core–shell self-assembly mechanism, *Nanoscale*, **2019**, 11, 2, 675-687.

[19] Adcock, A.K., Gibbons, B., Einkauf, J.D., Bertke, J.A., Rubinson, J.F., de Lill, D.T., Knope, K.E., Bismuth(iii)-thiophenedicarboxylates as host frameworks for lanthanide ions: synthesis, structural characterization, and photoluminescent behavior, *Dalton Trans*., **2018**, 47(38), 13419-13433.

[20] Dong, S., Feng, J., Fan, M., Pi, Y., Hu, L., Han, X., Liu, M., Sun, J., Recent developments in heterogeneous photocatalytic water treatment using visible light-responsive photocatalysts: a review, *RSC Adv*., **2015**, 5, 14610-14630.

[21] Riente, P., Matas Adams, A., Albero, J., Palomares, E., Pericàs, M. A., Light-Driven Organocatalysis Using Inexpensive, Nontoxic Bi_2O_3 as the Photocatalyst, *Angew. Chem. Int. Ed.,* **2014**, 53, 9613-9616.

[22] Suzuki, H., Kunioku, H., Kato, D., Hongo, K., Maezono, R., Higashi, M., Kunioku, H., Yabuuchi, M., Suzuki, H., Okajima, H., Zhong, C., Nakano, K., Abe, R., Kageyama, H., Valence Band Engineering of Layered Bismuth Oxyhalides towards Stable Visible-Light Water Splitting: Madelung Site Potential Analysis, *J. Am. Chem. Soc*., **2017**, 139, 18725-18731.

[23] Higashi, M., Tomita, O., Kato, D., Kageyama, H., Abe, R., Lead Bismuth Oxyhalides $PbBiO_2X$ (X =Cl, Br) as Visible-Light-Responsive Photocatalysts for Water Oxidation: Role of Lone-Pair Electrons in Valence Band Engineering, *Chem. Mater*., **2018**, 30, 5862-5869.

[24] Zaccariello, G., Back, M., Zanello, M., Canton, P., Cattaruzza, E., Riello, P., Alimonti, A., Benedetti, A, Formation and Controlled Growth of Bismuth Titanate Phases into Mesoporous Silica Nanoparticles: An Efficient Self-Sealing Nanosystem for UV Filtering in Cosmetic Formulation, *ACS Appl. Mater. Interfaces*, **2017**, 9, 1913-1921.

[25] Zaccariello, G., Back, M., Benedetti, A., Canton, P., Cattaruzza, E., Onoda, H., Glisenti, A., Alimonti, A., Bocca, B., Riello, P., Bismuth titanate-based UV filters embedded mesoporous silica nanoparticles: role of bismuth concentration in the self-sealing process, *J. Colloid Interface Sci*., **2019**, 549, 1-8.

[26] Park, B.H., Kang, B.S., Bu, S.D., Noh, T.W., Lee J., Jo, W., Lanthanum-substituted bismuth titanate for use in non-volatile memories, *Nature*, **1999**, 401, 682-684.

[27] Choi, W.S., Chismholm, M.F., Singh, D.J., Choi, T., Jellison, G.E., Lee, H.N., Wide bandgaptunability in complex transition metal oxides by site-specific substitution, *Nat. Commun*. **2012**, 3, 689.

[28] Sanna, S., Esposito, V., Andreasen, J. W., Hjelm, J., Zhang, W., Kasama, T., Simonsen, S. B., Christensen, M., Linderoth, S., Pryds, N., Enhancement of the chemical stability in confined δ- Bi_2O_3, *Nat. Mater*., **2015**, 14, 500-504.

[29] Sottmann, J., Herrmann, M., Vajeeston, P., Ruud, A., Drathen, C., Emerich, H., Wragg, D.S., Fjellvåg, H., Bismuth Vanadate and Molybdate: Stable Alloying Anodes for Sodium- Ion Batteries. *Chem. Mater*., **2017**, 29, 2803-2810.

[30] Konishi, H., Minato, T., Abe, T., Ogumi, Z., Influence of Electrolyte Composition on the Electrochemical Reaction Mechanism of Bismuth Fluoride Electrode in Fluoride Shuttle Battery, *J. Phys. Chem. C*, **2019**, 123, 10246-10252.

[31] Guennou, M., Viret, M., Kreisel, J., Bismuth-based perovskites as multiferroics, *Comptes Rendus Physique*, **2015**, 16, 182-192.

[32] Chen, A., Zhou, H., Bi, Z., Zhu, Y., Luo, Z., Bayraktaroglu, A., Phillips, J., Choi, E.-M., MacManus- Driscoll, J.L., Pennycook, S.J., Narayan, J., Jia, Q., Zhang, X., Wang., H., A New Class Of Room- Temperature Multiferroic Thin Films with Bismuth-Based Supercell Structure, *Adv. Mater*., **2013**, 25, 1028-1032.

[33] Nachache, R., Harnagea, C., Li, S., Cardenas, L., Huang, W., Chakrabartty, J., Rosei, F., Bandgap tuning of multiferroic oxide solar cells, *Nat. Photonics*, **2015**, 9, 61-67.

[34] Chen, J., Yang, X. Q., Qin, M. Y., Zhang, X. S., Xuan, Y., Zhao, Y. D., Hybrid nanoprobes of bismuth sulfide nanoparticles and CdSe/ZnS quantum dots for mouse computed tomography/fluorescence dual mode imaging, *J. Nanobiotechnology*, **2015**, 13, 76.

[35] Rabin, O., Manuel Perez, J., Grimm, J., Wojtkiewicz, G., Weissleder, R. An X-ray computed tomography imaging agent based on long-circulating bismuth sulphide nanoparticles, *Nat Mater*., **2006**, 5(2), 118-22.

[36] de Swart, J., Chan, H. S., Goorden, M. C., Morgenstern, A., Bruchertseifer, F., Beekman, F. J., de Jong, M., Konijnenberg, M. W., Utilizing high-energy γ-photons for high-resolution Bi SPECT in Mice, *J. Nucl. Med*., **2016**, 57(3), 486-492.

[37] Zheng, X., Shi, J., Bu, Y., Tian, G., Zhang, X., Yin, W., Gao, B., Yang, Z., Hu, Z., Liu, X., Yan, L., Gu, Z., Zhao, Y., Silica-coated bismuth sulfide nanorods as multimodal contrast agents for a non-invasive visualization of the gastrointestinal tract, *Nanoscale*, **2015**, 7, 12581.

[38] Chen, C.-C., Yang, C.-T., Chung, W.-H., Chang, J.-L., & Lin, W.-Y., Synthesis and characterization of $Bi_4Si_3O_{12}$, Bi_2SiO_5, and $Bi_{12}SiO_{20}$ by controlled hydrothermal method and their photocatalytic activity, *Journal of the Taiwan Institute of Chemical Engineers*, **2017**, 78, 157–167.

[39] Wei, W., Dai, Y., Huang, B., First-Principles Characterization of Bi-based Photocatalysts: $Bi_{12}TiO_{20}$, $Bi_2Ti_2O_7$, and $Bi_4Ti_3O_{12}$, *The Journal of Physical Chemistry C*, **2009**,113(14), 5658-5663.

[40] Cheng, H., Huang, B., Dai, Y., Engineering BiOX (X = Cl, Br, I) nanostructures for highly efficient photocatalytic applications, *Nanoscale*, **2014**, 6, 2009–26.

[41] Ye, L., Chen, J., Tian, L., Liu, J., Penga, T., Deng, K., BiOI thin film via chemical vapor transport: photocatalytic activity, durability, selectivity and mechanism, *Appl. Catal. B: Environ*., **2013**, 130–131, 1–7.

[42] Bhachu, D.S., Moniz, S.J.A., Sathasivam, S., Scanlon, D.O., Walsh, A., Bawaked, S.M., Mokhtar, M., Obaid, A.Y., Parkin, I.P., Tang, J., Carmalt. C.J., Bismuth oxyhalides: synthesis, structure and photoelectrochemical activity, *Chem. Sci*., **2016**, 7, 4832-4841.

[43] Wu, Y.-C., Chaing, Y.-C., Huang, C.-Y., Wang, S.-F., Yang, H.-Y., Morphology-controllable Bi_2O_3 crystals through an aqueous precipitation method and their photocatalytic performance, *Dyes and Pigments*, **2013**, 98(1), 25-30.

[44] Chen, Z., Jiang, H., Jin, W., Shi, C., Enhanced photocatalytic performance over $Bi_4Ti_3O_{12}$ nanosheets with controllable size and exposed (001) facets for Rho- damine B degradation, *Appl. Catal. B: Environ*., **2016**, 180, 698–706.

[45] Hou, J., Qu, Y., Krsmanovic, D., Ducati, C., Eder D., Kumar, R.V., Hierarchical assemblies of bismuth titanate complex architectures and their visible-light photocatalytic activities, *J. Mater. Chem*., **2010**, 20, 2418-2423.

[46] Yao, W.F., Wang, X.H., Xu, H., Cheng, X.F., Huang, J., Shang, S.X.,Yang, X.N., Wang, M., Photocatalytic property of bismuth titanate $Bi_{12}TiO_{20}$ crystals, *Applied Catalysis A: General*, **2003**, 243(1), 185-90.

[47] Akkaya, C., Ünal, U., Lanthanide doped bismuth tungstates: an investigation for LED and photocatalysis applications, *Eskişehir Technical University Journal of Science and Technology A - Applied Sciences and Engineering*, **2018**, 19, 1001-12.

[48] Liao, Y.H., Wang, J.X., Lin, J.S., Chung, W.H., Lin, W.Y., Chen, C.C., Synthesis photocatalytic activities and degradation mechanism of Bi_2WO_6 toward crystal violet dye, *Catal Today*, **2011**, 174, 148–59.

[49] Xu, L., Wan, Y., Xie, H., Huang, Y., Qiao, X., Qin, L., On structure, optical properties and photodegradated ability of aurivillius-type Bi_3TiNbO_9 nanoparticles, *J. Am. Ceram. Soc*., **2016**, 99, 3964–72.

[50] Cooper, J.K., Gul, S., Toma, M.F., Chen, L., Liu, Y.-S., Guo, J., Ager, J. W., Yano, J., Sharp, I.D., Indirect Bandgap and Optical Properties of Monoclinic Bismuth Vanadate, *The Journal of Physical Chemistry C*, **2005**, 119(6), 2969-2974.

[51] Ravidhas, C., Juliat, A.J., Sudhagar, P., Devadoss, A., Terashima, C., Nakata, K., Fujishima, A., Raj, A.M.E., Sanjeeviraja, C., Facile synthesis of nanostructured monoclinic bismuth vanadate by a co-precipitation method: Structural, optical and photocatalytic properties, *Materials Science in Semiconductor Processing*, **2015**, 30, 343-351.

[52] Seabold, J.A., Choi K.S., Efficient and stable photo-oxidation of water by a bismuth vanadate photoanode coupled with an iron oxyhydroxide oxygen evolution catalyst, *J. Am. Chem. Soc*., **2012**, 134, 2186–92.

[53] Saison, T., Chemin, N., Chanéac, C., Durupthy, O., Mariey, L., Maugé, F., Brezová V., Jolivet, J.-P., New insights into $BiVO_4$ properties as visible light photocatalyst, *J. Phys. Chem. C*, **2015**, 119, 12967-12977.

[54] Tachikawa, T., Ochi, T., Kobori, Y., Crystal-face-dependent charge dynamics on a $BiVO_4$ photocatalyst revealed by single-particle spectroelectrochemistry, *ACS Catal*., **2016**, 6, 2250-2256.

[55] Pu, Y., Li, Y., Huang, Y., Kim, S.I., Cai, P., Seo, H.J., Visible light-induced degradation of methylene blue by photocatalyst of bismuth layered Bi_7VO_{13} nanoparticles, *Mater. Lett*., **2015**, 141, 73–5.

[56] Lu, Y., Chen, L., Huang, Y., Cheng, H., Kim, S.I., Seo, H.J., Optical properties and visible light-driven photocatalytic activity of $Bi_{11}VO_{19}$ nanoparticles with δ-Bi_2O_3-structure, *J. Alloys Comp*., **2015**, 640, 226–32.

[57] Chen, R., Bi, J., Wu, L., Wang, W., Li, Z., Fu, X., Template-free hydrothermal synthesis and photocatalytic performances of novel Bi_2SiO_5 nanosheets, *Inorganic Chemistry*, **2009**, 48(19), 9072-9076.

[58] Zhang, L., Wang , W., Sun, S., Xu, J. , Shang, M., Ren, J., Hybrid Bi_2SiO_5 mesoporous microspheres with light response for environment decontamination, *Applied Catalysis B: Environmental*, **2010**, 100, 97-101.

[59] Zhang, P., Hu, J., Li, J., Controllable morphology and photocatalytic performance of bismuth silicate nanobelts/nanosheets, *RSC Adv*., **2011**, 1, 1072-1077.

[60] Duan, J., Liu, Y., Pan, X., Zhang, Y., Yu, J., Nakajim, K., Taniguchi, H., High photodegradation efficiency of rhodamine B catalysed by bismuth silicate nanoparticles, *Catal. Commun*., **2013**, 39, 65-69.

[61] Wei, W., Xie, J., Suci, M., Yan, Z., Zhu, J., Cui, H., Synthetic bismuth silicate nanostructures: Photocatalysts grown from silica aerogels precursors, *Journal of Materials Research*, **2013**, 28, 1658-1668.

[62] Liu, D., Wang, J., Zhang, M., Liu, Y., Zhu., Y. A superior photocatalytic performance of a novel Bi_2SiO_5 flower-like microsphere via a phase junction, *Nanoscale*, **2014**, 6, 15222-27.

[63] Batool, S. S., Hassan, S., Imran, Z., Rasool, K., Ahmad, M., Rafiq, M. A., Comparison of different phases of bismuth silicate nanofibers for photodegradation of organic dyes, *Int. J. Environ. Sci. Technol*., **2016**, 13, 1497–1504.

[64] Vodyankin, A.A., Ushakov, I.P., Belik, Y.A., Vodyankina, O.V., Synthesis and photocatalytic properties of materials based on bismuth silicates, *Kinet. Catal*., **2017**, 58, 593.

[65] Karthik, K., Devi, K.R.S., Pinheiro, D., Sugunan, S., Photocatalytic activity of bismuth silicate heterostructures synthesized via surfactant mediated sol-gel method, *Materials Science in Semiconductor Processing*, **2019**, 102, 104589.

[66] Wu, Y., Lu, J., Li, M., Yuan, J., Wu, P., Chang, X., Liu, C., Wang, X., Bismuth silicate photocatalysts with enhanced light harvesting efficiency by photonic crystal, *Journal of Alloys and Compounds*, **2019**, 810, 151839.

[67] Anku, W.W., Oppong, S., Govender, P., Bismuth-Based Nanoparticles as Photocatalytic Materials in Bismuth - Advanced Applications and Defects Characterization, *IntechOpen*, **2018**, ISBN 978-1-78923-263-9.

[68] Back, M., Ueda, J., Ambrosi, E., Cassandro, L., Cristofori, D., Ottini, R., Riello, P., Sponchia, G., Asami, K., Tanabe, S., Trave, E., Lanthanide-doped Bismuth-Based Fluoride Nanocrystalline Particles: Formation, Spectroscopic Investigation and Chemical Stability, *Chemistry of Materials*, **2019**, 10.1021/acs.chemmater.9b03164.

[69] Dianov, E.M., Dvoyrin, V.V., Mashinsky, V.M., Umnikov, A.A., Yashkov, M.V., Guryanov, A.N., CW bismuth fiber laser, *Quant. Electron.*, **2005**, 35, 1083–4.

[70] Sun, H.T., Yang, J.J., Fujii, M., Sakka, Y., Zhu, Y., Asahara, T., Highly fluorescent silica-coated bismuth doped aluminosilicate nanoparticles for near infrared bioimaging, *Small*, **2011**, 7, 199–203.

[71] Gaft, M., Reisfeld, R., Panczer, G., Boulon, G., Saraidarov, T., Erlish, S., The luminescence of Bi, Ag and Cu in natural and synthetic barite $BaSO_4$, *Opt. Mater.*, **2001**, 16, 279–90.

[72] Srivastava, A., Luminescence of divalent bismuth in $M^{2+}BPO_5$ ($M^{2+} = Ba^{2+}$, Sr^{2+} and Ca^{2+}), J. *Lumin.*, **1998**, 78, 239–43.

[73] Peng, M.Y., Wondraczek, L., Bi^{2+}-doped strontium borates for white-light-emitting diodes, *Opt. Lett.*, **2009**, 34, 2885–7.

[74] Peng, M.Y., Wondraczek, L., Photoluminescence of $Sr_2P_2O_7$:Bi^{2+} as a red phosphor for additive light generation, *Opt. Lett.*, **2010**, 35, 2544–6.

[75] Blasse, G., van der Steen, A. C., Luminescence characteristics of Bi^{3+}-activated oxides, *Solid State Commun.*, **1979**, 31, 993-994.

[76] van Zon, F.B.M., Koningsberger, D.C., Oomen, E.W.J.L., Blasse. G., An EXAFS study of the luminescent Bi^{3+} center in $LaPO_4$-Bi, *J. Solid State Chem.*, **1987**, 71, 396-402.

[77] Cavalli, E., Angiuli, F., Mezzadri, F., Trevisani, M., Bettinelli, M., Boutinaud P., Brik, M., Tunable luminescence of Bi^{3+}-doped $YP_xV_{1-x}O_4$ ($0 \leq x \leq 1$), *J. Phys.: Condens. Matter*, **2014**, 26, 385503.

[78] Srivastava, A.M., Camardello, S.J., Concentration dependence of the Bi^{3+} luminescence in $LnPO_4$ (Ln=Y^{3+}, Lu^{3+}), *Opt. Mater.*, **2015**, 39, 130-133.

[79] Babin, V., Chernenko, K., Demchenko, P., Mihokova, E., Nikl, M., Pashuk, I., Shalapska, T., Voloshinovskii, A., Zazubovich, S., Luminescence and excited state dynamics in Bi^{3+}-doped $LiLaP_4O_{12}$ phosphates, *J. Lumin.*, **2016**, 176, 324-330.

[80] Zorenko, Y., Pashkovsky, M., Voloshinovskii, A., Kuklinski, B., Grinberg, M., The luminescence of $CaWO_4$:Bi single crystal, *J. Lumin.*, **2006**, 116, 43-51.

[81] Kang, F., Peng, M., A new study on the energy transfer in the color-tunable phosphor $CaWO_4$:Bi, *Dalton Trans.*, **2014**, 43(1), 277-284.

[82] Pédrini, C., Boulon, G., Gaume-Mahn, F., Bi^{3+} and Pb^{2+} centres in alkaline-earth antimonate phosphors, *Phys. Status Solidi A*, **1973**, 15, K15-K18.

[83] Srivastava, A.M., Szarowski, A., On the quenching of Bi^{3+} luminescence in the pyrochlore Gd_2GaSbO_7, *J. Solid State Chem.*, **1999**, 146, 494-498.

[84] Yao, S., Zhou, X., Huang, Y., Wang, Z., Long, Y., Li, W., Luminescent properties of Bi^{3+}-activated $Ca_2Sb_2O_7$ nano-phosphor prepared by co-precipitation method, *J. Alloys Compd.*, **2015**, 653, 345- 350.

[85] Yao, S., Chen, L., Huang, Y., Li, W., Enhanced luminescence of $CaSb_2O_6:Bi^{3+}$ blue phosphors by efficient charge compensation, *Mater. Sci. Semicond. Process*., **2016**, 41, 265-269.

[86] Donker, H., Yamashita, N., Smit, W.M.A., Blasse, G., Luminescence decay times of the Sb^{3+}, Pb^{2+}, and Bi^{3+} ions in alkaline-earth sulfides, *Phys. Status Solidi B*, **1989**, 156, 537-544.

[87] Oboth, K.P., Lohmeier, F.J., Fischer, F., VUV and UV spectroscopy of Pb^{2+} and Bi^{3+} centres in alkaline-earth fluorides, *Phys. Status Solidi B*, **1989**, 154, 789-803.

[88] Wolfert, A., Oomen, E.W.J.L., Blasse, G., Host lattice dependence of the Bi^{3+} luminescence in orthoborates $LnBO_3$ (with Ln = Sc, Y, La, Gd, or Lu), *J. Solid State Chem*., **1985**, 59, 280-290.

[89] Blasse, G., The ultraviolet absorption bands of Bi^{3+} and Eu^{3+} in oxides, *J. Solid State Chem*., **1972**, 4, 52-54.

[90] Kang, F., Peng, M., Yang, X., Dong, G., Nie, G., Liang, W., Xu, S., Qiu, J., Broadly tuning Bi^{3+} emission via crystal field modulation in solid solution compounds $(Y,Lu,Sc)VO_4$:Bi for ultraviolet converted white LEDs, *J. Mater. Chem. C*, **2014**, 2, 6068-6076.

[91] Kang, F., Peng, M., Zhang, Q., Qiu, J., Abnormal Anti-Quenching and Controllable Multi- Transitions of Bi^{3+} Luminescence by Temperature in a Yellow-Emitting $LuVO_4:Bi^{3+}$ Phosphor for UV-Converted White LEDs, *Chem. Eur. J.*, **2014**, 20, 11522-11530.

[92] Kang, F., Zhang, Y., Wondraczek, L., Zhu, J., Yang, X., Peng, M., Processing-dependence and the nature of the blue-shift of Bi^{3+}-related photoemission in $ScVO_4$ at elevated temperatures, J. *Mater. Chem. C*, **2014**, 2, 9850-9857.

[93] Kang, F., Yang, X., Peng, M., Wondraczek, L., Ma, Z., Zhang, Q., Qiu, J., Red photoluminescence from Bi^{3+} and the influence of the oxygen-vacancy perturbation in $ScVO_4$: A combined experimental and theoretical study, *J. Phys. Chem. C*, **2014**, 118, 7515-7522.

[94] Kang, F., Zhang, H., Wondraczek, L., Yang, X., Zhang, Y., Lei, D.Y., Peng, M., Band-gap modulation in single Bi^{3+}-doped yttrium-scandium-niobium vanadates for color tuning over the whole visible spectrum, *Chem. Mater*., **2016**, 28, 2692-2703.

[95] Mahlik, S., Amer, M., Boutinaud, P., Energy level structure of Bi^{3+} in zircon and scheelite polymorphs of YVO_4, *J. Phys. Chem. C*, **2016**, 120, 8261-8265.

[96] Sun, Z., Wang, M., Yang, Z., Liu, K., Zhu., F., Crystal structure and luminescence properties of Bi^{3+} activated $Ca_2Y_8(SiO_4)_6O_2$ phosphors under near UV excitation, *J. Solid State Chem*., **2016**, 239, 165-169.

[97] Lacklison, D.E., Scott, G.B., Page, J.L., Absorption spectra of Bi^{3+} and Fe^{3+} in $Y_3Ga_5O_{12}$, *Solid State Comm.*, **1974**, 14, 861-863.

[98] Ilmer, M., Grabmaier, B.C., Blasse, G., Luminescence of Bi^{3+} in gallate garnets, *Chem. Mater*., **1994**, 6, 204-206.

[99] Nikl, M., Novoselov, A., Mihoková, E., Polák, K., Dusek, M., McClune, B., Yoshikawa, A., Fukuda, T., Photoluminescence of Bi^{3+} in $Y_3Ga_5O_{12}$ single-crystal host, *J. Phys.: Condens. Matter*, **2005**, 17, 3367-3375.

[100] Zorenko, Y., Gorbenko, V., Voznyak, T., Vistovsky, V., Nedilko, S., Nikl, M., Luminescence of Bi^{3+} ions in $Y_3Ga_5O_{12}$:Bi single crystalline films, *Radiat. Meas*., **2007**, 42, 882-886.

[101] Babin, V., Gorbenko, V., Krasnikov, A., Makhov, A., Nikl, M., Polak, K., Zazubovich, S., Zorenko, Y., Peculiarities of excited state structure and photoluminescence in Bi^{3+}-doped $Lu_3Al_5O_{12}$ single crystalline films, *J. Phys.: Condens. Matter*, **2009**, 21, 415502.

[102] Zorenko, Y., Mares, J.A., Kucerkova, R., Gorbenko, V., Savchyn, V., Voznyak, T., Nikl, M., Beitlerova, A., Jurek, K., Optical, luminescence and scintillation characteristics of Bi-doped LuAG and YAG single crystalline films, *J. Phys. D: Appl. Phys*., **2009**, 42, 075501.

[103] Yousif, A., Kumar, V., Seed Ahmed, H.A.A., Som, S., Noto, L.L., Ntwaeaborwa, O.M., Swart, H.C., Effect of Ga^{3+} doping on the photoluminescence properties of $Y_3Al_{5-x}Ga_xO_{12}$:Bi^{3+} phosphor, *ECS J. Solid State Sci. Technol*., **2014**, 3, R222-R227.

[104] Itoh, M., Katariri, T., Mitani, H., Fujita, M., Usuki, Y., Comparative study of excitonic structures and luminescence properties of $Bi_4Ge_3O_{12}$ and $Bi_{12}GeO_{20}$, *Phys. Stat. Sol. B*, **2008**, 245, 2733-2736.

[105] Barros, A., Deloncle, R., Deschamp, J., Boutinaud, P., Chadeyron, G., Mahiou, R., Cavalli, E., Brik, M.G., Optical properties and electronic band structure of $BiMg_2PO_6$, $BiMg_2VO_6$, $BiMg_2VO_6$:Pr^{3+} and $BiMg_2VO_6$:Eu^{3+}, *Opt. Matter.,* **2014**, 36, 1724-1729.

[106] Olchowka, J., Kabbour, H., Colmont, M., Adlung, M., Wickleder, C., Mentré, O., $ABiO_2X$ (A=Cd, Ca, Sr, Ba, Pb; X=halogen) Sillen X1 series: polymorphism versus optical properties, *Inorg. Chem.*, **2016**, 55, 7582-7592.

[107] Blasse G., Bril. A., Study of energy transfer from Sb^{3+}, Bi^{3+}, Ce^{3+} to Sm^{3+}, Eu^{3+}, Tb^{3+}, Dy^{3+}, J. *Chem. Phys.*, **1967**, 47, 1920-1926.

[108] Yan, S., Zhang, J., Zhang, X., Lu, S., Ren, X., Nie, Z., Wang, X., Enhanced Red Emission in $CaMoO_4$:Bi^{3+},Eu^{3+}, *J. Chem. Phys. C*, **2007**, 111, 13256-13260.

[109] Kang, F., Zhang, Y., Peng., M., Controlling the Energy Transfer via Multi Luminescent Centers to Achieve White Light/Tunable Emissions in a Single-Phased X2-Type Y_2SiO_5:Eu^{3+},Bi^{3+} Phosphor For Ultraviolet Converted LEDs, *Inorg. Chem.*, **2015**, 54, 1462-1473.

[110] Escudero, A., Carrillo-Carrión, C., Zyuzin, M.V., Ashraf, S., Hartmann, R., Núñez, N.O., Ocaña, M., Parak, W.J., Synthesis and Functionalization of Monodisperse Near-ultraviolet and Visible Excitable Multifunctional Eu^{3+}, Bi^{3+}:$REVO_4$ Nanophosphors for Bioimaging and Biosensing Applications, *Nanoscale*, **2016**, 8, 12221-12236.

[111] Chen, D., Yu, Y., Huang, P., Lin, H., Shan, Z., Zeng, L., Yang, A., Wang, Y., Color-tunable luminescence for Bi^{3+}/Ln^{3+}:YVO_4 (Ln=Eu, Sm, Dy, Ho) nanophosphors excitable by near-ultraviolet light, *Phys. Chem. Chem. Phys.*, **2010**, 12, 7775-7778.

[112] Huang, X.Y., Wang, J.X., Yu, D.C., Ye, S., Zhang, Q.Y., Sun, X.W., Spectral conversion for solar cell efficiency enhancement using YVO_4:Bi^{3+},Ln^{3+} (Ln=Dy, Er, Ho, Eu, Sm, and Yb) phosphors, *J. Appl. Phys.*, **2011**, 109, 113526.

[113] Ju, G., Hu, Y., Chen, L., Wang, X., Mu, Z., Wu, H., Kang, F., Luminescence properties of Y_2O_3:Bi^{3+}, Ln^{3+} (Ln=Sm, Eu, Dy, Er, Ho) and the sensitization of Ln^{3+} by Bi^{3+}, *J. Lumin*., **2012**, 132, 1853-1859.

[114] Wibowo, A. C., Vaughn, S. A., Smith, M. D., zur Loye, H.-C., Novel bismuth and lead coordination polymers synthesized with pyridine-2,5-dicarboxylates: two single component "white" light emitting phosphors, *Inorg. Chem.*, **2010**, 49, 11001-11008.

[115] Back, M., Trave, E., Mazzucco, N., Riello, P., Benedetti, A., Tuning the upconversion light emission by bandgap engineering in bismuth oxide-based upconverting nanoparticles, *Nanoscale*, **2017**, 9, 6353-6361.

[116] Back, M., Trave, E., Riello, P., Joos, J. J., Insight into the upconversion luminescence of highly efficient lanthanide-doped Bi_2O_3 nanoparticles, *The J. of Phys. Chem. C*, **2018**, 122, 13.

[117] Lei, P., Zhang, P., Yuan, Q., Wang, Z., Dong, L., Song, S., Xu, X., Liu, X., Feng, J., Zhang, H., Yb^{3+}/Er^{3+}-Codoped Bi_2O_3 Nanospheres: Probe for Upconversion Luminescence Imaging and Binary Contrast Agent for Computed Tomography Imaging, *ACS Appl. Mater. Interfaces*, **2015**, 7, 26346–26354.

[118] Huang, S., Zhu, N., Lou, Z., Gu, L., Miao, C., Yuan, H., Shan, A., Near-infrared photocatalysts of $BiVO_4/CaF_2$:Er^{3+}, Tm^{3+}, Yb^{3+} with enhanced upconversion properties, *Nanoscale*, **2014**, 6, 1362-1368.

[119] Singh, S., Lakshminarayana, G., Sharma, M., Excitation Induced Tunable Emission in Ce^{3+}/Eu^{3+} Codoped $BiPO_4$ Nanophosphors, *Journal of Spectroscopy*, **2015**.

[120] Naidu, B. S., Vishwanadh, B., Sudarsan, V., Vatsa, R. K., $BiPO_4$: A better host for doping lanthanide ions, *Dalton Transactions*, **2012**, 41(11), 3194.

[121] Hernández, J.A., Camarillo, E., Loro, H., Murrieta, H.S., $Bi_4Ge_3O_{12}$:Nd^{3+} and $Bi_{12}SiO_{20}$:Nd^{3+}: A comparative spectroscopic study, *Journal of Alloys and Compounds*, **2001**, 323–324, 714-717.

[122] Kumari, P., Dwivedi, Y., Vibrational and spectroscopic analysis of white light emitting Bi_2SiO_5 nanophosphor, *Spectrochimica Acta Part A: Molecular and Biomolecular Spectroscopy*, **2017**, 180, 79–84.

[123] El-Inany, G. A., Seleem, H. S., Helmy, R., Abdel-Salam, M. O., Saif, M., Synthesis and characterization of Sm^{3+} :$Bi_4Si_3O_{12}$ and dispersed into silica nanophosphor for sensing application, *Journal of Molecular Structure*, **2018**, 1173, 111–119.

[124] Lira, A.C., Camarillo, I., Camarillo, E., Ramos, F., Flores, M., Caldiño, U., Spectroscopic characterization of Er^{3+} transitions in $Bi_4Si_3O_{12}$, *J. Phys.: Condens. Matter*, **2004**, 16, 5925-5936.

[125] Wei, T., Zhang, T.B., Ma, Y.J., Xie, Y.F., Zhao, C.Z., Yang, F.M., Xiao, H.Y., Zhao, Y., Upconversion photoluminescence and temperature sensing properties of Er^{3+}-doped $Bi_4Ti_3O_{12}$ nanoparticles with good water-resistance performance, *RSC Adv.*, **2016**, 6, 7643-7652.

[126] Lira, A.C., Ramírez, M.O., García Solé, J., Caldiño, U., Photoluminescence of $Bi_4Si_3O_{12}$:Er^{3+} crystal excited in the commercial laser diode emission region, *Opt. Mater.*, **2007**, 29, 605-609.

[127] Lira, A.C., Martín-Rodríguez, E., Martínez-Martínez, R., Camarillo, I., Muñoz, G.H., García Solé, J., Caldiño, U., Spectroscopy of the $Bi_4Si_3O_{12}$:Er^{3+} glass for optical amplification and laser application, *Opt. Mater.*, **2010**, 32, 1266-1273.

[128] Yang, B., Xu, J., Zhang, Y., Chu, Y., Wang, M., Wen, Y., A yellow emitting phosphor Dy:$Bi_4Si_3O_{12}$ crystal for LED application, *Opt. Mater.*, **2014**, 135, 176-179.

[129] Wei, Q., Liu, G., Zhou, Z., Wan, J., Wang, J., Liu, Q., Combinatorial discovery of self-mixing phosphors $Bi_{4(1-x)}Si_3O_{12}$;RE_{4x}^{3+} (RE^{3+}=Dy^{3+}, Eu^{3+}) for direct white light emission, *RSC Adv.*, **2015**, 5, 85862-85871.

[130] Chen, F., Ju, M., Kuang, X., Yeung, Y., Insights into the Microstructure and Transition Mechanism for Nd^{3+}-Doped $Bi_4Si_3O_{12}$: A Promising Near-Infrared Laser Material, *Inorganic Chemistry*, **2018**, 57(8), 4563–4570.

[131] Mahmoud, H., Saif, M., Rania, F.I., Novel multi-functional Pr^{3+}:$Bi_{12}SiO_{20}$ luminescent nano-sensor for latent human prints, iron ions in drinking water and anti-counterfeiting application, *Journal of Alloys and Compounds*, **2019**, 805.

[132] Bidgoli, S.H., Attar, A.S., Bafandeh, M.R., Structural and Optical Properties of Sr-Modified Bismuth Silicate Nanostructured Films Synthesized by Sol Gel Method, *Journal of Nanostructures*, **2017**, 7(4), 258-265.

[133] Gunter, P., Holography, coherent light amplification and optical phase conjugation with photorefractive materials, *Phys. Rep*., **1982**, 93(4), 199-299.

[134] Mosquera, L., Oliveira, I., Frejlich, J., Hernandes, AC., Lanfredi, S., Carvalho, J.F., Dark conductivity, photoconductivity, and lightinduced absorption in photorefractive sillenite crystals, J. *Appl. Phys*., **2001**, 90(6), 2635-41.

[135] Burkov, V.I., Kargin, Y.F., Volkov, V.V., Zubovich, N.Y., Spectroscopic and chirooptical properties of doped sillenite crystals. 1. Absorption and circular-dichroism spectra of $Bi_{12}SiO_{20}$ and $Bi_{12}TiO_{20}$ crystals doped with phosphorus and vanadium, *Inorg. Mater*., **1994**, 30, 997-1001.

[136] Xie, H., Jia, C., Jianga, Y., Wang, X., Synthesis of $Bi_4Si_3O_{12}$ powders by a sol-gel method, *Mater. Chem. Phys*., **2012**, 133, 1003-1005.

[137] Armelao, L., Colombo, P., Fabrizio, M., Synthesis of Bi_2O_3 and $Bi_4(SiO_4)_3$ thin films by the sol-gel method, *J. Sol. Gel Sci. Technol*., **1998**, 13, 213-217.

[138] Kovács, L., Raymond, S.G., Luff, B.J., Peter, A., Townsend, P.D., Thermoluminescence spectra of eulytine $Bi_4Si_3O_{12}$ and $Bi_4Ge_3O_{12}$ single crystals, *J. Lumin*., **1994**, 60-61, 574-577.

[139] Fei, Y., Fan, S., Sun, R., Ishii, M., Study on phase diagram of Bi_2O_3-SiO_2 system for Bridgman growth of $Bi_4Si_3O_{12}$ single crystal, *Prog. Cryst. Growth. Charact.*, **2000**, 40, 183–8.

[140] Yiting, F., Shiji, F., Renying, S., Ishii, M., Study on phase diagram of Bi_2O_3-SiO_2 system for Bridgman growth of $Bi_4Si_3O_{12}$ single crystal, *Prog. Cryst. Growth Ch*., **2000**, 40, 183.

[141] Zhereb, V.P., Skorikov, V. M., Effect of Metastable Phases on the Structural Perfection of Single Crystals of Stable Bismuth Oxide Compounds, *Inorg. Mater*., **2003**, 39(11), 1181-1187.

[142] M.V. Lalic, S.O. Souza, The first-principles study of electronic and optical properties of BGO and BSO scintillators, *Opt. Mater*., **2008**, 30(7), 1189-1192.

[143] L. G. Sillén, *Ark. Kemi, Mineral. Geol*., **1937**, 12A, 1.

[144] Aurivillius, B., Sillén, L. G., The structure of γ-Bi_2O_3, *Nature*, **1945**, 155, 305–306.

[145] G. Gattow and H. Schroder, Über Wismutoxide. III. Die Kristallstruktur der Hochtemperaturmodifikation von Wismut(III)-oxid (δ-Bi_2O_3), *Z. Anorg. Allg. Chem*., **1962**, 318, 176–189.

[146] M. Weber, M. Schlesinger and M. Mehring, Evaluation of Synthetic Methods for Bismuth(III) Oxide Polymorphs: Formation of Binary versus Ternary Oxides, *Cryst. Growth Des*., **2016**, 16(10), 5678–5688.

[147] Wang, Y., He, R., Yang, M., Wen, T., Zhang, H., Liang, J., Lin, Z., Wang, Y., Li, G., Lin, J., Hydrothermal growths, optical features and first-principles calculations of sillenite-type crystals comprising discrete MO_4 tetrahedra, *Cryst. Eng. Comm.*, **2012**, 14(3), 1063–1068.

[148] Nakagawa, K., Kajita, N., Chen, J., Minemoto, T., Measurement of the electrogyratory coefficient in photorefractive $Bi_{12}SiO_{20}$ crystal, *J. Appl. Phys*., **1991**, 69, 954.

[149] Ricardo, J., Muramatsu, M., Palácios, F., Gesualdi, M. R. R., Valin, J. L., Prieto Lopez, M. A., Digital holographic microscopy with photorefractive sillenite $Bi_{12}SiO_{20}$ crystals, *Opt. Lasers Eng.*, **2013**, 51, 949–952.

[150] Biaggio, I., Hellwarth, R. W., Partanen, J. P., Band mobility of photoexcited electrons in $Bi_{12}SiO_{20}$, *Phys. Rev. Lett*., **1997**, 78, 891–894.

[151] Mythili, P., Kanagasekaran, T., Bhagavannarayana, G., Gopalakrishnan, R., Studies on crystal growth, optical and electrical characterization of pure and Dy-doped bismuth silicate single crystals, *J. Cryst. Growth*, **2012**, 338(1), 222–227.

[152] Lira, A. C., Caldiño, U., Ramírez, M. O., Sanz-García, J. A., Bausá, L. E., Site-selective spectroscopy of Er^{3+} ions in the $Bi_{12}SiO_{20}$ piezoelectric crystal, J. *Phys.: Condens. Matter*, **2001**, 13, 11067–11076.

[153] Hu, Y., Sinclair, D. C., Relaxor-like dielectric behaviour in stoichiometric sillenite $Bi_{12}SiO_{20}$, *Chem. Mater*., **2013**, 25, 48–54.

[154] Hou, D., Hu, X., Wen, Y., Shan, B., Hu, P., Xiong, X., Qiao, Y., Huang, Y., Electrospun sillenite $Bi_{12}MO_{20}$ (M=Ti, Ge, Si) nanofibers: general synthesis, band structure, and photocatalytic activity, *Phys. Chem. Chem. Phys*., **2013**, 15, 20698–20705.

[155] Han, Q., Zhang, J., Wang, X. Zhu, J., Preparing $Bi_{12}SiO_{20}$ crystals at low temperature through nontopotactic solid-state transformation and improving its photocatalytic activity by etching, *J. Mater. Chem. A*, **2015**, 3, 7413–7421.

[156] Fouskova, A, Cross, L.E., Dielectric properties of bismuth titanate, *J. of Appl. Phys.*, **1970**, 41(7), 2834-2838.

[157] Takenaka, T., Sakata, K., Grain orientation effects on electrical properties of bismuth layer structured ferroelectric $Pb_{1-x}(Na,Ce)_x/2Bi_4Ti_4O_{15}$ solid solution, *J. Appl. Phys*., **1984**, 55(4), 1092-9.

[158] Klebansky, E.O., Kudzin, A.Y., Pasalskii, V.M., Plyaka, S.N., Sadovskaya, L.Y., Sokolyanskii, G.K., Thin sol-gel bismuth silicate films, *Phys. Solid State*, **1999**, 41(6), 913-5.

[159] Yamaguchi, M., Nagatomo, T., Masuda, Y., Preparation of $Bi_4Ti_3O_{12}/Bi_2SiO_5/Si$ structures derived by metal organic decomposition technique, *Jpn. J. Appl. Phys*., **2001**, 40(9B), 5559-63.

[160] Sun, S, Lu, P, Fuierer, P.A., Oriented bismuth titanate thin films by single-solid-source metal-organic chemical vapour deposition, *J. Cryst. Growth*, **1999**, 205(1), 177-84.

[161] Wills, L.A., Feil, W.A., Wessels, B.W., Tonge, L.M., Marks, T.J., Growth studies of ferroelectric oxide layers prepared by organometallic chemical vapor deposition, *J. Cryst. Growth*, **1991**, 107(1-4), 712-5.

[162] Kim, J., Tsurumi, T., Kamiya, T., Daimon, M., Growth of bismuth silicate films on Si and its dielectric properties, *J. Appl. Phys*., **1994**, 75(6), 2924-8.

[163] Sato, Y., Shoji, I., Kurimura, S., Taira, T., Senguttuvan, N., Ishii, M., Koboyashi, M., Optical absorption and emission spectroscopy of $Nd:Bi_4Si_3O_{12}$ grown by Bridgeman method, *Adv. Solid State Lasers*, **2001**, 50, 67-71.

[164] Kobayashi, M., Ishii, M., Harada K., and Yamaga, I., Bismuth silicate $Bi_4Si_3O_{12}$, a faster scintillator than bismuth germinate $Bi_4Ge_3O_{12}$, *Nucl. Instrum. Methods Phys. Res*., **1996**, 372, 45–50.

[165] Yiting, F., Renying, S., Shiji F., Jiayue, X., Vertical Bridgman growth and scintillation properties of doped $Bi_4Si_3O_{12}$ crystals, *Cryst. Res. Technol*., **1999**, 34, 1149–1156**.**

[166] Jiayue, X., Bobo, Y., Yan, Z., Development of doped $Bi_4Si_3O_{12}$ crystals for scintillation, laser and LED applications, *Mater. Focus*, **2015**, 4, 20–27.

[167] Kobayashi, M., Harada, K., Hirose, Y., Ishii, M., Yamaga, I., *Nucl. Instrum. Meth. A*, **1997**, 400, 392.

[168] Sun, L., Gao, F., Huang, Q., White upconversion photoluminescence for Er^{3+}–Tm^{3+}–Yb^{3+} tri-codoped bismuth titanate ferroelectric thin films, *J. Alloys Compd*., **2014**, 588, 158–162.

[169] Kumari, P., Dwivedi, Y., Bright emission via energy transfer from Dy to Tb in Bi_2SiO_5 nanophosphor, **2018**, *Optical Materials*, 75, 31–37.

[170] Dai, X.-J., Luo, Y.-S., Fu, S.-Y., Chen, W.-Q., Lu, Y., Facile hydrothermal synthesis of 3D hierarchical Bi_2SiO_5 nanoflowers and their luminescent properties, *Solid State Sci*., **2010**, 12, 637–642.

[171] Wan, Z., Zhang, G., Synthesis and facet-dependent enhanced photocatalytic activity of Bi_2SiO_5/AgI nanoplate photocatalysts, *J. Mater. Chem. A3*, **2015**, 16737-16745.

[172] Cheng, G., Xiong, J., Yang, H., Lu, Z., Chen, R., Facile solvothermal synthesis of uniform sponge-like Bi_2SiO_5 hierarchical nanostructure and its application in Cr(VI) removal, *Mater. Lett*., **2012**, 25-28.

[173] Yamaguchi, M., Hiraki, K., Nagatomo, T., Masuda, Y., Preparation and properties of Bi_2SiO_5/Si structures, *Jpn. J. Appl. Phys*., **2000**, 39, 5512–5516.

[174] Taniguchi, H., Kuwabara, A., Kim, J., Kim, Y., Moriwake, H., Kim, S., T. Hoshiyama, T. Koyama, S. Mori, M. Takata, H. Hosono, Y. Inaguma and M. Itoh, Ferroelectricity driven by twisting of silicate tetrahedral chains, *Angew. Chem., Int. Ed*., **2013**, 52, 8088–8092.

[175] Kim, Y., Kim, J., Fujiwara, A., Taniguchi, H., Kim, S., Tanaka, H., Sugimoto, K., Kato, K., Itoh, M., Hosono, H., Takata, M., Hierarchical dielectric orders in layered ferroelectrics Bi_2SiO_5, *IUCrJ*, **2014**, 1, 160–164.

[176] Taniguchi, H., Nakane, T., Nagai, T., Moriyoshi, C., Kuroiwa, Y., Kuwabara, A., Mizumaki, M., Nitta, K., Okazaki, R., Terasaki, I., Heterovalent Pb-substitution of ferroelectric bismuth silicate Bi_2SiO_5, *J. Mater. Chem. C*, **2016**, 4, 3168–3174

[177] Seol, D., Taniguchi, H., Hwang, J.-Y., Itoh, M., Shin, H., Kim, S.W., Kim, Y., Strong anisotropy of ferroelectricity in lead-free bismuth silicate, *Nanoscale*, **2015**, 7, 11561–11565.

[178] Dai, X.J., Luo, Y.S., Fu, S.Y., Chen, W.Q., Lu, Y., Facile hydrothermal synthesis of 3D hierarchical Bi_2SiO_5 nanoflowers and their luminescent properties, *Solid State Sciences*, **2010**, 12(4), 637-642.

[179] Abbass, A.E., Swart, H.C., Coetsee, E., Kroon, R. E., White luminescence from sol–gel silica doped with silver, *J. Am. Ceram. Soc*., **2015**, 76(3), 1–5.

[180] Jiang, H., Wang, X., Wang, L., Yu, C., Mu, J., Molten Salt Synthesis of Bi_2SiO_5 Powders Based on Uniform Experiment, *Mater. Manuf. Processes*, **2013**, 28, 336- 340.

[181] Lu, J., Wang, X., Yu, C., Xu, Y., Bi_2SiO_5 nanosheets prepared by molten salt method, *J. Mater. Sci.-Mater. Electron*., **2012**, 23(9), 1770–1773.

[182] Chu, Y., Zhang, Q., Li, Y., Liu, Z., Xu, J., Zeng, H., Wang, H., Hydrothermal synthesis of $Bi_4Ge_3O_{12}$:Eu^{3+} phosphors with high thermal stability and enhanced photoluminescence property, *J. Alloy. Compd*, **2017**, 693, 308–314.

[183] Macedo, Z.S., Hernandes, A.C., Laser sintering of bismuth germanate ($Bi_4Ge_3O_{12}$) ceramics, *J. Am. Ceram. Soc*., **2002**, 85, 1870–1872.

[184] Xiang, D., Chu, Y., Xiao, X., Xu, J., Zhang, Z., Liu, Z., Zhang, Y., Yang, B., Tunable luminescence and energy transfer of Dy^{3+}-activated $Bi_4Si_3O_{12}$-$Bi_4Ge_3O_{12}$ pseudo-system phosphor for warm white-emitting, *Journal of Solid-State Chemistry*, **2018**, 268, 130–135.

[185] Sammes, N. M., Tompsett, G. A., Näfe, H., Aldinger, F., Bismuth Based Oxide Electrolytes - Sructure and Ionic Conductivity, *J. Eur. Ceram. Soc*., **1999**, 19, 1801-1826.

[186] Drache, M., Roussel, P., Wignacourt, J.-P., Structures of Oxide Mobility in Bi-Ln-O Materials: Heritage of Bi_2O_3, *Chem. Rev*., **2007**, 107, 80-96.

CHAPTER 5

Synthesis and Characterization of Lanthanide-doped Bismuth silicate (nano)systems as innovative platforms for multi-modal imaging

ABSTRACT: Bismuth-based nanocrystalline particles are recently attracting much attention as hosts for luminescent ions, such as lanthanides (Ln), for many applications. Thanks to their low toxicity and reduced costs they have been proposed for lighting devices and for disparate biological applications.

Here, we report the synthesis of uniform crystalline lanthanide-doped (Yb, Er, Ho and Tm) Bi_2SiO_5 upconverting nanoparticles embedded into a silica shell of a controlled thickness (Bi_2SiO_5:Ln@SiO_2) for the design of nanophosphors emitting in the VIS range, as versatile multi-modal imaging probes and potentially reliable ratiometric optical thermometers. Uniform and monodispersed Bi_2O_3 NPs were obtained, subsequently the fine control of the SiO_2 shell thickness was modelled on a theoretical and experimental approach. The formation of the Bi_2SiO_5 single phase, as a consequence of a thermal treatment, triggered by the local reactivity between Bi_2O_3 and SiO_2, in the Bi_2O_3@SiO_2 system, leads to a double layered Bi_2SiO_5@SiO_2 hollow nanosystem. A strategy for the control of the chromaticity emission was achieved through the accurate choice of the dopants and of their relative concentration.

Furthermore, NIR-emitting Nd^{3+}-doped bismuth-silicate (nano)systems were synthetized for the same purposes and thoroughly characterized: Bi_2SiO_5:Nd@SiO_2 (i) and $Bi_4Si_3O_{12}$:Nd@SiO_2 (ii) NPs, and bulk $Bi_{12}SiO_{20}$:Nd (iii). These three compounds form the Bi_2O_3-SiO_2 binary system (see Fig.1 in Chapter 4) and are the metastable Bi_2SiO_5, the eulytite $Bi_4Si_3O_{12}$ and the sillenite $Bi_{12}SiO_{20}$. Nd-doped Bi_2SiO_5 (i) and $Bi_4Si_3O_{12}$ (ii) nanoparticles were obtained via the hydrothermal route previously described for Ln^{3+}-doped nanoparticles, whereas the $Bi_{12}SiO_{20}$ (iii) bulk phase was synthetized through a solid-state reaction.

5.1 $Bi_2SiO_5:Ln^{3+}@SiO_2$ core-shell UCNPs

Bismuth-based materials are characterized by interesting properties triggered by the high refractive indexes, low bandgap energies and the stereochemical activity of the $6s^2$ lone-pair electrons (LPE) of Bi^{3+} [1], funding application in many different fields such as fuel cells[2], UV filters[3,4] and water splitting[5,6]. Recently, bismuth-based compounds also demonstrated to be very appealing hosts for luminescent ions such as lanthanides and transition metals, despite their narrow bandgap, showing potential applications as luminescent probes[7-10] and optical thermometers[11,12]. In addition, bismuth-based nanosystems are particularly suitable as probes for multi-imaging, due to the large attenuation coefficient of Bi (5.74 cm^2g^{-1} at about 100 keV) [13-16]. This makes them promising candidates as contrast agents for multimodal clinical imaging, for example for computed X-ray tomography[17,18], (CT), single-photon emission CT[19] (SPECT) and photoacoustic tomography[20] (PAT). Recently, Bi_2SiO_5 was proposed as a suitable host for upconverting systems[9], showing the stabilization of this metastable phase by means of a synthetic procedure involving the impregnation of mesoporous silica nanoparticles, that unfortunately lead to agglomerated and inhomogeneous nanoparticles, limiting their real applicability.

As seen in Chapter 2, Lanthanide ions (Ln^{3+}) are a well-known family of luminescent ions finding applications in a variety of optical fields moving from telecommunications,[21-24] lasing[25,26] and lighting[27,28] to bioimaging[29,30], nanothermometry[31-34] and anticounterfeiting[35,36], to name a few. In the recent years, a lot of interest was gained by the potential of luminescent nanothermometry to probe intracellular temperature[37,38] or to map the dissipation in microelectronic circuits[39] but also to locally probe phase transition temperatures[40] and to measure *in-situ* thermal gradients in catalytic reactions[41].

The uniformity of the nanoparticles is still a critical parameter for many families of compounds, especially when speaking of metal oxides. Thus, the development of synthetic procedures for highly monodispersed nanoparticles with homogeneous shape is a challenge. The reproducibility of the method proposed here was tested by preparing the samples three times for each step. Figure 1 summarizes the synthetic strategy adopted: (1) synthesis of monodisperse Ln-doped Bi_2O_3 NPs, (2) silica shell growth and (3) thermal treatment for the stabilization of the desired system, taking advantage of the diffusion and reactivity properties between the Bi_2O_3 core and the silica shell. Complete structural, morphological and optical investigations were conducted on this system.

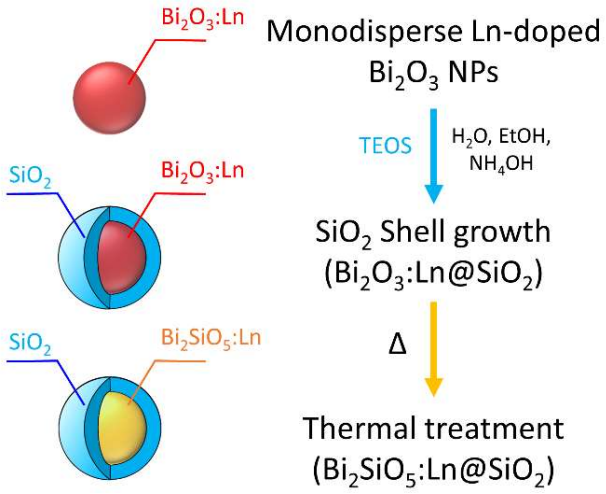

Fig.1 Schematic illustration of the synthesis procedure for lanthanide-doped Bi_2SiO_5@SiO_2.

5.1.1 Sample preparation

Bi_2O_3 NPs

Materials

Bismuth(III) nitrate pentahydrate ($Bi(NO_3)_3 \cdot 5H_2O$, 99.9%), Ytterbium(III) nitrate pentahydrate ($Yb(NO_3)_3 \cdot 5H_2O$, 99.9%), Erbium(III) nitrate pentahydrate ($Er(NO_3)_3 \cdot 5H_2O$, 99.9%), Holmium(III) nitrate pentahydrate ($Ho(NO_3)_3 \cdot 5H_2O$, 99.9%), Thulium(III) nitrate pentahydrate ($Tm(NO_3)_3 \cdot 5H_2O$, 99.9%), Sodium hydroxide (NaOH, >99%), Potassium hydroxide (KOH, ≥85%), ammonium hydroxide (NH_4OH), poly(vinylpyrrolidone) (PVP, MW = 10, 29, 40, 360 and 1300 kg/mol)) and ethylene glycol (EG, 99.8%) were purchased from Sigma Aldrich.
Urea ($CO(NH_2)_2$, >99%) was obtained from Fluka Analytical. Nitric acid (HNO_3, 65%) was purchased from Carlo Erba. All the chemicals were reagent grade and used without further purification.

Synthesis of Ln^{3+}-doped Bi_2O_3 NPs

Uniform Bi_2O_3 and Ln^{3+}-doped Bi_2O_3 NPs were prepared by means of a modification of the hydrothermal synthesis reported by Qin *et al.*[42]. In a typical synthetic process, a $Bi(NO_3)_3 \cdot 5H_2O$ stock solution (75 mM) was prepared by dissolution in HNO_3 (1 M). Subsequently, a certain quantity of PVP (7.5 µmol) was dissolved into 20 mL of the stock solution under magnetic stirring. PVPs with different molecular weights were tested. Separately, 5.4 mmol of the precipitant agent, either $CO(NH)_2$, NaOH, KOH or NH_4OH, were dissolved in EG (100 mL). Finally, the second solution was slowly poured into the first one. The mixture was stirred for a short time and then transferred into a stainless-steel autoclave with a Teflon liner. The autoclave was sealed and

maintained at 150°C for 3.5 h. The obtained products were centrifuged and washed 3 times with deionized water, once with mixed ethanol and water and once with ethanol only. Finally, the samples were dried for further characterizations. Various Ln^{3+} co-doped samples were prepared, by substitution of the adequate volume of the Bismuth precursor solution with the same volume of the desired Ln^{3+} solution in HNO_3. For this reason, bismuth and lanthanides stock solutions in HNO_3 were prepared with the same molarity. The samples produced are listed in Table 1.

Sample	Reactant	Yb^{3+} %at.	Er^{3+} %at.	Ho^{3+} %at.	Tm^{3+} %at.
#1	$CO(NH_2)_2$	-	0.5	-	-
#2	$CO(NH_2)_2$	-	1	-	-
#3	$CO(NH_2)_2$	-	2	-	-
#4	$CO(NH_2)_2$	-	4	-	-
#5	$CO(NH_2)_2$	-	6	-	-
#6	$CO(NH_2)_2$	-	8	-	-
#7	$CO(NH_2)_2$	-	12	-	-
#8	$CO(NH_2)_2$	6	1	-	-
#9	$CO(NH_2)_2$	10	1	-	-
#10	$CO(NH_2)_2$	6	-	1	-
#11	$CO(NH_2)_2$	6	-	-	0.5
#12	$CO(NH_2)_2$	6	0.5	-	0.5
#13	$CO(NH_2)_2$	6	1	-	0.5
#14	$CO(NH_2)_2$	6	-	1	0.5
#15	$CO(NH_2)_2$	6	1	0.5	0.5
#16	NaOH	-	5		
#17	NaOH	-	10	-	-
#18	NaOH	6	1	-	-
#19	NaOH	10	1	-	-

Table 1. Synthetized samples of Ln^{3+}-doped Bi_2O_3 NPs

Bi_2O_3@SiO_2 NPs

Materials

Ammonia solution (NH_3, 30%) was purchased from Carlo Erba. Ethanol anhydrous EtOH (CH_3CH_2OH, ≥99.5%) and Tetraethoxysilane TEOS ($Si(OC_2H_5)_4$, 98%). were purchased from Sigma Aldrich.
All the chemicals were reagent grade and used without further purification.

Synthesis of silica coating over bismuth oxide nanoparticles

For thin silica coating on the surface of the particles, 0.3 g of Bi_2O_3 NPs were ultrasonically and homogeneously dispersed in the mixture of 240 ml ethanol, 60 ml deionized water and 6 ml concentrated NH_3 solution (30%). Finally, TEOS was added

dropwise to the mixture in subsequent aliquots at precise time intervals. Different amounts of TEOS (0.160, 0.320, 0.640, 1.280, 2.560, 3.840 mL), with TEOS (μL):Bi_2O_3 (mg) ratio of about 0.5, 1, 2, 4, 8 and 12, were tested to obtain coatings of increasing thickness.
After stirring the mixture at room temperature for 6 h, the silica coated Bi_2O_3 particles were centrifuged and washed 3 times with ethanol, then dried at room temperature.

Bi_2SiO_5@SiO_2 NPs

To obtain the desired phase, the silica coated Bi_2O_3 nanoparticles were calcined in air for 2 hours. Different temperatures (namely 400, 500, 600 and 700° C) were tested.

5.1.2 Morphological and structural analysis

Hydrothermal synthesis of Bi_2O_3 NPs: Key parameters

Size and morphology of the obtained products were investigated by means of both scanning and transmission electron microscopy (SEM and TEM). By changing the precipitant agent and keeping PVP molecular weight constant to 40 kg/mol, the nanoparticles size showed high variability, moving from a distribution of nanoparticles with a diameter of 110 ± 15 nm with KOH (Fig.2a), to 120 ± 10 nm with NaOH (Fig.2b), 130 ± 10 nm with NH_4OH (Fig.2c) and 180 ± 20 nm when using urea (Fig.2d). As it can be evinced, NPs with inhomogeneous size distributions are obtained when using KOH or NH_4OH (Fig.2 a, c). This led to choose NaOH and urea as preferred precipitant agents (Fig.2 b, d). Moreover, also the effect of PVP molecular weight was investigated, either using NaOH (Fig.3 a, b, c, d) or urea (Fig.3 e, f, g, h) as precipitant agent. As can be observed in FE-SEM images, both the series of samples showed increasing mean size when increasing the MW of the capping agent.
It is worth noting that, despite the big efforts devoted in the last decades to the development of new strategies for colloidal nanosystems, the basic mechanisms for the formation of many NPs are still not completely clear. As reported by Thanh *et al.*[43], there is a lack of studies in particular for the growth of metal oxide NCs. Qin *et al*[42]. suggested a mechanism for the formation of the bismuth oxide nanoparticles consisting in a first step (i) where Bi-PVP complexes are formed through the coordination bridges between Bi^{3+} and the carbonyl oxygen of PVP, while the remaining PVP forms micelles encapsulating Bi-PVP complexes[44,45], and a second step (ii) in which the complexes could release Bi^{3+} which react with OH^- ions provided by the precipitant agent, slowing down the nucleation and consequently the crystal growth and leading to the formation of tiny primary nanoparticles, that subsequently aggregate to grow bigger secondary particles formed by by numerous interconnected nanospheres. The role of PVP as stabilizer also prevents a quick aggregation, modulating the size of Bi_2O_3 nanospheres[46]. The effect of PVP molecular weight on the size of nanoparticles is probably due to the increasing viscosity of the reaction system. However, the

underlying mechanism is still unclear and further investigation is needed to unravel the exact process.

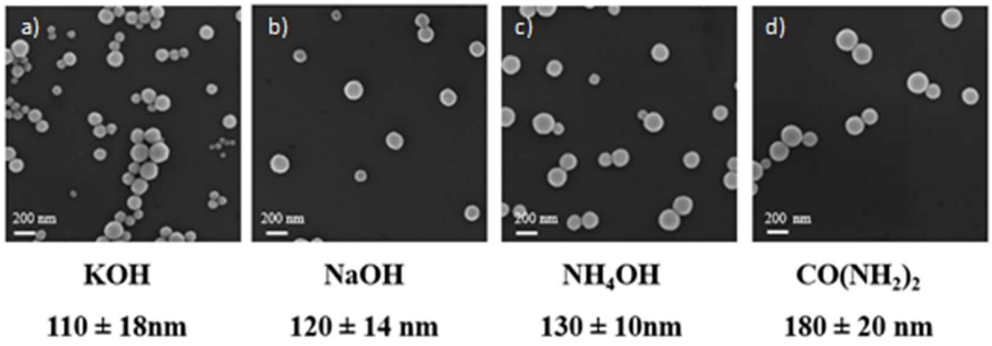

Fig.2 SEM images of Bi_2O_3 NPs synthetized by varying the precipitant agent: (a) KOH, (b) NaOH, (c) NH_4OH and (d) $CO(NH)_2$. Mean size of each sample (estimated by stastically sampling N=500 NPs) is indicated underneath SEM images.

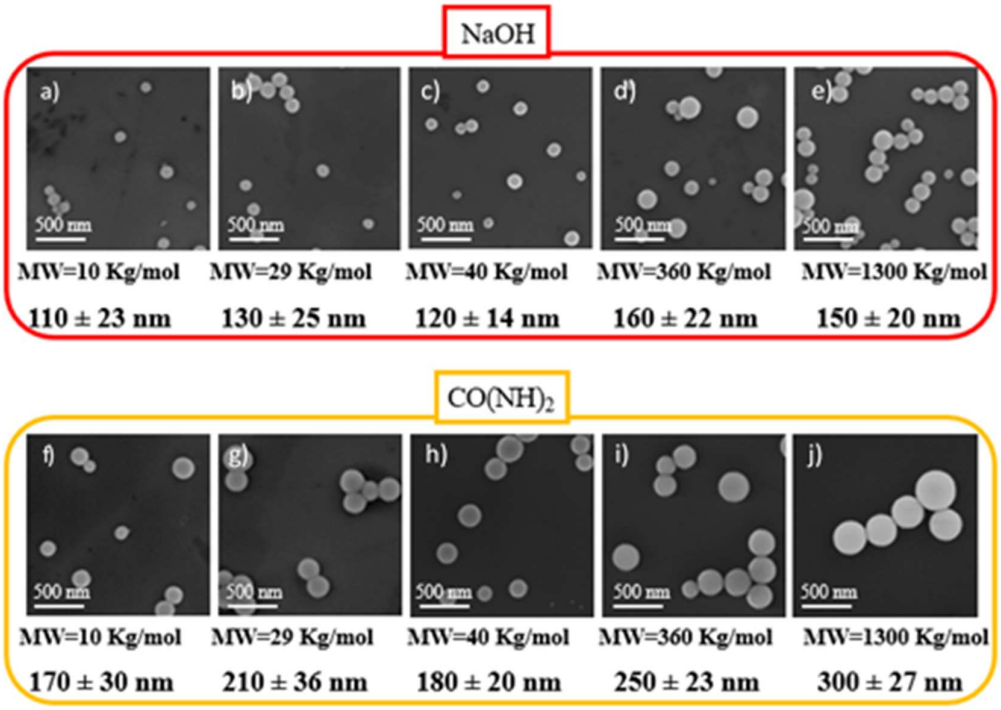

Fig.3 SEM images of two series of Bi_2O_3 NPs synthetized by varying the molecular weight of PVP capping agent, either with NaOH or Urea as precipitant agent: (a, f) MW=10 kg/mol, (b, g) MW=29 kg/mol, (c, h) MW=40 kg/mol, (d, i) MW=360 kg/mol and (e, j) MW=1300kg/mol. Mean size (estimated by statistically sampling N=500 NPs) is indicated underneath SEM images.

The smaller and bigger nanoparticles obtained by using respectively NaOH or urea (Fig.4 a, b) as precipitant agent to modify the pH of the reaction and using PVP40, were chosen and further investigated. The good monodispersion showed by both the samples (see size distributions bells in Fig.4 b, f) is a fundamental parameter for many biological applications. As shown by the TEM images in Fig.4 c, d, g and h, the nanoparticles are formed by primary small aggregates with a size of about 5 nm. It is interesting to note how the different precipitants lead to different NPs size, but the primary aggregates size seems to not be modified. This suggests the assembling process of the primary nanoparticles as the main factor determining the final nanoparticles size.

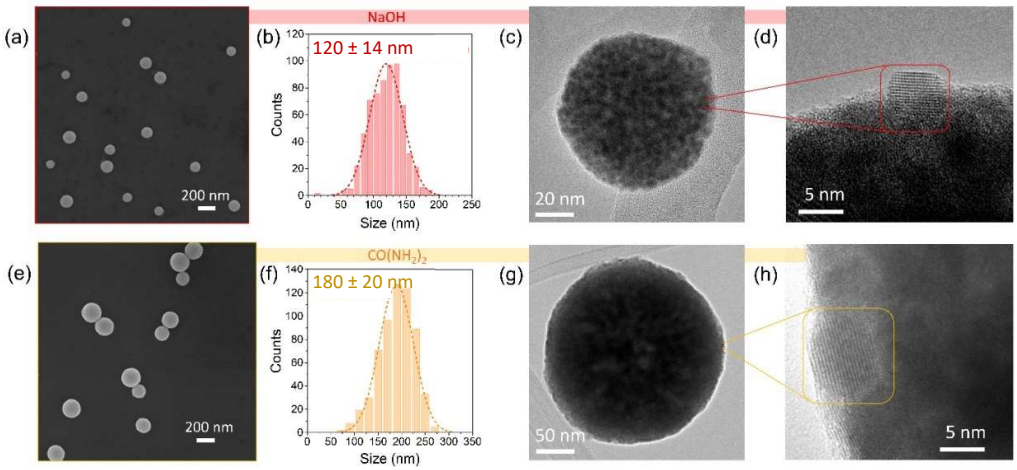

Fig.4 Uniform Bi_2O_3 NPs, synthetized with PVP with MW=40 kg/mol as capping agent and either with NaOH or Urea as precipitant agent: (a, e) SEM images, (b, f) size distributions (N=700), (c, g) single particle TEM and (d, h) HR-TEM images.

Contrary to what could be expected, based on the specific nanostructure of the obtained NPs, a small specific surface area and adsorptive capacity was determined by means of Nitrogen physisorption measurements for both NaOH and urea synthetized samples. The Brunauer Emmett Teller (BET) equation allowed to calculate a specific surface area of 13.9 and 7.7 m^2/g for NaOH and urea synthetized samples, respectively. As expected, nanospheres with the smallest size possess the largest BET surface area.
According to the IUPAC classification[47], both the absorption/desorption measurements follow the isothermal shape of type III (Fig.5 a, b), showing no hysterisis, typical of multilayer adsorption in non-porous solids. In addition, as a further confirmation of the non-porosity of the synthetized bismuth oxide NPs, a total pore volume of 0.1 and 0.04 cm^3/g was found for NaOH and urea samples, respectively.
Fig.6a shows FT-IR spectrum of Bi_2O_3 NPs, sintethized with urea. Peaks attributable to –C-H (2900 cm^{-1}), -C-H_2 (2850 cm^{-1}) and –C=O (1650 cm^{-1}) stretching vibrations and –C-H_2 (1450 cm^{-1}) bending vibrations could be identified, relatively to the presence of PVP on the surface of the nanoparticles. On the other hand, intermolecular

-O-H (broad peak at 3200 cm^{-1}), –C-OH (1250 cm^{-1}) and –C-H_2 stretching vibrations (2850 cm^{-1}) and–C-H_2 bending vibrations (1450 cm^{-1}) are imputable to the presence of unwashed ethylene glycol. The thermogravimetric analysis seems to confirm the presence of the two reagents. As can be observed in Fig.6b, the differential TG (red line) shows the peak corresponding to the onset of initial decomposition of ethylene glycol at 240°C and the peak relative to PVP decomposition at 350°C, that when coated on nanoparticles starts to decompose at lower temperatures respect to pure PVP, which decomposition usually happens at 380°C[48]. The registered total weight loss is of about 22%.

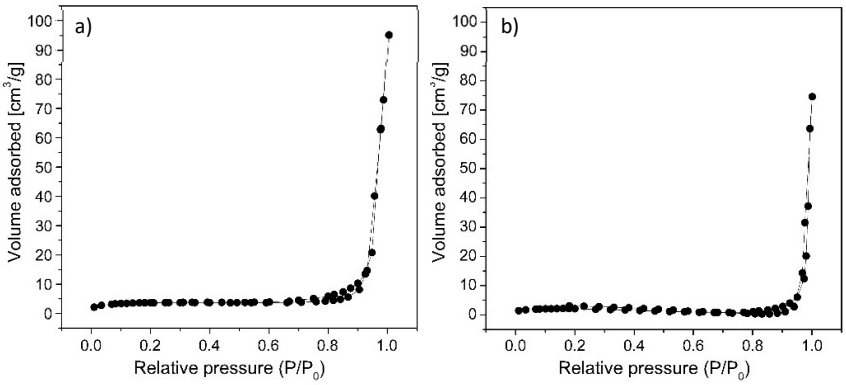

Fig.5 N_2 adsorption/desorption isothermal curves for Bi_2O_3 NPs, synthetized either with (a) NaOH or (b)urea as precipitant agent.

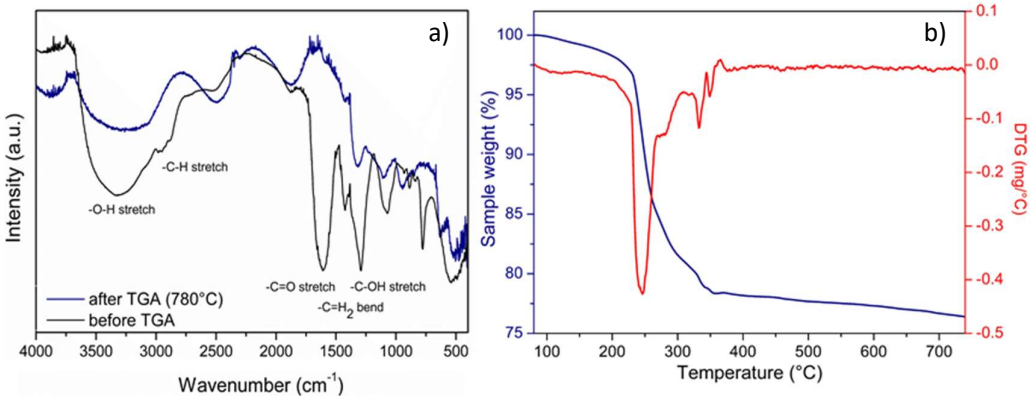

Fig.6 (a) FT-IR spectrum of Bi_2O_3 NPs before (black line) and after (blue line) the thermogravimetric analysis (780°C) showing the typical peaks for stretching and bending vibrations in EG and PVP, (b) TG (blue line) and DTG (red line) showing weight loss peaks relative to EG and PVP calcination at 240 and 350°C, respectively.

Fig.7 shows the XRPD pattern of the synthesized NPs. The broad peaks evidenced in the pattern could be related to an amorphous phase or to the broadening coming by the small size of the primary aggregates, even though the previously shown HR-TEM images (Fig.4 d, h) suggest the crystallinity of the aggregates of bismuth oxide.

However, at the present stage, it is difficult to unambiguously assign the Bi_2O_3 polymorph from the XRPD pattern.

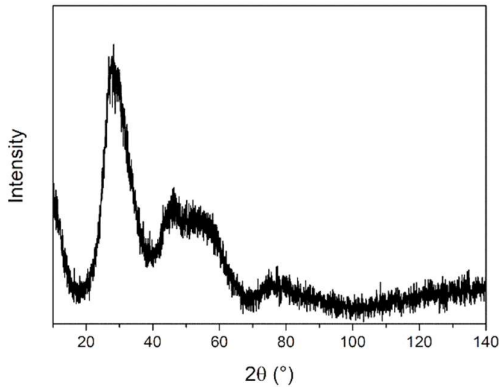

Fig.7 XRPD pattern of the synthetized Bi_2O_3 NPs.

For what concerns NPs synthetized with urea as the precipitant agent, the introduction of Er^{3+} ions into the hydrothermal reaction solution does not affect the nanoparticle growth up to 8 mol%, leaving morphology and size unchanged (see SEM images in Fig.8 and size distribution trend in Fig.9), while for higher concentrations the self-assembling process of the primary aggregates changes resulting in a modification of the spherical shape (see for instance SEM and HR-TEM images in Fig.10 a, b, c). However, as can be observed from the EDS spectra of a high-doped sample (Er^{3+} 12mol%), collected in different regions of the nanoparticle, the spines protruding from the spheres maintain the same composition as the core.

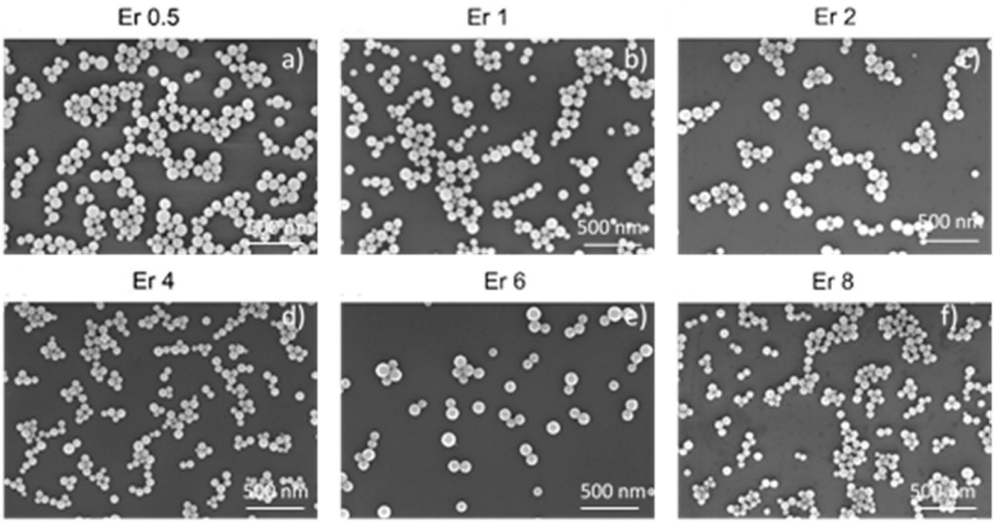

Fig.8 FE-SEM images of Er-doped Bi_2O_3 NPs, synthetized with urea as precipitant agent, with different at.% content of Er: (a) 0.5%, (b) 1%, (c) 2%, (d) 4%, (e) 6% and (d) 8%.

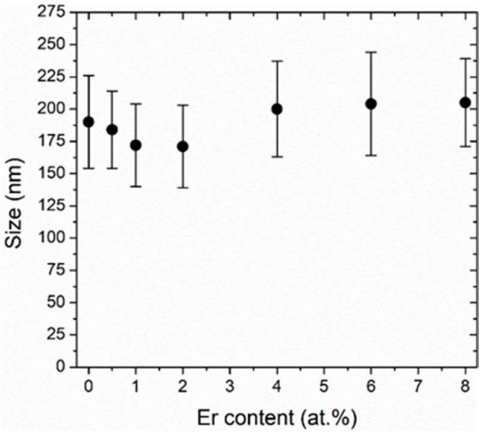

Fig.9 Size distributions of the Er-doped Bi_2O_3 NPs as a function of the Er content.

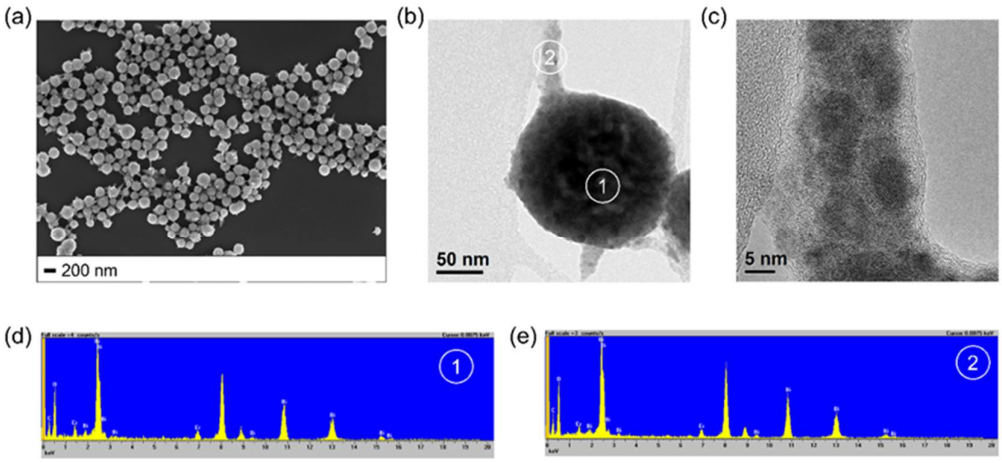

Fig.10 (a) FE-SEM, (b, c) HR-TEM images and (d, e) EDS analysis of Er-doped Bi_2O_3 NPs with 10%at. of Er.

When Yb^{3+} is introduced into the system, the limit to keep the spherical shape is about 6%at., above which the complete loss of the morphology occurs (see Fig.11). Speaking instead of NPs synthetized with NaOH as precipitant agent, doping contents of about 5%at. for Er^{3+} and of about 6%at. for Yb^{3+} are already enough to affect the morphology of the nanoparticles (see Fig.12). This differing effect observed for the different lanthanide ions and precipitant agents is not completely understood at the present stage and it is under investigation.

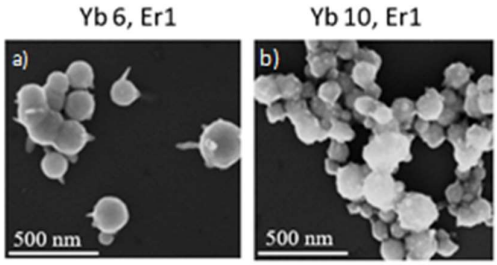

Fig.11 FE-SEM images of Yb-Er co-doped Bi_2O_3 NPs, synthetized with urea as precipitant agent, with different at.% content of Yb and Er: (a) Yb6-Er1% and (b) Yb10-Er1%.

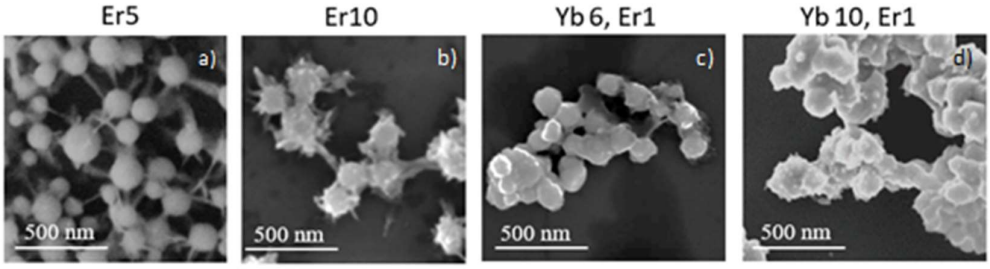

Fig.12 FE-SEM images of Er-doped and Yb-Er co-doped Bi_2O_3 NPs, synthetized with NaOH as precipitant agent, with different at.% content of Yb and Er: (a) Er 5%, (b) Er 10%, (c) Yb6-Er1% and (d) Yb10-Er1%.

Undoped Bi_2O_3 NPs and Bi_2O_3 NPs doped with 2%at. of Er were investigated by means of DSC analysis and the resulting phases were checked by means of XRPD. As summarized in Fig.13, the two samples show a different behaviour: (i) the undoped Bi_2O_3 is characterized by the $\alpha \rightarrow \delta$ phase transition during the heating cycle (735 °C) and two phase transitions, $\delta \rightarrow \gamma$ and $\gamma \rightarrow \alpha$, during the cooling cycle (at 640 and 515 °C, respectively), resulting in the final stabilization of the α-phase (Fig.13 a, b), while (ii) when doped with 2 at.% of Er, the system evolves through the $\beta \rightarrow \delta$ phase transition characterized by an exothermic peak at about 726°C and the inverse $\delta \rightarrow \beta$ phase transition (endothermic peak at 628 °C) during the cooling step to stabilize the β-phase at RT (Fig.13 c, d). The bulk Bi_2O_3-Er_2O_3 phase diagram is perfectly matched[49].

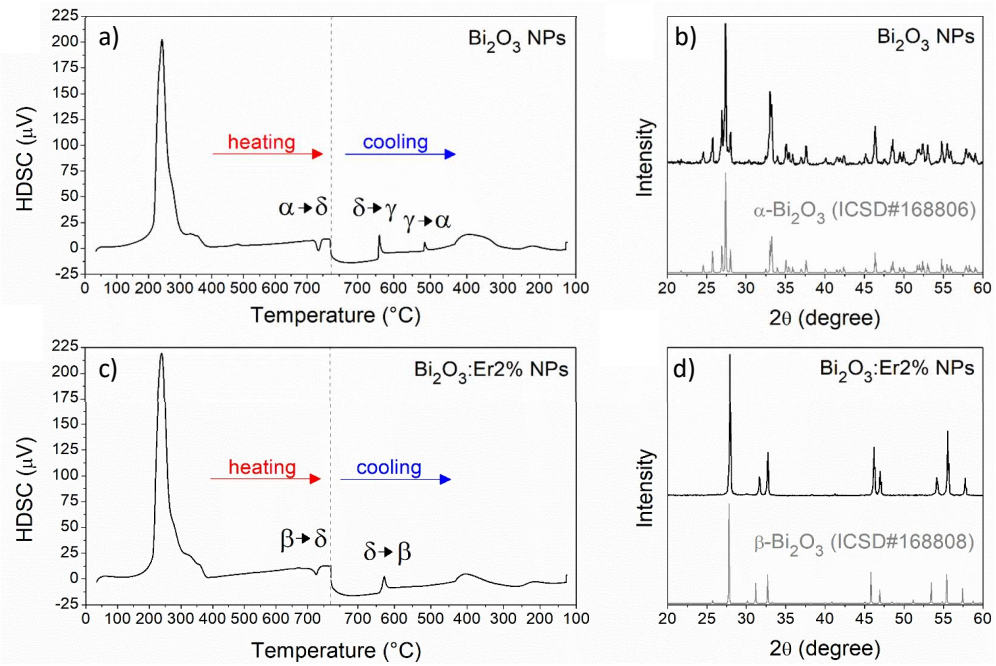

Fig.13 (a, c) DSC curves and (b, d) the XRPD patterns for the resulting crystalline phase of the undoped and 2 at.% Er-doped Bi_2O_3 NPs.

Silica shell control

Silica is typically used for realizing shells embedding nanoparticles, with the aim of reducing their activity or their toxicity. SiO_2 coatings promote water dispersion and chemical stability, with the great advantage to allow the functionalization of the outer NP surface, irrespective to their nature, through the silane chemistry. The synthesis of SiO_2 shells is of particular interest for protecting the surface of metal nanoparticles[35,36], and for coating quantum dots and inorganic nanocrystals[37], becoming thus a challenge. Moreover, in RE-doped nanoparticles, an inert silica coating has the unique advantage of reducing surface quenching effects over luminescence quantum yield[50]. Speaking of applications in nanomedicine, as reported by Gnanasammandhan *et al.*[38], the formation of amorphous silica shell on upconverting nanoparticles (UCNPs) is a fundamental step for the synthesis of photodynamic therapy (PDT) systems[39]. Therefore, novel approaches to synthesize core-shell nanosystems are highly desirable. Here, a simple protocol to control the silica shell thickness is firstly optimized. The proposed procedure consists in the well-known hydrolysis and condensation of tetraethyl orthosilicate (TEOS) through an ethanol/ammonia/water system (Stöber process[51]). A great advantage of the Stöber procedure lies in its simplicity. However, by fixing the amount of Bi_2O_3 NPs and ammonia as catalyst for the reaction, and increasing only the amount of TEOS added to the reaction mixture, the formation of non-shelling SiO_2 nanoparticles, in addition to the Bi_2O_3@SiO_2 core-shell NPs, was also detected when the TEOS (μL):Bi_2O_3 (mg) ratio was over 2, as evidenced in the SEM images and size distributions of Fig.14.

In particular, in the case of a TEOS (µL):Bi_2O_3 (mg) ratio equal to:
- 2, no silica stand-alone NPs were observed (Fig.14 a, d, g),
- 4, a certain amount of SiO_2 NPs formed, with a mean size of 90 nm, corresponding to the 3% among sampled nanoparticles (N=700) (Fig.14 b, e, h),
- 8, the percentage of silica Stöber NPs raised to 13% (Fig.14 c, f, i), over the statistical sampling on 700 NPs. Upon rising the TEOS amount, the size of the silica NPs (130 nm) grows in parallel with the shell thickness.

To overcome this drawback, a strategy consisting in subsequent additions of equal aliquots of 2 µL of TEOS per mg of Bi_2O_3 NPs at fixed interval of 2 hours in the reaction solution was used to grow thicker silica shells. As can be observed in Fig. 15 for a TEOS (µL):Bi_2O_3 (mg) equal to 4, this procedure allowed to avoid the formation of silica nanoparticles resulting in well dispersed Bi_2O_3@SiO_2 with homogenous silica shells. Fig.15 c and d represent the system after 2 subsequent additions of 2 µL of TEOS per mg of Bi_2O_3 NPs, where any non-shelling SiO_2 NPs can be observed. The huge difference in electronic density between Bi_2O_3 and SiO_2 allows to easily distinguish the core and the shell of the nanoparticles by means of electronic microscopy, by simply employing the backscattered electrons (BSE) mode of FE-SEM (Fig.15 b, d).

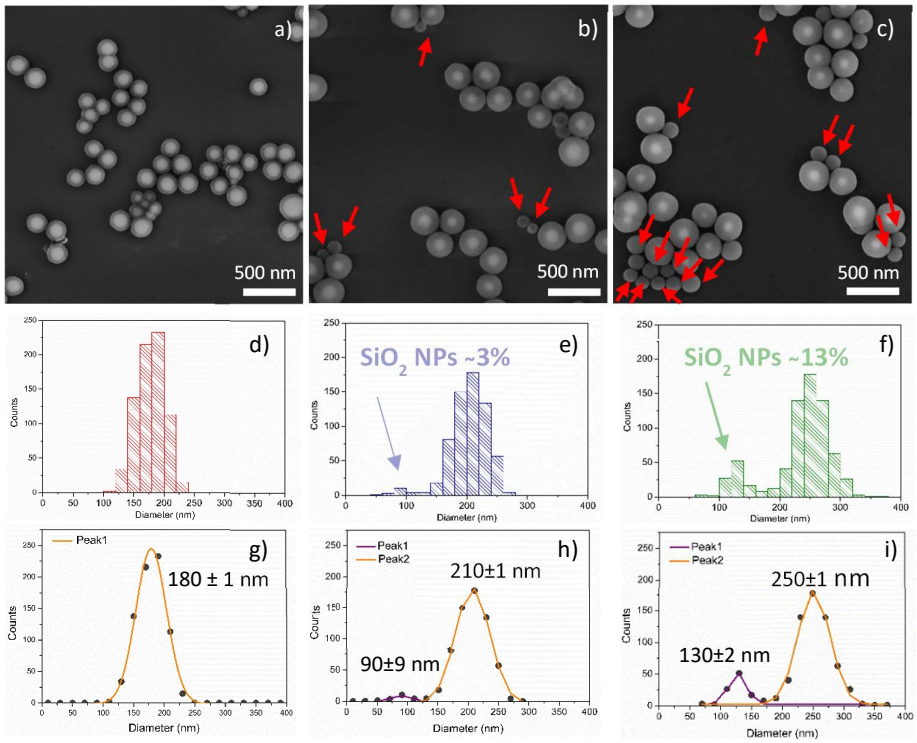

Fig.14 Effect of a single addition of equivalent volume of TEOS at once on the silica shell growth. (a, b, c) SEM images for a TEOS (µL):Bi_2O_3 (mg) ratio of 2, 4 and 8 eventually showing the formation of non-shelling silica NPs (indicated by red arrows), (d, e, f) size distributions (N=700) eventually showing the presence of a second population of SiO2 NPs and (g, h, i) gaussian distributions of NPs, showing mean size of Bi_2O_3@SiO_2 and SiO_2 NPs, when present.

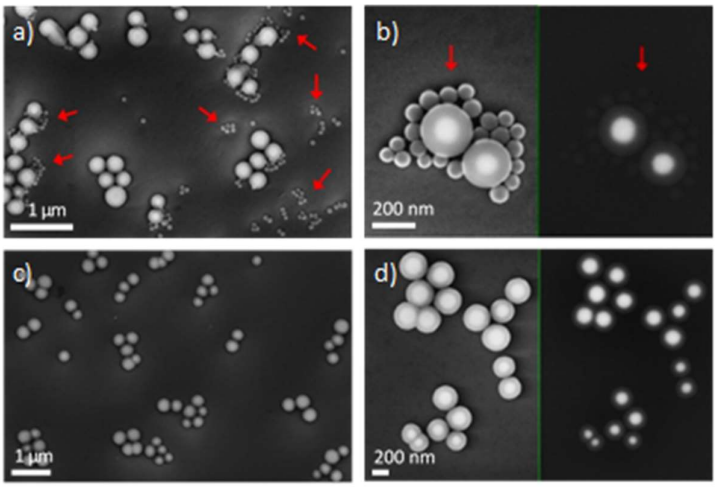

Fig.15 Effect of subsequent additions of equivalent aliquots of TEOS on the silica shell growth. (a, b) Conventional secondary electrons (SE) and backscattered electrons (BSE) SEM images for a TEOS (µL):Bi_2O_3 (mg) ratio of 4. The red arrows evidence the silica NPs formed during the SiO_2 shell growth on Bi_2O_3 NPs surface. (c, d) Representative SE and BSE SEM images of the silica shells grown on Bi_2O_3 NPs with two subsequent TEOS additions of 2 µL of TEOS per mg of Bi_2O_3 NPs.

The control on the silica shell is investigated by stabilizing shells of six different thickness for both the Bi_2O_3 NPs synthetized by addition of NaOH and urea (with a mean size of 120 and 180 nm, respectively). The results are discussed by combining an experimental and theoretical approach. Representative FE-SEM and TEM images of the Bi_2O_3@SiO_2 NPs obtained by a single addition of 2µL of TEOS per mg of Bi_2O_3 NPs are reported in Fig.16 a and b, showing the homogenous formation of the silica shell. Additional HR-TEM images of single particles with different silica shell thickness are shown in Fig.18. Fig.16c shows, as example, the distributions of the particles size with different silica shells for the Bi_2O_3 NPS prepared with NaOH, while Figure 16 d and e summarize representative images of the NPs as a function of the shell growth for the NPs synthetized by means of both urea and NaOH, respectively.
The growth of silica shell on the surface of Bi_2O_3 NPs as a function of the silicon precursor (TEOS) added into the reaction can be modelled based on simple geometric considerations. Experimentally, the shell thickness can be calculated as difference between the average values statistically estimated from the SEM/TEM images of the shelled and unshelled Bi_2O_3 NPs. From the practical point of view, it is interesting to describe the SiO_2 shell thickness growth (t_{shell}) on the Bi_2O_3 NPs for a fix number of NPs (fix weight of sample) as a function of the volume of TEOS added into the reaction mixture.
A simple theoretical model can be developed considering the geometrical scheme enlarged in Fig.17:

$$t_{shell}(\mathrm{mL_{TEOS}}) = r_{cs} - r_c = \sqrt[3]{\frac{3}{4\pi}V_{shell} + r_c^3} - r_c \qquad (1)$$

where r_{cs} and r_c represent the radius of the core NPs (Bi_2O_3) with and without the silica shell respectively, and the volume of the silica shell on a single Bi_2O_3 NP (V_{shell}) can be described based on chemical considerations as

$$V_{shell} = \frac{M_{w,\mathrm{SiO_2}} \cdot d_{\mathrm{TEOS}}}{d_{\mathrm{SiO_2}} \cdot M_{w,\mathrm{TEOS}}} \cdot \frac{\mathrm{mL_{TEOS}}}{n_{NP}} = \alpha \cdot \frac{\mathrm{mL_{TEOS}}}{n_{NP}} \qquad (2)$$

where $M_{w,\mathrm{Si\ _2}}$ and $M_{w,\mathrm{TEOS}}$ are the molar masses of SiO_2 and TEOS, respectively, $d_{\mathrm{SiO_2}}$ and d_{TEOS} are the densities of SiO_2 and TEOS (these parameters can be grouped into a single value α=0.123) and n_{NP} is the total number of NPs in the reaction chamber.

Fig.16f summarizes the results obtained from the statistical analysis of the SEM and TEM images to estimate the silica shell thickness as a function of the mL of TEOS added into the reaction ambient along with the theoretical curves from eq. 1, showing the good consistency between experiments and the theoretical model.

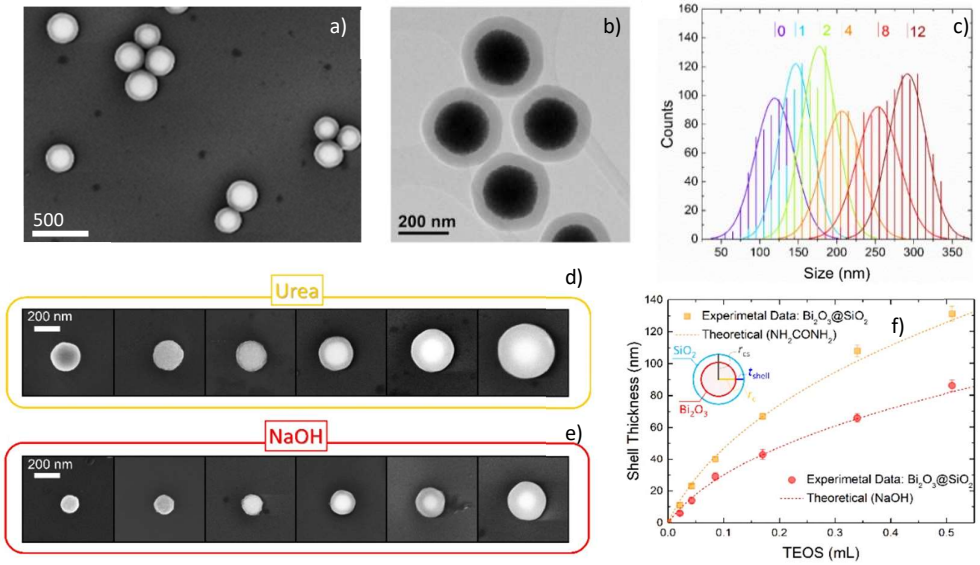

Fig.16 Fine control of the silica shell thickness on the Bi_2O_3 NPs surface. Representative SEM (a) and TEM (b) images of the core-shell Bi_2O_3@SiO_2 prepared by single addition of 2μL of TEOS per mg of Bi_2O_3 NPs synthetized by using urea. (c) Distributions of the diameter of the NPs as a function of TEOS (μL):Bi_2O_3 (mg) ratio (0, 1, 2, 4, 8 and 12) for the Bi_2O_3 NPs synthetized with NaOH. Representative SEM images of a single Bi_2O_3@SiO_2 nanoparticle as a function of silica shell growth (increasing thickness from left to right) for Bi_2O_3 prepared with (d) urea and (e) NaOH. (f) Experimental and theoretical shell thickness as a function of TEOS volume (mL) for a fixed amount of NPs (40 mg). Error bars represent the deviation of the mean value of three experiments. Inset: schematic geometrical representation used for the theoretical model of eq.1.

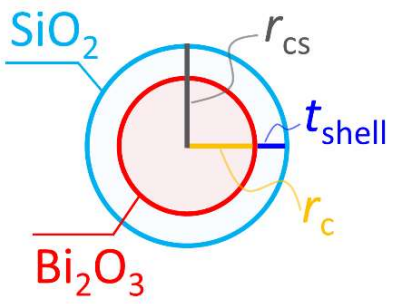

TEOS (μL):Bi_2O_3 (mg) ratio	**NaOH**		**$CO(NH)_2$**	
	Th. (nm)	**Ex.** (nm)	**Th.** (nm)	**Ex.** (nm)
0.5	8	6	13	11
1	15	14	24	23
2	26	29	40	40
4	42	44	65	67
8	65	66	99	108
12	81	86	123	131

Fig.17 (left) Schematic geometrical representation used for the theoretical model of eq. 1, where r_{cs} and r_c represent the radius of the core NPs (Bi_2O_3) with and without the silica shell respectively and t_{shell} represents the thickness of the silica embedding layer.

Table 2. (right) Theoretical and experimental values of the SiO_2 shell thickness with regard to the corresponding TEOS (μL):Bi_2O_3 (mg) ratio.

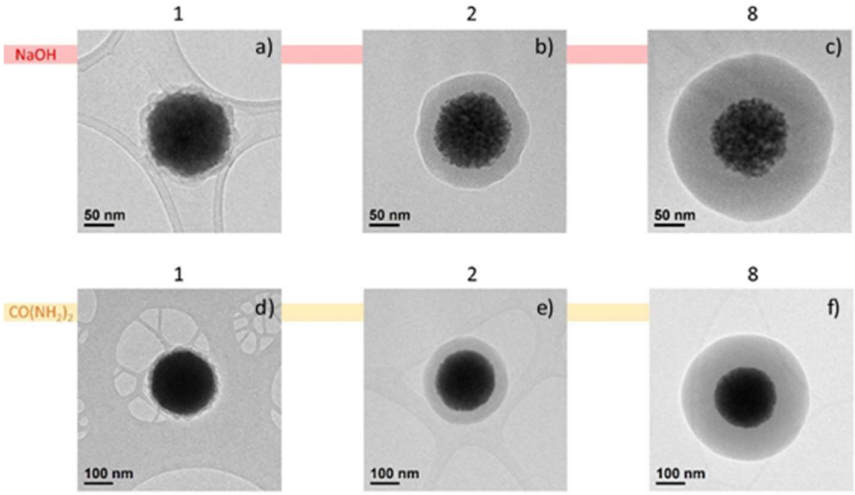

Fig.18 Representative HR-TEM single particle images for different SiO_2 shell thickness for the Bi_2O_3 NPs prepared with NaOH (a-c) and urea (d-f). The numbers represent the TEOS (μL):Bi_2O_3 (mg) ratio (1, 2, and 8).

Effect of temperature on the phase stabilization

With the aim to analyse the effect of the silica shell thickness on the stabilization of the desired phase, the thermal treatment effect was investigated for a series of Bi_2O_3:Er@SiO_2 NPs with increasing shell thickness, prepared with urea and doped with 2%at. of Er. Firstly, to select the suitable silica shell thickness, the system was studied by means of a combined thermal (differential scanning calorimetry, DSC), morphological (SEM) and structural (XRPD post DSC) analysis. The XRPD patterns of the systems after the DSC analysis to 770 °C (Fig.19 a, b) evidence the formation of a mixture of both cubic $Bi_4Si_3O_{12}$ and tetragonal Bi_2SiO_5 when a shell of 11±2 nm or 23±1 nm is employed. In the case of the Bi_2O_3@SiO_2 system with a silica shell of

40±2 nm, the pure tetragonal Bi_2SiO_5 phase, without the presence of peak coming from secondary phases, is obtained. In addition, as shown by the SEM images reported in Fig.19 c and d, the morphology of the NPs with a silica shell lower than 40 nm is completely lost after the thermal treatment while a silica shell of 40 nm allows to stabilize a single phase keeping the spherical morphology of the NPs.
This preliminary thermal/structural investigation suggests an optimal silica shell thickness of about 40 nm. Therefore, the structural study was performed by fixing this parameter.

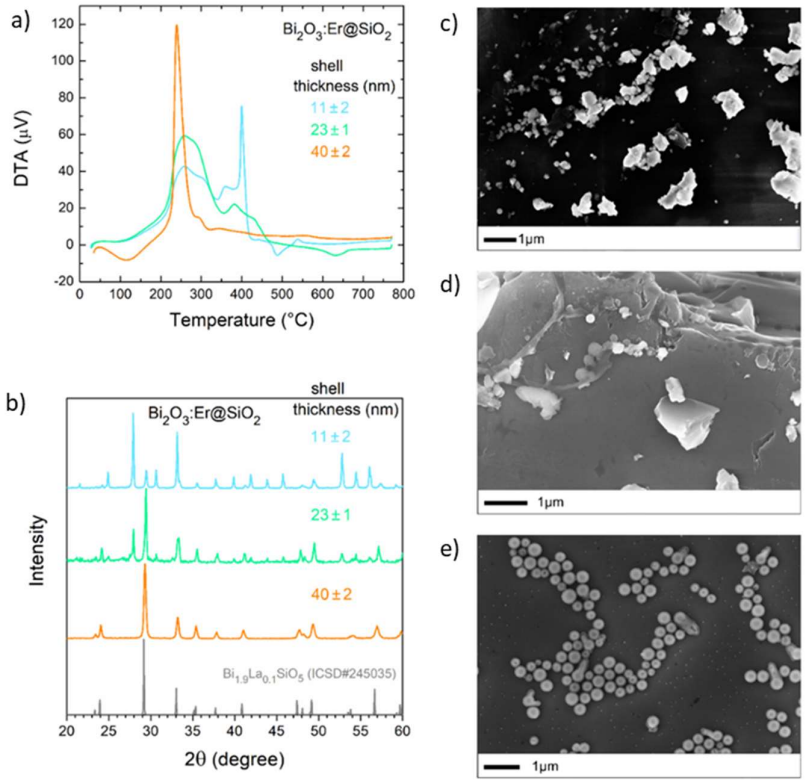

Fig.19 (a) DSC curves, (b) XRPD patterns and (c, d, e) SEM images of the Bi_2O_3:Er@SiO_2 NPs with different silica shell thickness (11±2 nm, 23±1 nm and 40±2 nm) after the DSC analysis.

Temperature dependence of *in-situ* synchrotron radiation XRPD analysis on an undoped Bi_2O_3@SiO_2 core-shell sample shows the stabilization of the monoclinic Cc crystal structure at room temperature (see Fig.20) in agreement with the investigation on bulk by Taniguchi *et al.*[52] It is interesting to note how, during the heating stage, the system evolves through the stabilization of the $I4/mmm$ structure (at 500 °C), a phase typically stabilized at ambient temperature by doping[53]. Taniguchi *et al.*[54] demonstrated the vanishing of the ferroelectric phase transition typical of undoped Bi_2SiO_5 with increasing the La substitution due to the change in the orientation of SiO_4 tetrahedra with a consequent disorder in the SiO_4 chains. The loss in the chains order is demonstrated to stem from the loss of the stereochemical activity of Bi^{3+} $6s^2$ lone electron pairs that bridge the SiO_4 tetrahedra to keep the chain order.

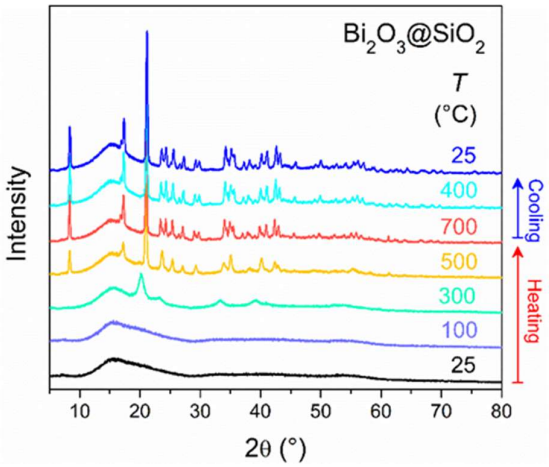

Fig.20 In-situ temperature dependent synchrotron radiation XRPD patterns (λ=1.12576 Å) of the undoped Bi_2O_3@SiO_2 system with a shell of about 40 nm.

With 40 nm shell, the effect of different thermal treatments was analysed by means of XRPD analysis also for a sample doped with 2%at. of Er, as summarized in Fig.21a. The treatment at 400°C results in the stabilization of pure β-Bi_2O_3 tetragonal phase. The stabilization of this metastable phase is driven by the Er^{3+} doping[7]. When the temperature is raised to 500 °C, the reaction between Bi_2O_3 and the SiO_2 shell begins and the stabilization of Bi_2SiO_5 is promoted. However, the small peak at about 28° attests the presence of a small fraction of unreacted Bi_2O_3. From 600°C, the pure tetragonal Bi_2SiO_5 phase with $I4/mmm$ space group (SG) is stabilized. Fig.21b shows the Rietveld refinement fit performed on the sample treated at 700 °C. The difference in the phase stabilization with respect to the undoped sample (Cc SG) stems from the doping effect[53,54]. The effect of the thermal treatment on the morphology of the system is investigated by means of FE-SEM and HR-TEM analysis. Fig.21c shows representative HR-TEM images of a single particle of the Bi_2O_3:Er@SiO_2 system at different temperatures. During the phase transformation from the as-prepared Bi_2O_3:Er@SiO_2 to β-Bi_2O_3:Er@SiO_2 at 400 °C and then to Bi_2SiO_5:Er@SiO_2 at higher temperatures, the spherical morphology of the NPs is kept (Fig.21 d and e show, as example, SEM images of the sample after thermal treatment at 400 °C and 700 °C, respectively). However, the HR-TEM images evidence an interesting evolution of the core; when the temperature increases, the dense core of the as-prepared system becomes gradually of low-density and finally, from 600 °C, the core is emptied and the NPs turn into a double layered-shell Bi_2SiO_5:Er@SiO_2 hollow nanosystem. This transformation stems from the proposed strategy that does not only consist in the encapsulation of the active Bi_2SiO_5 part into the silica shell, but it involves an *in-situ* reaction between the Bi_2O_3 core and the silica shell.

An additional evidence of the hollow nature of the system comes from the comparison of the local EDS spectra recorded from the SiO_2 shell, the Bi_2SiO_5:Er layer and the centre of the hollow particle (Fig.22). The spectra confirm the presence of bismuth and erbium only in the inner part of the NP. The EDS measurements were performed by fixing the acquisition time. Therefore, the lower intensity of the EDS spectra from the

centre of the NP with respect to the Bi_2SiO_5:Er layer (circles 3 and 2 in Fig.22, respectively) corroborates the hollow nature of the NPs. This unusual double layered Bi_2SiO_5@SiO_2 hollow nanoarchitecture induced by the thermal treatment is driven by the high diffusion of bismuth into silica[3,4], promoting the reaction from the core to the shell. It is interesting to remember that such property is widely exploited in the macroscopic world to produce lead-free low melting sealing agents for hermetic windows and modules.

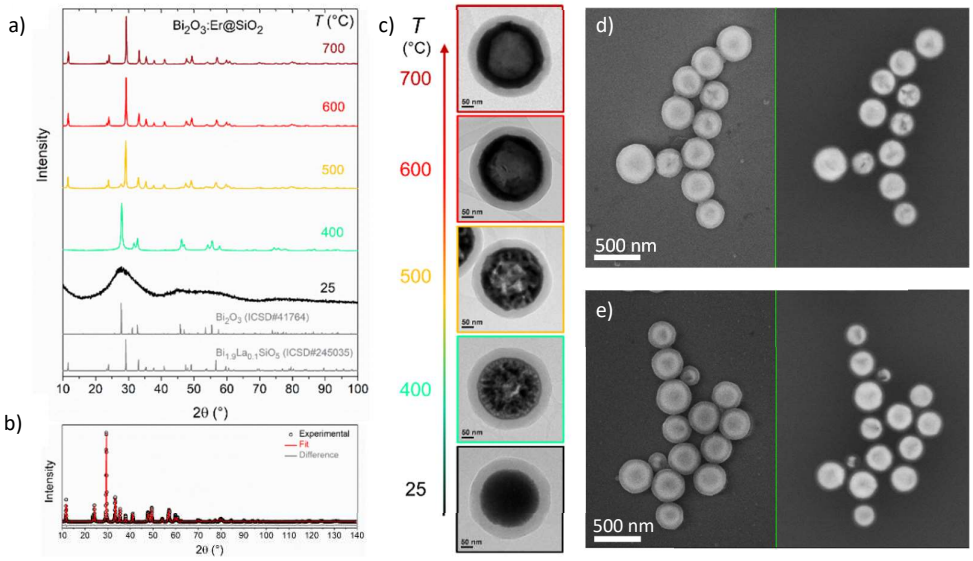

Fig.21 Study of thermal effect on the structural and morphological properties during the Bi_2O_3:Er@SiO_2 NPs: Bi_2SiO_5:Er@SiO_2 transition: (a) Temperature dependent XRPD patterns and (b) Rietveld refinement of the nanosystem annealed at 700 °C. (c) HR-TEM images of a single particle as a function of thermal treatment at different temperatures from 400 to 700°C, SE and BSE SEM images of 2%at. Er^{3+}-doped Bi_2O_3:Er@SiO_2 treated at (d) 400 °C and (e) 700 °C.

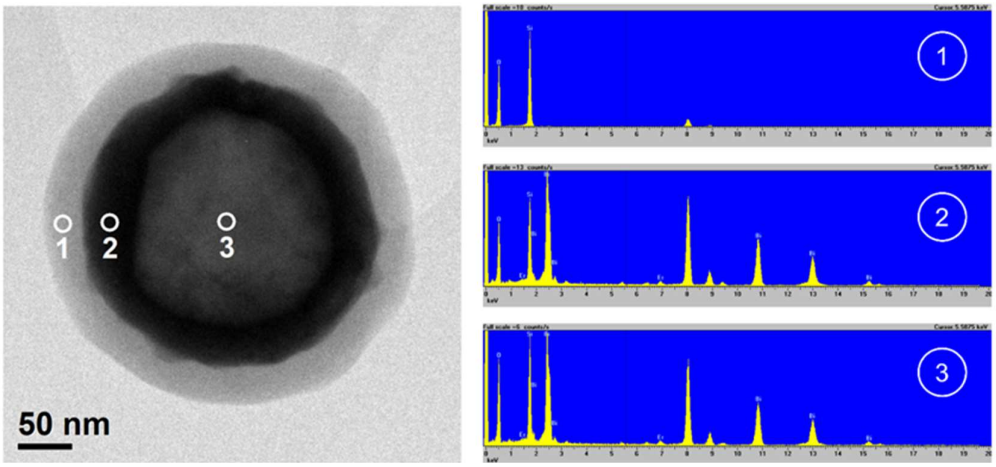

Fig.22 HR-TEM image (left) and EDS spectra (right) recorded for the Bi_2SiO_5:Er@SiO_2 sample treated at 700 °C: (1) SiO_2 shell, (2) Bi_2SiO_5:Er layer and (3) the centre of the hollow particle.

5.1.3 Optical characterization

With the aim to assess the suitability of the investigated nanosystem for the realization of a new class of UC nanophosphors, the emission properties and the resulting colour output tunability were investigated by doping with different sets of lanthanide ions typically used in upconverting systems: Yb^{3+} and one or more among Er^{3+}, Ho^{3+} and Tm^{3+} ions.

Fig.23 a, b and c and Fig.24 a, b, c and d show the upconverting PL emission spectra of the Ln^{3+}-doped samples, recorded in the visible range by exciting at 977 nm at room temperature.

When doping with the ion pair Yb-Er (Fig.23a), the spectrum is composed by the green emissions due to the $^2H_{11/2} \rightarrow {}^4I_{15/2}$ and $^4S_{3/2} \rightarrow {}^4I_{15/2}$ transitions and the red emission due to the $^4F_{9/2} \rightarrow {}^4I_{15/2}$ transition of Er^{3+}. In the case of Yb-Tm (Fig.23b), the much more intense NIR emission due to the $^3H_4 \rightarrow {}^3H_6$ transition dominates over the less intense emissions in the blue and red regions of the visible spectrum, attributable to $^1D_2 \rightarrow {}^3F_4$, $^1G_4 \rightarrow {}^3H_6$ and $^1G_4 \rightarrow {}^3F_4$ transitions of Tm^{3+}, respectively. Instead, when doping with the ion pair Yb-Ho (Fig.23c), the spectrum is dominated by the red emission of Ho^{3+} due to the $^5F_5 \rightarrow {}^5I_8$ transition, while less intense emission can be observed in green and far red regions of the spectrum, corresponding to the $^5S_2, {}^5F_4 \rightarrow {}^5I_8$ and $^5S_2, {}^5F_4 \rightarrow {}^5I_7$ transitions, respectively. For the energy level diagrams of each doping pair see Fig. 16, 17 and 18 in Chapter 2. Fig.24 a, b, c, and d represent the emission spectra of upconverting NPs doped with multiple combinations of Ln^{3+} ions, i.e. Yb-Er-Tm, Yb-Ho-Tm and Yb-Er-Ho-Tm, each presenting the characteristic emission features of each specific Ln^{3+} ion hosted in the crystalline matrix.

The upconverting nature of the transitions is confirmed by means of the log-log plot in Fig.23 d, e and f, for Yb-Er, Yb-Tm and Yb-Ho co-doped systems, respectively. In fact, it is often assumed that the order n of the upconversion process, i.e., the number n of photons required to pump the electron from the ground state to the emitting state, is indicated by the slope of the luminescence intensity versus pump power in double-logarithmic representation. Generally, a measured slope of x is indicative of an upconversion process that involves at least n photons, where n is the smallest integer greater than x (or equal to it if x is an integer)[55]. The results here obtained allowed for the interpretation of a measured intensity-versus-power dependence of multiphoton-excited luminescence, with respect to the order of the process. All the transitions investigated are ascribable to second order excitation processes, corresponding to two pump photons required to excite the specific emitting state (i.e. $^2H_{11/2}$, $^4S_{3/2}$ and $^4F_{9/2}$ for Er^{3+}, $^3H_4$ for Tm^{3+} and $^5S_2$, $^5F_4$, $^5F_5$ for Ho^{3+}, respectively), except for the emissions from $^1D_2$ and $^1G_4$ levels of Tm^{3+} ions, which are third order excitation processes, meaning that three photons are required to populate these excited states.

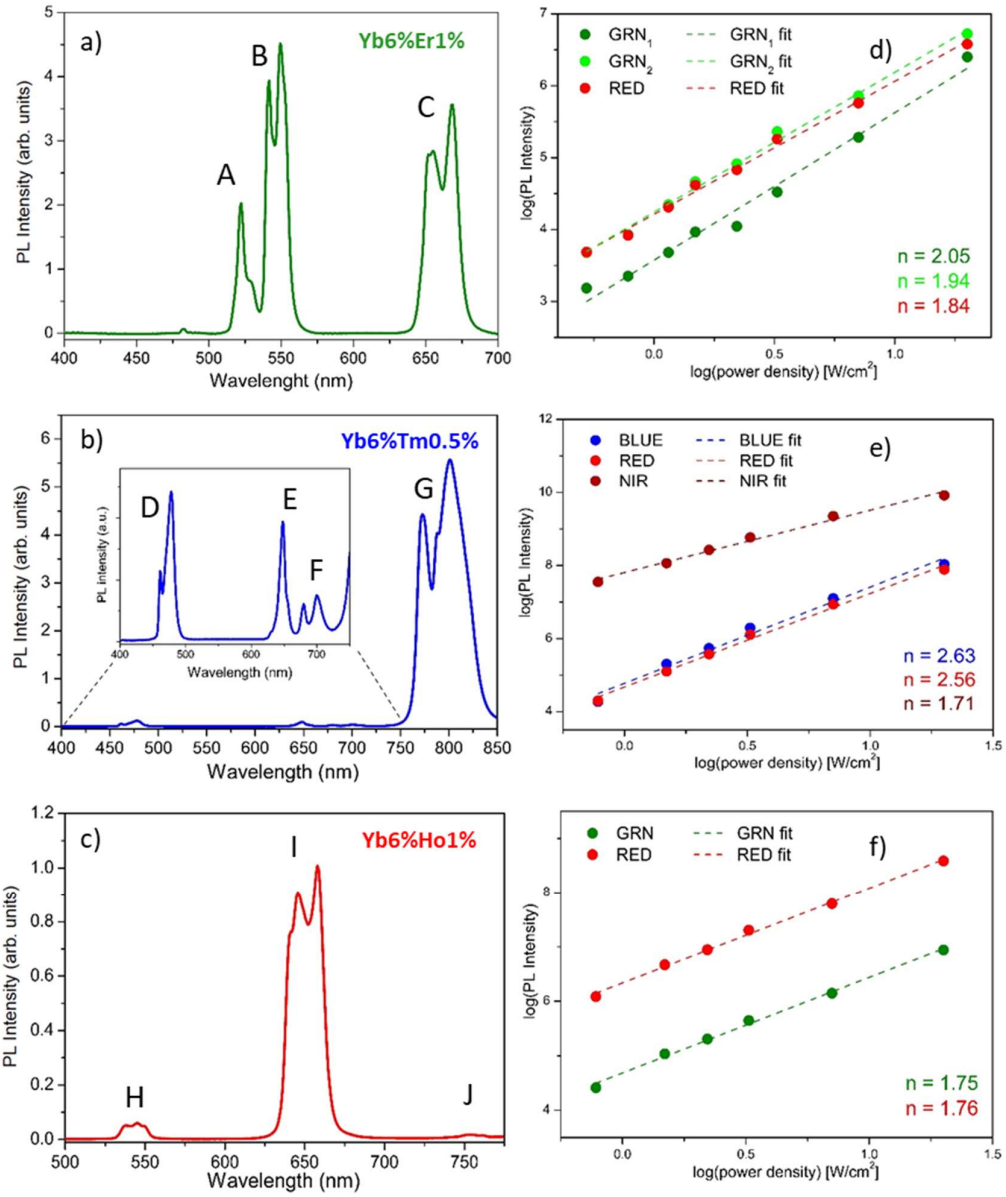

Fig.23 UC PL spectra (a, b, c) and double logarithmic plot (d, e, f) with linear fit of the luminescence intensity versus pump power to determine the order of the upconversion excitation processes, *of Yb-Er, Yb-Tm and Yb-Ho co-doped Bi_2SiO_5@SiO_2 NPs, respectively. Capital letters represent the transitions of Er^{3+} (A: $^2H_{11/2} \rightarrow {}^4I_{15/2}$; B: $^4S_{3/2} \rightarrow {}^4I_{15/2}$; C: $^4F_{9/2} \rightarrow {}^4I_{15/2}$), Tm^{3+} (D: $^1G_4 \rightarrow {}^3H_6$; E: $^1G_4 \rightarrow {}^3F_4$; F: $^3F_{2,3} \rightarrow {}^3H_6$; G: $^3H_4 \rightarrow {}^3H_6$) and Ho^{3+} (H: $^5S_2,{}^5F_4 \rightarrow {}^5I_8$; I: $^5F_5 \rightarrow {}^5I_8$; J: $^5S_2,{}^5F_4 \rightarrow {}^5I_7$).*

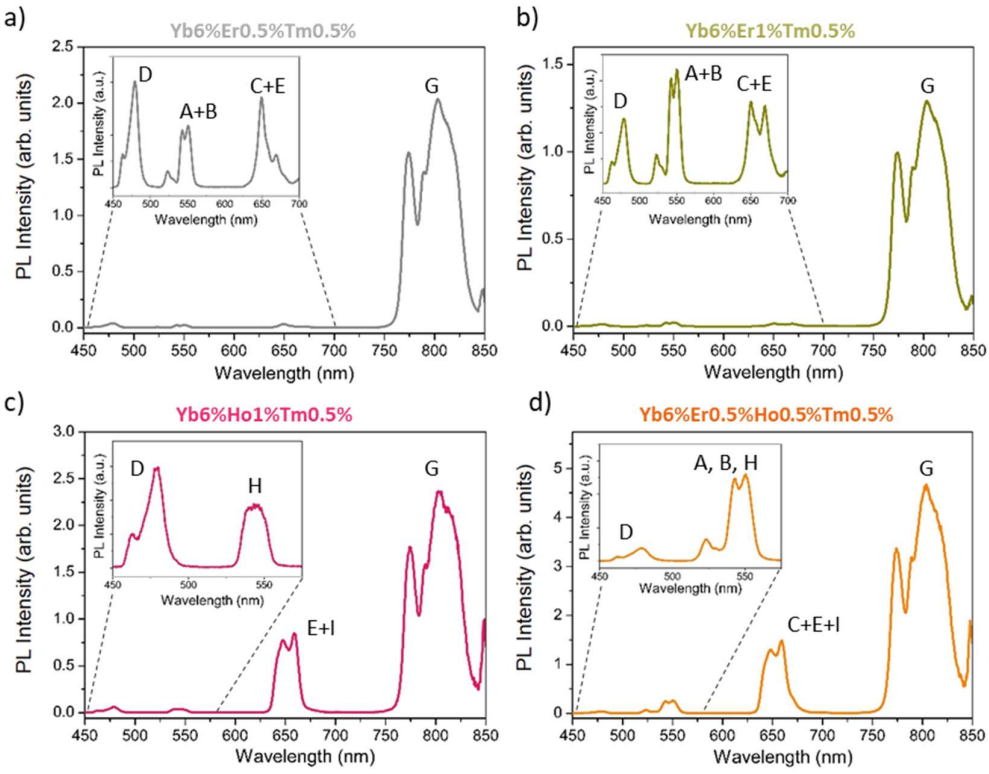

Fig.24 UC PL spectra (a, b, c, d) of Bi_2SiO_5@SiO_2 NPs doped with multiple combinations of Ln^{3+} ions, i.e. Yb-Er-Tm, Yb-Ho-Tm and Yb-Er-Ho-Tm, respectively. Capital letters represent the transitions of Er^{3+} (A: $^2H_{11/2} \rightarrow {}^4I_{15/2}$; B: $^4S_{3/2} \rightarrow {}^4I_{15/2}$; C: $^4F_{9/2} \rightarrow {}^4I_{15/2}$), Tm^{3+} (D: $^1G_4 \rightarrow {}^3H_6$; E: $^1G_4 \rightarrow {}^3F_4$; F: $^3F_{2,3} \rightarrow {}^3H_6$; G: $^3H_4 \rightarrow {}^3H_6$) and Ho^{3+} (H: $^5S_2,{}^5F_4 \rightarrow {}^5I_8$; I: $^5F_5 \rightarrow {}^5I_8$).

The CIE diagram, including the relative picture under 977 nm diode exposure, represented in Fig.25, demonstrates how easily controlled was the colour output, simply by acting on the choice and relative concentration of dopants. It is worth noting the bright emission originating from the irradiated samples and, in view of the realization of a white-emitting LED, the remarkable result obtained with the triple-doped sample, i.e. Yb-Er-Tm with at.% of 6, 1 and 0.5, respectively. Table 3 summarizes the CIE colour coordinates (x,y) of the samples under 977 nm excitation. Fig.26 a, b, and c show the diffuse reflectance spectrum and the Kubelka–Munk function of the Yb-Er, Yb-Tm and Yb-Ho co-doped samples, respectively. The absorption peaks of the lanthanide ions Er^{3+}, Tm^{3+} and Ho^{3+}, labelled with capital letters, are clearly detectable in the inset. Considering the Kubelka– Munk function F(R) and the direct bandgap nature of Bi_2SiO_5, the bandgap energy of the three samples was estimated by extrapolating the intercept of the fitted straight line at F(R)=0 in the $(F(R)\cdot h\nu)^2$ versus hν plot (Fig.26 d, e, f). An energy value of about 3.85 eV was obtained for all the samples, in the range of the typical values reported for Bi_2SiO_5[9,56], stating that the choice of dopants did not affect the bandgap energy of the material.

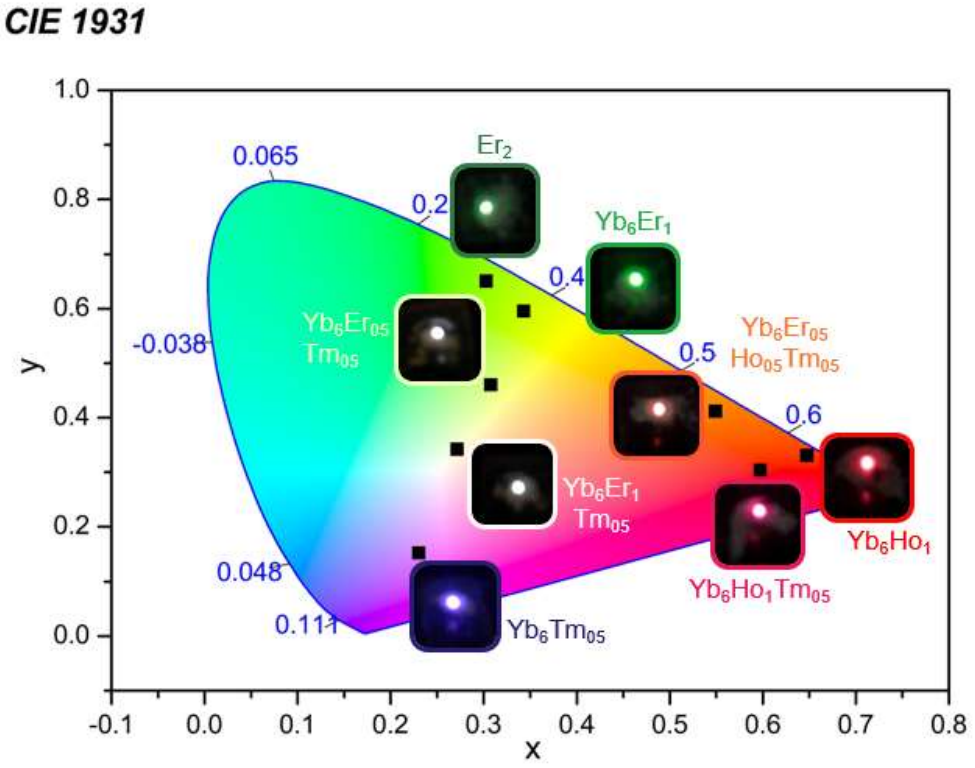

Fig.25 CIE diagram for all the Ln^{3+}-doped Bi_2SiO_5@SiO_2 NPs produced, including the relative picture under 977 nm diode exposure. The white-light emitting sample corresponds to the triple doping Yb-Er-Tm with at.% of 6, 1 and 0.5, respectively.

Dopants (at.%)	x	y
Er2	0.30259	0.65077
Yb6 Er1	0.34315	0.59561
Yb6 Tm0.5	0.23032	0.15257
Yb6 Ho1	0.64726	0.33147
Yb6 Er0.5 Tm0.5	0.30774	0.46051
Yb6 Er1 Tm0.5	0.27142	0.34246
Yb6 Ho1 Tm0.5	0.59732	0.30463
Yb6 Er0.5 Ho0.5 Tm0.5	0.54899	0.41230

Table 3. CIE coordinates for all the Ln^{3+}-doped Bi_2SiO_5@SiO_2 NPs produced.

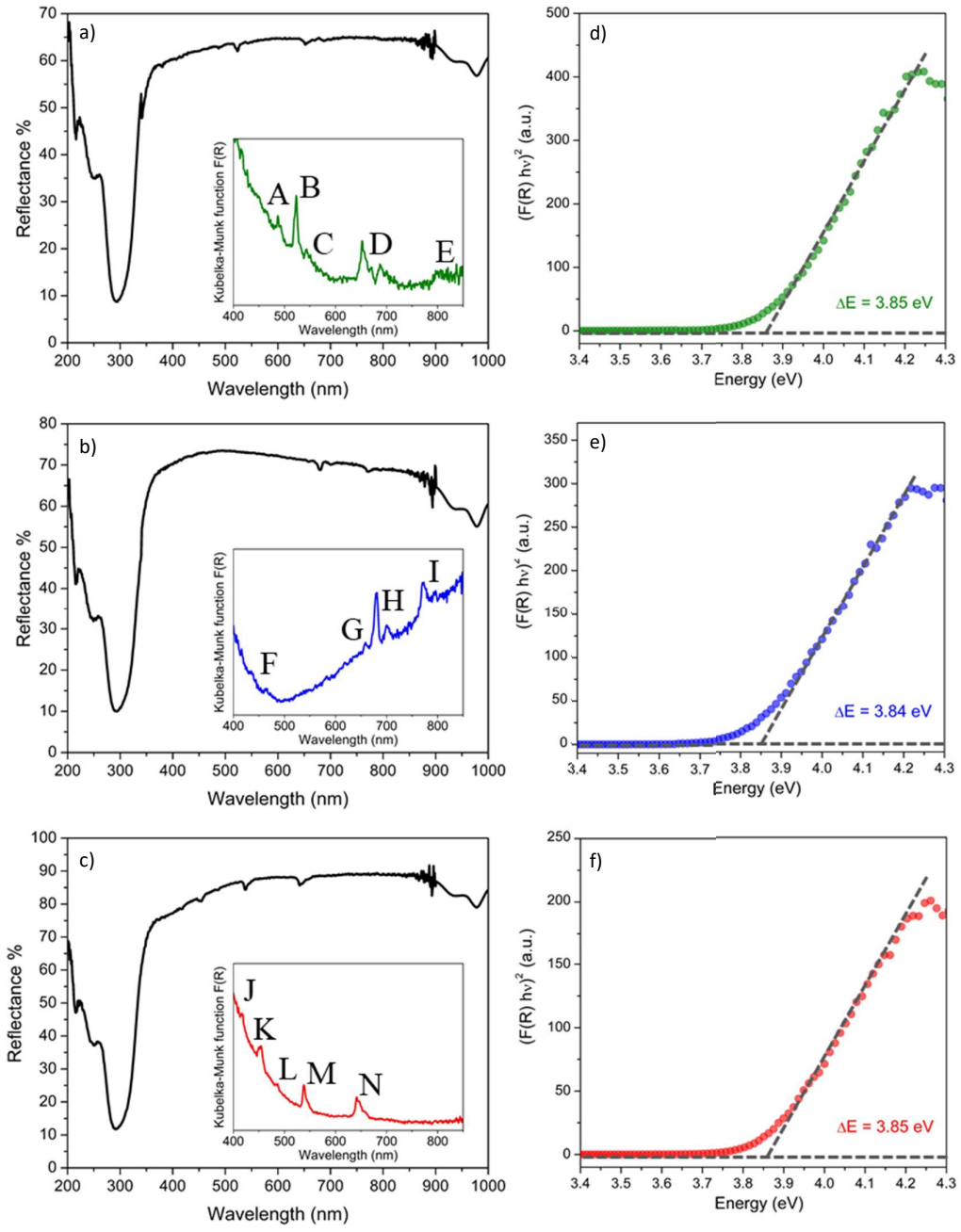

Fig.26 Diffuse reflectance spectra (a, b, c) of Yb-Er, Yb-Tm and Yb-Ho co-doped Bi_2SiO_5@SiO_2 NPs, respectively, with the Kubelka–Munk function (inset) and bandgap estimation (d, f, e) as the intercept of the fitted straight line at F(R)=0 in the $(F(R)\cdot h\nu)^2$ versus hv plot. Capital letters represent the transitions of Er^{3+} (A: $^4I_{15/2}\rightarrow{}^2F_{7/2}$, B: $^4I_{15/2}\rightarrow{}^2H_{11/2}$, C: $^4I_{15/2}\rightarrow{}^4S_{3/2}$, D: $^4I_{15/2}\rightarrow F_{9/2}$, E: $^4I_{15/2}\rightarrow{}^4I_{9/2}$), Tm^{3+} (F: $^3F_4\rightarrow{}^1D_2$, $^3H_6\rightarrow{}^1G_4$, G: $^3F_4\rightarrow{}^1G_4$, H: $^3H_6\rightarrow{}^3F_{2,3}$, I: $^3H_6\rightarrow{}^3H_4$), and Ho^{3+} (J: $^5I_8\rightarrow{}^5G_5$, K: $^5I_8\rightarrow{}^5G_6$, L: $^5I_8\rightarrow{}^5F_3$, M: $^5I_8\rightarrow{}^5S_2$, $^5F_4$, N: $^5I_8\rightarrow{}^5F_5$).

5.2 $Bi_2SiO_5:Nd^{3+}@SiO_2$ core-shell luminescent NPs

Nd^{3+}-doped NPs are able to emit NIR light under excitation with a low-cost diode laser and thus are regarded as excellent luminescent nanoprobes for various applications in the biological field[57-63].

In this case, $Bi_2SiO_5:Nd^{3+}@SiO_2$ NPs were synthetized following a procedure like that described in Section 5.1.1 for Ln^{3+}-doped Bismuth silicate nanoparticles, namely by using sodium hydroxide as the precipitating agent and doping the crystal lattice with the desired at.% of Nd^{3+} ions.

5.2.1 Sample preparation

Materials

Bismuth(III) nitrate pentahydrate ($Bi(NO_3)_3 \cdot 5H_2O$, 99.9%), Neodymium(III) nitrate hexahydrate ($Nd(NO_3)_3 \cdot 6H_2O$, 99.9%), sodium hydroxide (NaOH, >99%), ethylene glycol (EG, 99.8%) and tetraethyl orthosilicate (TEOS, 98%) were purchased from Sigma Aldrich. Poly(vinylpyrrolidone) (PVP, Mw = 40000) was obtained from Fluka Analytical. Nitric acid (HNO_3, 65%) and Ammonia solution (NH_3, 30%) were purchased from Carlo Erba.

All the chemicals were reagent grade and used without further purification.

Synthesis of $Bi_2SiO_5:Nd^{3+}@SiO_2$ nanoparticles

The synthetic procedure was very similar to that employed for $Bi_2SiO_5:Ln@SiO_2$ (see Section 5.1.1). Firstly, Nd^{3+}-doped Bi_2O_3 NPs were synthetized via a hydrothermal route. In a typical synthetic process, $Bi(NO_3)_3 \cdot 5H_2O$ and $Nd(NO_3)_3 \cdot 6H_2O$ solutions (75 mM) were prepared by dissolution of the respective salts in HNO_3 1 M. The two solutions were mixed with a ratio based on the relative dopant concentration chosen, to a final volume of 20 mL, then PVP40 (7.5 µmol) was added under magnetic stirring. Separately, NaOH (5.4 mmol) was dissolved in EG (100 mL). Finally, the second solution was slowly poured into the first one. The mixture was stirred for a short time and then transferred into a stainless-steel autoclave with a Teflon liner. The autoclave was sealed and maintained at 150° C for 3.5 h. The obtained products were centrifuged and washed 3 times with deionized water, once with mixed ethanol and water and once with ethanol only. Different dopant concentrations were tested (0.5, 1, 2, 5 %at.), to investigate the effect on both the crystalline structure and on the optical properties of the material.

For thin silica coating on the surface of the particles, we followed the same procedure reported in Section 5.1.1. Finally, $Bi_2O_3:Nd@SiO_2$ particles were calcined at 700°C for 2 h in air atmosphere to obtain the desired crystalline phase.

5.2.2 Morphological and structural analysis

Hydrothermal synthesis Bi_2SiO_5:Nd@SiO_2 NPs: the effect of the dopant concentration

With the aim to assess the effect of increasing atomic percentage of dopant substituted in the crystal lattice, FE-SEM images of the different samples were collected. All the NPs appeared to be spherical in shape and no evident differences in size or morphology were observed between the various samples of the $(Bi_{1-x}Nd_x)_2O_3$ series with x=0.005, 0.01, 0.02 and 0.05. Statistical analysis of FE-SEM images was conducted to estimate the size distribution of the NPs. As reported in Table 4, the mean size of the $(Bi_{1-x}Nd_x)_2O_3$ NPs, was very similar and of about 120 nm, regardless of the amount of dopant, and the size of all the particles of the series homogeneously increased of about 30/40 nm after silica coating, meaning that an inert shell about 15/20 nm thick formed to embed the active core, as expected in agreement with what experienced for Ln^{3+}-doped Bismuth silicate nanoparticles in the previous Section (5.1.2). It is worth noting that no uncoated bismuth oxide core was observed. Also, the thermal treatment did not induce any significant differences between the mean size of the various samples of this set.

As shown in Fig.27 a, the size distribution bells of the $(Bi_{1-x}Nd_x)_2O_3$ samples are all gaussian in shape, almost equally centered, and only a slight difference in FWHM could be appreciated, meaning that the populations of the less (x=0.005) and most (x=0.05) doped samples are moderately less homogeneous.

As an example, FE-SEM images and corresponding size distribution histograms of Bi_2O_3, Bi_2O_3@SiO_2 and Bi_2SiO_5@SiO_2 samples, with a 2%at. content of Nd^{3+} are reported in Fig.28.

EDX analysis was performed to examine the chemical composition of the starting Bi_2O_3 nanoparticles with a 2%at. content of Nd^{3+}. The spectrum in Fig.27b shows the presence of Bi, O, Nd, Al (from the sample holder) and C (from carbon tape) elements. The signal of Nd, even if relatively low, suggests the successful doping of Nd^{3+} into Bi_2O_3 host.

Nd %at.	Bi_2O_3 NPs (nm)	Bi_2O_3@SiO_2 NPs (nm)	Bi_2SiO_5@SiO_2 NPs (nm)
0.5	121 ± 27	162 ± 30	166 ± 23
1	117 ± 19	163 ± 25	167 ± 21
2	117 ± 21	161 ± 29	164 ± 22
5	125 ± 31	155 ± 25	156 ± 24

Table 4. Mean size of Bi_2O_3, Bi_2O_3@SiO_2 and Bi_2SiO_5@SiO_2 NPs by increasing the atomic percentage of Nd^{3+} dopant ions substituted in the crystal lattice.

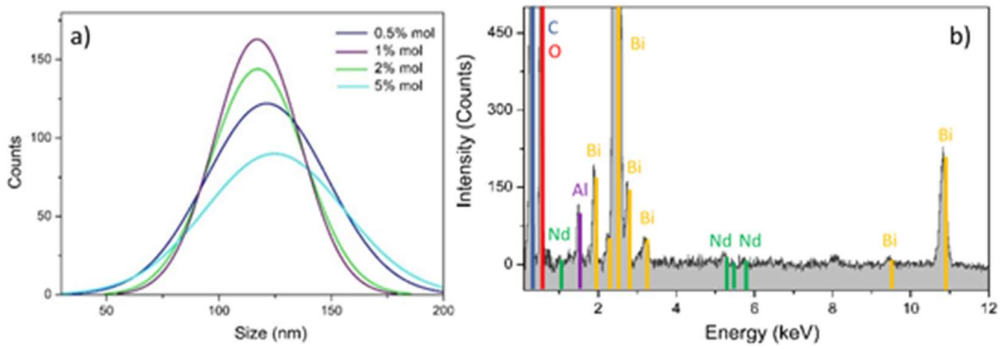

Fig.27 (a) Size distribution gaussian bells for the four samples of the $(Bi_{1-x}Nd_x)_2O_3$ series with x=0.005, 0.01, 0.02 and 0.05; (b) EDX spectrum of Bi_2O_3 NPs with a 2%at. content of Nd^{3+}.

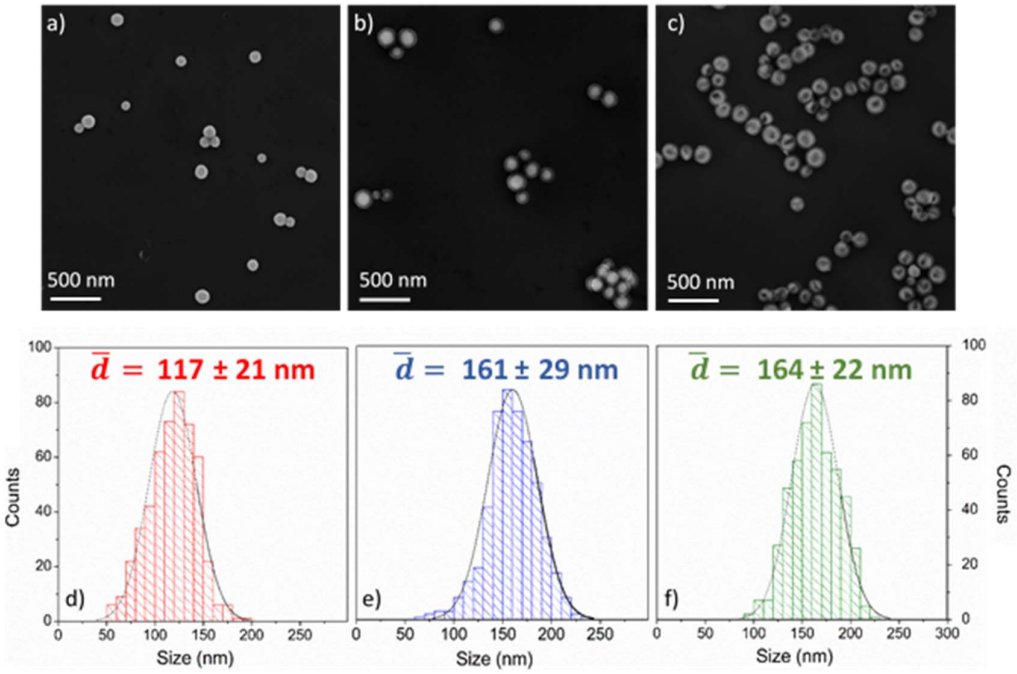

Fig.28 FE-SEM images (a, b, c) and corresponding size distributions (N=700) (d, e, f) of Bi_2O_3, Bi_2O_3@SiO_2 and Bi_2SiO_5@SiO_2 samples, with a 2%at. content of Nd^{3+}.

The X-ray powder diffraction patterns (XRPD) of the substituted compound with composition $(Bi_{1-x}Nd_x)_2SiO_5$ with x=0.005, 0.01, 0.02 and 0.05 are given in Fig.29a. As it can be observed, the substituted phase presents a different structure than that of the parent undoped compound. The tetragonal form of Bi_2SiO_5 was fully stabilized by substitution of Bi^{3+} by Nd^{3+}, with a minimum 1%at. content, after recrystallization of a glass form with the same composition, while the undoped Bi_2SiO_5 pattern can be indexed to the orthorhombic space group *Cmc*21. The $(Bi_{1-x}Nd_x)_2SiO_5$ patterns looks slightly different, with the disappearance of some reflexions, indicating that a small doping on the Bi^{3+} site is likely to induce a symmetry increase. In first approximation,

the pattern of $(Bi_{0.98}Nd_{0.02})_2SiO_5$ NPs (Fig.29b) can be indexed to a body-centred tetragonal space group (ICSD#245035), as previously reported by Georges et al. for La^{3+} substituted Bi_2SiO_5[53]. Doping up to 5%at., other additional peaks are observed, attributable to the presence of a small percentage of a SiO_2 polymorph, i.e. cristobalite, matching with ICSD card #010760941. The quite broad diffraction peaks may be due to the crystallization from a glassy phase, that leads to very small crystallographic coherent domains.

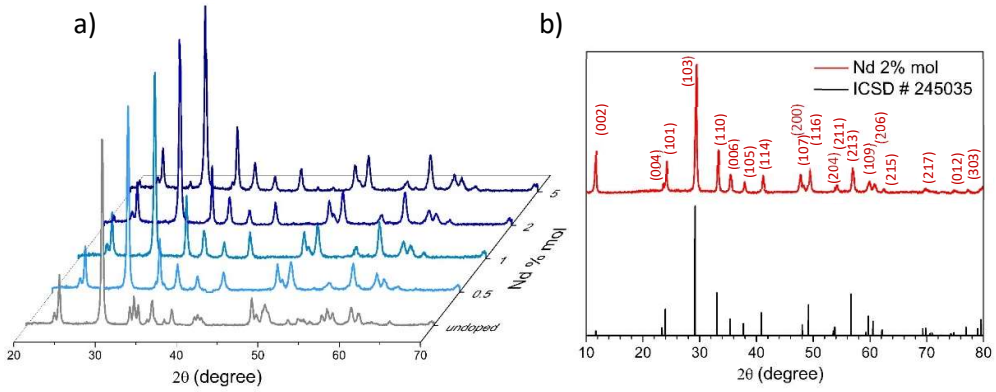

Fig.29 XRPD patterns of (a) the synthetized Bi_2SiO_5 nanoparticles, with different Nd^{3+} content and (b) $(Bi_{0.98}Nd_{0.02})_2SiO_5$ NPs compared to the corresponding ICSD#245035 crystal structure.

5.2.3 Optical characterization

In neodymium-doped luminescent materials, luminescence brightness is strongly dependent on Nd^{3+} concentration[64-66]. Indeed, the luminescent brightness of Nd^{3+}-doped systems is traditionally calculated as the $[Nd^{3+}]\cdot\Phi_{lum}$ product, in which $[Nd^{3+}]$ is the neodymium concentration and Φ_{lum} is the emission quantum yield (that corresponds to the fraction of excited Nd^{3+} ions that de-excite through radiative transitions)[67]. As a consequence of concentration quenching, both cross-relaxation and energy migration processes between Nd^{3+} ions make Φ_{lum} decrease with increasing Nd^{3+} concentration. This leads to the existence of an optimum Nd^{3+} concentration maximizing the luminescence brightness.

From photoluminescence spectra collected at room temperature reported in Fig.30a, it is possible to elucidate the influence of the Nd^{3+} content on the luminescence brightness. PL intensity of Nd^{3+}:Bi_2SiO_5@SiO_2 NPs (obtained under the same 590 nm excitation power) was maximum for the 2%at. dopant content NPs. Indeed, integrated PL intensity increased with the Nd^{3+} concentration until 2%at., due to the absence of relevant energy transfer processes, while suddenly dropped in the case of 5%at. content (Fig.30b). As previously reported for other neodymium-doped luminescent systems, this is due to cross-relaxation processes and concentration-activated energy migration, that increase the nonradiative decay rate[68].

As a consequence, also in agreement with the XRD results on the crystalline phase, we focused our attention to 2%at. doped Nd^{3+}:Bi_2SiO_5@SiO_2 NPs. It should be noted here that probably the passive SiO_2 coating plays an important role by minimizing the possible quenching of Nd^{3+} fluorescence caused by surface defects that would occur in non-shielded active cores[69].

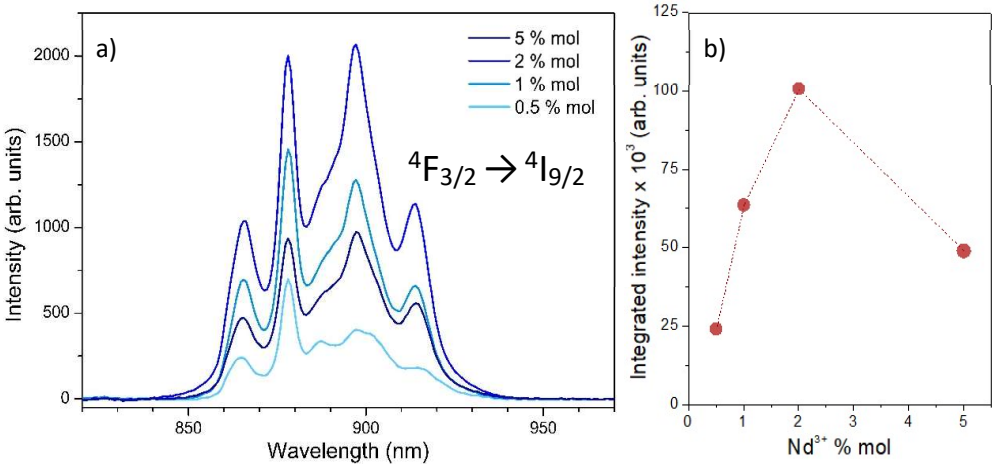

Fig.30 (a) PL spectra and (b) integrated intensities of $^4F_{3/2} \rightarrow {}^4I_{9/2}$ transition relative to the various samples of the $(Bi_{1-x}Nd_x)_2O_3$ series with x=0.005, 0.01, 0.02 and 0.05, where the dots represent experimental data and dashed lines are added as a guide for the eye.

Emission and excitation spectra of 2%at. doped Bi_2SiO_5:Nd@SiO_2 sample are simultaneously reported in Fig.31a. Under 590 nm light excitation, at room temperature, these nanoparticles show a very intense Nd^{3+} emission band at around 890 nm, within the first biological window, relative to the $^4F_{3/2} \rightarrow {}^4I_{9/2}$ transition. On the other hand, the excitation spectrum shows every absorption line relative to Nd^{3+} doped Bi_2SiO_5@SiO_2, as schematically reported in the energy level diagram in Fig.31b.

Fig.32a shows the diffuse reflectance spectrum and the Kubelka–Munk function of the $(Bi_{0.98}Nd_{0.02})_2SiO_5$ sample, in which the absorption peaks of Nd^{3+} are clearly detectable. Considering the Kubelka–Munk function F(R) and the direct bandgap nature of Bi_2SiO_5, previously described with first-principles calculations of the band structure by Kuwabara *et al.*[70], Park *et al.*[71] and Zhang *et al.*[72], the bandgap energy was estimated by extrapolating the intercept of the fitted straight line at F(R)=0 in the $(F(R)\cdot h\nu)^2$ versus Energy (hν) plot (Fig.32b). An energy value of 3.75 eV was obtained for the sample, in agreement with typical values reported for Bi silicates[73-75].

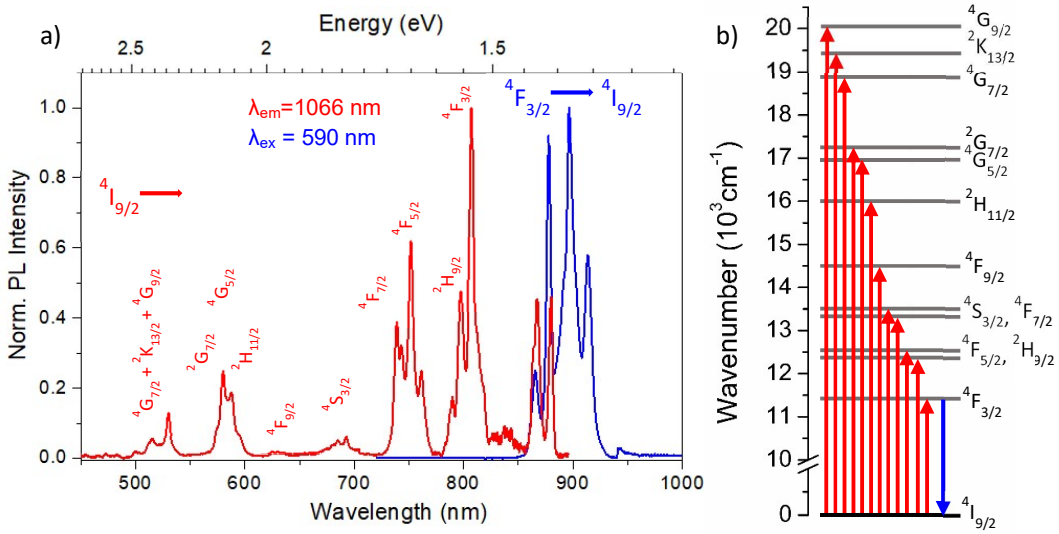

Fig.31 (a) Emission (blue line) and excitation (red line) spectra of $(Bi_{0.98}Nd_{0.02})_2SiO_5$ NPs and (b) Nd^{3+} schematic energy level diagram with typical absorption and emission lines indicated as red and blue arrows, respectively.

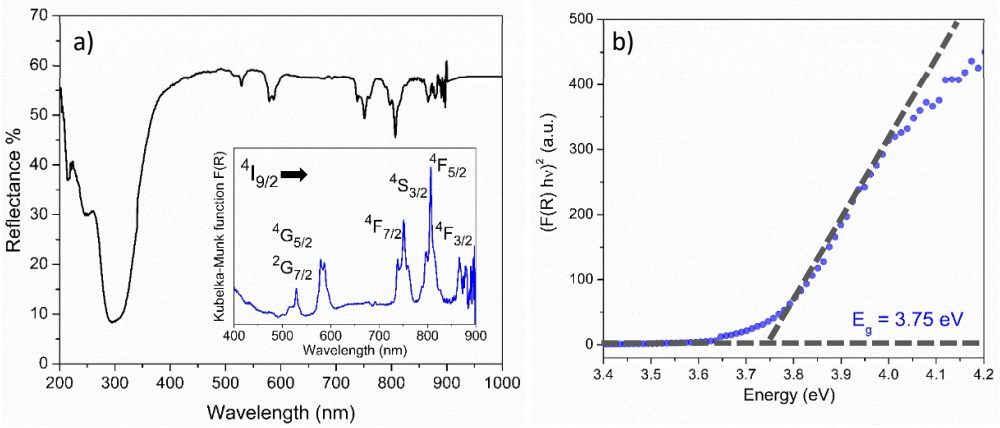

Fig.32 (a) Diffuse reflectance spectra with the Kubelka–Munk function (inset) and (b) Tauc plot for the bandgap estimation of $(Bi_{0.98}Nd_{0.02})_2SiO_5$ NPs.

5.3 $Bi_4Si_3O_{12}:Nd^{3+}@SiO_2$ core-shell luminescent NPs

As seen in Chapter 4, the Bi_2O_3-SiO_2 binary system (Fig.1, Chapter 4) mainly consists of three different compounds[76], depending on the molar ratio betweeen the two oxides and on the crystallization temperature, each with a distinctive crystalline phase: the sillenite $Bi_{12}SiO_{20}$, the eulytite $Bi_4Si_3O_{12}$ and the metastable Bi_2SiO_5.

$Bi_4Si_3O_{12}$ has previously been investigated as phosphor host[77-82], but only few works report on the synthesis of this compound at the nanoscale. However, none of them suggests its application with multi-modal imaging or optical thermometry purposes.

5.3.1 Sample preparation

In this case, $Bi_4Si_3O_{12}$:Nd^{3+}@SiO_2 NPs were synthetized following the same three-steps procedure described in the previous Section for Bi_2SiO_5@SiO_2 Nd^{3+}-doped nanoparticles (5.2.1). Namely, the synthesis of Nd^{3+}-doped Bi_2O_3 NPs via a hydrothermal route, the coating with a 40 nm thick SiO_2 shell to embed and protect the active cores from the surrounding environment and reduce surface quenching effects, and finally a thermal treatment. As presumed from the Bi_2O_3-SiO_2 binary system, different temperatures were tested, i.e. 800°C, 900°C and 1000°C. The dopant content was fixed at 2%at., since that had previously showed maximum PL intensity and little concentration quenching effect.

5.3.2 Morphological and structural analysis

The powder diffraction patterns (XRPD) of the substituted compound with composition $(Bi_{0.98}Nd_{0.02})_4Si_3O_{12}$, calcined at different temperatures are given in Fig.33a. As it can be observed, the 800°C thermal treatment induces the crystallization of the tetragonal form of Bi_2SiO_5, the same observed in the previous section when calcining at 700°C. The pattern of the sample calcined at 900°C looks completely different, with the disappearance of the Bi_2SiO_5 reflexions, substituted by $Bi_4Si_3O_{12}$ peaks. On the other hand, when calcined at 1000°C other additional peaks are observed, attributed to a small percentage of another minor phase, i.e. tetragonal SiO_2. The pattern of $(Bi_{0.98}Nd_{0.02})_4Si_3O_{12}$ NPs calcined at 900°C (Fig.33b) can be indexed to a cubic structure with the *I-43d* space group (ICSD#84519). At this temperature the crystal phase is pure, and the current doping level does not cause any peak shift or second phase reflections.

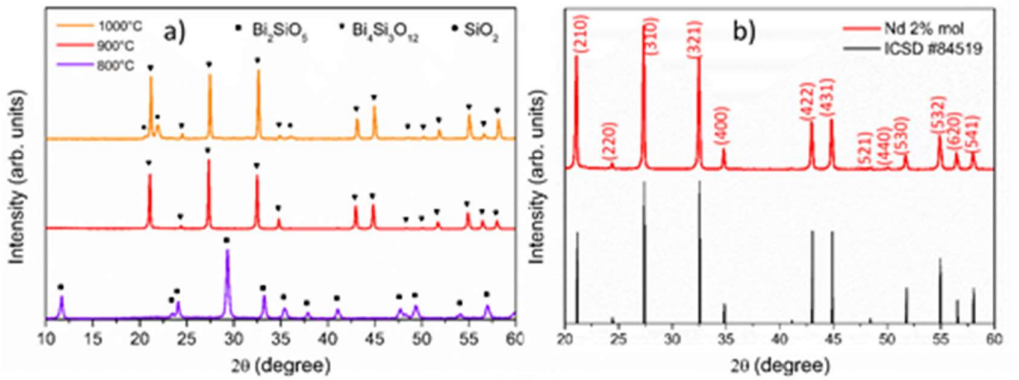

Fig.33 XRPD patterns of (a) Bi_2O_3:Nd^{3+}@SiO_2 NPs calcined at different temperatures: 800°C (purple line), 900°C (red line) and 1000°C (orange line), respectively; (b) $Bi_4Si_3O_{12}$:Nd^{3+}@SiO_2 nanoparticles, with a 2%at. Nd^{3+}-content and compared to the $Bi_4Si_3O_{12}$ crystal structure (ICSD#84519).

FE-SEM images in Fig.34 (a, b, c) show the samples calcined at 800 °C, 900°C and 1000°C, respectively. Fig.34b clearly points out that the thermal treatment at 900°C, despite leading to the crystallization of the desired phase, has a detrimental effect on the separation and morphology of the nanoparticles, causing a certain grade of aggregation that begins already at 800°C. At 1000°C the complete aggregation of the NPs occurs, leading to the formation of clusters with size of the order of micrometers. This can be due to the fact that the phase transition process may pass through a glassy molten phase, that leads to the coalescence between adjacent nanoparticles.

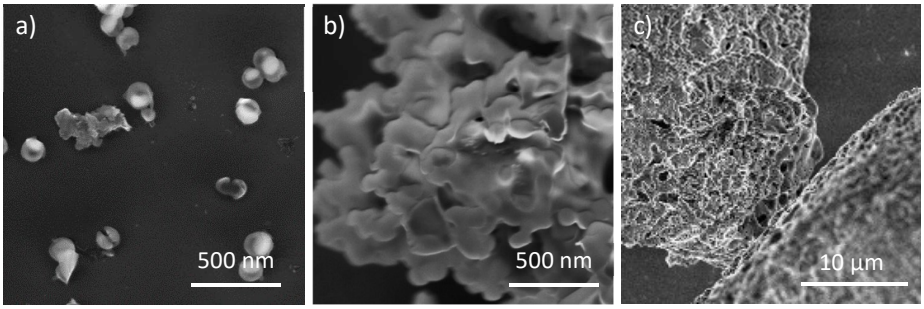

Fig.34 FE-SEM images of Bi_2O_3:Nd^{3+}@SiO_2 NPs with a 2%at. content of Nd^{3+}, calcined at different temperatures: 800°C (a), 900°C (b) and 1000°C (c), respectively.

5.4 Nd^{3+}-doped $Bi_{12}SiO_{20}$

$Bi_{12}SiO_{20}$ crystals doped with RE^{3+} ions gained great attention because of favorable photoconductive, photorefractive, electro-optic and magneto-optic properties[83-85]. Particular interest has been focused on the influence of different doping ions to optimize the optical properties on the basis of practical applications[86,87]. In fact, intrinsic defects, as well as impurity doping, play an important role in the optical behavior of materials[88].

The three-steps synthetic route adopted to obtain the other two BSO phases, respectively Bi_2SiO_5 (5.2.1) and $Bi_4Si_3O_{12}$ (5.3.1), proved to be inefficient for the synthesis of the $Bi_{12}SiO_{20}$ crystalline phase. Thus, we decided to produce it in the bulk form.

$Bi_{12}SiO_{20}$ materials are usually synthesized in the form of single crystals by the Czochralski method[87,89-95]. The reported wet chemical routes comprise the hydrothermal method[96], the sol–gel process[97,98], the impregnation method[99] and the solution crystallization method[100]. Similarly, also the molten state method is very common[101,102]. Little is reported on solid phase reaction synthesis[90], and as far as we know, it has not yet been reported the use of $Bi_{12}SiO_{20}$ as a luminescent sensor for contactless thermometry to probe, for instance, the dissipations *in situ* of integrated chips or to follow the catalytic reactions[41].

5.4.1 Sample preparation

Materials

Bismuth oxide powder (Bi_2O_3, 99.9%, size 10 μm), silicon dioxide powder (SiO_2, 99.8%, size 44 μm), Neodymium(III) nitrate hexahydrate ($Nd(NO_3)_3 \cdot 6H_2O$, 99.9%), purchased from Sigma-Aldrich, and ethanol (CH_3CH_2OH, 99.8%, Fluka) were of analytical grade and used without further purification. The oxide powders were dried in an air oven before the preparation of the samples.

Synthesis of $Bi_{12}SiO_{20}$ powders

Bi_2O_3 and SiO_2 powders were dried and weighed following the molar ratio of 6:1. The powders were mixed using a quartz ball milling machine and then uniaxially pressed with a compression force of about 60 kN, in the form of tablets (d=20 mm, h=3mm). A $Nd(NO_3)_3 \cdot 6H_2O$ stock solution, with fixed molarity, was prepared by dissolving the salt in a certain amount of ethanol. The Nd^{3+}-doped sample was then prepared simply by adding the proper volume of the stock solution to the oxide powders, followed by wet-mixing in a quartz jar. Sintering was carried out in air in a chamber furnace (Ashing Furnace AAF, with a Carbolite Gero 301 controller), with a heating rate of 10°C/min. As reported by Fu *et al.*[90], the solid-phase reaction between monoclinic α-Bi_2O_3 and hexagonal SiO_2 is a diffusion-controlled process, and the reaction is affected by both temperature and time. In this case we kept the same duration for each heat treatment, while varying the final temperature.

5.4.2 Morphological and structural analysis

The X-ray powder diffraction patterns (XRPD) of mixed oxide powders, calcined at different temperatures are given in Fig.35a. As it can be observed, the patterns relative to thermal treatments at temperatures ≤500°C correspond to the monoclinic structure of Bi_2O_3. At 500°C only a small percentage of $Bi_{12}SiO_{20}$ starts to appear. With increasing temperatures (600-700°C) this fraction rises, while Bi_2O_3 reflections tend to disappear. The pattern of the sample calcined at 750°C can be indexed to a body centred cubic structure with the *I-23* space group (ICSD#28443) (Fig.35b). At this temperature the crystal phase is pure, and the current doping level does not cause any peak shift or second phase reflections. The elementary cubic cell consists of two structural units, SiO_4 tetrahedral (located at the corners and centre of the cube) and BiO_n distorted octahedra (n = 7) connecting the SiO_4 groups. It has been previously determined that Ln^{3+} ions, in particular Nd^{3+} ions, occupy six-fold oxygen coordination Bi^{3+} distorted crystallographic sites with C1 symmetry[103]. Some authors, however, have reported the presence of a quite different additional Nd^{3+} centre whose crystal field symmetry is nearly cubic[104].

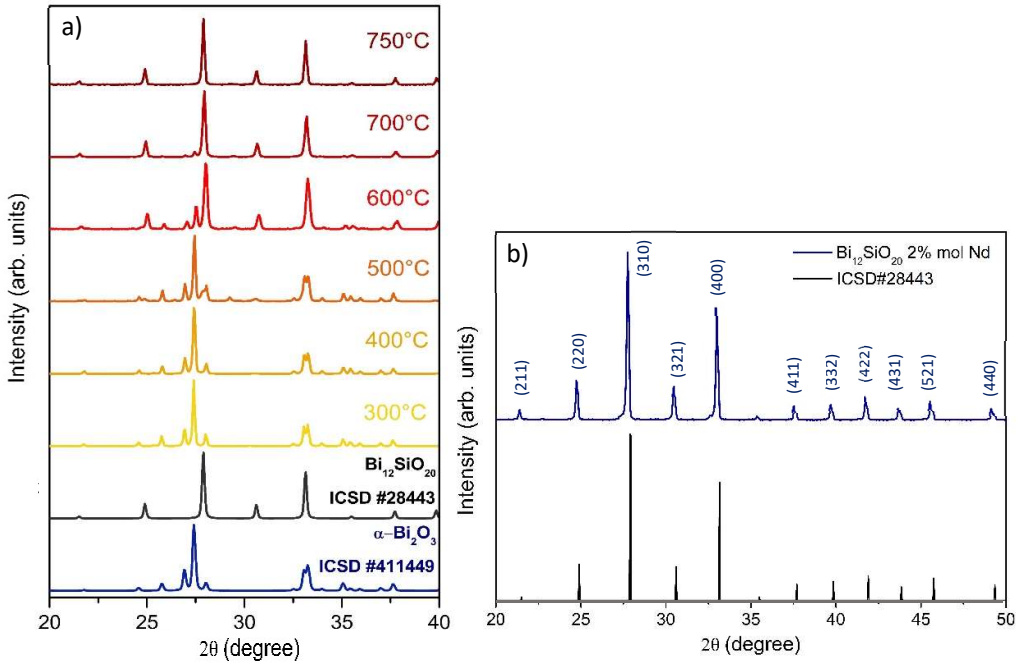

Fig.35 XRPD patterns of (a) Bi_2O_3-SiO_2 powders sintered at increasing temperatures, compared to the α-Bi_2O_3 (ICSD#411449) and $Bi_{12}SiO_{20}$ crystal structures (ICSD#28443), (b) $Bi_{12}SiO_{20}$:Nd^{3+} bulk powders, with a 2%at. Nd^{3+}-content compared to the $Bi_{12}SiO_{20}$ crystal structure (ICSD#28443).

5.4.3 Optical characterization

Emission and excitation spectra of the 2%at. Nd^{3+}-doped $Bi_{12}SiO_{20}$ sample are reported in Fig.36a. Under 590 nm light excitation, at room temperature, this material shows an intense Nd^{3+} emission band at around 900 nm, within the first biological window, relative to the $^4F_{3/2} \rightarrow {}^4I_{9/2}$ transition, while $^4F_{5/2} \rightarrow {}^4I_{9/2}$ transition at 810 nm results extinguished at room temperature. Moreover, two characteristic emission bands are visible in the NIR region: $^4F_{3/2} \rightarrow {}^4I_{11/2}$ at about 1080 nm and $^4F_{3/2} \rightarrow {}^4I_{13/2}$ around 1350 nm, respectively. The excitation spectrum shows various absorption lines relative to Nd^{3+} as schematically reported in the energy level diagram in Fig.36b.

The comparison between spectral shapes of the three different Nd^{3+}-doped bismuth silicate (BSO) phases is reported in Fig.37. As it can be observed although the spectral shapes are similar, each phase owns its characteristic features that potentially allow to qualitatively distinguish the different crystal structures.

Fig.38a shows the diffuse reflectance spectrum and the Kubelka–Munk function of the $(Bi_{0.98}Nd_{0.02})_{12}SiO_{20}$ sample, in which the absorption peaks of Nd^{3+} are clearly detectable. Considering the Kubelka–Munk function F(R) and the indirect bandgap nature of this semiconductor[100], the bandgap energy was estimated by extrapolating the intercept of the fitted straight line at F(R)=0 in the $(F(R)\cdot h\nu)^{1/2}$ versus Energy (hν) plot (Fig.38b). An energy value of 2.9 eV was obtained for the sample, in agreement with typical values reported for $Bi_{12}SiO_{20}$[105-108].

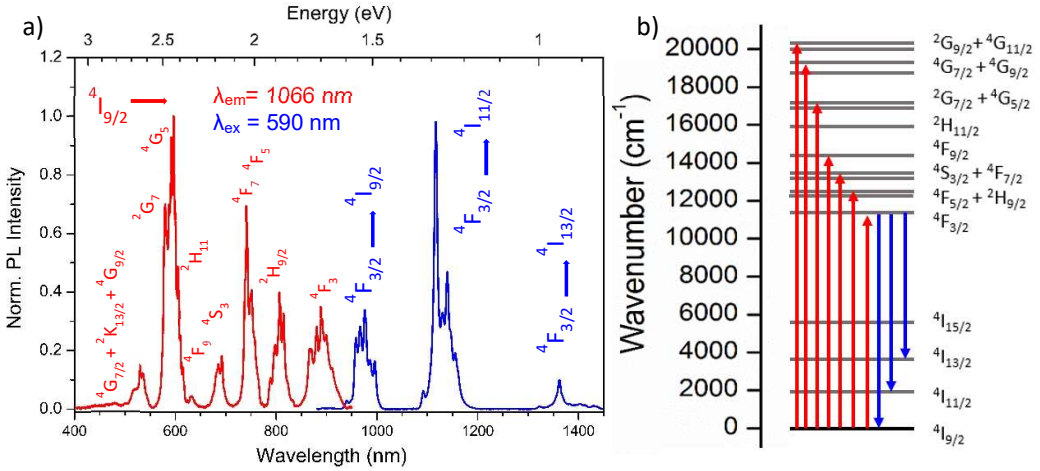

Fig.36 (a) Emission (blue line) and excitation (red line) spectra of $(Bi_{0.98}Nd_{0.02})_{12}SiO_{20}$ NPs and (b) Nd^{3+} schematic energy level diagram with typical absorption and emission lines indicated as red and blue arrows, respectively.

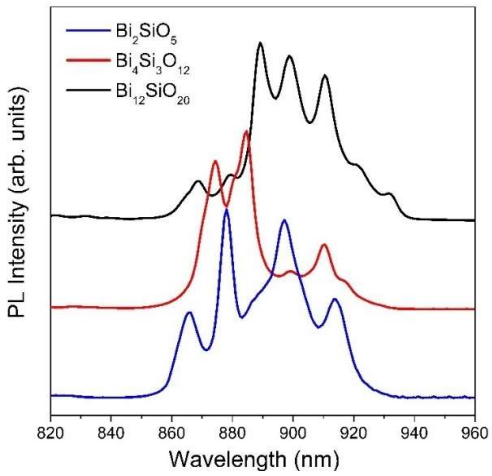

Fig.37 Spectral shapes of the three different Nd^{3+}-doped BSO compounds: Bi_2SiO_5 (blue line), $Bi_4Si_3O_{12}$ (red line) and $Bi_{12}SiO_{20}$ (black line).

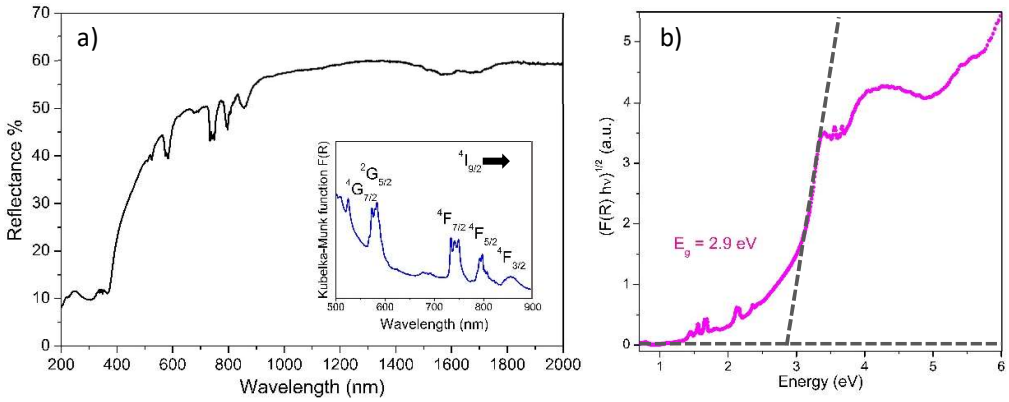

Fig. 38 (a) Diffuse reflectance spectra with the Kubelka–Munk function (inset) and (b) Tauc plot for the bandgap estimation of $(Bi_{0.98}Nd_{0.02})_{12}SiO_{20}$ powders.

5.5 Conclusions

In this Chapter, we have discussed the synthesis of highly monodispersed Ln^{3+} doped Bi silicate UCNPs obtained through a three steps strategy: synthesis of Ln-doped Bi_2O_3 NPs, silica coating on the NPs surface and finally a thermal treatment to obtain the desired BSO crystalline phase.

The main purpose of this study was to obtain homogeneous nanophosphors with improved control over chromaticity output. We investigated various synthetic parameters, such as the precipitant and the capping agent to be added during the hydrothermal synthesis, the optimal concentration of dopants, the thickness of the silica coating and the calcination temperature, to obtain upconverting Ln-doped $Bi_2SiO_5@SiO_2$ NPs of the desired size and shape.

We showed the structural and morphological evolution of this core-shell nanosystem, demonstrating (i) the stabilization of the metastable Bi_2SiO_5 phase triggered by the local reactivity between Bi_2O_3 and SiO_2 and (ii) the unexpected formation of a unique double layered $Bi_2SiO_5@SiO_2$ hollow nanosystem, composed by a crystalline Bi_2SiO_5 core and a glassy silica shell. Moreover, we evidenced a difference in the crystalline phase stabilization between the doped and undoped samples, belonging to different space groups, that arises from the doping effect.

The successful incorporation of lanthanide ions promoted the activation of PL emission in the VIS range under near-IR excitation. Thus, we investigated the UC PL properties of the system, showing the possibility to finely control of the chromaticity output in the whole CIE diagram by means of an accurate choice of the type and relative concentration of lanthanide ions.

Moreover, NIR-emitting $Bi_2SiO_5@SiO_2$ and $Bi_4Si_3O_{12}@SiO_2$ NPs were synthetized following the same three-steps procedure, by doping instead with Nd^{3+}-ions. In this case, during the last step, the nanoparticles were calcined at different temperatures, 700 and 900 °C respectively, to obtain the two different crystalline phases. However, the thermal treatment at a higher temperature had a side effect, causing the coalescence and consequent aggregation of the nanoparticles.

On the other hand, the $Bi_{12}SiO_{20}$ bulk phase was obtained by solid phase reaction synthesis, by mixing the starting oxide powders and sintering the obtained tablets.

Materials and Methods

Experimental Details. Size and morphology of the synthetized powders were observed using a Carl Zeiss Sigma VP Field Emission Scanning Electron Microscope (FE-SEM), equipped with a Bruker Quantax 200 microanalysis detector for EDS. The EDS spectra were recorded under the same conditions (20 keV) for all the samples.

Transmission Electron Microscopy (TEM) images were taken at 300 kV with a JEOL JEM-3010 instrument with ultrahigh resolution (UHR) pole-piece (0.17 nm point resolution), equipped with a Gatan slow scan CCD camera (model 794). The powder was dispersed in ethanol by means of sonication and then deposited onto a holey carbon film coated copper grid.

The nitrogen physisorption measurements have been collected at liquid nitrogen temperature (−196°C) using a Micromeritics ASAP 2010 volumetric adsorption analyzer. The Brunauer Emmett Teller (BET) equation has been used to calculate the specific surface area from the adsorption branches data.
The Diffuse Reflectance Fourier Transform Infrared Spectroscopy (DRIFT-IR) spectra with a NEXUS-FT-IR instrument implementing a Nicolet AVATAR Diffuse Reflectance accessory have been recorded.
The Thermogravimetric Analysis (TGA) and the Differential Scanning Calorimetry (DSC) have been performed with a Linseis TGA 1000 apparatus in air, from 25 to 900°C with a heating rate of 10°C min^{-1}. Samples (around 25 mg) were dried in advance and then placed in an alumina crucible.
X-ray powder diffraction (XRPD) measurements were performed by means of a Philips X'Pert diffractometer with a PW 1319 vertical goniometer with Bragg–Brentano geometry, equipped with a focusing graphite monochromator and a proportional counter with a pulse-height discriminator. Nickel-filtered Cu Kα radiation and a step-by-step technique were employed (steps of 0.05° in 2θ), with a collection time of 30 s per step.
Upconversion photoluminescence (UCPL) spectroscopy measurements on Bi_2SiO_5:Ln@SiO_2 UCNPs were collected exciting with a CNI MDL-III-980 diode laser as 980 nm photon pumping source, with output power of 2 W over a spot of 5×8 mm^2 (power density of 5 W/cm^2). PL measurements on Nd-doped samples were performed with a 590 nm LED as excitation source. The emission spectra were acquired by means of a QE65 Pro Ocean Optics spectrometer. Neutral density filters were used to attenuate the pumping radiation.

Further XRD measurements were performed at the Materials Characterisation by X-ray diffraction (MCX) beamline of Elettra Synchrotron in Trieste.

The diffuse reflectance spectra were measured by means of a spectrophotometer (UV3600, Shimadzu) equipped with an integrating sphere. Barium sulfate is used as a standard for calibration.
Photoluminescence excitation (PLE) spectra were measured by an InGaAs photodiode (IGA-030-H, Electro-Optical System Inc.) coupled with a short-cut (990 nm) and a long-cut (1300 nm) filter, a monochromator (SpectraPro-300i, Acton Research Corporation) to tune the excitation wavelengths and a 100 W halogen lamp (MHAA-100W, Moritex Corporation) as excitation source.
These measurements have been performed at the Graduate School of Human and Environmental Studies of Kyoto University (Japan).

References

[1] Walsh, A., Watson, G.W., Payne, D.J., Edgell, R.G., Guo, J., Glans, P.A., Learmonth, T., Smith, K.E., Electronic Structure of the α and δ Phase of Bi_2O_3: A Combined ab initio and X-Ray Spectroscopy Study, *Phys. Rev. B*, **2006**, 73, 235104.

[2] Sanna, S., Esposito, V., Andreasen, J. W., Hjelm, J., Zhang, W., Kasama, T., Simonsen, S. B., Christensen, M., Linderoth, S., Pryds, N., Enhancement of the Chemical Stability in Confined δ-Bi_2O_3, *Nat. Mater.*, **2015**, 14, 500-504.

[3] Zaccariello, G., Back, M., Zanello, M., Canton, P., Cattaruzza, E., Riello, P., Alimonti, A., Benedetti, A., Formation and Controlled Growth of Bismuth Titanate Phases into Mesoporous Silica Nanoparticles: An Efficient Self-Sealing Nanosystem for UV Filtering in Cosmetic Formulation, *ACS Appl. Mater. Interfaces,* **2017**, 9, 1913-1921.

[4] Zaccariello, G., Back, M., Benedetti, A., Canton, P., Cattaruzza, E., Onoda, H., Glisenti, A., Alimonti, A., Bocca, B., Riello, P., Bismuth titanate-based UV filters embedded mesoporous silica nanoparticles: Role of bismuth concentration in the self-sealing process, *J. Colloid Interface Sci.,* **2019**, 549, 1-8.

[5] Kato, D., Hongo, K., Maezono, R., Higashi, M., Kunioku, H., Yabuuchi, M., Suzuki, H., Okajima, H., Zhong, C., Nakano, K., Abe, R., Kageyama, H., Valence Band Engineering of Layered Bismuth Oxyhalides towards Stable Visible-Light Water Splitting: Madelung Site Potential Analysis, *J. Am. Chem. Soc.,* **2017**, 139, 18725-18731.

[6] Suzuki, H., Kunioku, H., Higashi, M., Tomita, O., Kato, D., Kageyama, H., Abe, R., Lead Bismuth Oxyhalides $PbBiO_2X$ (X = Cl, Br) as Visible-Light-Responsive Photocatalysts for Water Oxidation: Role of Lone-Pair Electrons in Valence Band Engineering, *Chem. Mater.,* **2018**, 30, 5862-5869.

[7] Back, M., Trave, E., Mazzucco, N., Riello, P., Benedetti, A., Tuning the Upconversion Light Emission by Bandgap Engineering in Bismuth Oxide-Based Upconverting Nanoparticles, *Nanoscale,* **2017**, 9, 6353-6361.

[8] Back, M., Trave, E., Riello, P., Joos, J. J., Insight into the Upconversion Luminescence of Highly Efficient Lanthanide-Doped Bi_2O_3 Nanoparticles, *J. Phys. Chem. C,* **2018**, 122, 7389-7398.

[9] Back, M., Trave, E., Zaccariello, G., Cristofori, D., Canton, P., Benedetti, A., Riello, P., Bi_2SiO_5@g-SiO_2 Upconverting Nanoparticles: A Bismuth-Driven Core-Shell Self-Assembly Mechanism, *Nanoscale,* **2019**, 11, 675-687.

[10] Back, M., Ueda, J., Lahtine, E., Cassandro, L., Cristofori, D., Ottini, R., Riello, P., Sponchia, G., Asami, K., Tanabe, S., Trave, E., Lanthanide-Doped Bismuth-Based Fluoride Nanocrystalline Particles: Formation, Spectroscopic Investigation, and Chemical Stability, *Chem. Mater.,* **2019**, 31, 8504-8514.

[11] Back, M., Trave, E., Ueda, J., Tanabe, S., Ratiometric Optical Thermometer Based on Dual Near-Infrared Emission in Cr^{3+}-Doped Bismuth-Based Gallate Host, *Chem. Mater.,* **2016**, 28, 8347-8356.

[12] Back, M., Ueda, J., Brik, M. G., Lesniewski, T., Grinberg, M., Tanabe, S., Revisiting Cr^{3+}-Doped $Bi_2Ga_4O_9$ Spectroscopy: Crystal Field Effect and Optical Thermometric Behaviour of Near-Infrared-Emitting Singly-Activated Phosphors, *ACS Appl. Mater. Interfaces,* **2018**, 10, 41512-41524.

[13] Rabin, O., Perez, J.M., Grimm, J., Wojtkiewicz, G., Weissleder, R., An X-ray Computed Tomography Imaging Agent Based on Long-Circulating Bismuth Sulphide Nanoparticles, *Nat. Mater.,* **2006**, 5, 118-122.

[14] Liu, J., Zheng, X., Yan, L., Zhou, L., Tian, G., Yin, W., Wang, L., Liu, Y., Hu, Z., Gu, Z., Chen, C., Zhao, Y., Bismuth Sulfide Nanorods as a Precision Nanomedicine for in Vivo Multimodal Imaging-Guided Photothermal Therapy of Tumor, *ACS Nano* **2015**, 9, 696-707.

[15] Li, Z., Hu, Y., Howard, K. A., Jiang, T., Fan, X., Miao, Z., Sun, Y., Besenbacher, F., Yu, M., Multifunctional Bismuth Selenide Nanocomposites for Antitumor Thermo-Chemotherapy and Imaging, *ACS Nano,* **2016**, 10, 984-997.

[16] Li, Z., Hu, Y., Miao, Z., Xu, H., Li, C., Zhao, Y., Li, Z., Chang, M., Ma, Z., Sun, Y., Besenbacher, F., Huang, P., Yu, M., Dual-Stimuli Responsive Bismuth Nanoraspberries for Multimodal Imaging and Combined Cancer Therapy, *Nano Lett.* **2018**, 18, 6778-6788.

[17] Chen, J., Yang, X. Q., Qin, M. Y., Zhang, X. S., Xuan, Y., Zhao, Y. D., Hybrid nanoprobes of bismuth sulfide nanoparticles and CdSe/ZnS quantum dots for mouse computed tomography/fluorescence dual mode imaging, *J. Nanobiotechnology*, **2015**, 13, 76.

[18] Rabin, O., Manuel Perez, J., Grimm, J., Wojtkiewicz, G., Weissleder, R., An X-ray computed tomography imaging agent based on long-circulating bismuth sulphide nanoparticles, *Nat Mater.,* **2006**, 5(2), 118-22.

[19] de Swart, J., Chan, H. S., Goorden, M. C., Morgenstern, A., Bruchertseifer, F., Beekman, F. J., de Jong, M., Konijnenberg, M. W., Utilizing high-energy γ-photons for high-resolution 213Bi SPECT in Mice, *J. Nucl. Med.,* **2016**, 57(3), 486-492.

[20] Zheng, X., Shi, J., Bu, Y., Tian, G., Zhang, X., Yin, W., Gao, B., Yang, Z., Hu, Z., Liu, X., Yan, L., Gu, Z., Zhao, Y., Silica-coated bismuth sulfide nanorods as multimodal contrast agents for a non-invasive visualization of the gastrointestinal tract, *Nanoscale*, **2015**, 7, 12581.

[21] Mears, R. J., Reekie, L., Jauncey, I. M., Payne, D. N., Low-Noise Erbium-Doped Fibre Amplifier Operating at 1.54 μm, *Electron. Lett*., **1987**, 23, 1026-1028.

[22] Cattaruzza, E., Back, M., Battaglin, G., Riello, P., Trave, E., Er-Doped Alumina Crystalline Films Deposited by Radiofrequency Magnetron Co-Sputtering, *Opt. Mater*., **2011**, 33, 1135-1138.

[23] Tanabe, S., Glass and Rare-Earth Elements: A Personal Perspective, *Int. J. Appl. Glass Sci.,* **2015**, 6, 305-328.

[24] Trave, E., Back, M., Cattaruzza, E., Gonella, F., Enrichi, F., Cesca, T., Kalinic, B., Scian, B., Bello, V., Maurizio, C., Mattei, G., Control of Silver Clustering for Broadband Er^{3+} Luminescence Sensitization in Er and Ag Co-Implanted Silica, *J. Lumin*., **2018**, 197, 104-111.

[25] Snitzer, E., Optical Maser Action of Nd^{3+} in a Barium Crown Glass, *Phys. Rev. Lett*., **1961**, 7, 444-446.

[26] Geusic, J. E., Marcos, H. M., Van Uitert, L. G., Laser Oscillations in Nd-Doped Yttrium Aluminium, Yttrium Gallium and Gadolinium Garnets, *Appl. Phys. Lett*., **1964**, 4, 182-184.

[27] George, N.C., Denault, K.A., Seshadri, R., Phosphors for solid-state white lighting, *Annu. Rev. Mater. Res*. **2013**, 43, 481-501.

[28] Wang, L., Xie, R.-J., Suehiro, T., Takeda, T., Hirosaki, N., Down-conversion nitride materials for solid state lighting: recent advances and perspectives, *Chem. Rev*., **2018**, 118, 1951-2009.

[29] Zhou, B., Shi, B., Jin, D., Liu, X., Controlling Upconversion Nanocrystals for Emerging Applications, *Nat. Nanotechnol*., **2015**, 10, 924-936.

[30] Zhou, J., Leaño Jr., J. L., Liu, Z., Jin, D., Wong, K.-L., Liu, R.-S., Bünzli, G.-C. G., Impact of Lanthanide Nanomaterials on Photonic Devices and Smart Applications, *Small*, **2018**, 14, 1801882.

[31] Brites, C. D. S., Millán, A., Carlos, L. D., Lanthanide in Luminescent Thermometry in Handbook on the Physics and Chemistry of Rare Earths, Bünzli, J.-C. G., Pecharsky, V. K., Eds., Elsevier: Amsterdam, **2016**, Vol. 49, pp 339-427.

[32] Dramićanin, M., Luminescence Thermometry: Methods, Materials, and Applications, Woodhead Publishing Series in Electronic and Optical Materials, Woodhead Publishing, **2018**.

[33] Jaque, D., Vetrone, F., Luminescence Nanothermometry. *Nanoscale*, **2012**, 4, 4301-4326.

[34] Quintanilla, M., Liz-Marzán, L. M., Guiding Rules for Selecting a Nanothermometer, *Nano Today*, **2018**, 19, 126-145.

[35] Andres, J., Hersch, R. D., Moser, J.-E., Chauvin, A.-S., A New Anti-Counterfeiting Feature Relying on Invisible Luminescent Full Color Images Printed with Lanthanide-Based Inks, *Adv. Funct. Mater*., **2014**, 24, 5029-5036.

[36] Marin, R., Back, M., Mazzucco, N., Enrichi, F., Frattini, R., Benedetti, A., Riello, P., Unexpected Optical Activity of Cerium in Y_2O_3:Ce^{3+}, Yb^{3+}, Er^{3+} Up and Down-Conversion System, *Dalton Trans*., **2013**, 42, 16837−16845.

[37] Vetrone, F., Naccache, R., Zamarrón, A., de la Fuente, A. J., Sanz-Rodríguez, F., Martinez Maestro, L., Martin Rodriguez, E., Jaque, D., García Solé, J., Capobianco, J. A., Temperature Sensing Using Fluorescent Nanothermometers, *ACS Nano*, **2010**, 4, 3254-3258.

[38] Zhu, X., Feng, W., Chang, J., Tan, Y.-W., Li, J., Chen, M., Sun, Y., Li, F., Temperature-Feedback Upconversion Nanocomposite for Accurate Photothermal Therapy at Facile Temperature, *Nat. Commun*., **2016**, 7, 1-10.

[39] Aigouy, L., Tessier, G., Mortier, M., Charlot, B., Scanning Thermal Imaging of Microelectronic Circuits with a Fluorescent Nanoprobe, *Appl. Phys. Lett*., **2005**, 87, 184105.

[40] Back, M., Ueda, J., Xu, J., Murata, D., Brik, M. G., Tanabe S. Ratiometric Luminescent Thermometers with a Customized Phase-Transition-Driven Fingerprint in Perovskite Oxides, *ACS Appl. Mater. Interfaces*, **2019**, 11, 38937-38945.

[41] Geitenbeek, R. G., Nieuwelink, A.-E., Jacobs, T. S., Salzmann, B. B. V., Goetze, J., Meijerink, A., Weckhuysen, B. M., In Situ Luminescence Thermometry to Locally Measure Temperature Gradients during Catalytic Reactions, *ACS Catal*., **2018**, 8, 2397-2401.

[42] Qin, F., Zhao, H., Li, G., Yang, H., Li, J., Wang, R., Liu, Y., Hu, J., Sun, H., Chen, R., Size-Tunable Fabrication of Multifunctional Bi_2O_3 Porous Nanospheres for Photocatalysis, Bacteria Inactivation and Template-Synthesis, *Nanoscale*, **2014**, 6, 5402-5409.

[43] Thanh, N. T. K., Maclean, N., Mahiddine, S., Mechanisms of Nucleation and Growth of Nanoparticles in Solution, *Chem. Rev*., **2014**, 114, 7610-7630.

[44] Wang, Y. W., Hong, B. H., Kim, K. S., Size control of semimetal bismuth nanoparticles and the UV− visible and IR absorption spectra, *J. Phys. Chem. B*, **2005**, 109, 7067.

[45] Wang, Y., Chen, J., Chen, L., Chen, Y.-B., Wu, L.-M., Shape-Controlled Solventless Syntheses of Nano Bi Disks and Spheres, *Cryst. Growth Des*., **2010**, 10(4), 1578-1584

[46] Koczkur, K. M., Mourdikoudis, S., Polavarapu, L., Skrabalak, S. E., Polyvinylpyrrolidone (PVP) in Nanoparticle Synthesis, *Dalton Trans.,* **2015**, 44, 17883-17905.

[47] Rouquerol, F., Rouquerol, J., Sing, K., Adsorption by powder & porous solids: Principles, methodology and applications, Academic Press, London, **1999**, Chapter 1.

[48] Du, Y. K., Yang, P., Mou, Z. G., Hua, N. P., Jiang, L., Thermal decomposition behaviors of PVP coated on platinum nanoparticles, *J. Appl. Polym. Sci*., **2006**, 99, 23-26.

[49] Datta, R. K., Meehan, J. P., The System Bi_2O_3-R_2O_3 (R=Y,Gd)., *Z. Anorg. Allg. Chem.,* **1971**, 383, 328-337.

[50] Wang, Z., Meijerink. A., Concentration Quenching in Upconversion Nanocrystals, *The journal of physical chemistry C: Nanomaterials and interfaces*, **2018**, 122(45), 26298-26306.

[51] Stöber, W., Fink, A., Bohn, E., Controlled growth of monodisperse silica spheres in the micron size range, *J. Colloid Interface Sci*., **1968**, 26, 62-69.

[52] Taniguchi, H., Kuwabara, A., Kim, J., Kim, Y., Moriwake, H., Kim, S., Hoshiyama, T., Koyama, T., Mori, S., Takata, M., Hosono, H., Inaguma, Y., Itoh, M., Ferroelectricity Driven by Twisting of Silicate Tetrahedral Chains, *Angew. Chem. Int*., **2013**, 52, 8088-8092.

[53] Georges, S., Goutenoire, F., Lacorre, P., Crystal Structure of Lanthanum Bismuth Silicate $Bi_{2-x}La_xSiO_5$ (x~0.1), *J. Solid State Chem*., **2006**, 179, 4020-4028.

[54] Taniguchi, H., Tatewaki, S., Yasui, S., Fujii, Y., Yamaura, J., Terasaki, I., Structural Variations and Dielectric Properties of $(Bi_{1-x}La_x)_2SiO_5$ ($0 \leq x \leq 0.1$): Polycrystallines Synthesized by Crystallization of Bi-Si-O and Bi-La-Si-O Glasses, *Phys. Rev. Mater*., **2018**, 2, 045603.

[55] Pollnau, M., Gamelin, D. R., Lüthi, S. R., Güdel, H. U., Hehlen, M. P., Power dependence of upconversion luminescence in lanthanide and transition-metal-ion systems, *Physical Review B*, **2000**, 61(5), 3337–3346.

[56] Liu, D., Wang, J., Zhang, M., Liu, Y., Zhu, Y., A superior photocatalytic performance of a novel Bi_2SiO_5 flower-like microsphere via a phase junction, *Nanoscale*, **2014**, 6, 15222-15227.

[57] G. Chen, T. Y. Ohulchanskyy, S. Liu, W.-C. Law, F. Wu, M. T. Swihart, H. Agren, P. N. Prasad, Core/Shell $NaGdF_4:Nd^{3+}/NaGdF_4$ Nanocrystals with Efficient Near-Infrared to Near-Infrared Downconversion Photoluminescence for Bioimaging Applications, *ACS Nano*, **2012**, 6, 2969.

[58] Rocha, U., Kumar, K. U., Jacinto, C., Villa, I., Sanz-Rodriguez, F., del Carmen Iglesias de la Cruz, M., Juarranz, A., Carrasco, E., van Veggel, F. C. J. M., Bovero, E., Garcia Sole J., Jaque D., Neodymium-doped LaF_3 nanoparticles for fluorescence bioimaging in the second biological window, *Small*, **2014**, 10, 1141.

[59] Wang, R., Li, X., Zhou, L., Zhang, F., Epitaxial seeded growth of rare-earth nanocrystals with efficient 800 nm near-infrared to 1525 nm short-wavelength infrared downconversion photoluminescence for in vivo bioimaging. *Angew. Chem., Int. Ed*. **2014**, 53, 12086.

[60] I. Villa, A. Vedda, I. X. Cantarelli, M. Pedroni, F. Piccinelli, M. Bettinelli, A. Speghini, M. Quintanilla, F. Vetrone, U. Rocha, C. Jacinto, E. Carrasco, F. Sanz Rodriguez, A. Juarranz, B. del Rosal, D. H. Ortgies, P. H. Gonzalez, J. G. Sole, D. J. Garcia, 1.3 μm emitting $SrF_2:Nd^{3+}$ nanoparticles for high contrast *in vivo* imaging in the second biological window, *Nano Res*., **2015**, 8, 649.

[61] W. Shao, G. Chen, A. Kuzmin, H. L. Kutscher, A. Pliss, T. Y. Ohulchanskyy, P. N. Prasad, Tunable Narrow Band Emissions from Dye-Sensitized Core/Shell/Shell Nanocrystals in the Second Near-Infrared Biological Window, *J. Am. Chem. Soc*., **2016**, 138, 16192.

[62] Dai, Y., Yang, D. P., Yu, D. P., Cao, C., Wang, Q. H., Xie, S. H., Shen, L., Feng, W., Li, F. Y., Mussel-Inspired Polydopamine-Coated Lanthanide Nanoparticles for NIR-II/CT Dual Imaging and Photothermal Therapy, *ACS Appl. Mater. Interfaces*, **2017**, 9, 26674.

[63] Fan, Y., Wang, P., Lu, Y., Wang, R., Zhou, L., Zheng, X., Li, X., Piper, J.A., Zhang, F., Lifetime-engineered NIR-II nanoparticles unlock multiplexed in vivo imaging, *Nat. Nanotechnol*., **2018**, 13(10), 941-946.

[64] Powell, R. C., Physics of Solid-State Laser Materials, *Springer-Verlag*, New York, **1998**.

[65] Campbell, J. H., Suratwala, T. I., Nd-Doped Phosphate Glasses for High-Energy/High-Peak-Power Lasers, *J. Non-Cryst. Solids*, **2000**, 318, 318– 341.

[66] Santos, D. R. S., Santos, C. N., Camargo, A. S. S., Silva, W. F., Santos, W. Q., Vermelho, M. V. D., Astrath, N. G. C., Malacarne, L. C., Li, M. S., Hernandes, A. C. et al., Thermo-optical Characteristics and Concentration Quenching Effects in Nd^{3+} Doped Yttrium Calcium Borate Glasses, *J. Chem. Phys*., **2011**, 134, 124503.

[67] Lupei, V., Lupei, A., Georgescu, S., Taira, T., Sato, Y., Ikesue, A., The Effect of Nd Concentration on the Spectroscopic and Emission Decay Properties of Highly Doped Nd:YAG, *Ceramics Phys. Rev. B: Condensed Matter Phys.,* **2001,** 64, 092102.

[68] Henderson, B., Imbusch, G. F., Optical Spectroscopy of Inorganic Solids, *Oxford Science Publications*, New York, **2006**.

[69] Rocha, U., Jacinto da Silva, C., Ferreira Silva, W., Guedes, I., Benayas, A., Martinez Maestro, L., Acosta Elias, M., Bovero, V., van Veggel, F. C. J. M., García Solé, J. A., Jaque, D. Subtissue thermal sensing based in neodymium-doped LaF_3 nanoparticles, *ACS Nano,* **2013**, 7, 1188−1199.

[70] Kuwabara, H. Taniguchi, H. Moriwake and M. Itoh, The 5th International Symposium on Advanced Microscopy and Theoretical Calculations Book of abstract, **2016**, 4, 69.

[71] Park, J., Kim, B.G., Mori, S., Oguchi, T., Tetrahedral tilting and ferroelectricity in Bi_2AO_5 (A=Si, Ge) from first principles calculations, *Journal of Solid State Chemistry*, **2016**, 235, 68- 75.

[72] Zhang, L., Wang, W., Sun, S., Xu, J. , Shang, M., Ren, J., Hybrid Bi_2SiO_5 mesoporous microspheres with light response for environment decontamination, *Applied Catalysis B: Environmental*, **2010**, 100, 97-101.

[73] Back, M., Trave, E., Zaccariello, G., Cristofori, D., Canton, P., Benedetti, A., Riello, P., Bi_2SiO_5@g-SiO_2 upconverting nanoparticles: a bismuth-driven core-shell self-assembly mechanism, *Nanoscale*, **2019**, 11, 675-687.

[74] Yang, C.-T., Chung, W.-H., Chang, J.-L., Lin, W.-Y., Synthesis and characterization of $Bi_4Si_3O_{12}$, Bi_2SiO_5 and $Bi_{12}SiO_{20}$ by controlled hydrothermal method and their photocatalytic activity, *Journal of the Taiwan Institute of Chemical Engineers*, **2017**.

[75] Wang, J., Zhang, G., Li, J., Wang, K., Novel Three-Dimensional Flowerlike BiOBr/Bi_2SiO_5 p–n Heterostructured Nanocomposite for Degradation of Tetracycline: Enhanced Visible Light Photocatalytic Activity and Mechanism, *ACS Sustainable Chem. Eng*., **2018**, 6(11), 14221.

[76] Fei, Y., Fan, S., Sun, R., Ishii, M., Study on phase diagram of Bi_2O_3-SiO_2 system for Bridgman growth of $Bi_4Si_3O_{12}$ single crystal, *Prog. Cryst. Growth. Charact*., **2000**, 40, 183–8.

[77] Lira, A.C., Camarillo, I., Camarillo, E., Ramos, F., Flores, M., Caldiño, U., Spectroscopic characterization of Er^{3+} transitions in $Bi_4Si_3O_{12}$, *J. Phys.: Condens. Matter*, **2004**, 16, 5925-5936.

[78] Lira, A.C., Ramírez, M.O., García Solé, J., Caldiño, U., Photoluminescence of $Bi_4Si_3O_{12}:Er^{3+}$ crystal excited in the commercial laser diode emission region, *Opt. Mater*., **2007**, 29, 605-609.

[79] Lira, A.C., Martín-Rodríguez, E., Martínez-Martínez, R., Camarillo, I., Muñoz, G.H., García Solé, J., Caldiño, U., Spectroscopy of the $Bi_4Si_3O_{12}:Er^{3+}$ glass for optical amplification and laser application, *Opt. Mater*., **2010**, 32, 1266-1273.

[80] Yang, B., Xu, J., Zhang, Y., Chu, Y., Wang, M., Wen, Y., A yellow emitting phosphor Dy:$Bi_4Si_3O_{12}$ crystal for LED application, *Opt. Mater*., **2014**, 135, 176-179.

[81] Wei, Q., Liu, M., Zhou, Z., Wan, J., Wang, J., Liu, Q., Combinatorial discovery of self-mixing G phosphors $Bi_{4(1-x)}Si_3O_{12}:RE_{4x}^{3+}$ (RE^{3+}=Dy^{3+}, Eu^{3+}) for direct white light emission, *RSC Adv*., **2015**, 5, 85862-85871.

[82] Chen, F., Ju, M., Kuang, X., Yeung, Y., Insights into the Microstructure and Transition Mechanism for Nd^{3+}-Doped $Bi_4Si_3O_{12}$: A Promising Near-Infrared Laser Material, *Inorganic Chemistry*, **2018**, 57(8), 4563–4570.

[83] Gunter, P., Holography, coherent light amplification and optical phase conjugation with photorefractive materials, *Phys. Rep*., **1982**, 93, 199-299.

[84] Rajbenbach, H., Huignard, J., Self-induced coherent oscillations with photorefractive $Bi_{12}SiO_{20}$ amplifier, *Opt. Lett*., **1985**, 10, 137.

[85] Solymar, L., Webb, D. J., Grunnet-Jepsen, A., The Physics and Applications of Photorrefractive Materials, **1996**, Clarendon Press.

[86] Arizmendi, L., Cabrera, J., Agullo-Lopez, F., Characterization of $Bi_{12}GeO_{20}$ processed in a microgravity environment, *Int. J. Optoelectron*, **1992**, 7, 149.

[87] Marinova, V., Veleva, M., Petrova, D., Kourmoulis, I. M., Papazoglou, D. G., Apostolidis, A. G., Vanidhis, E. D., Deliolanis, N.C., Optical properties of $Bi_{12}SiO_{20}$ single crystals doped with 4d and 5d transition elements, *J. Appl. Phys*., **2001**, 89, 2686.

[88] Lira, A., Caldino, U., Ramírez, M. O., Sanz-García, J. A., Bausá, L. E., Site-selective spectroscopy of Er^{3+} ions in the $Bi_{12}SiO_{20}$ piezoelectric crystal, *Journal of Physics: Condensed Matter*, **2011**, 13(48), 11067–11076.

[89] Aldrich, R. E., Hou, S. L., Harvill, M. L., Electrical and optical properties of $Bi_{12}SiO_{20}$, *J. Appl. Phys*., **1971**, 42(1), 493–494.

[90] Fu, S., Ozoe, H., Solid-phase reaction in synthesis of $Bi_{12}SiO_{20}$ source-rods for single-crystal growth in a floating zone**,** *J. Mat. Res*., **1996**, 11(10), 2575–2582.

[91] Xu, H., Zhang, Y., Zhang, H., Yu, H., Pan, Z., Wang, Y., Sun, S., Wang J., Boughton, R.I., Growth and characterization of Nd:$Bi_{12}SiO_{20}$ single crystal, *Optics Communications*, **2012**, 285(19), 3961-3966.

[92] Egorysheva, A. V., Milenov, T. I.., Rafailov, P. M, Thomsen, C., Petrova, R., Skorikov, V.M., Gospodinov, M. M., Lattice distortions in a $Bi_{12}SiO_{20}$ crystal caused by doping with copper, *Solid State Communications*, **2009**, 149(39-40), 1616-1618.

[93] Ramırez, M. O., Lira, A., Sanz Garcıa, J. A., Bausa, L.E., Caldino, U., Optical spectroscopy of Er^{3+}-doped $Bi_{12}SiO_{20}$ piezoelectric crystal, *Journal of Alloys and Compounds,* **2002**, 341, 275–279.

[94] Marinova, V., Liu, R. C., Lin, S. H., Hsu, K. Y., Quasi-nonvolatile storage in Ru-doped $Bi_{12}SiO_{20}$ crystals by two-wavelength holography, *Opt Express*., **2012**, 20(18), 19628-19634.

[95] Skorikov, V. M., Zakharov, I. S., Volkov, V. V., Spirin, E. A., Transmission and Absorption Spectra of $Bi_{12}GeO_{20}$, $Bi_{12}SiO_{20}$, and $Bi_{12}TiO_{20}$ Single Crystals, *Inorganic Materials*, **2002**, 38(2), 172-178.

[96] Chen, C.-C., Yang, C.-T., Chung, W.-H., Chang, J.-L., Synthesis and characterization of $Bi_4Si_3O_{12}$, Bi_2SiO_5, and $Bi_{12}SiO_{20}$ by controlled hydrothermal method and their photocatalytic activity, *Journal of the Taiwan Institute of Chemical Engineers*, **2017**, 78, 157-167.

[97] Bautista-Ruiz, J. H., Olaya-Flórez, J. J., Aperador-Chaparro, W. A., Biocompatibility of bismuth silicate coatings deposited on 316L stainless steel by sol-gel process, *Revista Facultad de Ingeniería*, **2017**, 84, 27-34.

[98] Jain, M., Tripathi, A. K., Goel, T. C., Pillai, P. K. C., Preparation and Characterization of Bismuth Silicate (BSO) Thin Film by the Sol–Gel Technique, *J. Mater. Sci. Lett.,* **1999**, 1(8), 479-481.

[99] Derhachov, M., Moiseienko, V., Kutseva, N., Abu Sal, B., Holze, R., Pliaka, S., Yevchyk, A., Structure, Optical and Electric Properties of Opal-Bismuth Silicate Nanocomposites, *Acta Physica Polonica A*, **2018**, 133(4).

[100] Han, Q., Zhang, J., Wang, X., Zhu, J., Preparing $Bi_{12}SiO_{20}$ crystals at low temperature through nontopotactic solid-state transformation and improving its photocatalytic activity by etching, *J. Mater. Chem. A*, **2015**, 3, 7413.

[101] Lu, J., Wang, X., Jiang, H., Xu, Y., Synthesis of Bismuth Silicate Powders by Molten Salt Method, *Materials and Manufacturing Processes*, **2013**, 28(2), 126-129.

[102] Lu, J. Q., Wang, X. F., Jiang, H. T., Synthesis of Pure $Bi_{12}SiO_{20}$ Powder by Molten Salt Method, *Applied Mechanics and Materials*, **2012**, 182-183, 52-56.

[103] Kaminskii, A. A., Bagaev, S. N., Garcıa Sole, J., Eichler, H. J., Fernandez, J., Jaque, D., Findeisen, J., Balda, R., Agullo Rueda, F., irst Observations of Stimulated Emission and of Stimulated Raman Scattering in Acentric Cubic Nd^{3+}:$Bi_{12}SiO_{20}$ Crystals , *Quantum Electron*, **1999**, 29, 6-8.

[104] Oleaga, A., Balda, R., Fernández, J., Serrano, M. D., & Dieguez, E., Nd^{3+}active sites in $Bi_{12}SiO_{20}$:Nd:V codoped crystals, *Journal of Luminescence*, 1997, 71(4), 305–312.

[105] Kostova, B., Gospodinov, M., Konstantinov, L., Optical absorption of $Bi_{12}SiO_{20}$:M (M = Cr, P, Cr+P), *AIP Conference Proceedings*, **2010**, 1203.

[106] Panchenko, T. V., Dyachenko, A. A., Khmelenko, O. V., Photoluminescence of $Bi_{12}SiO_{20}$ crystals, *Ukrainian journal of physical optics*, **2016**, 17(1), 39-45.

[107] Briat, B., Panchenko, T. V., Bou Rjeily, H., Hamri, A., Optical and magneto-optical characterization of the Al acceptor levels in $Bi_{12}SiO_{20}$, *J. Opt. Soc. Am. B*, **1998**, 15, 2147-2153.

[108] Oberschmid, R., Absorption Centers of $Bi_{12}GeO_{20}$ and $Bi_{12}SiO_{20,}$ *Crystals, Phys. Stat. Sol*., **1985**, 89, 263-270.

CHAPTER 6

Bi_2SiO_5@SiO_2 NPs: assessment of bio-compatibility, reactivity and chemical stability

ABSTRACT: Considering the proposed potential fields of application for lanthanide-doped bismuth silicate-silica core-shell nanoparticles, and their related issues, such as for instance the need for high bio-compatibility and great chemical stability, it was vital to define some essential features of the system under examination.

Here, we report the assessment of few crucial properties of Bi_2SiO_5@SiO_2 NPs, such as toxicity, anti-microbial effect, photochemical reactivity and chemical stability.

The cytotoxicity was tested by exposure of four different cell lines to various agents, such as few starting reagents and the NPs here synthetized. Anti-microbial properties were investigated by plating different bacterial cells on Nutrient Agar containing the nanoparticles to be tested. Photocatalytic reactivity was proved in terms of degradation efficiency towards Methyl Orange dye. Finally, the chemical stability at different pH was assessed upon exposure to acid environments.

Bismuth silicate-silica core-shell nanoparticles proved to be greatly biocompatible, as expected, with low photocatalytic reactivity and high resistance to acid environment up to pH<1. In addition, Bi_2SiO_5@SiO_2 NPs did not exert any significant inhibitory effect towards bacterial cells.

Bismuth-based nanoparticles are attracting much attention in the last decade. Thanks to their excellent optical and electrical properties, cost-effectiveness and low toxicity, they have been proposed for disparate uses, ranging from lighting devices to batteries, photocatalysts, UV filters, fuel cells and recently also for biological applications, as contrast agents for multimodal clinical imaging.
Despite this outstanding success, nano-objects are very sensitive to high temperatures and harsh environments, and such a serious drawback is often limiting their real use in certain fields of application. This is particularly severe in the case of bismuth-based compounds, making the development of highly stable bismuth-based nanoparticles a challenge.
Considering the potential purposes of the system here proposed, i.e. lanthanide-doped bismuth silicate-silica core-shell nanoparticles, as bioimaging and temperature sensing nanoprobes, and the issues related to these fields of application, such as the need for high bio-compatibility and great chemical stability, it became essential to assess some crucial features. Among them are cytotoxic and anti-microbial properties, photocatalytic reactivity and the resistance to acid environments.

6.1 Cell viability assay

The cytotoxicity of some starting reagents, i.e. ethylene glycol and PVP, and of Bi_2O_3, Bi_2O_3@SiO_2 and Bi_2SiO_5@SiO_2 NPs was tested on MRC-5, MDA-MB-231, OvCar3 and HCT-116 cell lines by means of a bioluminescence assay that measures the metabolic capacity to assess cell viability, as a function of the intracellular ATP content[1]. In fact, the amount of ATP is directly proportional to the number of cells present in culture[2-4]. Viable cells under normal conditions maintain a relatively constant amount of ATP through a balance of production/consumption pathways[5]. The capacity for ATP synthesis is lost during cell death and remaining ATP is rapidly hydrolyzed. The decrease in ATP concentration corresponds to a reduction in luciferin–luciferase luminescence[6]. The luciferin-luciferase reaction for this assay is shown in Figure 1. Mono-oxygenation of luciferin is catalyzed by luciferase in the presence of Mg^{2+}, ATP, which is contributed by viable cells, and molecular oxygen. A stable “glow-type” luminescent signal is thus generated.

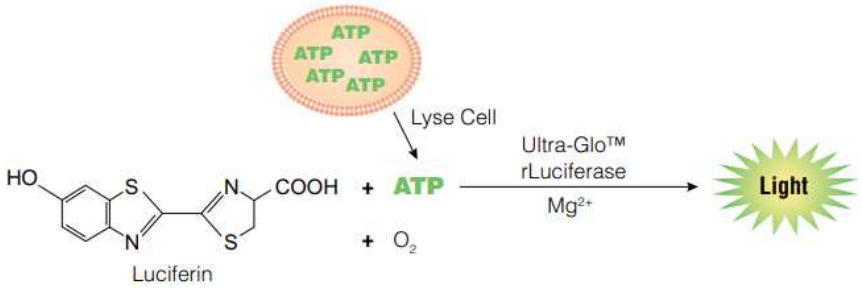

Fig.1 CellTiter-Glo® 2.0 Assay principle from CellTiter-Glo® 2.0 Assay Technical Manual (Promega).

The cells were incubated with suspensions of either starting reagents or NPs with various concentrations (from 0.1 to 100 μg/mL). After the exposure to the tested agents, the luminescence of the luciferase reaction was analyzed. The experiments were performed in triplicate.

According to the ATP assay over 4 different cell lines in Fig.2 a, b, c and d, the same concentration of the various types of nanoparticles caused a difference in cell viability. In fact, Bi_2O_3 NPs showed a larger effect on reducing cell viability than Bi_2O_3@SiO_2 NPs did, which became even larger respect to Bi_2SiO_5@SiO_3 NPs. The results suggest that unwashed ethylene glycol on the surface of Bi_2O_3 NPs, which presence was earlier confirmed by FT-IR and TG measurements (see Fig. 6 a, b in Chapter 5), could be related to the cytotoxic effect. As expected, in vitro experiments showed that Bi_2SiO_5@SiO_2 NPs, where the EG present on the surface was combusted during the thermal treatment, did not alter cell viability at concentrations up to 100 μg/ml over all the cancer cell lines tested, illustrating high biocompatibility. PVP confirmed its low toxicity and very high biocompatibility[7], not exerting any effect on cell viability even at high concentrations.

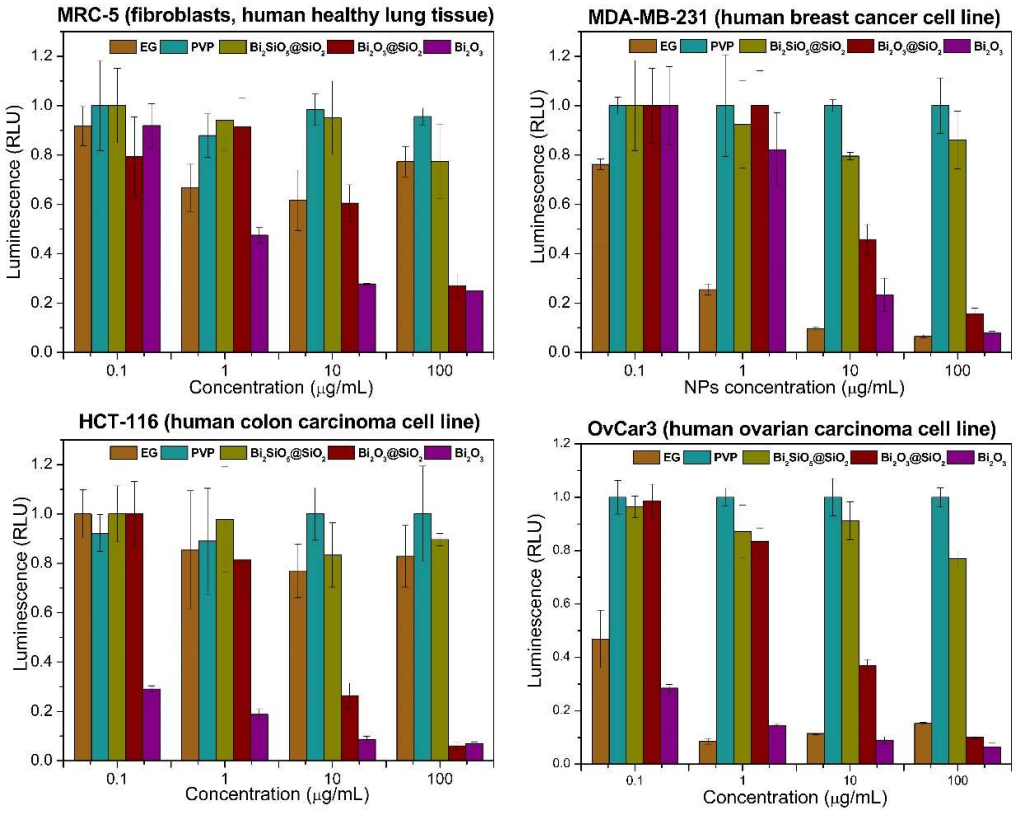

Fig.2 ATP levels for different types of cell lines, expressed as a function of luciferase luminescence (RLU, relative luminescence units). Cell viability was investigated against various concentrations of starting reagents (ethylene glycol and PVP), and NPs corresponding to the three synthetic steps (i.e. Bi_2O_3, Bi_2O_3@SiO_2 and Bi_2SiO_5@SiO_2 NPs). The data were normalized on the luminescence of the negative control (with any agent added to the cell colture).

6.2 Anti-microbial properties

Antibacterial tests were conducted by plating bacterial cells (either Gram-positive *Staphylococcus Aureus* or Gram-negative *Escherichia Coli*) on Nutrient Agar (NA) containing a range of concentrations of the different nanoparticles to be tested (Bi_2O_3, Bi_2O_3@SiO_2 and Bi_2SiO_5@SiO_2 NPs). All experiments were conducted in triplicate. The results are reported in Figure 3 as viability (%) vs. NPs concentration, in order to compare the toxicity of the NPs resulting from each intermediate synthetic step.
None of the three types of NPs showed growth inhibition effect on Gram-positive *S. Aureus*, even at high concentration, equal to 200 μg/mL, indicative of no toxic effect of the NPs. Regarding instead Gram-negative *E. Coli*, only Bi_2O_3 NPs showed antimicrobial activity, with a half maximal inhibitory concentration (IC_{50}) estimated to be in the range between 12.5 and 25 μg/mL. On the other hand, Bi_2O_3@SiO_2 and Bi_2SiO_5@SiO_2 NPs did not exert any inhibitory effect on E. Coli, even at high concentrations (up to 200 μg/mL).

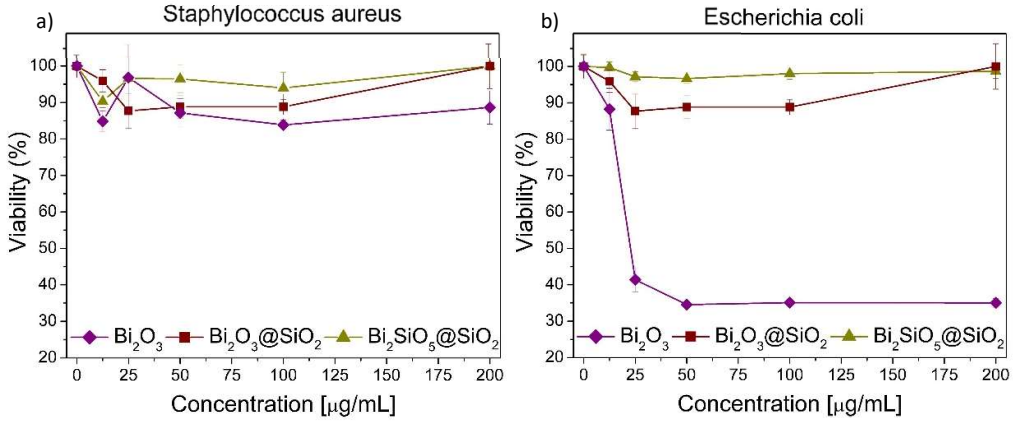

Fig.3 Viability (%) of the (a) Gram-positive S. Aureus and (b) Gram-negative E. Coli vs. increasing concentrations of Bi_2O_3, Bi_2O_3@SiO_2 and Bi_2SiO_5@SiO_2 NPs, normalized on the positive control viability.

These results suggest a toxic effect of Bi_2O_3 NPs only towards Gram-negative E. Coli. The precise mechanism, probably due to some toxic moieties on the surface of the NPs that exert a non-homogeneous effect because of the difference in cell structures between Gram-negative and Gram-positive bacteria, is yet to be determined and requires further investigations.
Among numerous studies on the antibacterial effect of metal oxides, only few concern bismuth oxide. Luo *et al.*[8], mentioned that Bi_2O_3 nanospheres have potential in treating of drug-resistant bacteria. Chen *et al.*[9] demonstrated no inhibition of Bi_2O_3 nanoparticles against *Helicobacter pylori*, while Qin *et al.*[10] showed that Bi_2O_3 nanospheres exhibit size-dependent antibacterial activity towards *S. aureus* in the range of 1–8 μg/mL, in contrast with what demonstrated in this work. Moreover, Abeer *et al.*[11] concluded that Bi_2O_3 with concentration 100μg/ml have an excellent activity and potential effect in reducing

pathogenic bacterial growth of *Staphylococcus aureus, Escherichia coli* and *Klebsiella sp.* As a consequence of the conflicting results reported in literature, it is legitimate to assume that the chemical route employed to obtain Bi_2O_3 NPs, and thus their size and surface chemistry, may influence the magnitude of their antimicrobial activity.
Speaking of Bi_2O_3@SiO_2 and Bi_2SiO_5@SiO_2 NPs, silica is well known for its biocompatibility. Only composite systems, based on the conjugation of SiO_2 with, for instance, titania[12], copper[13] or silver[14,15] show inhibition properties against pathogenic bacteria, while any antimicrobial activity is reported for pure silica NPs. In addition, no reports have been found in the literature on Bi_2SiO_5 antimicrobial properties.

6.3 Photocatalytic activity

If considering the application of Bi_2SiO_5@SiO_2 NPs in various biological/nanomedicine fields or as temperature sensor in catalytic reactions, it is evident that the widely demonstrated bismuth silicate photocatalytic reactivity[16-20] could represent a drawback. However, the presence of a silica coating could be beneficial to the mitigation of the bismuth silicate unwanted photocatalytic activity.
The photocatalytic properties of Bi_2SiO_5@SiO_2 NPs were investigated by following the photo-oxidation of the Methyl Orange (MO) indicator in aqueous phase. Titania Degussa P-25 (Rutile/Anatase ratio of 85/15) was used as a reference for its well-known photoreactivity under different UV wavelengths and its highest photocatalytic efficiency among the readily available samples of TiO_2[21].
Absorption spectra were collected as a function of time, monitoring the degradation of Methyl Orange. When dissolved in water, the UV–visible spectrum of Methyl Orange shows two absorption maxima (Fig.4)[22]. The first band is observed at about 280 nm and the second one, more intense and distinctive of a substituted azobenzene[23], at 465 nm. The latter one, in terms of absorption maximum at 465 nm, is typically used to monitor the photocatalytic degradation of MO.
It was interesting to note that the methyl-orange characteristic peak at 465 nm decreased with time in the presence of TiO_2 powder, almost disappearing already after 2 hours, while remained unaffected in the presence of Bi_2SiO_5@SiO_2 NPs.
A calibration curve (Fig.5a) was built by measuring absorption maxima at 465 nm of different concentrations of Methyl Orange in water. The best fit was later used to determine MO concentration at different time intervals in the presence of TiO_2 powder or Bi_2SiO_5@SiO_2 NPs.
Fig.5b represents the changes in the concentration (C/C_0) of MO in aqueous solution under UV light irradiation. After initial 30 minutes of equilibration in the dark, a small amount of MO is adsorbed on the surface of TiO_2. On the contrary, the MO concentration does not decrease in the case of Bi_2SiO_5@SiO_2 NPs. The amount of dye adsorbed in the dark depends on different factors, such as the surface area and the Point of Zero Charge (PZC) of the materials[24]. Degussa P-25 TiO_2, has standardized features: anatase/rutile mixture ratio, non-porosity, BET surface area ~ 55 ± 15 m^2g^{-1} and average particle size ~30 nm[21]. In this case TiO_2 powder has a larger surface area

respect to the non-porous and bigger Bi_2SiO_5@SiO_2 NPs here synthetized, this leads to the adsorption of a larger amount of dye. Moreover, in the case of silica coated nanoparticles, the surface becomes more strongly negatively charged at higher pH. Above the silica PZC, at the slightly acidic natural pH of the dye solution, H^+ ions are depleted from the silanol groups on the silica surface, increasing the negative charge and hindering the absorption of the anionic dye. On the contrary, MO adsorption is more favoured on the TiO_2 degussa powder, which has a PZC significantly higher (pH ~6.3[25]) than that of silica.

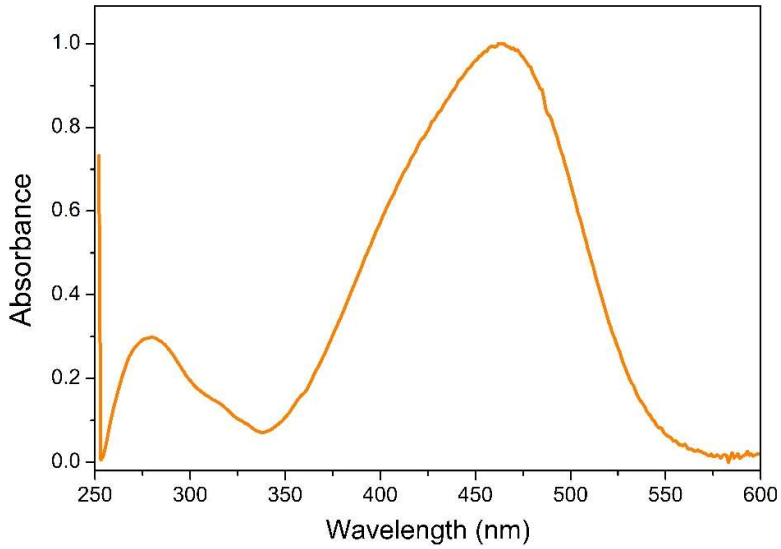

Fig.4 UV-VIS spectrum for methyl orange, showing the two typical absorption bands, at about 280 and 465 nm, respectively.

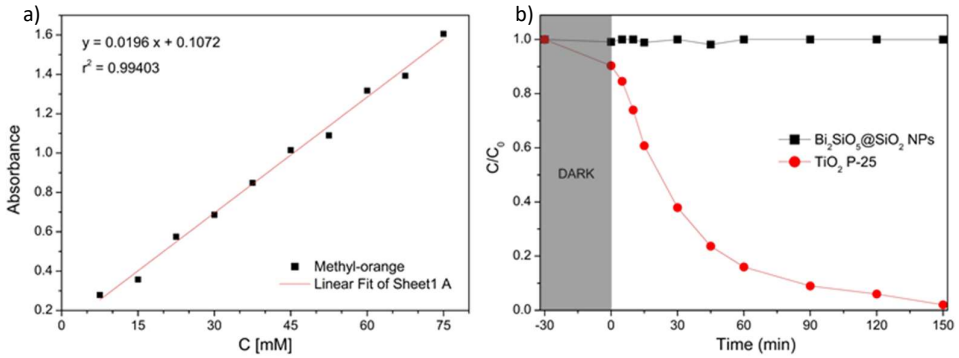

Fig.5 (a) Calibration curve with absorbance values at 465 nm of different Methyl Orange concentrations in aqueous solution, (b) Photo-oxidation of an aqueous solution of MO as a function of time, under UV LED irradiation for TiO_2 P-25 powder (red squares) and Bi_2SiO_5@SiO_2 NPs (black squares). The grey frame represents the equilibration time in the dark.

MO degradation in the presence of TiO_2 P-25 has a constant rate proportional to the concentration of the dye in solution. In agreement with this, the calculated kinetic

constant showed a value of 0.0278 min^{-1} ($t_{½}$ ~ 25 min). The complete decolorization of MO solution (Fig.6) was achieved within 2.5 h of irradiation. On the other hand, the MO degradation in the presence of Bi_2SiO_5@SiO_2 NPs was so inefficient, that it can be regarded as a non-photocatalytic nanosystem, most probably because of the surface shielding provided from the silica coating, whose non-photocatalytic nature has been previously stated[26]. Therefore, after this potential hurdle has been dismantled, Bi_2SiO_5@SiO_2 NPs proved to be suitable for biological/nanomedicine or temperature sensing applications.

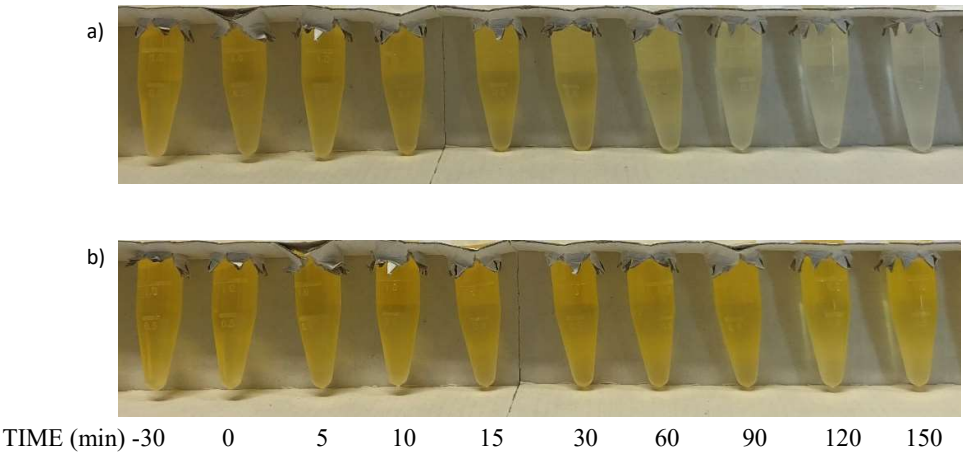

Fig.6 Solution decolouration as a function of MO degradation in time, in the presence of (a) TiO_2 P-25 powder and (b) Bi_2SiO_5@SiO_2 NPs.

6.4 Chemical stability: overcoming the acid solubility of Bismuth-based compounds

By considering potential applications as biomarker for tumoral cell temperature or as thermometer for chemical reactors, the main challenge is to retain the stability of the material as it interacts with the surrounding environment. Chemical stability at different pH is an important requirement.

Generally, Bismuth compounds are quite insoluble in neutral water, however they become readily soluble in acid solutions. In fact, it is well known that a limiting factor for the use of bismuth oxide in such applications is its high solubility in acid solutions. Moreover, $NaBiF_4$ was recently demonstrated to be unstable in water[27] and one of the most popular upconverting nanosystem, $NaYF_4$:Yb,Er, suffers of dissolution when it is in water[28].

Therefore, the investigation of the chemical stability to different environments is fundamental to address the real potential of the developed system. Fig.7 shows the comparison between Bi_2O_3 and Bi_2SiO_5@SiO_2 NPs before and after the exposure for 3 hours to acid solutions of different pH. The SEM images clearly evidence a different behaviour: Bi_2O_3 NPs are quite sensitive to acid solutions with mild pH values, while

are completely dissolved in strongly acid mediums, while the $Bi_2SiO_5@SiO_2$ nanosystem shows high chemical stability to acid environment, regardless of the pH value of the solution.

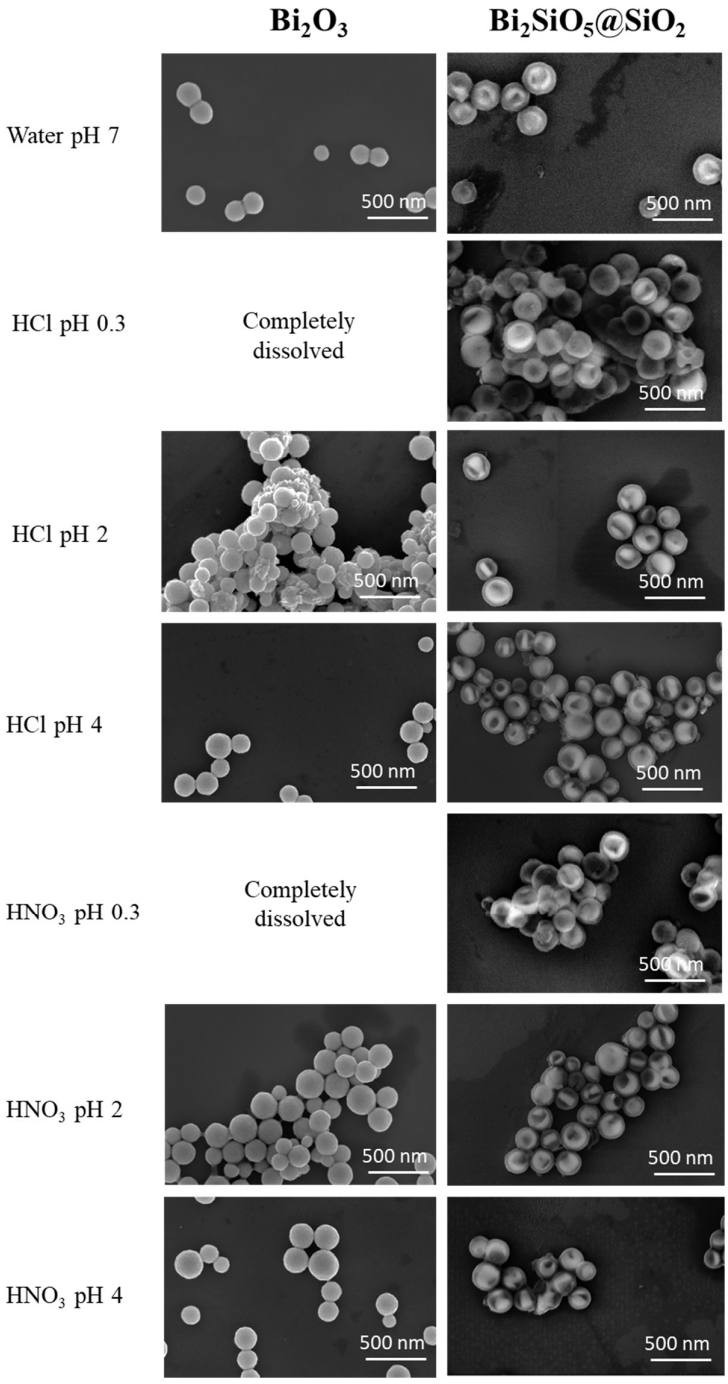

Fig.7 SEM images of Bi_2O_3 and $Bi_2SiO_5@SiO_2$ NPs before and after the exposure to acid solutions, either HCl or HNO_3, with different pH values for 3 hours.

This is further confirmed by XRPD patterns collected on dried $Bi_2SiO_5@SiO_2$ NPs powders after the exposure, under magnetic stirring and for increasing time intervals,

to a strongly acid solution, i.e. HNO_3 1M. Fig.8 confirms that any structural modifications occurs, even after 72 hours of exposure, and represents the final validation of the high chemical stability of $Bi_2SiO_5@SiO_2$ NPs.
The strategy employed is therefore demonstrated to be suitable to overcome the bottleneck of the instability in acid environments up to pH<1.

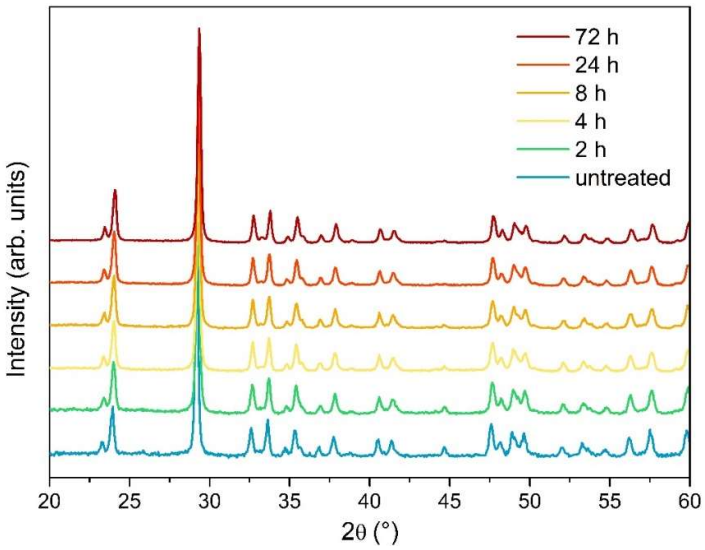

Fig.8 XRPD patterns of $Bi_2SiO_5@SiO_2$ NPs exposed for increasing time intervals, to HNO_3 1M.

6.5 Conclusions

In this Chapter, we have probed some critical features of the system under investigation.
The low toxicity of $Bi_2SiO_5@SiO_2$ NPs was assessed on four different cell lines, demonstrating the high biocompatibility properties of the investigated system. Moreover, any significative antimicrobial activity was found.
The particular structure of these NPs, composed of optically active cores embedded in an inert insulating glassy shell, leads to unique properties and suitability to disparate fields of application. In fact, we demonstrated how the shielding silica coating resets Bismuth silicate photocatalytic reactivity, not anymore representing a hurdle for the applicability of $Bi_2SiO_5@SiO_2$ NPs in various biological/nanomedicine fields or as sensor in catalytic reactions. Moreover, the insulating effect from the surrounding environment confers high chemical stability and resistance to acid mediums, the lack of which represented for Bismuth-based materials a limiting factor for long time. This opens the way also to potential applications as biomarker for tumoral cell temperature or as thermometer for chemical reactors.

Materials and Methods

Experimental Details. Cell viability was measured by means of the CellTiter-Glo® luminescence assay (Promega, Madison, Wisconsin, US) using an Infinite 200 PRO instrument (Tecan, Switzerland). The cells were incubated with suspensions of NPs with various concentrations (from 0.1 to 100 μg/mL) for 96 h. After the exposure to the tested agents, a reagent mixture containing cell lysis solution, luciferase, and luciferase substrate, was added to the wells. The plates were allowed to incubate at room temperature for 10 minutes to stabilize the luminescent signal. The luminescence of the luciferase reaction was then analyzed. The experiments were performed in triplicate, at the Oncological Treatment Centre (CRO) in Aviano

Antibacterial tests were conducted by plating bacterial cells on Nutrient Agar containing a range of concentrations of the different nanoparticles to be tested. For each material, agar plates were prepared by adding appropriate amounts of a stock NPs suspension to nutrient agar, to reach final concentrations of 12.5, 25, 50, 100 and 200 μg/mL. Plates for negative controls were prepared without any addition of NPs. Either Gram-positive *Staphylococcus Aureus* or Gram-negative *Escherichia Coli*, were inoculated into Nutrient Broth and grown overnight at 37°C. After OD_{600} measurement and appropriate dilution, about 400 Colony Forming Units (CFUs) were plated on Nutrient Agar in Petri dishes and grown overnight at 37°C. Pictures of plates were acquired with Geliance 600 Images System and colonies were counted using ImageJ software (National Institute of Health, Bethesda, MD, USA). All experiments were conducted in triplicate.

X-ray powder diffraction (XRPD) measurements were performed by means of a Philips X'Pert diffractometer with a PW 1319 vertical goniometer with Bragg–Brentano geometry, equipped with a focusing graphite monochromator and a proportional counter with a pulse-height discriminator. Nickel-filtered Cu Kα radiation and a step-by-step technique were employed (steps of 0.05° in 2θ), with a collection time of 30 s per step.

Morphology of the powders were observed using a Carl Zeiss Sigma VP Field Emission Scanning Electron Microscope (FE-SEM).

For the photocatalytic degradation of Methyl Orange, the dye (50 mg) was firstly dissolved in of distilled water (25 mL). The solution was further diluted with a ratio 1:80 in distilled water, to obtain a concentration of 0.025 mg/mL (~75 mM). Either TiO_2 powder or $Bi_2SiO_5@SiO_2$ NPs (50 mg each) were separately suspended via sonication in 50 mL of Methyl Orange solution in water. The specimens were stirred in the dark for 30 minutes to allow the equilibration between the two species and then irradiated using a 125W medium pressure Hg lamp (Helios). The solution absorption was measured as a function of time using an Agilent 8453 UV-VIS spectrophotometer, at increasing time intervals: 0, 5, 10, 15, 30, 60, 90, 120 and 150 minutes. Sample aliquots of 2 mL were collected at each time interval and filtered using 0.2 μm hydrophilic PTFE Millex syringe filters.

References

[1] Crouch, S.P., Kozlowski, R., Slater, K.J., Fletcher, J., The use of ATP bioluminescence as a measure of cell proliferation and cytotoxicity, *Journal of immunological methods*, **1993**, 160(1), 81–8.

[2] Kangas, L., Gronroos, M., Nieminen, A.L., Bioluminescence of cellular ATP: a new method for evaluating cytotoxic agents in vitro, *Med. Biol.*, **1984**, 62(6), 338-343.

[3] Pellegatti, P., Falzoni, S., Pinton, P., Rizzuto, R., Di Virgilio, F., A novel recombinant plasma membrane-targeted luciferase reveals a new pathway for ATP secretion, *Molecular biology of the cell*, **2005**, 16(8), 3659–65.

[4] Branchini, B.R., Southworth, T.L., Fontaine, D.M., Kohrt, D., Talukder, M., Michelini, E., et al., An enhanced chimeric firefly luciferase-inspired enzyme for ATP detection and bioluminescence reporter and imaging applications, *Analytical biochemistry*, **2015**, 484, 148–53.

[5] Tantama, M., Yellen, G., Imaging changes in the cytosolic ATP-to-ADP ratio, *Methods in enzymology*, **2014**, 547, 355–71.

[6] Lewinski, N.A., Nanoparticle Cytotoxicity, Bhushan B. (eds) Encyclopedia of Nanotechnology, Springer, Dordrecht, **2012**.

[7] Koczkur, K. M., Mourdikoudis, S., Polavarapu, L., Skrabalak, S. E., Polyvinylpyrrolidone (PVP) in Nanoparticle Synthesis, *Dalton Trans.,* **2015**, 44, 17883-17905.

[8] Luo, Y., Hossain, M., Wang, C., Qiao, Y., An, J., Ma, L., Su, M., Targeted nanoparticles for enhanced X-ray radiation killing of multidrug-resistant bacteria, *Nanoscale,* **2013,** *5*(2), 687-694.

[9] Chen, R., So, M. H., Yang, J., Deng, F., Che, C.-M., Sun, H., Fabrication of bismuth subcarbonate nanotube arrays from bismuth citrate, *Chem. Commun*., **2006**, 21, 2265-2267.

[10] Qin, F., Zhao, H., Li, G., Yang, H., Li, J., Wang, R., Liu, Y., Hu, J., Sun, H., Chen, R., Size-Tunable Fabrication of Multifunctional Bi_2O_3 Porous Nanospheres for Photocatalysis, Bacteria Inactivation and Template-Synthesis, *Nanoscale*, **2014**, 6, 5402-5409.

[11] Abeer, A., Determination of Antimicrobial Activity of Bi_2O_3 nanospheres Against Multi-Drug Resistant Pathogenic Bacteria, *AL-Qadisiyah Journal for Administrative and Economic Sciences*, **2018**.

[12] Levchuk, I., Kralova, M., Rueda Márquez, J. J., Moreno-Andrés, J., Gutiérrez, S., Dzik, P., Parola, S., Sillanpää, M., Vahala, R. Manzano, M., Antimicrobial activity of printed composite TiO_2/SiO_2 and TiO_2/SiO_2/Au thin films under UVA-LED and natural solar radiation, *Applied Catalysis B-Environmental*, **2018**, 239, 609 – 618.

[13] Varghese, S., Elfakhri, S.O., Sheel, D.W., Sheel, P., Bolton, F.J., Foster, H.A., Antimicrobial activity of novel nanostructured Cu-SiO_2 coatings prepared by chemical vapour deposition against hospital related pathogens, *AMB Express*, **2013**, 3(1), 53.

[14] Jia, H., Hou, W., Wei, L., Xu, B., Liu, X., The structures and antibacterial properties of nano-SiO_2 supported, silver/zinc-silver materials, *Dent Mater*., **2008**, 24(2), 244-9.

[15] Malekzadeh, M., Yeung, K.L., Halali, M., Chang, Q., Preparation and antibacterial behaviour of nanostructured Ag@SiO_2–penicillin with silver nanoplates, *New J. Chem*., **2019**, 43(42), 16612-16620.

[16] Zhang, P., Hu, J., Li, J., Controllable morphology and photocatalytic performance of bismuth silicate nanobelts/nanosheets, *RSC Adv*., **2011**, 1, 1072-1077.

[17] Liu, D., Wang, J., Zhang, M., Liu, Y., Zhu, Y., A superior photocatalytic performance of a novel Bi_2SiO_5 flower-like microsphere via a phase junction, *Nanoscale*, **2014**, 6, 15222-15227.

[18] Gu, W., Teng, F., Liu, Z., Liu, Z., Yang, J., Teng, Y., Synthesis and photocatalytic properties of Bi_2SiO_5 and $Bi_{12}SiO_{20}$, *Journal of Photochemistry and Photobiology A: Chemistry*, **353**, 2018, 395-400.

[19] Wang, J., Zhang, G., Li, J., Wang, K., Novel Three-Dimensional Flowerlike BiOBr/Bi_2SiO_5 p–n Heterostructured Nanocomposite for Degradation of Tetracycline: Enhanced Visible Light Photocatalytic Activity and Mechanism, *ACS Sustainable Chemistry & Engineering,* **2018,** 6 (11), 14221-14229.

[20] Li, L., Long, Y., Chen, Y., Wang, S., Wang, L.L., Zhang, S., Jiang, F., Facile synthesis of Fe/Bi_2SiO_5 nanocomposite with enhanced photocatalytic activity for degradation of 17β-Estradiol(E2), *Solid State Sciences*, **2018**, 83, 143-151.

[21] Mills, A., Davies, R. H., Worsley, D., Water purification by semiconductor photocatalysis, *Chemical Society Reviews*, **1993**, 22(6), 417.

[22] Hadi, Hussein & Wahab, Hilal, Visible Light Photocatalytic Decolourization of Methyl Orange Using N-Doped TiO_2 Nanoparticles, *Journal of Al-Nahrain University-Science*, **2015**, 18, 1-9.

[23] Oakes, J., Gratton, P., Kinetic investigations of the oxidation of Methyl Orange and substituted arylazonaphthol dyes by peracids in aqueous solution, *J. Chem. Soc.,Perkin Trans. 2*, **1998**, 12, 2563-2568.

[24] Zaccariello, G., Moretti, E., Storaro, L., Riello, P., Canton, P., Gombac, V., Benedetti, A., TiO_2–mesoporous silica nanocomposites: cooperative effect in the photocatalytic degradation of dyes and drugs, *RSC Adv*., **2014**, 4(71), 37826–37837.

[25] Liao, H., Reitberger, T., Generation of Free OH_{aq} Radicals by Black Light Illumination of Degussa (Evonik) P25 TiO_2 Aqueous Suspensions, *Catalysts*, **2013**, 3, 418-443.

[26] Hendrix, Y., Lazaro, A., Yu, Q. L., Brouwers, H. J. H., Influence of synthesis conditions on the properties of photocatalytic titania-silica composites, *Journal of Photochemistry and Photobiology A: Chemistry*, **2019**, 371, 25-32.

[27] Back, M., Ueda, J., Lahtine, E., Cassandro, L., Cristofori, D., Ottini, R., Riello, P., Sponchia, G., Asami, K., Tanabe, S., Trave, E., Lanthanide-Doped Bismuth-Based Fluoride Nanocrystalline Particles: Formation, Spectroscopic Investigation, and Chemical Stability, *Chem. Mater.,* **2019**, 31, 8504-8514.

[28] Lahtinen, S., Lyytikäinen, A., Päkkilä, H., Hömppi, E., Perälä, N., Lastusaari, M., Soukka, T., Disintegration of Hexagonal $NaYF_4:Yb^{3+},Er^{3+}$ Upconverting Nanoparticles in Aqueous Media: The Role of Fluoride in Solubility Equilibrium, *J. Phys. Chem. C,* **2017**, 121, 656-665.

CHAPTER 7

Upconverting Bi_2SiO_5@SiO_2 NPs for ratiometric contact-less optical nanothermometry

ABSTRACT: The development of nanomaterials with high sensitivity to external stimuli such as temperature, is critical to investigate the driving force of biological processes but also catalytic mechanisms in extreme environments.

In this chapter two luminescent temperature sensors based on Er^{3+}/Yb^{3+} (i), and Tm^{3+}/Yb^{3+} (ii) RE-doped Bi_2SiO_5@SiO_2 upconverting NPs are discussed. Doped Bi_2SiO_5@SiO_2 NPs were studied in the temperature range from 80 K to 800 K, in order to analyze their thermometric response and asses their applicability as optical temperature sensors based on the FIR technique.

For each sample, depending on the dopant ions, different pairs of thermally coupled levels have been considered, measuring the emission intensity ratio between them:

- the $^2H_{11/2}$ level (~520 nm) and $^4S_{3/2}$ level (~550 nm) for the sample co-doped with 6%at. Yb^{3+} and 1%at. Er^{3+} ions;
- $^3F_{2,3}$ (~700 nm) and $^3H_4$ (~800 nm) thermally coupled levels and $^1G_4$ (~650 nm) and $^3F_{2,3}$ (~700 nm) levels for the sample co-doped with 6%at. $Yb^{3+}$and 0.5 %at. Tm^{3+}ions;

The results obtained allowed to compute a relative sensitivity S_r of 1.1%K^{-1} (at 300K) (i), 1.3%K^{-1} (at 400K) for the $^3F_{2,3}/^3H_4$ FIR and 1.95% (at 300 K) for the $^3F_{2,3}/^1G_4$ FIR (ii), respectively, and are comparable with the relative thermal sensitivity values reported in literature for similar Ln^{3+}-based thermometers. Er^{3+}/Yb^{3+}: Bi_2SiO_5 NPs proved to be able to detect variations of temperature of the order of tenths of a Kelvin degree. Moreover, the measurements showed a high grade of repeatability.

The UCNPs used in this work remained unaltered when submitted to temperatures as high as 850 K.

7.1 $Bi_2SiO_5:Yb^{3+}/Er^{3+}@SiO_2$ core-shell NPs

$Bi_2SiO_5:Yb^{3+}/Er^{3+}@SiO_2$ upconverting NPs previously synthesized are able to convert long-wavelength light (980 nm) to a shorter wavelength one, in the red and green regions of the visible spectrum (see PL spectrum in Fig.26a, Chapter 5), through a two-photon process (see double logarithmic plot in Fig.26d, Chapter 5).

The two emission bands originating from Er^{3+} in the green region, assigned to the $^2H_{11/2}\rightarrow{}^4I_{15/2}$ and $^4S_{3/2}\rightarrow{}^4I_{15/2}$ transitions, centered at about 525 and 548 nm respectively, carry the temperature information. In fact, the two levels are very close in energy, separated by only a short energy gap ($\Delta E\sim800\ cm^{-1}$), thus allowing the level with higher energy ($^2H_{11/2}$) to be thermally populated by the $^4S_{3/2}$ level, as previously observed in other works[1-11]. In this case, the relative electronic population of the two levels in thermal equilibrium follows a Boltzmann-type distribution, allowing to compute the Fluorescence Intensity Ratio (FIR) as follows:

$$FIR = \frac{I_{525}}{I_{548}} \propto \left(-\frac{\Delta E}{k_B T}\right) \quad (1)$$

where I_{525} and I_{548} are the integrated intensities of the two $^2H_{11/2}\rightarrow{}^4I_{15/2}$ and $^4S_{3/2}\rightarrow{}^4I_{15/2}$ transitions.

As predicted, the normalized emission spectra collected at increasing temperatures in Fig.1 show a clear change in the emission intensity induced by temperature, whereas UC emission wavelengths remain unaffected.

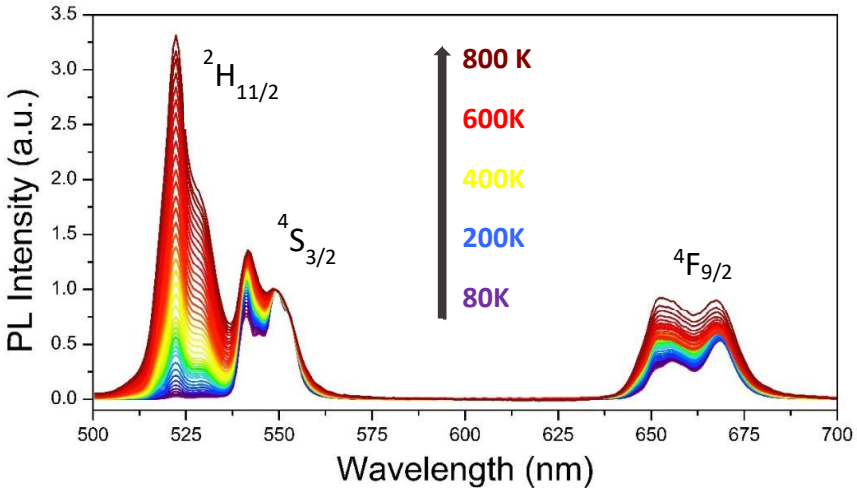

Fig.1 Temperature dependence of PL emission spectra in the 80−800 K range, normalized to the $^4S_{3/2}$ line.

The observations from Fig.2a are quite interesting. A different behaviour for various emission bands of the same activator can be observed at increasing temperature. The overall UC luminescence intensity and the intensities of the transitions from lower energy emitting levels ($^4S_{3/2}$, $^4F_{9/2}$) start to be quenched at 300K and by 500 K are more than halved. In this case, both the large size of the nanoparticles and the silica inert shell surrounding the optically active core account for the thermal quenching of the luminescence intensity, because non-radiative relaxation routes are favoured. On the contrary, the integrated intensity of the $^2H_{11/2} \rightarrow {}^4I_{15/2}$ emission line is found to be continuously enhanced with increasing temperature until 440 K, followed then by thermal quenching. The emission intensity results enhanced by a factor of more than 6-fold from 80 to 440 K. This uncommon result can be explained as follows: the decreased surface quenching of Yb^{3+} results in more efficient energy transfer processes towards activator ions, favouring the UC emissions from higher levels. Moreover, various nonradiative relaxation pathways are involved for the UC emissions at longer wavelengths. Therefore, the UCPL at shorter wavelengths is more probably enhanced than that at longer wavelengths with increasing temperatures. However, further investigations would be beneficial to have an insight of the mechanism behind the thermal enhancement or quenching of UC processes.

The inverse behaviour observed between of the two thermally coupled levels, with emission intensity from $^4S_{3/2}$ constantly decreasing and intensity from $^2H_{11/2}$ slowly increasing until 440 K and then rather stationary, implies a linearly ascending FIR, i.e. the ratio between the integrated intensities of the two emitting levels.

It is worth to mention that the potential employment of these UCNPs for biomedical applications would restrict the temperature range between 300 and 320 K. As evidenced in Fig.2b, in this range an increase of the emission intensity of 7% from the $^2H_{11/2}$ level and a decrease of the emission intensity of 6% from the $^4S_{3/2}$ level is observed. The linearity of the Arrhenius plot in Fig.2c, showing the dependence of ln(FIR) on the inverse temperature 1/T, evidences the thermal equilibrium between the two excited states, in a wide temperature range between 280 and 800 K. The best fit ($\ln(I_{525}/I_{548})=1.84–964(1/T)$), allowed to calculate an energy gap of 670 cm^{-1} between the two thermally coupled levels. If compared to the value estimated by the emission spectrum collected at 300 K in Fig.2d (ΔE = 806 cm^{-1}), as the distance in energy between the barycentres of the two emission bands, a certain discrepancy is evident. The underestimation from the Arrhenius plot could be due to the overlapping of emission bands from the thermally coupled levels, that may cause a certain error in the estimation of the FIR, as previously observed in literature[12].

Fig.2e and 2f depict the temperature dependence of the absolute and relative sensitivity (calculated from eq. 2 and 3 in Chapter 3), respectively, showing a value of S_a of about $1.9 \cdot 10^{-3}$ K^{-1} and S_r of 1.1% K^{-1} in the physiological temperature range (~300 K). In comparison with other nano- or sub-micron sized thermometric systems[1,3,6,8], it is noteworthy that the results here reported are encouraging, both in terms of relative sensitivity at 300 K and operating range of temperatures (see Table 1 for comparison with various Yb^{3+}/Er^{3+} thermometric systems already reported in literature).

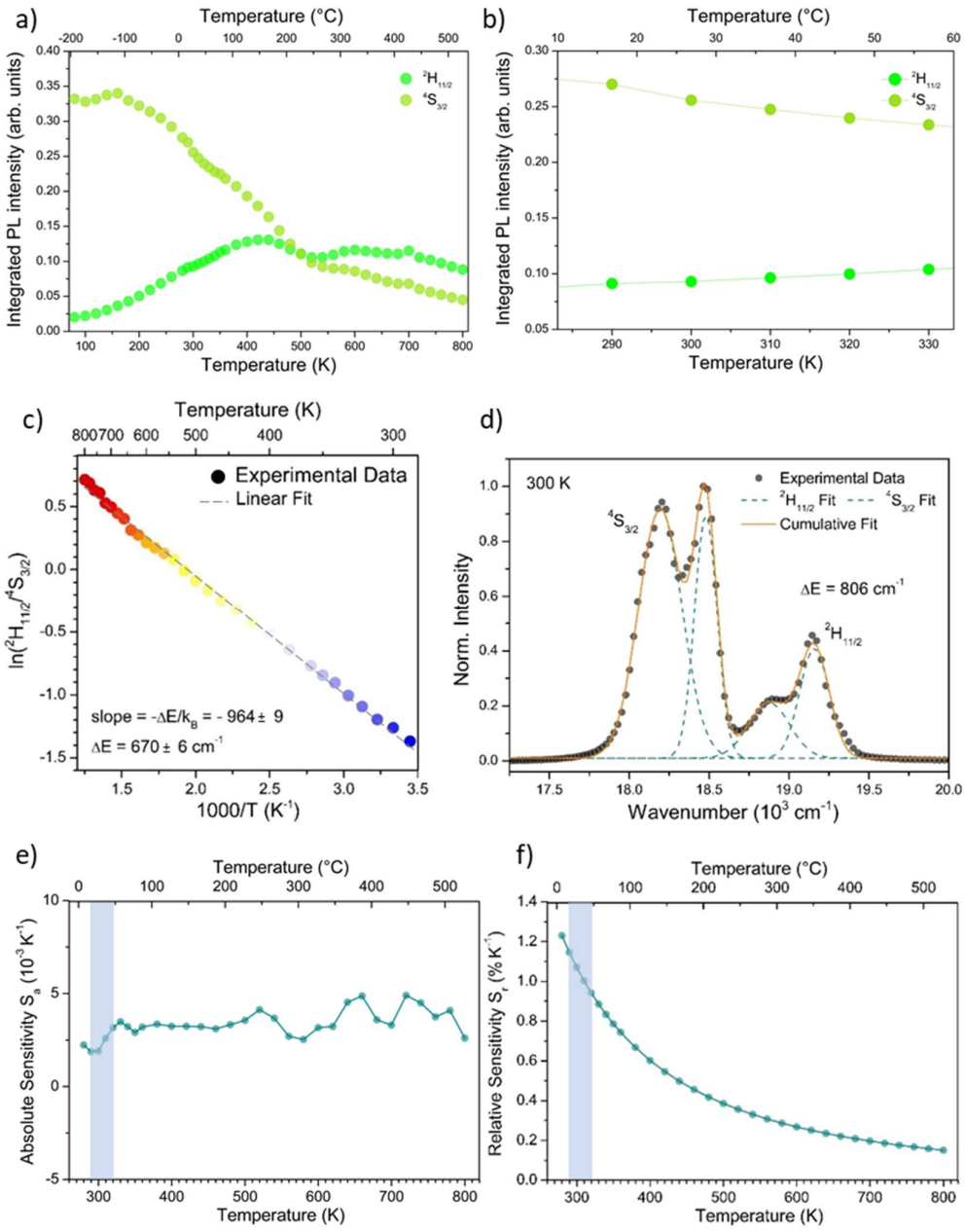

Fig.2 Temperature dependence of integrated UC PL intensities of the Er^{3+} transitions from $^2H_{11/2}$ (green dots) and $^4S_{3/2}$ (yellow dots) to ground state $^4I_{15/2}$ (a) in the whole temperature range tested and (b) in the physiological range (290-320K). The lines between symbols have been added for guiding the eye. (c) Arrhenius plot in the temperature range of linearity for the Boltzmann law (280-800 K) and estimation of the distance in energy (ΔE) between the two thermally coupled levels (d)Fit of the spectrum collected at 300 K, for the empirical estimation of ΔE as the distance between the barycenters ($x_{4S3/2}$= 18.3x10^3 cm^{-1}, $x_{2H11/2}$= 19.1x10^3 cm^{-1}) of the two multiplets. (e) Absolute sensitivity of the Yb^{3+}/Er^{3+}-based thermometric system, (f) Relative sensitivity of the Yb^{3+}/Er^{3+}-based thermometric system. (The blue frame indicates the physiological temperature range).

Sample	S_r, T (% K^{-1}, K)	T range (K)	method
Bi_2SiO_5 NPs	1.10 (300)	280-800	$^2H_{11/2}/^4S_{3/2}$
$NaYF_4$[1]	1.00 (318)	293-318	$^2H_{11/2}/^4S_{3/2}$
Gd_2O_3 NCs[3]	0.20 (600)	295-1000	$^2H_{11/2}/^4S_{3/2}$
$LiNbO_3$ NPs[6]	0.68 (290)	280-450	$^2H_{11/2}/^4S_{3/2}$
$YbTi_2O_7$ particles[8]	0.72 (290)	300-600	$^2H_{11/2}/^4S_{3/2}$

Table.1 Comparison of relative sensitivities S_r at given temperature, operating temperature ranges and FIR method of different nano- or sub-micron sized Yb-Er thermometric systems.

Fig.3a shows the temperature uncertainty, representing the smallest change of temperature that can be detected, as a function of temperature (calculated from eq. 5 in Chapter 3). As it can be seen, the system ensures an elevate reliability in the physiological range, being able to detect variations of temperature of the order of tenths of a Kelvin degree.

Finally, the repeatability (or test-retest reliability) was measured by means of a thermal cycling experiment, based on four consecutive heating-cooling cycles between 300 and 800 K, as shown in Fig.3b. The computed repeatability (calculated from eq. 9 in Chapter 3) is lager then 99%, representing the high reproducibility of the measurements.

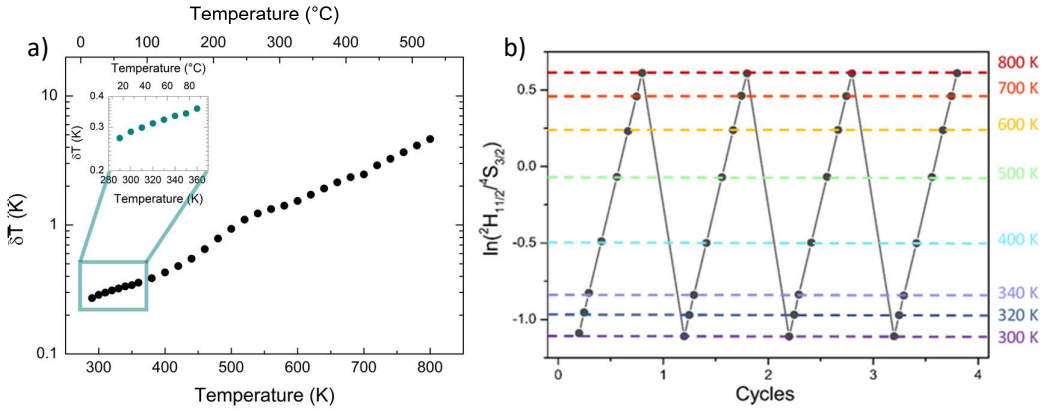

Fig.3 (a) Temperature uncertainty and (b) Repeatability, upon four subsequent temperature cycling between 300 and 800 K. The computed parameter R was >99%.

7.2 $Bi_2SiO_5:Yb^{3+}/Tm^{3+}@SiO_2$ core-shell NPs

Previously synthesized $Bi_2SiO_5:Yb^{3+}/Tm^{3+}@SiO_2$ upconverting NPs are also able to convert long-wavelength light (980 nm) to a shorter wavelength one, in the blue, red and NIR regions of the spectrum (see PL spectrum in Fig.26b, Chapter 5), through a multiple-photon process (see double logarithmic plot in Fig.26e, Chapter 5).

7.2.1 $^3F_{2,3}/^3H_4$ fluorescence intensity ratio

In the case of Tm^{3+}, different transitions can convey the temperature information. Among them are the deep red $^3F_{2,3}\rightarrow{}^3H_6$ and the NIR $^3H_4\rightarrow{}^3H_6$ transitions, centered at 700 and 800 nm respectively. The two thermally coupled levels are quite distant in energy, separated by an energy gap of about $\Delta E\sim1785$ cm^{-1}, still allowing the level with higher energy ($^3F_{2,3}$) to be thermally populated by the lower $^3H_4$ level[13], leading to the change of intensity ratio between the 700 and 800 nm emissions[14], with increasing temperature. In this case, the relative electronic population of the two levels in thermal equilibrium follows a Boltzmann-type distribution, allowing to compute the Fluorescence Intensity Ratio (FIR) as follows:

$$FIR = \frac{I_{700}}{I_{800}} \propto \left(-\frac{\Delta E}{k_B T}\right) \quad (2)$$

where I_{700} and I_{800} are the integrated intensities of the two $^3F_{2,3}\rightarrow{}^3H_6$ and $^3H_4\rightarrow{}^3H_6$ transitions. However, the weak 700 nm light band from $^3F_{2,3}\rightarrow{}^3H_6$ is difficult to detect[12] and for this reason the majority of works covers thermometric systems based on the NIR/blue ratio between $^3F_{2,3}\rightarrow{}^3H_6$ /$^1G_4\rightarrow{}^3H_6$ transitions[14] (despite the large distance in energy between the two levels) or on transitions from Stark sub-levels of the $^1G_4$ level[15,16] (though showing little relative sensitivity).

The normalized emission spectra collected at increasing temperatures in Fig.4a show a clear change in the emission intensities for the considered emission bands, even displaying the quenching of the luminescence efficiency from some Stark sublevels of the $^3H_4\rightarrow{}^3H_6$ transition, which becomes less favored at high temperatures.

A slightly inhomogeneous behaviour for the two considered emission bands of Tm^{3+} can be observed with increasing temperature in Fig.4b. The overall UC luminescence intensity (not shown) closely follows the trend of the intensity of the $^3H_4\rightarrow{}^3H_6$ transition (red dots). In fact, the integrated intensity of the $^3H_4\rightarrow{}^3H_6$ transition is much larger than that of the band corresponding to the $^3F_{2,3}\rightarrow{}^3H_6$ transition (orange dots), by a factor of more than 200-fold over the whole temperature range. Both the transitions show an initial enhancement of emission intensities, that gives then way to a strong emission quenching. The intensity of the transition from the $^3H_4$ emitting level starts to be quenched at 270K and by 800 K is one-hundredth of its maximum. On the other side, the intensity of the transition from the $^3F_{2,3}$ levels is enhanced by a factor of almost 10-fold from 80 to 450 K, then starts to drop becoming more than halved by 800 K. The partially offset behaviour of the emission intensities for the two thermally

coupled levels implies an ascending FIR, even though not linearly increasing over the whole temperature range.

In fact, from the Arrhenius plot (Fig.4c), it is worth noting that the population of the two states follows the laws of thermalization only at high temperatures. Below 400 K other radiative or non-radiative processes may dominate the thermalization rate, leading to a "decoupling" effect[12]. Below this temperature, the two levels cannot be considered as fully thermally coupled. This effect is evident at low temperatures, where the FIR shows a large deviation from the linear prediction. For this reason, it would be wiser to explore the FIR between $^3F_{2,3}$ and $^3H_4$ levels of Tm^{3+} only for high temperature measurements[13].

The linearity of the Arrhenius plot is true only in a selected range of temperatures, between 400 and 800 K. The best fit ($\ln(I_{700}/I_{800})=0.460–2130(1/T)$), allowed to calculate an energy gap of 1480 cm^{-1} between the two thermally coupled levels. If compared to the value estimated by the emission spectrum collected at 300 K in Fig.4d (ΔE = 1795 cm^{-1}), as the distance in energy between the barycentres of the two emission bands, a large discrepancy is to be noted. This is probably due the large energy gap between the two excited states.

In this case, the sensitivity of the thermometer based on $^3F_{2,3}$ and $^3H_4$ thermally coupled energy levels is much higher if compared to other cases, because of the larger energy gap between the two. Fig.4e and 4f depict the temperature dependence of the absolute and relative sensitivity, respectively, showing a maximum value of S_a of about $0.2 \cdot 10^{-3}$ K^{-1} at 700 K and S_r of 1.3% K^{-1} at 400 K, the lowest temperature in the range of validity of the Boltzmann population distribution. Such a low absolute sensitivity is due to the small extent of the FIR parameter for the integrated PL intensities of the two thermally coupled transitions.

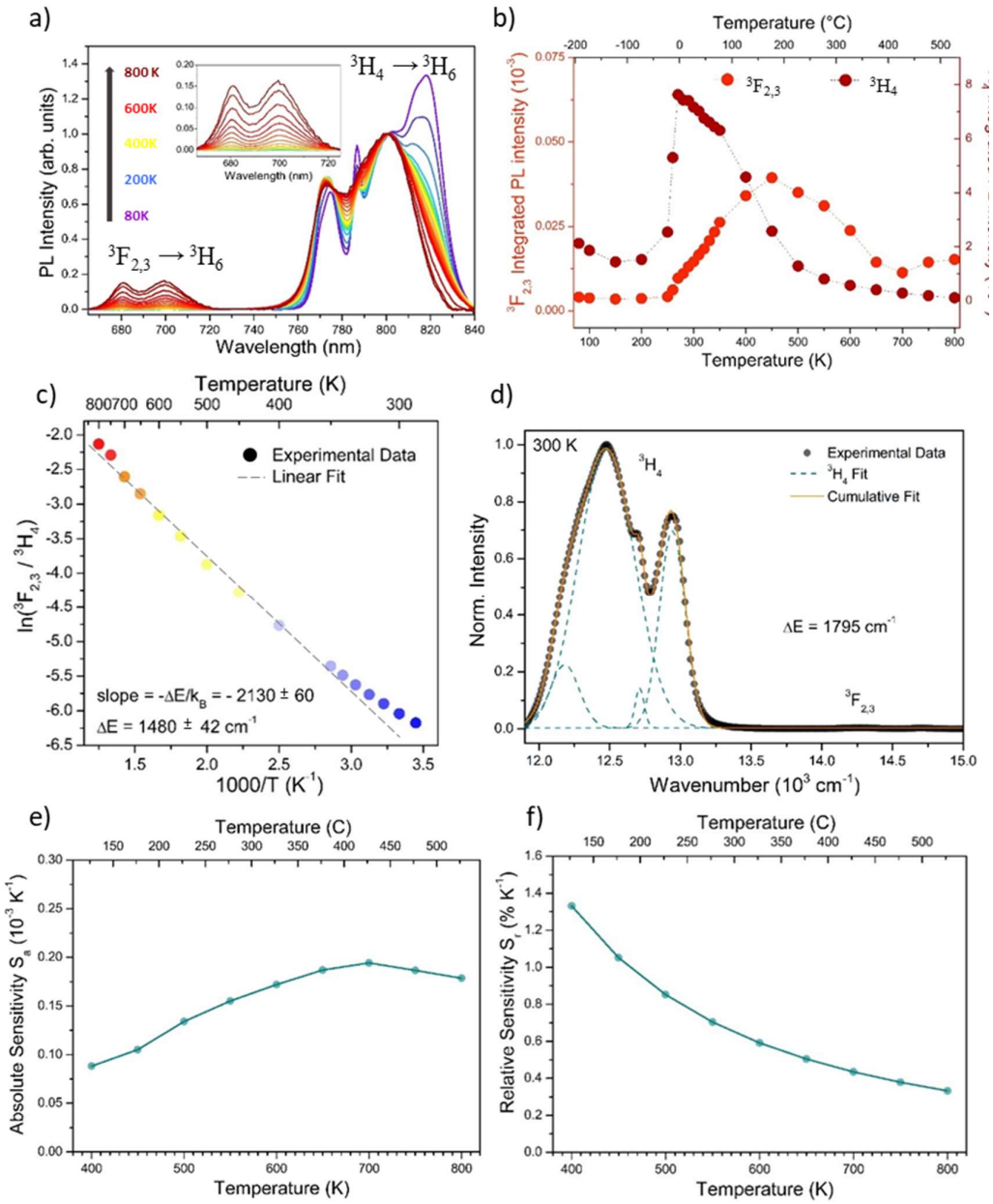

Fig.4 (a) Temperature dependence of PL emission spectra in the 80−800 K range, normalized to the $^3H_4$ line. (b) Temperature dependence of integrated UC PL intensities of the Tm^{3+} transitions from $^3F_{2,3}$ (orange dots) and $^3H_4$ (red dots) to ground state $^3H_6$. The dotted lines between symbols have been added for guiding the eye. (c) Arrhenius plot, where the linearity for the Boltzmann law is true in a selected range of temperatures (400-800 K), and estimation of the distance in energy (ΔE) between the two thermally coupled levels. (d) Fit of the spectrum collected at 300 K, for the empirical estimation of ΔE as the distance between the barycenters (x_{3H4}=12.5x10^3 cm^{-1}, $x_{3F2,3}$=14.3x10^3 cm^{-1}) of the two multiplets. (e) Absolute sensitivity of the $^3F_{2,3}/^3H_4$ Yb^{3+}/Tm^{3+}-based thermometric system, in the range of validity of the Boltzmann law. (f) Relative sensitivity of the $^3F_{2,3}/^3H_4$ Yb^{3+}/Tm^{3+}-based thermometric system, in the range of validity of the Boltzmann law.

As mentioned above, the population of the two states follows the laws of thermalization only at temperatures higher than 400 K. Despite this, the dependence of the ln(FIR) on the inverse temperature shows a linear trend also at temperatures between 280 and 400K (Fig.5). Thus, the best fit of the Arrhenius plot, ($\ln(I_{700}/I_{800}) = -1.28–1420(1/T)$), could eventually serve as a calibration curve for the estimation of the temperature in the range 280-400 K.

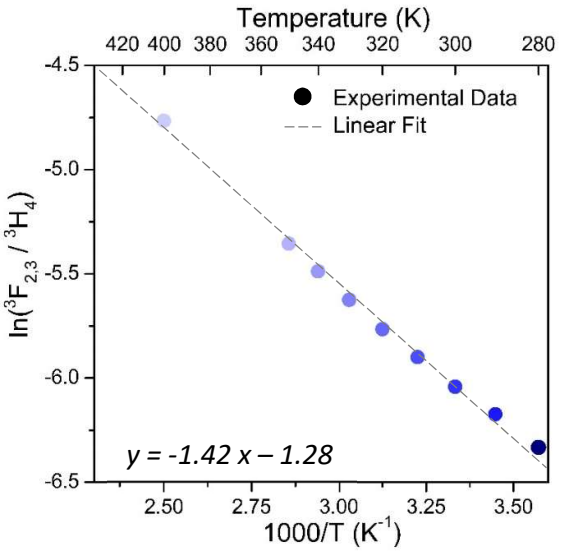

Fig.5 Arrhenius plot, between 280 and 400 K.

7.2.2 $^3F_{2,3}/^1G_4$ fluorescence intensity ratio

Even Tm^{3+} emitting levels excited via a three-photon excitation mechanism, such as the $^1G_4$ [15,17], can be considered. In this case, the fluorescence intensity ratio is based on $^3F_{2,3}\rightarrow{}^3H_6$ and $^1G_4\rightarrow{}^3F_4$ red transitions, centered at 700 and 650 nm respectively. The two levels are very distant in energy, separated by an energy gap of about 8000 cm^{-1}, and thus cannot be considered as thermally coupled. Nonetheless, the electronic population of the $^3F_{2,3}/^1G_4$ levels seems to follow anyway a Boltzmann-like distribution. As can be observed from the schematic energy level diagram for the Yb^{3+}-Tm^{3+} ion pair (Fig.17 in Section 2.6.2), a two-photon process is responsible for the population of $^2F_{2,3}$ Tm^{3+} excited states and a non-radiative relaxation occurs then from $^2F_{2,3}$ to $^3H_4$ level. The absorption of an additional third photon finally leads to the population of $^1G_4$ level starting from $^3H_4$ level. The radiative transition $^1G_4\rightarrow{}^3F_4$ is then responsible of the red emission at about 650 nm. The electronic population of the $^3H_4$ level, that is thermally coupled with $^3F_{2,3}$ levels, follows a Boltzmann electronic distribution and shows to decrease with temperature (see Fig.4b in the previous Section). In this way, this process could also influence the electronic population of higher-energy $^1G_4$ level, explaining the Boltzmann-like distribution even if the two levels are not directly in thermal equilibrium.

The relative electronic distribution of the two levels follows anyway a Boltzmann-like distribution, even if the two levels are not directly in thermal equilibrium. Thus, the Fluorescence Intensity Ratio (FIR) was computed as follows:

$$FIR = \frac{I_{700}}{I_{650}} \propto \left(-\frac{\Delta E}{k_B T}\right) \quad (3)$$

where I_{700} and I_{650} are the integrated intensities of the two transitions: from the excited state $^3F_{2,3}$ to ground state $^3H_6$ and from the excited state $^1G_4$ to the $^3F_4$ level.

The normalized emission spectra collected at increasing temperatures in Fig.6a show that the lower-energy levels ($^3F_{2,3}$) get populated with increasing temperature, in contrast to $^1G_4$ level. In fact, as shown in Fig.6b, the integrated emission intensities of the two emission bands at 650 and 700 nm, exhibit a different temperature-dependent behavior. The intensity of $^3F_{2,3} \rightarrow {}^3H_6$ transition (700 nm) is enhanced monotonously by a factor of more than 3-fold between 250 and 400 K, followed by thermal quenching. On the other hand, the intensity of the emission band at 650 nm first rises with the increase of temperature until 260 K and then decreases. The ln(FIR) in the Arrhenius plot (Fig.6c), follows the linear prediction only at low temperatures (between 260 and 400 K). The best fit ($\ln(I_{700}/I_{650}) = 5.68–1755(1/T)$), allowed to calculate an energy gap of 1220 cm^{-1}, as previously estimated for the thermometer based on the ratio between the thermally coupled levels $^3F_{2,3}/^3H_4$ in the same temperature range in Fig. 5 ($\Delta E \sim 1000$ cm^{-1}).

Fig.6e and 6f depict the temperature dependence of the absolute and relative sensitivity. In this case, the sensitivities of the thermometer based on $^3F_{2,3}$ and $^1G_4$ energy levels are unprecedently high. The absolute and relative sensitivity show a value of S_a of about $16.8 \cdot 10^{-3}$ K^{-1} and S_r of 1.95% K^{-1} at 300 K, respectively. These values are superior to other previously reported for Tm^{3+}-doped temperature sensors with the FIR technique based on the $^3F_{2,3}$ and $^1G_4$ levels.

In comparison with other nano- or micro-sized thermometric systems[14,15,18,19], based on different pairs of thermally coupled levels, it is noteworthy that the results here reported are very favorable, showing high relative sensitivity values and wide operating ranges of temperature (see Table 2), irrespective of the pair of emitting levels considered, either $^3F_{2,3}/^3H_4$ or $^3F_{2,3}/^1G_4$.

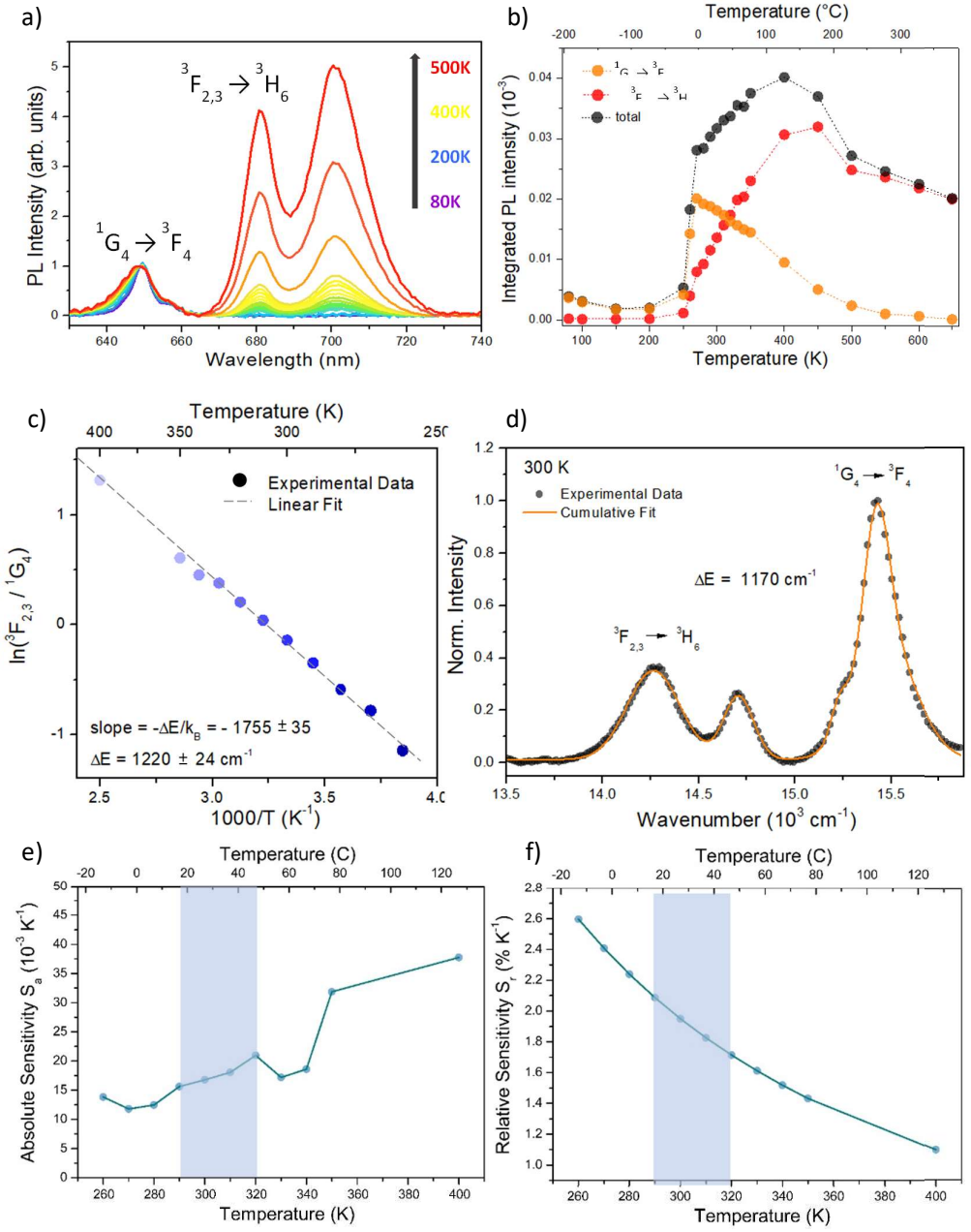

Fig.6 (a) Temperature dependence of PL emission spectra in the 80−500 K range, normalized to the $^1G_4$ line. (b) Temperature dependence of integrated UCPL intensities of the Tm^{3+} transitions from $^3F_{2,3}$ level to ground state $^3H_6$ (red dots) and from $^1G_4$ to $^3F_4$ level (orange dots). The dotted lines have been added for guiding the eye. (c) Arrhenius plot, where the linearity for the Boltzmann law is true in a selected range of temperatures (260-400 K), and estimation of the distance in energy (ΔE) between the two levels. (d) Fit of the spectrum collected at 300 K, for the empirical estimation of ΔE as the distance between the barycenters ($x_{3F2,3}$=14.27x10^3 cm^{-1}, x_{1G4}=15.44 x10^3 cm^{-1}) of the two bands. (e) Absolute sensitivity of the $^3F_{2,3}/{}^1G_4$ Yb^{3+}/Tm^{3+}-based thermometric system, in the range of validity of the Boltzmann law, (f)Relative sensitivity of the $^3F_{2,3}/{}^1G_4$ Yb^{3+}/Tm^{3+}-based thermometric system. (The blue frame indicates the physiological temperature range).

Sample	S_r, T (% K^{-1}, K)	T range (K)	method
Bi_2SiO_5 NPs	1.30 (400)	400-800	$^3F_{2,3}/^3H_4$
Bi_2SiO_5 NPs	1.95 (300)	260-400	$^3F_{2,3}/^1G_4$
$NaYF_4$ NCs[14]	1.53 (417)	300-500	$^3F_{2,3}/^1G_4$
$NaNbO_3$ NCs[15]	0.08 (293)	293-353	$^1G_4$ Stark levels
CaF_2 NPs[18]	0.20 (315)	293-318	$^3H_4$ Stark levels
$NaYbF_4$ particles[19]	0.05 (430)	400-700	$^1D_2$ /$^1G_4$

Table.2 Comparison of relative sensitivities S_r at given temperature, operating temperature ranges and FIR method of different nano- or sub-micron sized Yb-Tm thermometric systems.

7.3 Conclusions

In this Chapter, we have proposed Ln^{3+}-doped Bi_2SiO_5 NPs as new ratiometric luminescent probes for optical thermometry. For this purpose, we have investigated the temperature dependence of the emission intensity in a wide range of temperatures, evidencing at least one pair of thermally coupled excited states for each activator. Among the investigated dopants, are Er^{3+} and Tm^{3+} ions as activators, coupled with Yb^{3+} as sensitizer.

Tm^{3+}/Yb^{3+} systems offer in principle the advantage of a larger tissue penetration depth, thanks to the strong emission at around 800 nm. On the other hand, Er^{3+} green emission lies in the same region of the spectrum where tissue scattering and specific absorptions of tissue components (such as oxygenated blood, deoxygenated blood and melanin) are high, causing short tissue penetration depths and restricting the effective applicability of Er^{3+} ions in bio-imaging[20,21]. Moreover, a 980 nm infrared laser as excitation source is not the best option for biological applications, falling between the first and second biological windows, where light absorption from water arises.

In general, for what concerns the systems here investigated, superior relative sensitivities S_r at 300 K and broader operating temperature ranges were found when compared to the values reported in previous works on similar Ln^{3+}-doped systems[1,2,18,22-25 (i); 14 (ii)].

By analysing the FIR between the thermally coupled levels $^2H_{11/2}/^4S_{3/2}$ of Er^{3+}/Yb^{3+} co-doped Bi_2SiO_5@SiO_2 NPs system, we found a relative sensitivity value (S_r) at 300K of about 1.1% K^{-1}, a wide operating temperature range (280-800), a small temperature uncertainty, representing the ability of the system to detect changes of temperature of the order of tenths of a Kelvin degree, and very high repeatability (>99%) upon thermal cycling experiment.

Tm^{3+}/Yb^{3+} co-doped Bi_2SiO_5@SiO_2 NPs showed high relative sensitivity S_r, irrespective of the pair of emitting levels considered, may it be the thermally coupled pair $^3F_{2,3}/^3H_4$ or $^3F_{2,3}/^1G_4$. However, in the first case, when considering the luminescence intensity ratio between $^3F_{2,3}$ and $^3H_4$ levels, the electronic population of the two states follows the laws of thermalization only above 400 K. For this reason, it

would be wiser to exclude the physiological temperature range and apply this method only for high temperature measurements (400-800K), thus hindering eventual biological applications. On the other hand, when considering the UC emissions originating from $^3F_{2,3}$ and $^1G_4$ states, even if they are not directly thermally coupled, high relative sensitivities were achieved in a lower temperature range from 260 to 400K, reaching a value of 1.95% K^{-1} at 300K. This outcome is superior to other previously reported S_r values for Tm^{3+} ions doped temperature sensors using the FIR technique based on the same emitting levels.

Despite these promising results, significant challenges remain, including for example the optimization of concentration and ratio of the dopants, the synthesis of UCNPs with higher quantum yields and the improvement of the host material, with the ultimate purpose of resolving temperature with an uncertainty of at least ± 0.1 °C.

Materials and Methods

Experimental Details. Upconversion photoluminescence (UCPL) measurements were performed with the use of laser diode (LD) from Thorlabs operating at 977 nm as excitation source. The temperature dependence of UCPL spectra (80−850 K) was investigated with a temperature-controlled stage (10 035 L, Linkam). All the spectra were calibrated by means of a standard halogen lamp (DH-2000CAL, Ocean Optics) to obtain spectra in the photon flux scale. In addition, the photon flux per constant wavelength interval function, $\phi(\lambda)$, is converted to photon flux per energy interval using the Jacobian transformation:

$$\frac{d\phi(E)}{dE} \propto \frac{d\phi(\lambda)}{d\lambda}\lambda^2 \tag{4}$$

These measurements have been performed at Kyoto University.

References

[1] Vetrone, F., Naccache, R., Zamarrón, A., Juarranz de la Fuente, A., Sanz-Rodríguez, F., Martinez Maestro, L., Martin Rodriguez, E., Jaque, D., García Solé, J., Capobianco, J. A., Temperature sensing using fluorescent nanothermometers, *ACS Nano* **2010**, 4, 3254−3258.

[2] Pandey, A., Rai, V. K., Kumar, V., Kumar, V., Swart, H. C. Upconversion based temperature sensing ability of Er^{3+}–Yb^{3+}codoped $SrWO_4$: An optical heating phosphor, *Sens. Actuators, B*, **2015**, 209, 352−358.

[3] Singh, S.K., Kumar, K., Rai, S.B., Er^{3+}/Yb^{3+} codoped Gd_2O_3 nano-phosphor for optical thermometry, *Sensors and Actuators A: Physical*, **2009**, 149(1), 16-20.

[4] Tikhomirov, V. K., Adamo, G., Nikolaenko, A. E., Rodriguez, V. D., Gredin, P., Mortier, M., Zheludev, N. I., Moshchalkov, V. V. Cathodo- and photoluminescence in Yb^{3+}-Er^{3+} co-doped PbF_2 nanoparticles, *Opt. Expres*s, **2010**, 18, 8836-8846.

[5] Manzani, D., Petruci, da Silveira, J. F., Nigoghossian, K., Cardoso, A. A., Ribeiro, S. J. L., A portable luminescent thermometer based on green up-conversion emission of Er^{3+}/Yb^{3+} co-doped tellurite glass, *Scientific Reports*, **2017**, 7, 41596.

[6] Quintanilla, M., Cantelar, E., Cussó, F., Villegas, M., Caballero, A. C., Temperature Sensing with Up-Converting Submicron-Sized $LiNbO_3$:Er^{3+}/Yb^{3+}Particles, *Applied Physics Express*, **2011**, 4(2).

[7] Cai, Z.P., Xu, H.Y., Point temperature sensor based on green upconversion emission in an Er:ZBLALiP microsphere, *Sensors and Actuators A: Physic*al, **2003**, 108(1–3), 187-192.

[8] Cao, B.S., He, Y.Y., Feng, Z.Q., Li, Y.S., Dong, B., Optical temperature sensing behavior of enhanced green upconversion emissions from Er–Mo:$Yb_2Ti_2O_7$ nanophosphor, *Sensors and Actuators B: Chemical*, **2011**, 159(1), 8-11.

[9] León-Luis, S. F., Rodríguez-Mendoza, U. R., Lalla, E., Lavín, V., Temperature sensor based on the Er^{3+} green upconverted emission in a fluorotellurite glass, *Sensors and Actuators B: Chemical*, **2011**, 158(1), 208-213.

[10] Dong, B., Yang, T., Lei, M.K., Optical high temperature sensor based on green up-conversion emissions in Er^{3+} doped Al_2O_3, *Sensors and Actuators B: Chemical*, **2007**, 123(2), 667-670.

[11] Pandey, A., Som, S., Kumar, V., Kumar, V., Kumar, K., Rai, V. K., Swart, H.C., Enhanced upconversion and temperature sensing study of Er^{3+}–Yb^{3+} codoped tungsten–tellurite glass, *Sensors and Actuators B: Chemical*, **2014**, 202, 1305-1312.

[12] Xu, W., Gao, X., Zheng, L., Zhang, Z., Cao, W., An optical temperature sensor based on the upconversion luminescence from Tm^{3+}/Yb^{3+} codoped oxyfluoride glass ceramic, *Sensors and Actuators B: Chemical*, **2012**, 173, 250-253.

[13] Xing, L.L., Xu, Y. L., Wang, R., Xu, W., Zhang, Z.G., Highly sensitive optical thermometry based on upconversion emissions in Tm^{3+}/Yb^{3+} codoped $LiNbO_3$ single crystal, *Opt. Lett*., **2014**, 39, 454.

[14] Zhou, S.S., Jiang, G.C., Li, X.Y., Jiang, S., Wei, X.T., Chen, Y.H., Yin, M., Duan,

C.K., Strategy for thermometry via Tm^{3+}-doped $NaYF_4$ core-shell nanoparticles, *Opt. Lett.*, **2014**, 39, 6687.

[15] Pereira, A.F., Upendra Kumar, K., Silva, W.F., Santos, W.Q., Jaque, D., Jacinto, C., Yb^{3+}/Tm^{3+} co-doped $NaNbO_3$ nanocrystals as three-photon-excited luminescent nanothermometers, *Sensors and Actuators B: Chemical*, **2015**, 213, 65-71.

[16] Li, D., Wang, Y., Zhang, X., Yang, K., Liu, L., Song, Y., Optical temperature sensor through infrared excited blue upconversion emission in Tm^{3+}/Yb^{3+} codoped Y_2O_3, *Optics Communications*, **2012**, 285, 1925–1928.

[17] Horton, N. G., Wang, K., Kobat, D., Clark, C. G., Wise, F. W., Schaffer, C. B., Xu, C. In vivo three-photon microscopy of subcortical structures within an intact mouse brain, *Nat Photon*, **2013**, 7, 205-209.

[18] Dong, N. N., Pedroni, M., Piccinelli, F., Conti, G., Sbarbati, A., Ramirez-Hernandez, J. E., Maestro, L. M., Iglesias-de la Cruz, M. C., Sanz-Rodriguez, F., Juarranz, A., Chen, F., Vetrone, F., Capobianco, J. A., Sole, J. G., Bettinelli, M., Jaque, D., Speghini, A., NIR-to-NIR two-photon excited $CaF_2:Tm^{3+},Yb^{3+}$ nanoparticles: multifunctional nanoprobes for highly penetrating fluorescence bio-imaging., *ACS Nano*, **2011**, 5, 8665–8671.

[19] Wang, X., Zheng, J., Xuan, Y., Yan, X. Optical temperature sensing of NaYbF4: Tm3+@SiO2 core-shell micro-particles induced by infrared excitation, *Optics Express,* **2013**, 21(18).

[20] Frangioni, J. V., In Vivo Near-Infrared Fluorescence Imaging, *Curr. Opin. Chem. Biol*., **2003**, 7, 626–634.

[21] Marquez, G., Wang, L. H. V., Lin, S. P., Schwartz, J. A., Thomsen, S. L. Anisotropy in the Absorption and Scattering Spectra of Chicken Breast Tissue, *Appl. Opt*., **1998**, 37, 798–804.

[22] Aigouy, L., Tessier, G., Mortier, M., Charlot, B., Scanning thermal imaging of microelectronic circuits with a fluorescent nanoprobe, *Appl. Phys. Lett*., **2005**, 87, 184105.

[23] Aigouy, L., Saïdi, E., Lalouat, L., Labeguerie-Egea, J., Mortier, M., Löw, P., Bergaud, C. AC thermal imaging of a microwire with a fluorescent nanocrystal: influence of the near field on the thermal contrast, *J. Appl. Phys.,* **2009**, 106, 074301.

[24] Saıdi, E., Samson, B., Aigouy, L., Volz, S., Low, P., Bergaud, C., Mortier, M. Scanning thermal imaging by near-field fluorescence spectroscopy*, Nanotechnology*, **2009**, 20, 115703.

[25] Balabhadra, S., Debasu, M. L., Brites, C. D. S., Ferreira, R., Carlos, L. Upconverting Nanoparticles Working as Primary Thermometers in Different Media, *The Journal of Physical Chemistry C*., **2017**, 121(25), 13962-13968.

CHAPTER 8

Nd^{3+}-doped bismuth silicate systems as ratiometric NIR-emitting optical thermometers

ABSTRACT: In this chapter few luminescent temperature sensors based on Nd^{3+} ions are discussed. All three compounds of the Bi_2O_3-SiO_2 binary system (see Fig.1 in Chapter 4), the metastable Bi_2SiO_5, the eulytite $Bi_4Si_3O_{12}$ and the sillenite $Bi_{12}SiO_{20}$, have been investigated.

All the different Nd^{3+}-doped compounds were studied in the temperature range from roughly 80 K to 800 K, in order to analyze their thermometric response and asses their applicability as optical temperature sensors based on the FIR technique. For each sample, the $^4F_{5/2}$ (~800 nm) and $^4F_{3/2}$ (~890 nm) pair of thermally coupled levels has been considered, measuring the emission intensity ratio between them.

The results obtained allowed to compute a relative sensitivity S_r of 1.4% K^{-1} for (i) Bi_2SiO_5@SiO_2 NPs, 1.4%K^{-1} for (ii) $Bi_4Si_3O_{12}$ @SiO_2 NPs and 1.5% K^{-1} for (iii) bulk $Bi_{12}SiO_{20}$, respectively. The measurements showed a high grade of repeatability.

Compared to previously discussed Er^{3+}/Yb^{3+} doped Bi_2SiO_5@SiO_2 nanoparticles, Nd^{3+} doped NPs (i) showed similar relative sensitivity values at 300 K (S_r = 1.1% K^{-1} and S_r = 1.4% K^{-1}, for Er^{3+}/Yb^{3+} and Nd^{3+} respectively), similar wide operating temperature ranges (200-800 K and 280-850 K, for Er^{3+}/Yb^{3+} and Nd^{3+} respectively) and high repeatability (>99%). However, Nd^{3+}-doped materials are usually more suitable for bio-imaging applications, since its typical radiative transitions occur in the NIR range, corresponding to the biological transparency window.

8.1 Nd^{3+} NIR-emitting optical thermometers

Nd^{3+}-doped luminescent materials are very versatile for biological applications, particularly as thermal sensors, due to the fact that both excitation and emission lie in the biological window, where the optical absorption from tissues is low[1], even allowing to obtain a depth penetration of tens millimetres, that is many times larger than that obtained with Yb^{3+}/Er^{3+} co-doped probes for deep-tissue imaging[2]. In this case the only source available was a 590 nm light diode, corresponding to another absorption band of Neodymium, but in principle an 800 nm NIR light source would fit best with biological applications. Respect to the previous systems (Chapter 7), the Nd^{3+} based temperature sensing relies on Stokes emission instead of on UC mechanism, resulting in an emission quantum yield two orders of magnitude higher[3].

Regarding Nd^{3+} ions, few different options are available to calculate the FIR parameter, depending on the thermally coupled energy levels considered, each pair with both advantages and disadvantages. For example, if considering (i) $^4F_{5/2}\rightarrow{}^4I_{9/2}$ and $^4F_{3/2}\rightarrow{}^4I_{9/2}$ transitions or (ii) $^4F_{7/2}\rightarrow{}^4I_{9/2}$ and $^4F_{3/2}\rightarrow{}^4I_{9/2}$ transitions, the disadvantage resides in the fact that the emission intensities from the excited levels $^4F_{7/2}$ (~750 nm) and $^4F_{5/2}$ (~810 nm) are ~10^3 times lower respect to the intensity from the $^4F_{3/2}$ (~890 nm) level, eventually making complicated to apply the FIR method. On the other hand, if considering (iii) two Stark components of the $^4F_{3/2}$ multiplet, the short distance in energy between the two lines has the adverse effect of reducing the relative sensitivity of at least one order of magnitude.

Up to now, the vast majority of works on Nd^{3+}-based thermal sensors reports about the FIR parameter as the ratio between intensities of the two Stark sublevels of the $^4F_{3/2}$ multiplet[3-5]. Only few, including this study, deal instead with the ratio between $^4F_{5/2}\rightarrow{}^4I_{9/2}$ and $^4F_{3/2}\rightarrow{}^4I_{9/2}$ transitions. These two emission bands lie in the NIR region, centered at about 810 and 890 nm respectively, and are separated by a quite short energy gap (~900 cm^{-1}). In this case the electronic population of the $^4F_{5/2}$ level increases at the expense of the $^4F_{3/2}$ level, with increasing temperatures, following a Boltzmann-type distribution. The Fluorescence Intensity Ratio (FIR) is calculated as follows:

$$FIR = \frac{I_{810}}{I_{890}} \propto \left(-\frac{\Delta E}{k_B T}\right) \quad (1)$$

where I_{810} and I_{900} are the integrated intensities of the two $^4F_{5/2}\rightarrow{}^4I_{9/2}$ and $^4F_{3/2}\rightarrow{}^4I_{9/2}$ transitions.

The advantage of considering these two transitions in the initial region of the NIR, corresponding to the first biological window (BWI), resides in the fact that a cheap silicon-based detection apparatus can be employed to register the PL emission spectra, respect to transitions occurring in the far NIR region.

8.2 $Bi_2SiO_5:Nd^{3+}@SiO_2$ core-shell NPs

The normalized emission spectra collected at increasing temperatures in Fig.1a show a clear change in the PL emission intensities for the considered emission bands, whereas emission wavelengths remain unaffected. The most relevant emission intensity changes are observed for the $^4F_{5/2} \rightarrow {}^4I_{9/2}$ transition.

The trend of the integrated intensities of the two considered emission bands of Nd^{3+} with increasing temperature can be observed in Fig.1b. The overall luminescence intensity (grey dots) constantly increases from 80 to 700 K, then remains constant until 850 K. The intensity of the transition from $^4F_{3/2}$ level shows an initial enhancement until 550 K, of about 1.6-fold, that gives then way to a slight emission quenching. On the other side, the intensity of the transition from the $^4F_{5/2}$ levels increases uninterruptedly, and is enhanced by a factor of more than 20-fold from 80 to 850 K.

The linearity of the Arrhenius plot in Fig.1c, evidences the thermal equilibrium between the two excited states, in a wide range of temperature, between 280 and 850K. The best fit ($\ln(I_{810}/I_{890})=0.194–1290(1/T)$), allowed to calculate an energy gap of 897 cm^{-1} between the two thermally coupled levels. This accords excellently with the value estimated by the emission spectrum collected at 300 K ($\Delta E = 905\ cm^{-1}$), as the distance in energy between the barycentres of the two emission bands (Fig.1d), ensuring a high degree of reliability.

Fig.1e and 1f depict the temperature dependence of the absolute and relative sensitivities, respectively, showing a value of S_a of $0.25 \cdot 10^{-3}\ K^{-1}$ and S_r of 1.4% K^{-1} in the physiological temperature range. S_r is interestingly high, mainly because of the large energy difference between the thermally coupled levels employed for the FIR method. In comparison with other nano- or sub-micron sized thermometric systems[1, 3-5], it is noteworthy that the results here reported are excellent, both in terms of relative sensitivity in the physiological temperature range and operating range of temperatures.

Finally, the repeatability (or test-retest reliability) was measured by means of a thermal cycling experiment, based on four consecutive heating-cooling cycles between 300 and 800 K, as shown in Fig.2. The computed repeatability is larger than 99%, representing the high reproducibility of the measurements.

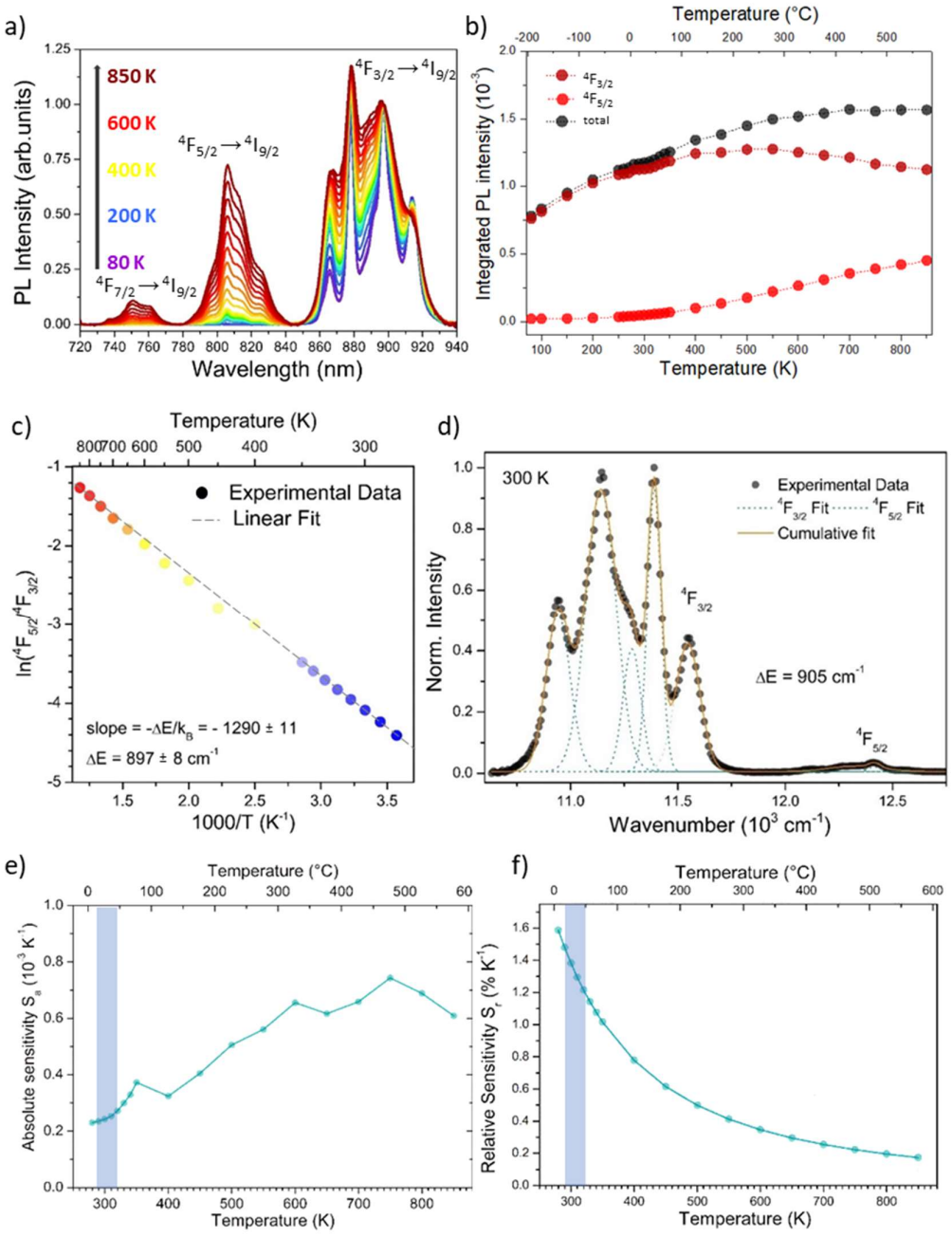

Fig.1 (a) Temperature dependence of PL emission spectra in the 80−850 K range, normalized to the $^4F_{3/2}$ line; (b) Temperature dependence of integrated PL intensities of the Nd^{3+} transitions from $^4F_{5/2}$ (red dots), $^4F_{3/2}$ (dark red dots) and the total sum of their intensities (grey dots); (c) Arrhenius plot in the temperature range of linearity for the Boltzmann law (280-850 K) and estimation of the distance in energy (ΔE) between the two thermally coupled levels; (d)Fit of the spectrum collected at 300 K, for the empirical estimation of ΔE as the distance between the barycenters ($x_{4F3/2}$=11.4x10^3 cm^{-1}, $x_{4F5/2}$=12.3x10^3 cm^{-1}) of the two multiplets; (e) Absolute sensitivity of the Bi_2SiO_5: Nd^{3+}@SiO_2 thermometric system; (f) Relative sensitivity of the Bi_2SiO_5: Nd^{3+}@SiO_2 thermometric system. (The blue frame indicates the physiological temperature range).

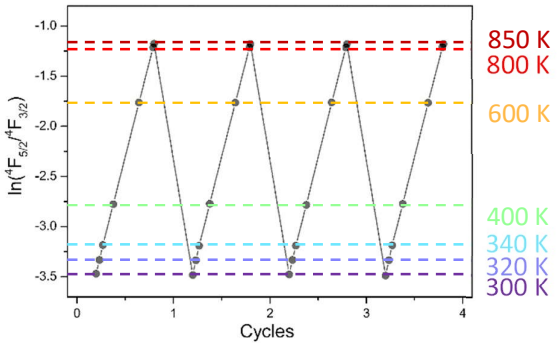

Fig.2 Repeatability upon temperature cycling between 250 and 850 K, R>99%.

8.3 $Bi_4Si_3O_{12}:Nd^{3+}@SiO_2$ core-shell NPs

With the aim to figure out the potential of the $Bi_4Si_3O_{12}:Nd^{3+}@SiO_2$ NPs system as ratiometric nanothermometer, the temperature dependence of the PL emission spectra of the system was investigated in a wide temperature range (100-700 K).

As previously observed also for Bi_2SiO_5: $Nd^{3+}@SiO_2$ NPs, the emission spectra collected for $Bi_4Si_3O_{12}:Nd^{3+}@SiO_2$ NPs at increasing temperatures, normalized on the $^4F_{3/2}\rightarrow{}^4I_{9/2}$ transition, reported in Fig.3a show increasing emission intensities for the bands relative to $^4F_{7/2}\rightarrow{}^4I_{9/2}$ and $^4F_{5/2}\rightarrow{}^4I_{9/2}$ transitions, whereas emission wavelengths remain unaffected. In particular, the most relevant emission intensity changes are observed for the $^4F_{5/2}\rightarrow{}^4I_{9/2}$ transition, as expected.

The integrated intensities of the thermally coupled emission bands of Nd^{3+} as a function of temperature, reported in Fig.3b, show that the overall luminescence intensity (grey dots) increases from 100 to 520 K, and then starts to drop. This reflects the emission intensity from $^4F_{3/2}$ level that after an initial enhancement until 500 K, of about 1.5-fold, starts to decrease because of thermal quenching. On the other side, the intensity of the transition from the $^4F_{5/2}$ levels increases uninterruptedly, and is enhanced by a factor of more than 30-fold from 100 to 700 K.

The plot of the logarithm of the FIR thermometric parameter versus 1000/T reported in Fig.3c exhibits a good linearity between 260 and 700 K, demonstrating that the temperature dependence of the population ratio between the two excited states obeys to the Boltzmann distribution. The best fit ($\ln(I_{810}/I_{890})=0.757–1205(1/T)$), allowed to calculate an energy gap of 837 cm^{-1} between the two thermally coupled levels. This is quite close to the value estimated by the emission spectrum collected at 300 K ($\Delta E=1020\ cm^{-1}$), as the distance in energy between the barycentres of the two emission bands (813 and 887 nm, respectively), as depicted in Fig.3d.

Finally, the temperature dependence of the absolute and relative sensitivities, as indicators of the efficiency of the system in the range of linearity of the Boltzmann law, are reported in Fig 3e and 3f. The calculated values are $S_a = 0.4\cdot10^{-3}\ K^{-1}$ and S_r of 1.4% K^{-1} in the physiological range. S_r is interestingly high, and comparable to the relative sensitivity found in the previous section for Bi_2SiO_5: $Nd^{3+}@SiO_2$.

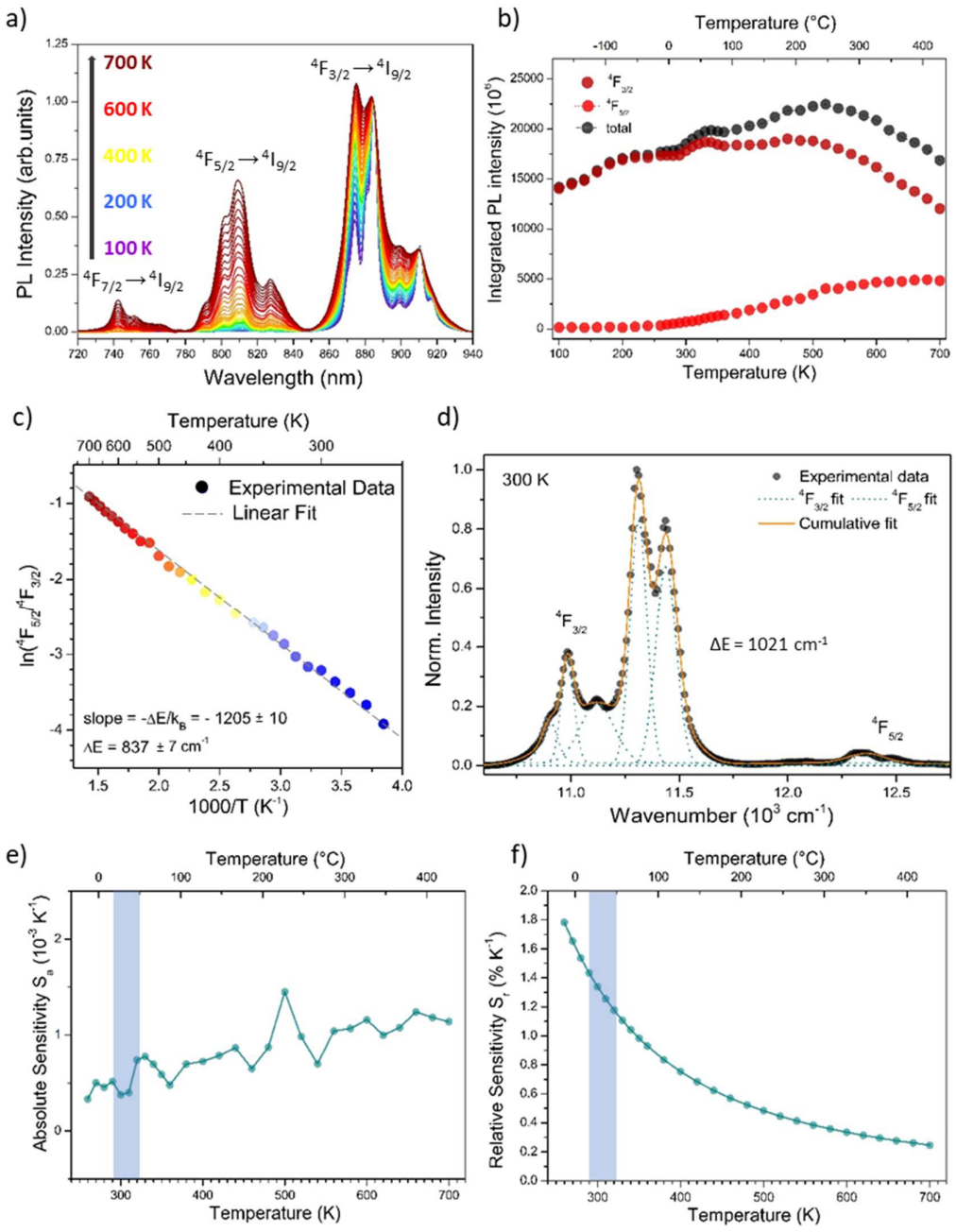

Fig.3 (a) Temperature dependence of PL emission spectra in the 100−700 K range, normalized to the $^4F_{3/2}$ line; (b) Temperature dependence of integrated PL intensities of the Nd^{3+} transitions from $^4F_{5/2}$ (red dots), $^4F_{3/2}$ (dark red dots) and the total sum of their intensities (grey dots); (c) Arrhenius plot in the temperature range of linearity for the Boltzmann law (260-700 K) and estimation of the distance in energy (ΔE) between the two thermally coupled levels; (d)Fit of the spectrum collected at 300 K, for the empirical estimation of ΔE as the distance between the barycenters ($x_{4F3/2}=11.3x10^3$ cm^{-1}, $x_{4F5/2}=12.3x10^3$ cm^{-1}) of the two multiplets, (e)Absolute sensitivity of the $Bi_4Si_3O_{12}:Nd^{3+}@SiO_2$ NPs thermometric system; (f) Relative sensitivity of the $Bi_4Si_3O_{12}:Nd^{3+}@SiO_2$ NPs thermometric system. (The blue frame indicates the physiological temperature range).

8.4 Nd^{3+}-doped $Bi_{12}SiO_{20}$

The temperature dependence of the UCPL emission spectra of the system was investigated in a wide temperature range (80-700 K). The emission spectra collected at increasing temperatures, normalized on the $^4F_{3/2}\rightarrow{}^4I_{9/2}$ transition to emphasize the relative increase of the emission from the $^4F_{5/2}$ excited state (Fig.4a), show a clear change in the emission intensities for the considered emission bands, whereas emission wavelengths remain unaffected. As seen in the previous sections for other Nd-doped Bismuth silicate systems, the most relevant emission intensity changes are observed for the $^4F_{5/2}\rightarrow{}^4I_{9/2}$ transition.

The trend of the integrated intensities of the two considered emission bands of Nd^{3+} with increasing temperature can be observed in Fig.4b. The overall luminescence intensity (grey dots) increases from 80 to 200 K, then starts to decrease and by 550 K drops to very low values. This reflects the emission intensity from $^4F_{3/2}$ level that after an initial enhancement until, starts then to decrease and by 550 K its intensity starts to be drastically reduced because of thermal quenching. On the other hand, the intensity of the transition from the $^4F_{5/2}$ levels increases until 550 K and is enhanced by a factor of about 75-fold from 80 to 550 K.

The linearity of the ln(FIR) versus 1000/T reported in Fig.4c, evidences the thermal equilibrium between the two excited states, in a wide range of temperature, between 260 and 700 K. The best fit ($\ln(I_{820}/I_{900})=0.614–1380(1/T)$), allowed to calculate an energy gap of 959 cm^{-1} between the two thermally coupled levels. This is in good accordance with the value estimated by the emission spectrum collected at 300 K ($\Delta E=1110\ cm^{-1}$), as the distance in energy between the barycentres of the two emission bands (Fig.4d).

Fig.4e and 4f depict the temperature dependence of the absolute and relative sensitivities, respectively, showing a value of S_a of $0.3\cdot10^{-3}\ K^{-1}$ and S_r of 1.5% K^{-1} in the physiological range. S_r is interestingly high, due to the large energy difference between the thermally coupled level, as observed for other Nd^{3+}-doped thermometric system based on the fluorescence intensity ratio between $^4F_{5/2}$ and $^4F_{3/2}$ emitting levels.

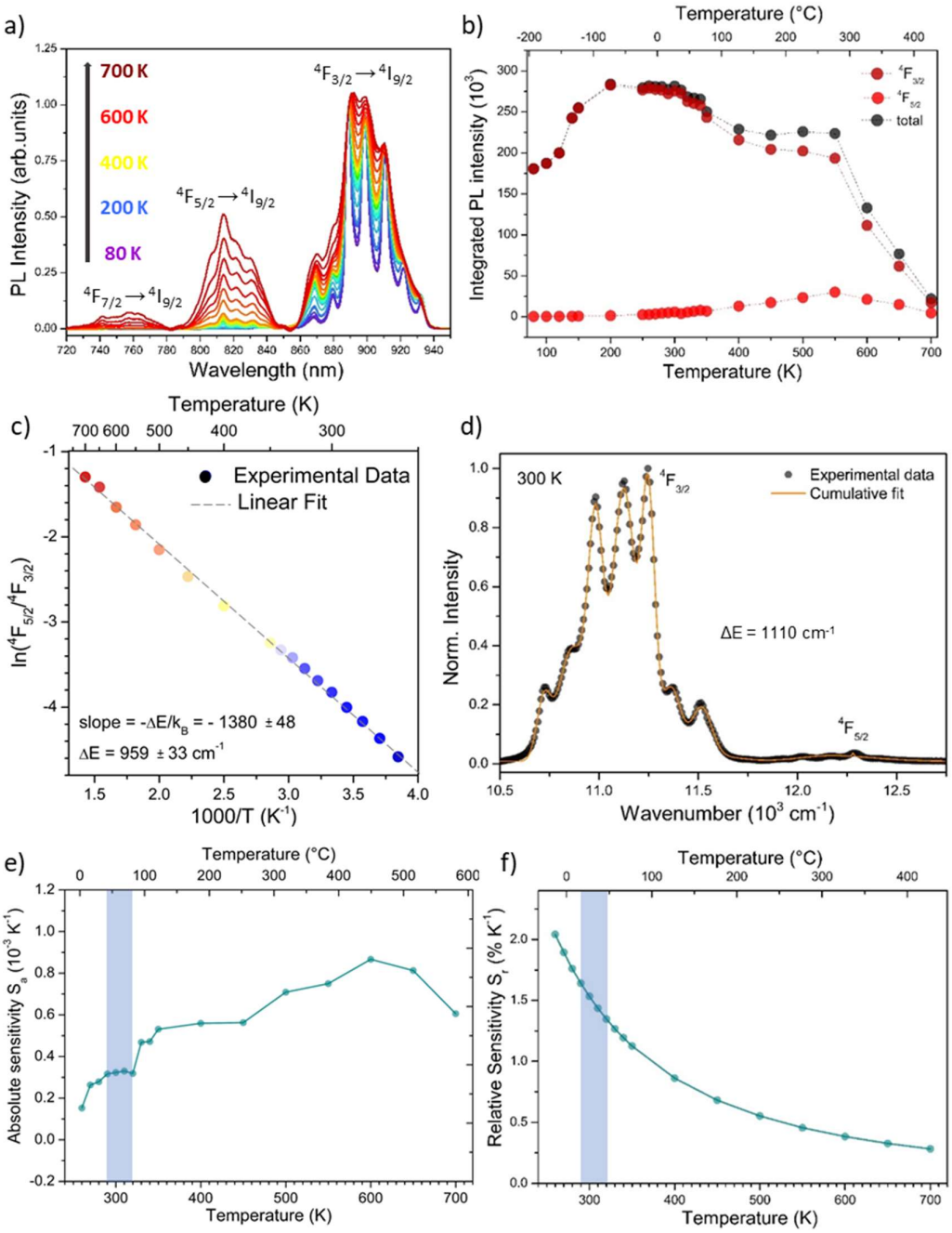

Fig.4 (a) Temperature dependence of PL emission spectra in the 80−700 K range, normalized to the $^4F_{3/2}$ line; (b) Temperature dependence of integrated PL intensities of the Nd^{3+} transitions from $^4F_{5/2}$ (red dots), $^4F_{3/2}$ (dark red dots) and the total sum of their intensities (grey dots); (c) Arrhenius plot in the temperature range of linearity for the Boltzmann law (260-700 K) and estimation of the distance in energy (ΔE) between the two thermally coupled levels; (d) Fit of the spectrum collected at 300 K, for the empirical estimation of ΔE as the distance between the barycenters ($x_{4F3/2}$=11.1x10^3 cm^{-1}, $x_{4F5/2}$=12.2x10^3 cm^{-1}) of the two multiplets; (e) Absolute sensitivity of the $Bi_{12}SiO_{20}$:Nd^{3+}@SiO_2 NPs thermometric system; (f)Relative sensitivity of the $Bi_{12}SiO_{20}$:Nd^{3+}@SiO_2 NPs thermometric system. (The blue frame indicates the physiological temperature range).

8.5 Conclusions

In this Chapter, we have proposed Nd^{3+}-doped bismuth silicate materials as luminescent probes for optical thermometry. Three different matrices, with specific crystal structures, have been investigated: Bi_2SiO_5, $Bi_4Si_3O_{12}$ and $Bi_{12}SiO_{20}$, while Nd^{3+} dopant content was kept fixed at 2%at., since it showed the best performance in terms of luminescence intensity.

To investigate the thermometric performance of the three different phases, we focused on the temperature dependence of the emission intensity in a wide range of temperatures, considering a pair of thermally coupled excited states. The two investigated thermal sensing peaks, corresponding to the $^4F_{5/2}$ (~810 nm) and $^4F_{3/2}$ (~890 nm) radiative transitions to the ground level, are both situated within the first biological window, where the penetration of tissues is deeper due to a reduction in light absorption from water and lipids[6], opening the way for sub-tissue thermal sensing.

In general, for what concerns the systems here investigated, similar relative sensitivities S_r at 300K and operating temperature ranges were found. Table 1 summarizes the Sa and Sr values calculated at 300K, and the temperature ranges of validity for the three systems investigated.

Sample	S_a (10^{-3} K^{-1})	S_r (% K^{-1})	T range (K)
Bi_2SiO_5@SiO_2 NPs	0.25	1.4	280-850
$Bi_4Si_3O_{12}$ @SiO_2 NPs	0.40	1.4	260-700
$Bi_{12}SiO_{20}$ bulk	0.3	1.5	260-700

Table 1. Comparison between the thermometric performance of the different Nd^{3+}-doped bismuth silicate systems studied.

This outcome is similar to what previously reported in literature for the same pair of thermally coupled levels[1,7]. On the other hand, if compared to the works based on the FIR between Stark sublevels[3-5], a superior thermometric performance, both in terms of relative sensitivity and operating range of temperature, is found.

Despite these promising results, significant challenges remain, including the optimization of the dopant concentration to avoid concentration quenching effects and the improvement of the host matrix.

Materials and Methods

Experimental Details.

Photoluminescence (PL) measurements were performed with the use of a USB-powered LED mount (LEDMT1F, Thorlabs) with a 590 nm LED (FWHM = 16 nm), equipped with a collimator, and collecting with a Si CCD spectrometer (QE-65Pro, Ocean Optics) coupled with a fiber. The temperature dependence of PL spectra (80−850 K) was investigated with a temperature-controlled stage (10 035 L, Linkam). All the spectra were calibrated by means of a standard halogen lamp (DH-2000CAL,

Ocean Optics) to obtain spectra in the photon flux scale. In addition, the photon flux per constant wavelength interval function, $\phi(\lambda)$, is converted to photon flux per energy interval using the Jacobian transformation:

$$\frac{d\phi(E)}{dE} \propto \frac{d\phi(\lambda)}{d\lambda}\lambda^2 \tag{2}$$

These measurements have been performed at Kyoto University.

References

[1] Balabhadra, S., Debasu, M. L., Brites, C. D. S., Nunes, L. A. O., Malta, O. L., Rocha, J., Bettinelli, M., Carlos, L. D. Boosting the sensitivity of Nd^{3+}-based luminescent nanothermometers, *Nanoscale,* **2015**, 7, 17261−17267.

[2] Savchuk, O., Carvajal, J. J., De la Cruz, L. G., Haro-González, P., Aguiló, M., Díaz, F., Luminescence thermometry and imaging in the second biological window at high penetration depth with Nd:KGd(WO4)2 nanoparticles, *J. Mater. Chem. C*, **2016**, 4(31), 7397-7405.

[3] Wawrzynczyk, D., Bednarkiewicz, A., Nyk, M., Strek, W., Samoc, M. Neodymium(III) doped fluoride nanoparticles as noncontact optical temperature sensors, *Nanoscale*, **2012**, 4, 6959−6961.

[4] Rocha, U., Jacinto da Silva, C., Ferreira Silva, W., Guedes, I., Benayas, A., Martinez Maestro, L., Acosta Elias, M., Bovero, V., van Veggel, F. C. J. M., García Solé, J. A., Jaque, D. Subtissue thermal sensing based in neodymium-doped LaF_3 nanoparticles, *ACS Nano* **2013**, 7, 1188−1199.

[5] Benayas, A., del Rosal, B., Pérez-Delgado, A., Santacruz-Gómez, K., Jaque, D., Hirata, G. A., Vetrone, F. Nd:YAG Near-Infrared luminescent nanothermometers, *Adv. Opt. Mater*. **2015**, 3, 687−694.

[6] Sordillo, L., Pratavieira, S., Pu, Y., Salas-Ramirez, K., Shi, L., Zhang, L., Budansky, Y., Alfano, R. Third therapeutic spectral window for deep tissue imaging Proceedings of SPIE - The International Society for Optical Engineering, **2014**.

[7] Jiang, G., Wei, X., Zhou, S., Chen, Y., Duan, C.-K., Yin, M., Neodymium doped lanthanum oxysulfide as optical temperature sensors, *Journal of Luminescence*, **2014**, 152, 156-159.

CHAPTER 9

Conclusions and future perspectives

The technological revolution we are facing nowadays due to the introduction of nanotechnology in daily life has led to an increasing demand towards the development of new efficient nanomaterials. Nevertheless, the real integration of nanoparticles and nanotechnology in industrial and scientific applications has yet to reach its apex and this is particularly true for biological applications. In this field, luminescent nanomaterials can address several challenges and provide innovative solutions, due to their unique optical properties different from other conventional bulk fluorophores. In parallel, many other fields of photonics, such as lasing, energy harvesting, anti-counterfeiting and lightening are investing on nanotechnologies, continuing to break new-frontiers. In this context, the phrenetic race to the innovation demands continuous technical progresses and the development of new luminescent nanomaterials with improved performances.

From the technological point of view, if from one hand the uniformity of the nanoparticles is still a critical parameter for many families of compounds, on the other hand, the ability to control the response of the materials to external stimuli could pave the way for new applications. In recent years, a lot of interest was gained by the potential of luminescent nanothermometry to probe intracellular temperature or to map the dissipation in microelectronic circuits, but also to locally probe phase transition temperatures and to measure *in-situ* thermal gradients in catalytic reactions. In this view, the stability of nanomaterials towards different harsh parameters, such as high temperatures, pressure or acid/basic environments, has become a fundamental requirement.

With this challenge in mind, we proposed a new bismuth-based luminescent nanosystem for a wide spectrum of potential applications, that could range from multi-modal bioimaging to anti-counterfeiting, lightening, intra-cellular temperature sensing and contact-less thermometry in catalytic reactions. In particular, low toxicity, low cost and high atomic number (Z) bismuth-based compounds are extremely suitable for the development of diagnostic nanoprobes, allowing to integrate numerous imaging techniques.

We discussed the development of a new class of UCNP: Bi_2SiO_5:Ln@SiO_2, through a

simple three-steps strategy: the synthesis of monodisperse Ln-doped Bi_2O_3 NPs, the growth of a silica shell and finally a thermal treatment for the stabilization of the desired system. Uniform, monodispersed, crystalline, lanthanide-doped (Yb, Er, Ho and Tm) nanoparticles were obtained, with a high control on particle shape and size (which can be complicated in particular in the case of oxides). The formation of the Bi_2SiO_5 single phase was triggered by the local reactivity between Bi_2O_3 and SiO_2, in the Bi_2O_3@SiO_2 system, leading to a double layered Bi_2SiO_5@SiO_2 hollow nanosystem. The accurate choice of precipitant and capping agents allowed to modulate the size of the obtained spherical NPs. The fine control of the SiO_2 shell thickness as a function of the silicon precursor (TEOS) added into the reaction, was modelled on a theoretical and experimental approach. The silica coating thickness proved to be a fundamental parameter on the stabilization of the expected phase, alongside calcination temperature. The improvement of all these factors, led in the end to the stabilization of the metastable Bi_2SiO_5 phase. Moreover, the ideal dopant concentration was established, in order to keep morphology and size unchanged. The tunability of the UC emission was investigated by co-doping the system with different combinations and relative concentrations of lanthanide ions. A cell viability assay was conducted on four different cell lines, demonstrating the high biocompatibility of Bi_2SiO_5:Ln@SiO_2 UCNPs. We proved also that the silica coating was beneficial to the mitigation of the well-known bismuth silicate photocatalytic activity, that in this case resulted to be unwanted, eventually representing a limiting factor to some destinations of use. By considering potential applications as biomarker for tumoral cell temperature or as thermometer for chemical reactors, another key parameter is the stability of the material to the surrounding environment. As a matter of fact, chemical stability at different pH is an essential requirement. For this reason, we investigated the resistance of Bi_2SiO_5@SiO_2 NPs to the exposure to acid solutions with different pH, proving the overcoming of the bottleneck of the instability in acid environments, that is typical for bismuth-based materials, up to pH<1.

With the aim to design an ideal optical nanothermometer for a broad temperature range to be used in biological and different catalytic environments, the key parameters are (i) a high degree of reliability, (ii) the ability to discriminate small variation of temperature together with (iii) increased stability at high temperatures and extreme environments. A unique reliability can be achieved by designing a ratiometric thermometer based on the Maxwell-Boltzmann distribution of two thermally coupled excited states. The potential of the Bi_2SiO_5:Ln@SiO_2 nanosystem as ratiometric nanothermometer was then demonstrated, investigating the temperature dependence of the emission intensity from the thermally coupled levels of Er^{3+} ($^2H_{11/2}$/$^4S_{3/2}$) (i), Tm^{3+} ($^3F_{2,3}$/$^3H_4$ and $^3F_{2,3}$/$^1G_4$) (ii) and Nd^{3+} ($^4F_{5/2}$/$^4F_{3/2}$) (iii), in a wide range of temperatures (80-800K). Among the most important parameters used to evaluate the potentials of the system, the relative sensitivity S_r was demonstrated to be a figure of merit useful to compare the performances irrespective to the nature of the thermometer. S_r, calculated in the range of linearity of the Boltzmann law, showed appealing values for all the three systems: 1.1 (i), 1.3 (ii) and 1.4% K^{-1} (iii), respectively. All the measurements showed a high degree of repeatability. As a

comparison, also Nd^{3+}-doped $Bi_4Si_3O_{12}$@SiO_2 NPs (iv) and bulk $Bi_{12}SiO_{20}$ (v), i.e. the other compounds of the Bi_2O_3-SiO_2 binary system, were investigated. Similar S_r values were found: 1.4 (iv) and 1.5%K^{-1} (v), respectively.

We concluded that the visible emitted wavelength generated by Er^{3+} ions restricts their real bioapplication due to their short tissue penetration depths (caused by tissue scattering and specific absorptions of tissue components such as melanin and hemoglobin). Tm^{3+} ions might be considered as an alternative, thanks to the strong emission at around 800 nm lying within the first biological window (700-950 nm). However, a 980 nm infrared laser as excitation source, required to excite Yb^{3+} co-doped UC systems, is not the best option for biological applications, falling between the first and second biological windows, where light absorption from water arises.

On the other hand, Nd^{3+}-doped luminescent materials are very versatile for biological applications, particularly as thermal sensors, due to the fact that both excitation and emission lie in the biological window, where the optical absorption from tissues is low, even allowing to obtain a depth penetration of tens millimetres, that is many times larger than that typically obtained with Yb^{3+}/Er^{3+} co-doped probes for deep-tissue imaging. However, they usually suffer from low thermal sensitivity. This means that up to date, a flawless thermometric probe has yet to be discovered.

This research showed promising results and answered many questions. Nevertheless, ample room is available for experimental and theoretical investigations to be conducted in the future.

Speaking of the properties of Bi_2SiO_5:Ln@SiO_2 NPs, despite the encouraging outcome, some challenges remain, such as the improvement of the emission efficiency by optimization of the ratio and relative concentration of dopants, the better control of particle size, the optimization of the colloidal stability, and the improvement of temperature resolution and sensitivity.

Towards the eventual translation to the fabrication of Bi_2SiO_5:Ln@SiO_2 as probes for bioimaging, efforts should be focused on the need to overcome the biological obstacles faced by Bi-NPs *in vivo*, optimizing their physicochemical properties for a better cellular internalization and extensively investigating the *in vivo* toxicity of the NPs. In fact, surface functionalizations are tremendously important to determine the toxicity and the effectivity of NPs when they are introduced into the body. To improve the circulation time of the nanostructures, PEG modification could help escaping the reticulo-endothelial system and some nonspecific uptake mechanisms. Moreover, the synthesis of targeted NPs would be essential to improve the possibility of using these materials in medical imaging, allowing to vastly reduce the concentration of NPs to be administered, minimizing toxicity and side-effects.